Formation and Eruption of Coronal Magnetic Flux Ropes: Observations and Modelling

Alexander William James

A dissertation submitted in partial fulfillment

of the requirements for the degree of

Doctor of Philosophy

of

University College London.

Department of Space and Climate Physics

University College London

23rd June 2019

I, Alexander William James, confirm that the work presented in this thesis is my own. Where information has been derived from other sources, I confirm that this has been indicated in the thesis.

Abstract

Coronal mass ejections (CMEs) are eruptions of billions of tonnes of plasma and associated magnetic fields from the solar atmosphere that can affect the near-Earth environment. In order to produce accurate long-term forecasts of space weather, we need to develop the ability to predict CMEs days before they occur. This requires a full understanding of the mechanisms involved in triggering and driving CMEs, which in turn involves discerning the pre-eruptive configuration of the coronal magnetic field.

In this thesis, I use extreme-ultraviolet observations to infer that the pre-eruptive coronal configuration of a CME that occurred on 14 June 2012 was that of a magnetic flux rope. This flux rope formed in a hyperbolic flux tube (HFT) configuration via magnetic reconnection high up in the solar corona — a scenario which has not previously been studied in great quantity or detail. It is proposed that the coronal reconnection that formed the flux rope was forced by the observed 'orbiting' motion of newly-emerging magnetic flux in the photosphere.

A numerical model of the coronal magnetic field on 14 June 2012 is produced via the nonlinear force-free field extrapolation of photospheric field measurements. The model shows exceptional agreement with the observational analysis, confirming the presence of the HFT flux rope. Furthermore, the model suggests that the eruption of the flux rope was driven by the torus instability.

Four additional cases of pre-eruptive HFT flux ropes are identified, and similar photospheric 'orbiting' motions are observed whilst the flux ropes formed. This suggests that these motions are systematically involved in triggering the formation of HFT flux ropes via magnetic reconnection in the corona.

Impact Statement

Plasma and magnetic fields can be ejected from the Sun in the form of coronal mass ejections (CMEs), which can cause a range of potentially-damaging effects on Earth and in the near-Earth environment. The research in this thesis is a step towards understanding the causes of CMEs, and therefore towards being able to accurately forecast these 'space weather' effects.

Producing space weather forecasts that enable us to prepare for the impact of CMEs may in some cases require the prediction of CMEs before they occur. To be able to do this, we must first develop an understanding of the mechanisms involved in CME initiation, including the configuration of the pre-eruptive magnetic field, the processes that form pre-eruptive structures, the timescales these structures are stable for, and the mechanisms that drive their eventual eruptions.

In this thesis, I provide new insight in to each of these open topics using a combination of observational and modelling techniques. I identify signatures that are indicative of the formation of pre-eruptive magnetic flux ropes, and determine the mechanisms by which flux ropes form and erupt. Space weather forecasters could monitor the Sun for similar signatures to improve their capabilities of recognising the development of potentially-eruptive structures.

The results obtained in this thesis can also be applied to improving the operation of upcoming missions, such as the European Space Agency's *Solar Orbiter* spacecraft. *Solar Orbiter* aims to investigate solar magnetic activity, including CMEs, but will only take remote sensing observations during limited time-windows. Therefore, its remote sensing observations will need to be planned effectively, and the conclusions obtained in this thesis will be valuable for selecting target regions

on the Sun at the appropriate times to observe CMEs.

Outside the field of solar physics, knowledge of solar activity can be applied to other stars. This will be necessary when considering the relationship between exoplanets and their stars. Furthermore, here on Earth, the instabilities of toroidal plasma structures studied in this work are relevant to the development of nuclear fusion techniques in tokamaks.

Publications

1. Baker, D., van Driel-Gesztelyi, L., Brooks, D.H., Valori, G., **James, A.W.**, Laming, J.M., Long, D.M., Demoulin, P., Green, L.M., Matthews, S.A., Olah, K., and Kovari, Z. (2019). Transient Inverse-FIP Plasma Composition Evolution within a Confined Solar Flare. Astrophysical Journal, 875:35. doi:10.3847/1538-4357/ab07c1.

2. Baker, D., Brooks, D.H., van Driel-Gesztelyi, L., **James, A.W.**, Demoulin, P., Long, D.M., Warren, H.P., Williams, D.R. (2018). Coronal Elemental Abundances in Solar Emerging Flux Regions. Astrophysical Journal, 856:71. doi:10.3847/1538-4357/aaadb0.

3. Palmerio, E., Kilpua, E.K.J., Möstl, C., Bothmer, V., **James, A.W.**, Green, L.M., Isvanin, A., Davies, J.A., Harrison, R.A. (2018). Coronal Magnetic Structure of Earthbound CMEs and In Situ Comparison. Space Weather, 12:442-460. doi:10.1002/2017SW001767.

4. **James, A.W.**, Valori, G., Green, L.M., Liu, Y., Cheung, M.C.M., Guo, Y., van Driel-Gesztelyi, L. (2018). An Observationally Constrained Model of a Flux Rope that Formed in the Solar Corona. Astrophysical Journal Letters, 855:L16. doi: 10.3847/2041-8213/aab15d.

5. **James, A.W.**, Green, L.M., Palmerio, E., Valori, G., Reid, H.A.S., Baker, D., Brooks, D.H., van Driel-Gesztelyi, L., Kilpua, E.K.J. (2017). On-Disc Observations of Flux Rope Formation Prior to Its Eruption. Solar Physics, 292:71. doi: 10.1007/s11207-017-1093-4.

6. Palmerio, E., Kilpua, E.K.J., **James, A.W.**, Green, L.M., Pomoell, J., Isvanin, A., Valori, G. (2017). Determining the Intrinsic CME Flux Rope Type Using Remote-sensing Solar Disk Observations. Solar Physics, 292:39. doi: 10.1007/s11207-017-1063-x.

Acknowledgements

I acknowledge the support of the Leverhulme Trust Research Project Grant 2014-051 and the Royal Society. HMI and AIA are instruments onboard SDO, a mission for NASA's Living with a Star program. Data are courtesy of the SDO science teams. *Hinode* is a Japanese mission developed and launched by ISAS/JAXA, with NAOJ as domestic partner and NASA and STFC (UK) as international partners. *Hinode* is operated by these agencies in co-operation with ESA and NSC (Norway). This research has made use of SunPy, an open-source and free community-developed solar data analysis package written in Python (SunPy Community et al., 2015).

I would like to thank to Graham Barnes, K.D. Leka, Yang Liu, and Emilia Kilpua for hosting and assisting me when I visited their institutions. I also give thanks to Jose-Carlos del Toro Iniesta for visiting MSSL to give a course on spectropolarimetry. Furthermore, to Erika Palmerio, who visited MSSL during one of the first weeks of my PhD and has been a valued collaborator and friend ever since.

I am grateful for all of the support, advice, and encouragement given by my supervisors Prof. Lucie Green, Dr. Gherardo Valori, and Prof. Lidia van Driel-Gesztelyi. Further to this, the entire MSSL solar group has provided me with so much assistance and inspiration. This includes and extends to every member of office G01, who have been (and will continue to be) incredible friends, along with so many other MSSL students. I would also like to thank Christopher Owen and Alan Hood for taking the time to read and examine this thesis.

Last but not least, I am thankful to my parents, my brother, and Rachel Smith, who have all given me so much support.

Acronyms

AIA *Atmospheric Imaging Assembly*, pp. 7, 52–54, 56, 98, 99, 101, 105, 109, 110, 112, 116, 119, 120, 123, 129, 130, 133, 145–147, 151, 159, 166, 172

AR active region, pp. 37, 98, 101, 105, 109, 112, 114, 116, 120–122, 124–127, 130, 133, 139, 146, 151, 153, 154, 158, 159, 161, 166, 167, 170, 172, 174, 175, 180–182

BPSS bald patch separatrix surface, pp. 41, 42, 44, 97, 98, 119, 123, 140, 146, 179, 188, 190

CCD charge-coupled device, pp. 53, 54, 57–59, 61, 64, 99

CEA cylindrical equal-area, pp. 62, 85, 86, 99, 104, 127, 129

CME coronal mass ejection, pp. 3, 4, 46–48, 51, 52, 64, 73, 75, 95, 96, 98–101, 105, 115–117, 120, 122–124, 126, 127, 130, 136, 139, 141, 142, 144–147, 151, 153, 154, 157–159, 161, 166, 167, 170, 172, 174, 175, 178–183, 185–188, 190–192

DEM differential emission measure, pp. 110, 125, 133

DKIST Daniel K. Inouye Solar Telescope, p. 192

EIS *EUV Imaging Spectrometer*, pp. 64, 98, 99, 110

EST European Solar Telescope, p. 192

EUV extreme-ultraviolet, pp. 3, 24, 37, 40, 42, 44, 52, 53, 68, 97–99, 101, 105, 109, 110, 117, 124, 126–129, 133, 142, 145–147, 151, 154, 159, 166, 172, 179, 186

EUVI *Extreme-Ultraviolet Imager*, pp. 72, 153

FIP first-ionisation potential, pp. 98, 110, 111, 120

FWHM full width at half maximum, pp. 58, 59

GIC geomagnetically induced current, pp. 47, 185

GOES *Geostationary Operational Environmental Satellite*, pp. 67, 68, 99, 105, 119, 147, 153, 154, 159, 161, 166, 167, 170, 172, 174, 175

HFT hyperbolic flux tube, pp. 3, 41, 42, 44, 97, 98, 119, 123, 139–141, 143, 144, 146, 151, 159, 166, 172, 178, 179, 181, 183, 184, 186, 188–190

HMI *Helioseismic and Magnetic Imager*, pp. 7, 10, 56–59, 61, 62, 64, 73, 93, 96, 98, 99, 101, 104, 105, 109, 110, 112, 120, 126, 127, 129, 146–148, 154, 161, 167, 174

ICME interplanetary coronal mass ejection, pp. 47, 100, 101, 117

ISS image stabilisation system, p. 57

LASCO *Large Angle and Spectrometric Coronagraph*, pp. 70, 71, 99–101, 115, 145, 151, 153, 159, 172

LFFF linear force-free field, pp. 77, 78

LHS left-hand side, pp. 29, 75

MHD magnetohydrodynamic, pp. 27–29, 50, 51, 75, 81, 135, 140, 178, 190

NLFFF nonlinear force-free field, pp. 3, 79, 80, 83, 91, 94, 95, 126–130, 138, 139, 187, 189, 190, 192

NOAA National Oceanic and Atmospheric Administration, pp. 37, 62, 98, 101, 105, 109, 112, 114, 116, 120–122, 124–127, 130, 133, 139, 146, 151, 153, 154, 158, 159, 161, 166, 167, 170, 172, 174, 175, 180–182

NRH Nançay Radioheliograph, pp. 66, 98, 100, 112, 114, 115, 123

PFSS potential field source surface, p. 114

PIL polarity inversion line, pp. 39, 40, 42, 44, 98, 105, 146, 150, 151, 153, 159, 166, 181, 190

QSL quasi-separatrix layer, pp. 41–43, 45, 140

RHS right-hand side, pp. 28, 31, 75, 81

SDO *Solar Dynamics Observatory*, pp. 7, 52, 54, 56, 64, 93, 98, 99, 101, 123, 125, 126, 129, 132, 133, 142, 143, 145–147, 153, 154, 161, 174

SECCHI *Sun Earth Connection Coronal and Heliospheric Investigation*, p. 72

SEP solar energetic particle, pp. 47, 185

SHARP Spaceweather HMI Active Region Patch, pp. 62, 86, 96, 99, 101, 127, 146–148, 154, 161, 167, 174

SOHO *Solar and Heliospheric Observatory*, pp. 69–71, 99, 101, 145

SOT *Solar Optical Telescope*, p. 93

STEREO *Solar Terrestrial Relations Observatory*, pp. 71, 72, 99, 100, 145, 153, 166

UV ultraviolet, pp. 52, 53

XRS *X-ray Sensor*, pp. 68, 99, 147

XRT *X-ray Telescope*, p. 105

Contents

List of Figures

List of Tables

Chapter 1

An Introduction to the Sun

1.1 Structure of the Sun

The Sun is approximately 4.6 billion years old (Bonanno and Fröhlich, 2015) and is currently in the main-sequence phase of its stellar life cycle. It is predicted to remain so for a further 6.4 billion years (Sackmann et al., 1993). The radius of the Sun ($R_\odot$) is approximately 696 Mm (from its centre to the photosphere; see Section 1.1.2.1).

The Sun consists of plasma: gas that has been ionised under heating, and has a magnetic field. Different layers of solar structure can be classified based on the temperature and density of plasma, and these layers are described in Sections 1.1.1 and 1.1.2.

1.1.1 The Solar Interior

Extending out to 0.25 $R_\odot$ from the centre of the Sun is the hot, dense core. The core has a temperature of 15 MK, which is hot enough for the nuclear fusion of hydrogen into helium along the proton-proton chain (Phillips, 1995). In addition to positrons and neutrinos, gamma ray photons are emitted during the fusion process.

Surrounding the core is a layer that extends from roughly $0.25-0.7$ $R_\odot$ in which the transfer of energy is dominated by radiation. The photons produced by nuclear fusion in the core have a very short mean free-path in the radiative zone due to the high density of free electric charges. Therefore, individual photons will undergo many Thomson scattering events before they escape the radiative zone.

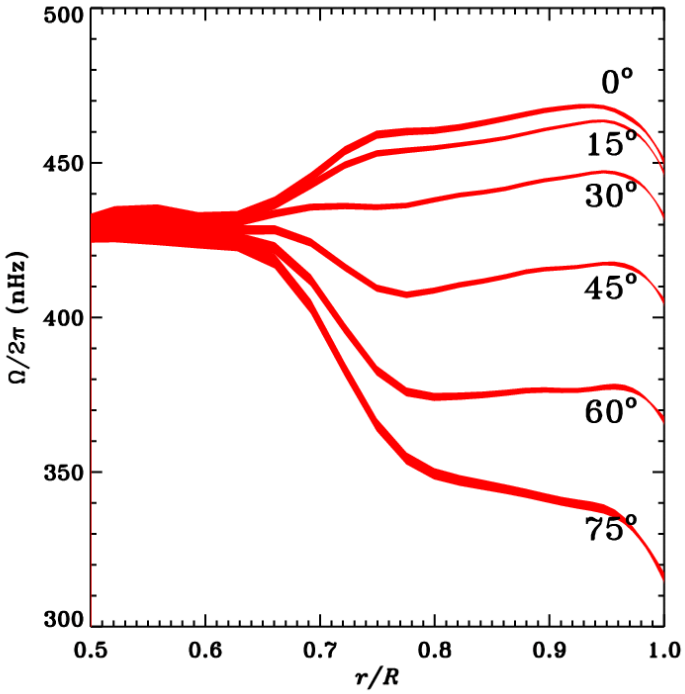

Figure 1.1: Rotational frequency varies with both latitude and radius throughout the convective zone ($0.7-1.0$ $R_\odot$). Image from the Global Oscillation Network Group (`https://gong.nso.edu/gallery/disk2k10/data/resource/torsional/torsional.html`).

Across the radiative zone, the temperature drops to ≈1 MK (Phillips, 1995).

The increase in opacity with radial distance from $0.7-1.0$ $R_\odot$ establishes a steep temperature gradient. This temperature gradient is sufficient to enable convection, and therefore this layer of the Sun is called the convective zone. Here, bulk motions bring plasma up to the surface where it may then radiate photons, cool down, and sink once again. This establishes cells of convection beneath the solar surface.

Unlike the radiative zone, which rotates as a solid-body, the convective zone rotates differentially. In other words, the rotational velocity of the convective zone depends on depth beneath the surface and latitude, with faster rotation at low latitudes and slower rotation at high latitudes (see Figure 1.1).

The difference in rotational velocity between the radiative zone and the convective zone creates a thin ($\sim$ 30 Mm) layer of strong shearing, called the tachocline. This is where the solar dynamo is located, amplifying the Sun's magnetic

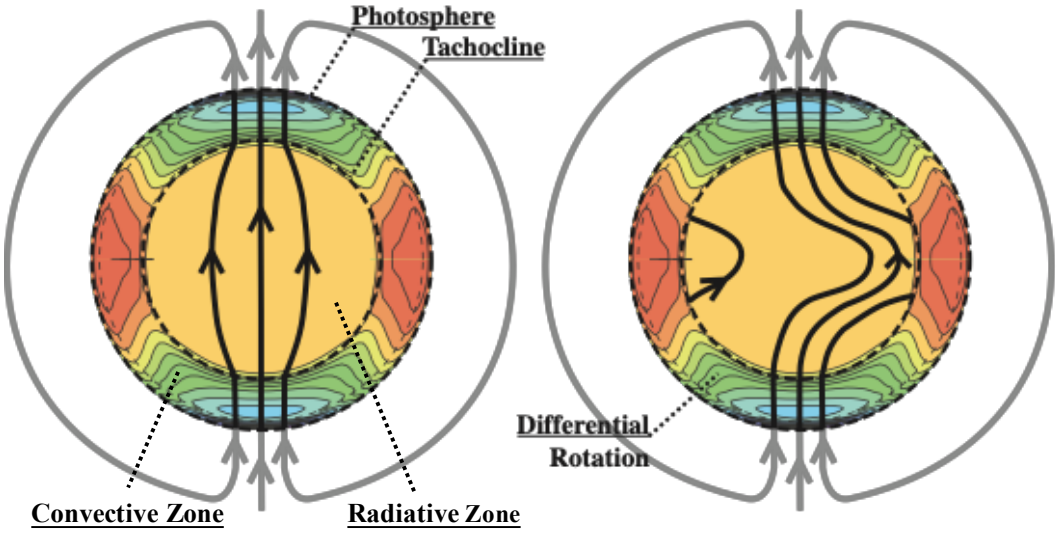

Figure 1.2: The solar dynamo. The differential rotation of the convective zone is faster (red) at low latitudes and slower (blue) at high latitudes. The gradient in rotational velocity between the radiative and convective zones shears the poloidal (north-south) magnetic field, introducing a toroidal (east-west) component. Adapted from Higgins (2012).

field and introducing a toroidal field-component to the previously poloidal field (see Figure 1.2).

1.1.2 The Solar Atmosphere

Here, the layers of the Sun above 1 $R_\odot$ are collectively called the solar atmosphere. The differential rotation seen in the convective zone also occurs at the base of the solar atmosphere.

1.1.2.1 The Photosphere

The photosphere is the layer from which visible light escapes the Sun (*i.e.*, where the optical depth $= 1$) and can travel freely away from the Sun. Therefore, it is commonly regarded as the Sun's "surface". The photosphere is $\sim$500 km thick, has a temperature of $\approx$ 6000 K and a particle (hydrogen) density of 10^{23} m^{-3}.

As introduced previously, the layer beneath the photosphere consists of convection cells where hot plasma rises towards the surface and cool plasma falls back down. The tops of these convection cells manifest in the photosphere as 'granules' that are $\approx$1 Mm wide (Hood and Hughes, 2011). The pattern of granulation in the

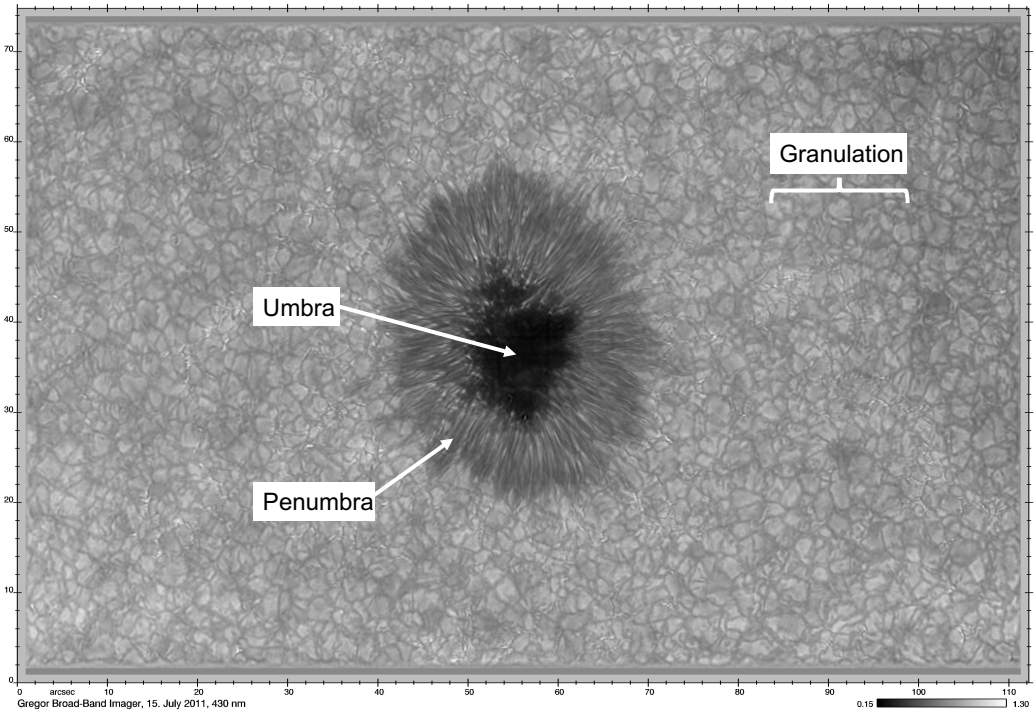

Figure 1.3: An image of the solar photosphere taken at 430 nm by the GREGOR telescope, featuring granulation and a sunspot (umbra and penumbra). Figure adapted from Schmidt et al. (2012).

photosphere can be seen in Figure 1.3. Larger-scale convection cells called supergranules are also observed. Supergranules are ≈30 Mm wide and contain many individual granules (Rieutord and Rincon, 2010).

Sunspots are relatively dark features that are observed in the photosphere where magnetic fields generated in the solar interior penetrate through the surface. Since they are the photospheric manifestation of emerging closed magnetic loop systems, sunspots generally exist in pairs. Sunspot pairs are aligned roughly in the east-west direction, such that they may be labelled as a 'leading' spot and a 'trailing' spot in the sense of solar rotation. The magnetic fluxes of trailing polarities are often dispersed over larger areas than in leading sunspots (*e.g.* van Driel-Gesztelyi and Green, 2015), meaning that sometimes only the leading polarity appears as a coherent dark spot.

The presence of a strong radial magnetic field component suppresses convection beneath the solar surface, meaning that heat from the interior will not be transported to the surface as efficiently. This is why sunspots are cooler and appear

darker than their photospheric surroundings. The magnetic field is most-radial at the centre of a sunspot, whereas the field has a stronger horizontal component around the edge. Therefore, a sunspot is seen to have a dark, central 'umbra' and a less-dark surrounding 'penumbra' (see Figure 1.3). Typical magnetic field strengths in sunspot umbrae can be ~ 3000 G (Hood and Hughes, 2011).

1.1.2.2 The Chromosphere and Transition Region

Above the photosphere is the chromosphere. The chromosphere is ≈ 10 Mm thick, across which the temperature increases from 6000 K to 35000 K. The chromosphere has a hydrogen density of 10^{19} m^{-3}.

Above the chromosphere is the transition region. Here, the temperature increases dramatically from 10^5 K to 10^6 K across only 100 km.

1.1.2.3 The Corona

Above the transition region is the extremely hot ($10^6 - 10^7$ K) but tenuous (10^{15} particles m^{-3}) corona. The corona emits strongly in the extreme-ultraviolet (EUV) part of the electromagnetic spectrum.

Plasma flows along magnetic field lines in the corona (see Section 1.2.2.2) and emits EUV light. The corona therefore appears bright above groups of sunspots where strong magnetic field loops are formed. These areas are known as active regions, which are discussed in greater detail in Section 1.3.1.

1.2 Magnetic Fields

When discussing magnetic fields, it is useful to define the concept of magnetic field lines. Magnetic field lines are theoretical lines that are tangential to the magnetic field vector at all points.

The solar magnetic field is amplified in the solar interior at the tachocline in a process known as the solar dynamo. Plasma flows along loops of magnetic field (see Section 1.2.2.2 for a discussion of Alfvén's law of magnetic flux being 'frozen-in' to plasma), and we can therefore introduce the concept of a magnetic flux tube. A magnetic flux tube is defined such that the magnetic field is tangent to its (lateral) surface, and therefore the magnetic flux through any cross-section of the tube is

constant. This has the effect that any plasma within the tube stays within the tube.

We may understand how magnetic fields are transported from the tachocline to the surface by considering a magnetic flux tube in a surrounding medium where there is no magnetic field. In their review of flux emergence, Cheung and Isobe (2014) describe how, if the pressure within the flux tube (gas pressure + magnetic pressure) is balanced by the pressure of its surroundings (gas pressure only), then the internal gas pressure of the flux tube must be lower than the external gas pressure. For this to be true, a flux tube with the same temperature as its surroundings must have a lower density than its surroundings, and will therefore be buoyant and rise towards the solar surface (Parker, 1955).

As a rising flux tube approaches the photosphere, the density of the surrounding environment decreases until eventually the flux tube is no longer buoyant. On its own, the flux tube is unable to continue rising and therefore cannot penetrate through the surface into the solar atmosphere. Subsequently-rising flux tubes pile-up beneath the photosphere, causing an increase in magnetic pressure. As the magnetic pressure increases, a buoyancy instability may set in, enabling a small amount of magnetic flux to emerge in to the solar atmosphere (Acheson, 1979; Archontis et al., 2004; Reviewed by Hood and Hughes, 2011). Additionally, convective motions in granules can help carry magnetic flux in to the photosphere on small scales (as described by Pariat et al., 2004). To summarise, convection causes a magnetic flux tube to undulate as parts of the tube rise and fall. Parts of a serpentine flux tube emerge in to the atmosphere as small loops, creating observable patterns of alternating positive and negative magnetic flux in the photosphere. Further motion can cause oppositely-oriented parts of the flux tube to converge, enabling magnetic reconnection (see Section 1.2.3 for more on reconnection). This reconnection forms 'Ω-loops' that expand in to the solar atmosphere, as well as dipped 'U-loops' that can submerge beneath the photosphere.

It has been shown that, unless flux tubes are twisted, they will not survive the tumultuous journey through the convective zone (Emonet and Moreno-Insertis, 1998; Hughes et al., 1998).

Where strong magnetic field penetrates the surface, we see dark features called sunspots (as described in Section 1.1.2.1).

1.2.1 Plasma Properties

A (fully-ionised) plasma is a collection of freely moving electrons and ions. Due to their lower mass, electrons are much more mobile than ions (for equal energy) and form 'clouds' around positive charges. The apparent total charge, and therefore the electrostatic force, falls to zero within a certain distance from the ions, known as the Debye length. The Debye length, λ_D, is defined as

$$\lambda_D = \sqrt{\frac{\varepsilon_0 k_B T}{e^2 n_0}}, \tag{1.1}$$

where ε_0 is the permittivity of free space, k_B is the Boltzmann constant, T is the plasma temperature, e is the charge of an electron, and n_0 is the average number density of the plasma. In the corona ($T \sim 10^6$ K, $n_0 \sim 10^{15}$ m^{-3}), the Debye length is $\lambda_D \sim 10^{-3}$ m. This quasi-neutrality condition is one of the properties that a system of charged particles needs to satisfy to behave as a plasma. The physical length scales required to describe coronal systems are much larger than λ_D, *e.g.*, sunspots and active regions are typically $\sim 10^7$ m and $\sim 10^8$ m across, respectively. Therefore, coronal gas satisfies the above condition for quasi-neutrality and is a plasma.

In the presence of magnetic fields, charged particles gyrate around magnetic field lines. A plasma may be regarded as strongly magnetised if the gyroradius of charged particles in a magnetic field is short compared to the collisional mean free path of the particles. The gyroradius of an ion is defined as

$$r_{g,i} = \frac{m_i v_{\perp,i}}{|q_i| B}, \tag{1.2}$$

where m_i is the ion mass, $v_{\perp,i}$ is the velocity of the ion perpendicular to the magnetic field, $q_i = Z_i e$ is the charge of the ion, and B is the magnetic field strength. Equation 1.2 shows that $r_{g,i} \sim \frac{1}{B}$, so stronger magnetic fields result in shorter gyroradii, and

that the ion gyroradius is larger than the electron gyroradius by a factor $\frac{\sqrt{m_i}}{Z_i\sqrt{m_e}}$ for equal temperature, assuming that $v_{\perp,i} = \sqrt{\frac{3k_BT}{m_i}}$.

From Chiuderi and Velli (2015), the collisional mean free path of two charged ions is

$$\lambda_{mfp} = \frac{\pi}{n_0}\left(\frac{6\varepsilon_0 k_B T}{Z_1 Z_2 e^2}\right)^2, \tag{1.3}$$

where Z_1 and Z_2 are the charge numbers of the two ions, n_0 is the average number density of the plasma, ε_0 is the permittivity of free space, k_B is the Boltzmann constant, and T is the plasma temperature.

In the solar corona, ($T \sim 10^6$ K, $n_0 \sim 10^{15}$ m^{-3}, $B \sim 10^{-3}$ T, $v_\perp \sim 10^6$ m s^{-1}), typical values of the electron gyroradius and electron-electron collisional mean free path are $r_g \sim 10^{-2}$ m and $\lambda_{mfp} \sim 10^6$ m. Since $r_g \ll \lambda_{mfp}$ in the corona, the coronal plasma may be considered to be strongly-magnetised.

1.2.2 Magnetohydrodynamics (MHD)

Magnetohydrodynamics (MHD) is a branch of physics that can be used to describe the behaviour of quasineutral, non-relativistic, magnetised fluids. In Section 1.2.1, it was shown that coronal plasma satisfies these conditions.

The MHD equations describe plasma as a single fluid with mass density, ρ, bulk velocity, $\mathbf{v}$, scalar pressure, p, and magnetic field, $\mathbf{B}$. The ideal (non-dissipative) MHD equations are

$$\frac{\partial \rho}{\partial t} + \nabla\cdot(\rho\mathbf{v}) = 0 \tag{1.4}$$

$$\rho\left(\frac{\partial}{\partial t} + \mathbf{v}\cdot\nabla\right)\mathbf{v} = \mathbf{J}\times\mathbf{B} - \nabla p + \mathbf{F} \tag{1.5}$$

$$\frac{\rho^\gamma}{\gamma-1}\left[\frac{\partial}{\partial t}\left(\frac{p}{\rho^\gamma}\right) + \mathbf{v}\cdot\nabla\left(\frac{p}{\rho^\gamma}\right)\right] = 0 \tag{1.6}$$

$$\frac{\partial \mathbf{B}}{\partial t} = \nabla\times(\mathbf{v}\times\mathbf{B}). \tag{1.7}$$

This is a closed system of 8 equations in the 8 primary variables of MHD (where the vector quantities $\mathbf{v}$ and $\mathbf{B}$ each represent 3 components). The magnetic field, $\mathbf{B}$,

satisfies the condition

$$\nabla \cdot \mathbf{B} = 0, \tag{1.8}$$

the plasma pressure p is defined from the equation of state of an ideal gas

$$p = nk_B T, \tag{1.9}$$

γ is the ratio of specific heats (typically $\gamma = 5/3$), $\mathbf{F}$ represents additional forces (*e.g.* gravity, when relevant), and $\mathbf{J}$ is the electric current density. The definition of $\mathbf{J}$ comes from the Maxwell-Ampère equation:

$$\nabla \times \mathbf{B} = \mu_0 \mathbf{J} + \frac{1}{c^2}\frac{\partial \mathbf{E}}{\partial t}, \tag{1.10}$$

where μ_0 is the permeability of free space. The relative importance of the two terms on the RHS of Equation 1.10 can be examined by introducing typical length-, time-, and speed-scales, ($l_0 = v_0 t_0$; $\nabla \sim \frac{1}{l_0}$, $\frac{\partial \mathbf{X}}{\partial t} \sim \frac{X}{t_0}$). From Faraday's Law

$$\nabla \times \mathbf{E} = -\frac{\partial \mathbf{B}}{\partial t}, \tag{1.11}$$

we see that $E \sim \frac{Bl_0}{t_0}$. Substituting this in to Equation 1.10, we see that the second term on the RHS (the 'displacement current' term) is second-order in $\frac{v_0}{c}$. In the non-relativistic limit ($v_0 \ll c$), the Maxwell-Ampère equation then simplifies to

$$\mathbf{J} = \frac{1}{\mu_0}\nabla \times \mathbf{B}. \tag{1.12}$$

Equations 1.4, 1.5, and 1.6 represent the conservation of mass, momentum, and energy, respectively. Equation 1.7 is the ideal magnetic induction equation, describing how the magnetic field varies with time in the absence of resistivity.

1.2.2.1 Plasma Beta

In the corona, the ideal MHD momentum equation (1.5) can be written as

$$\rho\left(\frac{\partial}{\partial t} + \mathbf{v} \cdot \nabla\right)\mathbf{v} + \nabla p = \mathbf{J} \times \mathbf{B}. \tag{1.13}$$

We can examine the relative importance of terms in Equation 1.13 by introducing space, time, and velocity scales. By analysing the Lorentz force term on the RHS and using Equation 1.12, we can write

$$\mathbf{J} \times \mathbf{B} \equiv \frac{1}{\mu_0}(\nabla \times \mathbf{B}) \times \mathbf{B} \sim \frac{B^2}{l_B}. \tag{1.14}$$

Similarly, the velocity term on the LHS

$$\rho(\frac{\partial}{\partial t} + \mathbf{v} \cdot \nabla)\mathbf{v} \sim \frac{\rho v}{t_B}, \tag{1.15}$$

and the pressure term

$$\nabla p \sim \frac{p}{l_p}. \tag{1.16}$$

Here, for an order-of-magnitude estimation, the assumption is made that the terms in the velocity expression occur on the same scales as the Lorentz forces ($l_B = v_B t_B$; $v_B = v$), but pressure forces may occur on different scales ($l_p = v_p t_p$).

From the proportionalities above, the ratio of the Lorentz force and velocity terms in the MHD momentum equation may be written as

$$\frac{\rho(\frac{\partial}{\partial t} + \mathbf{v} \cdot \nabla)\mathbf{v}}{\mathbf{J} \times \mathbf{B}} \sim \frac{\rho v l_B}{t_B B^2} \sim \frac{v^2}{v_A^2}, \tag{1.17}$$

where v_A is the Alfvén speed at which magnetic disturbances travel:

$$v_A = \sqrt{\frac{B^2}{\mu_0 \rho}}. \tag{1.18}$$

This shows that the relative importance of the velocity and Lorentz-force terms in the MHD momentum equation are determined by the ratio of the Alfvèn speed and the typical velocity scale with which mass moves. In the low corona, $v_A \gg v$, so the Lorentz force term dominates the velocity term of the momentum equation.

Now, taking the ratio of the pressure term to the Lorentz term, we obtain:

$$\frac{\nabla p}{\mathbf{J} \times \mathbf{B}} \sim \frac{l_B}{l_p}\frac{p}{B^2}, \tag{1.19}$$

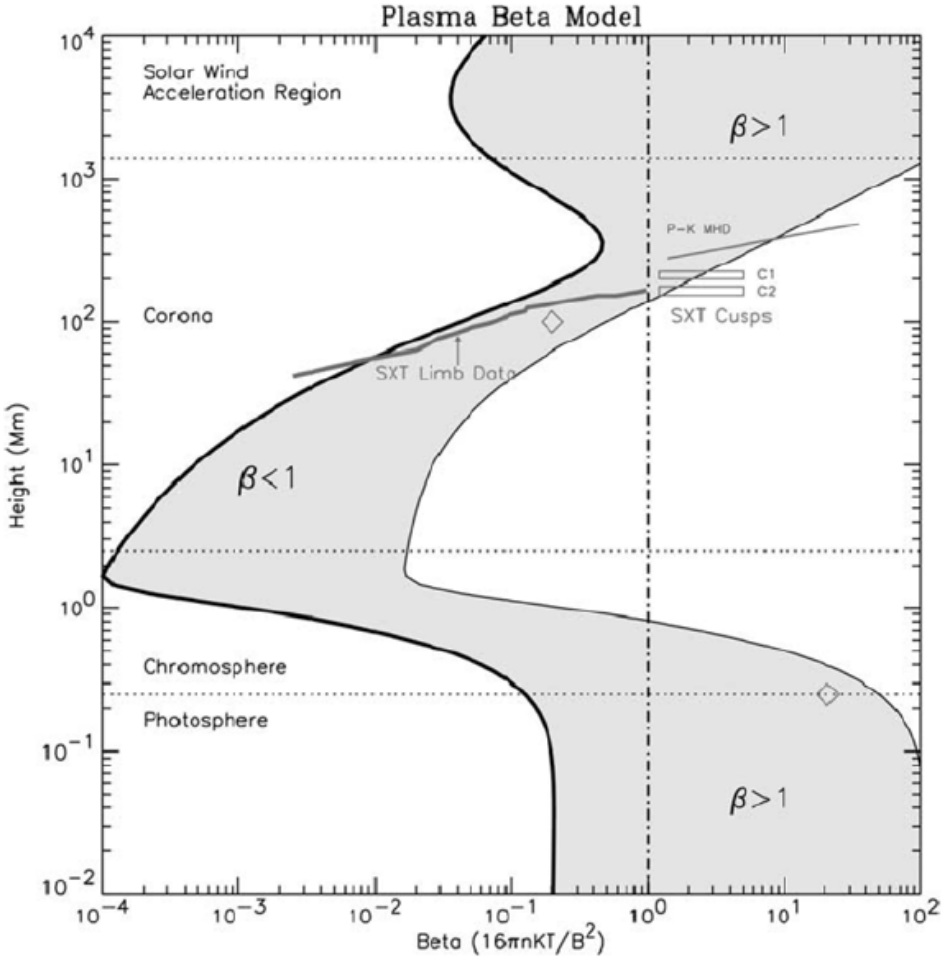

Figure 1.4: Figure 3 of Gary (2001). The variation of plasma β with height in the solar atmosphere. $\beta \gtrsim 1$ in the photosphere, but decreases in the choromosphere. In the low-to-mid corona, $\beta < 1$, but high-up in the corona, β increases to order unity again.

from which a quantity known as plasma beta is defined as the ratio between the plasma pressure and the magnetic pressure:

$$\beta \equiv \frac{2\mu_0 p}{B^2}. \tag{1.20}$$

If plasma pressure is larger than or comparable to magnetic pressure (*e.g.*, in the photosphere) or if $l_p \ll l_B$, then $\beta \gtrsim 1$. However, in the corona, magnetic pressure dominates plasma pressure, and $\beta < 1$ (see Figure 1.4), so the Lorentz force dominates the pressure-gradient force. We can estimate β by using Equation 1.20 and substituting $p = nk_BT$ (Equation 1.9). In the photosphere ($n \sim 10^{23}$ m^{-3},

$T \approx 6 \times 10^3$ K, $B \sim 0.1$ T), $\beta_{ph} \sim 1$, whereas in the corona ($n \sim 10^{15}$ m^{-3}, $T \sim 10^6$ K, $B \sim 10^{-3}$ T), $\beta_{cor} \sim 10^{-2}$.

1.2.2.2 The Magnetic Reynolds Number

When considering finite resistivity (non-ideal), the induction equation is

$$\frac{\partial \mathbf{B}}{\partial t} = \nabla \times (\mathbf{v} \times \mathbf{B}) + \eta \nabla^2 \mathbf{B}, \tag{1.21}$$

where η is the diffusivity, which is related to resistivity (ρ_e) and conductivity (σ) as $\eta = \frac{\rho_e}{\mu_0} = \frac{1}{\mu_0 \sigma}$. The first term on the RHS of Equation 1.21 describes advection, and the second term describes diffusion. The relative importance of each term is quantified with the magnetic Reynolds number,

$$R_m = \frac{\nabla \times (\mathbf{v} \times \mathbf{B})}{\eta \nabla^2 \mathbf{B}} \sim \frac{vl}{\eta}, \tag{1.22}$$

where v and l are characteristic velocity and length scales of the system being considered.

In many astrophysical cases, including in the solar corona, typical length scales are large compared to velocities, and conductivity is high, so $R_m \gg 1$. In the limit where changes to the magnetic field are controlled only by advection, the electrical conductivity is considered infinite and magnetic fields are "fastened" (or "frozen-in") to plasmas (Alfvén's Theorem, Alfvén, 1943; plasma can flow along individual field lines, but not perpendicularly between them).

The $R_m \lesssim 1$ case can occur when characteristic length scales are small, as in the solar photosphere, and/or resistivity is significant. In this case, Alfvén's theorem does not hold and magnetic field lines are able to diffuse through plasma.

1.2.3 Magnetic Reconnection

The hot solar corona is generally assumed to be a perfect conductor ($R_m \sim 10^9 - 10^{12}$; Hood and Hughes, 2011), but there are some situations where this assumption breaks down. When resitivity is significant and length-scales are small (*e.g.* in electric current sheets), $R_m \sim 1$, and the 'diffusion term' of the induction equation

(Equation 1.21) becomes important. Alfvén's theorem of magnetic field lines being frozen-in to plasma is violated, and, by the effect of localised diffusion, the magnetic field can change topology, thus connecting regions of plasma that were not magnetically connected before. In this way, magnetic reconnection can have global consequences despite typically being a localised effect.

For example, consider two oppositely-directed magnetic field lines approaching each other, such that the scale-length associated with the gradient of the magnetic field is decreasing. An electric current sheet will form between the magnetic field lines (cf. Equation 1.12), and the field lines may diffuse through the plasma. This process is known as magnetic reconnection: the reconfiguration of the magnetic field towards a more energetically-favourable state (*i.e.*, a state with reduced electric current).

Magnetic reconnection is a universal process allowed by violation of the frozen-in law, but may be driven by many different processes. On the Sun, plasma motions from convective cells and differential rotation can move the photospheric footpoints of coronal magnetic field loops. The continual relative motion of footpoints as well as the emergence of magnetic flux from beneath the surface shears coronal loops, adding more and more free energy to the magnetic field in the form of electric currents. Magnetic reconnection enables the increasingly non-potential magnetic field to return to a more energetically-favourable state, converting and releasing free energy. The free energy liberated by the change in field-connectivity is released in the form of jets that are accelerated away from the reconnection region.

Magnetic reconnection is the fundamental process behind solar flaring (see Section 1.3.2 for more about solar flares). Solar flares can release vast quantities of energy in minutes. Therefore, any model of magnetic reconnection must account for the reconfiguration of a field over such a short timescale.

The Sweet-Parker model (Sweet, 1956; Parker, 1957; illustrated in Figure 1.5) describes stationary, 2-D magnetic reconnection at an 'X-point' that separates different magnetic domains. Oppositely-directed magnetic field lines flow towards each other with velocity U_i from an ideal (non-resitive) regime in to a diffusion re-

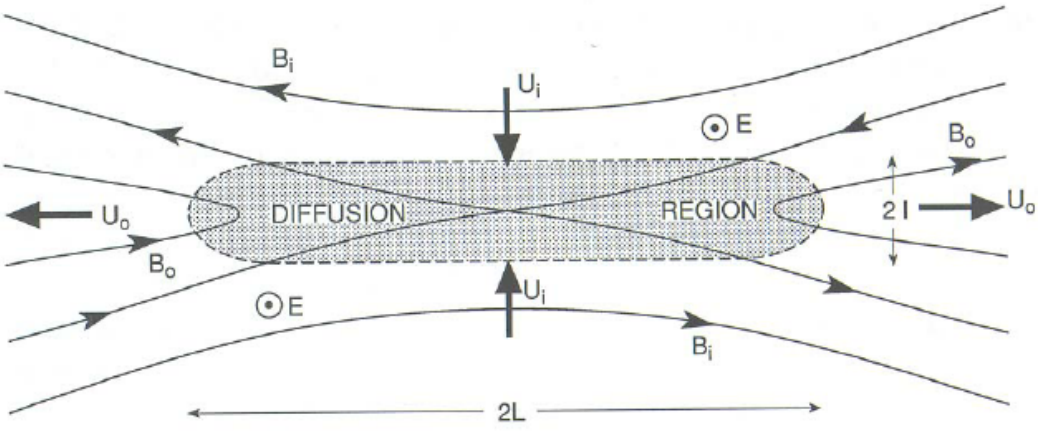

Figure 1.5: Illustration of Sweet-Parker reconnection (Kivelson and Russell, 1995). Magnetic field lines flow toward an 'X-point' with velocity U_i. The field lines enter a diffusion region (width $2L$, thickness $2l$) where they may slip through plasma, reconfigure, and flow outward with velocity U_o.

gion where resistivity is important. The diffusion region has width $2L$ and thickness $2l$ around the X-point. The magnetic field lines slip through the plasma in the diffusion region and reconnect with each other, before flowing away from the X-point with an outflow velocity U_o.

We may determine the rate of reconnection by relating quantities in the system to each other using conservation laws. Firstly, by the conservation of inflowing and outflowing mass:

$$U_i L \sim U_o l. \tag{1.23}$$

Secondly, by comparing the (slow) inflowing magnetic energy to the (fast) outflowing kinetic energy:

$$\frac{B_i^2}{2\mu_0} \sim \frac{\rho U_o}{2}, \tag{1.24}$$

which can be rearranged for U_o to give

$$U_o \sim \sqrt{\frac{B^2}{\mu_0 \rho}} \equiv v_A, \tag{1.25}$$

i.e. the outflow travels with the Alfvén velocity (as defined in Equation 1.18). Finally, the component of the electric field out of the plane, E_z, is conserved across

the layer. The inflowing electric field follows the relation $E_z = U_i B_i$ (where B_i is the strength of the inflowing magnetic field), and the electric current density inside the diffusion region is $\mathbf{J} = \frac{1}{\mu_0}\nabla \times \mathbf{B} \sim \frac{B_i}{\mu_0 l}$ (from Equation 1.12). The (resistive) electric field inside the diffusion region is $\mathbf{E} = \frac{\mathbf{J}}{\sigma}$, so conservation of E_z leads to

$$U_i B_i = \frac{J_z}{\sigma} \sim \frac{B_i}{\mu_0 l \sigma}. \tag{1.26}$$

From this, we see that

$$U_i \sim \frac{\eta}{l}. \tag{1.27}$$

Using Equations 1.23, 1.25, and 1.27, the rate of Sweet-Parker magnetic reconnection is

$$R = \frac{U_i}{U_o} = \frac{l}{L} \sim \frac{\eta}{l v_A} \sim R_m^{-1/2}, \tag{1.28}$$

where R_m is the magnetic Reynolds number with the Alfvén velocity as its characteristic velocity (Equation 1.22; discussed in Section 1.2.2.2). R_m defined in this way is sometimes also known as the Lundquist number. Following the Sweet-Parker mechanism, a solar flare would develop on the order of a few weeks (Kivelson and Russell, 1995), which is far too slow to explain observed solar flares (which occur over minutes or hours). Other models of reconnection have been proposed that have higher reconnection rates than the Sweet-Parker model (*e.g.*, the tearing mode instability — see Furth et al., 1963 and a recent revision by Pucci and Velli, 2014), but the mechanisms themselves are beyond the scope of this thesis.

1.2.4 Magnetic Helicity

Individual magnetic field lines (and by practical extension, magnetic flux tubes) may writhe along their length, be twisted around one-another, or be inter-linked with each other (each illustrated in Figure 1.6). The twist, writhe, and linkage of magnetic fields is quantified by magnetic helicity, H, expressed as

$$H = \int_V \mathbf{A} \cdot \mathbf{B} \, \mathrm{d}V, \tag{1.29}$$

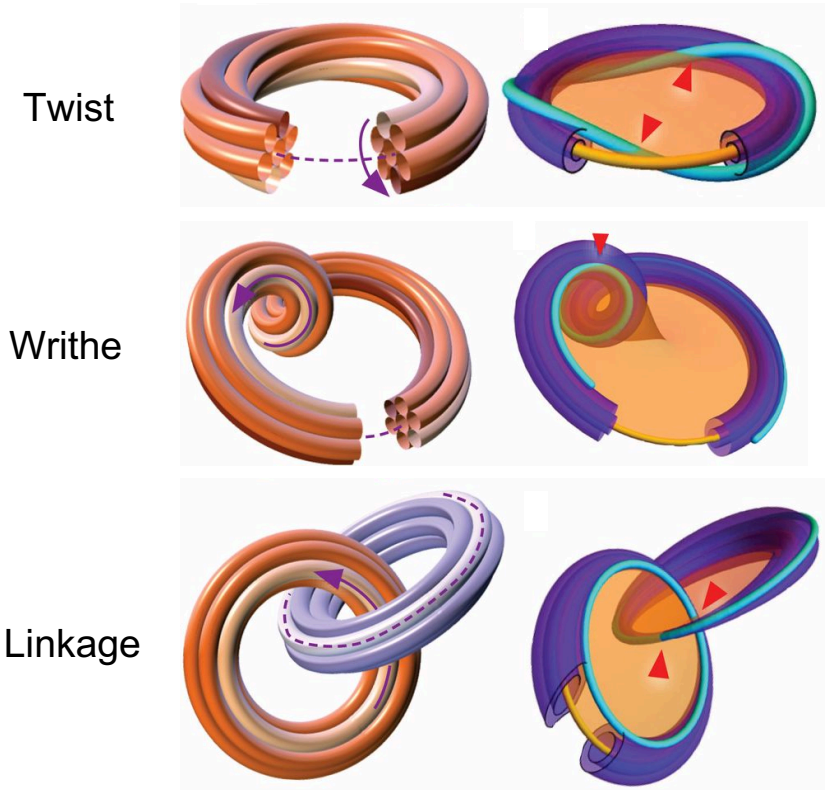

Figure 1.6: Magnetic helicity quantifies the twist, writhe, and linkage of magnetic fields. Figure adapted from Scheeler et al., 2017.

where $\mathbf{B}$ is the magnetic field, V is the volume, and $\mathbf{A}$ is the magnetic vector potential defined as

$$\mathbf{B} = \nabla \times \mathbf{A}. \tag{1.30}$$

In a vaccuum, if a straight rope of magnetic flux tubes twisted around each other has $H > 0$, then the chirality of the magnetic field is right-handed, and when $H < 0$ the chirality is left-handed.

From Equation 1.30, we see that $\mathbf{B}$ is invariant to the gauge transformation

$$\mathbf{A} \rightarrow \mathbf{A}' = \mathbf{A} + \nabla\psi, \tag{1.31}$$

where ψ is an arbitrary function of space and time, since $\nabla \times (\nabla\psi) = 0$. This gauge transformation changes the magnetic helicity in the following way:

$$H \rightarrow H' = H + \int_V \mathbf{B} \cdot \nabla\psi \, \mathrm{d}V = H + \int_S \mathbf{n} \cdot \mathbf{B}\psi \, \mathrm{d}S, \tag{1.32}$$

where the vector identities A.1 and A.2 have been used with Equation 1.8 ($\nabla \cdot \mathbf{B} = 0$), and where $\mathbf{n}$ is the vector normal to the surface S that encloses the volume, V. In order for H to be invariant to any gauge transformation, the normal component of the magnetic field must vanish at the surface, *i.e.*

$$\mathbf{n} \cdot \mathbf{B}|_S = 0. \tag{1.33}$$

1.2.4.1 Relative Magnetic Helicity

In situations where Equation 1.33 is not satisfied (such as at the photospheric boundary of a coronal field volume, where magnetic flux emerges from the solar interior), H is gauge-dependent. We may instead define a *relative helicity* between two magnetic fields that have the same distribution of normal field component at their boundary (Berger and Field, 1984; Finn and Antonsen Jr, 1985). The relative magnetic helicity is defined as

$$H_r = \int_V (\mathbf{A}_1 + \mathbf{A}_0) \cdot (\mathbf{B}_1 - \mathbf{B}_0) \, \mathrm{d}V, \tag{1.34}$$

and is gauge invariant.

The computation of relative helicity may be used to analyse the magnetic helicity of a magnetic field that contains electric currents ($\mathbf{B} = \mathbf{B}_p + \mathbf{B}_j$) by using the potential, current-free field ($\mathbf{B}_p$), as a reference. The relative helicity can be used to represent only the magnetic helicity associated with the current-carrying part of the field (as used *e.g.* in Pariat et al., 2017), as

$$H_j = \int_V (\mathbf{A} - \mathbf{A}_p) \cdot (\mathbf{B} - \mathbf{B}_p) \, \mathrm{d}V. \tag{1.35}$$

Potential and non-potential magnetic fields are discussed further in Chapter 3 along with methods by which they may be computed.

1.2.4.2 Conservation of Magnetic Helicity

Magnetic helicity is a conserved quantity in a highly-conductive fluid contained in a closed magnetic surface (*i.e.*, in a $R_m \gg 1$ plasma with no normal-component of $\mathbf{B}$

and **v** at its boundary; Woltjer, 1958). It has also been shown that magnetic helicity is almost perfectly conserved in almost-ideal conditions (Taylor, 1974; Berger and Field, 1984).

Local helicity may change by transferring it from one area to another, even in the absence of dissipation. For example, magnetic helicity can enter the corona through the photosphere via magnetic flux emergence. Therefore, without a mechanism to remove helicity from the corona, it will continue to increase locally. Coronal mass ejections (CMEs) are one way in which magnetic fields may be carried away from the Sun (Rust, 1994), transporting the associated magnetic helicity with them into interplanetary space (see Section 1.3.3).

1.3 Solar Magnetic Activity

1.3.1 Active Regions

In a review, van Driel-Gesztelyi and Green (2015) build on the definition given by D'Azambuja (1953) to say that an active region is "the totality of all observable phenomena preceding, accompanying and following the birth of sunspots including radio-, X-ray-, EUV- and particle emission." Even after coherent sunspots decay and become dispersed regions of magnetic flux, the coronal conditions may still warrant being described as an active region.

Since 1972, every sunspot region that has emerged or rotated on to the solar disc has been assigned a unique number by the National Oceanic and Atmospheric Administration (NOAA) to help catalogue them. For example, on 2 May 2010, the 11,067$^{\text{th}}$ active region identified in this way was catalogued as NOAA AR 11067. This notation of active region identification is used throughout this thesis. If the same sunspot region/active region lives long enough to rotate off of the solar disc at the western limb and across the far-side of the Sun, it will be given a new NOAA identifier when it reappears at the eastern limb.

1.3.1.1 Observed Trends of Active Regions

The number of sunspots and level of solar activity varies cyclically between maxima and minima. The mean time between one solar minimum (or maximum) and the

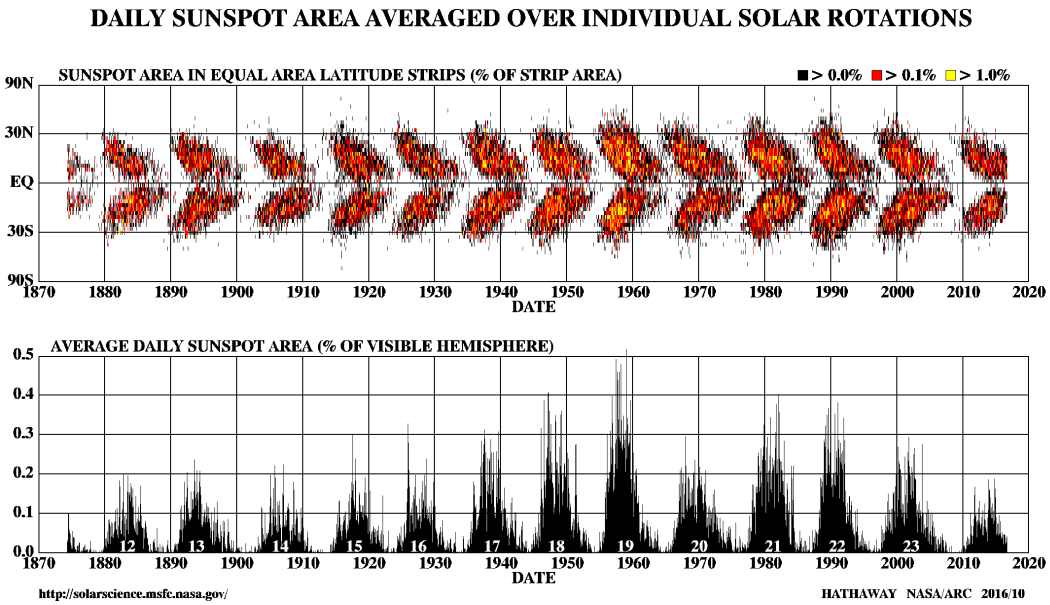

Figure 1.7: Top: latitude of sunspots over time. Bottom: average daily sunspot area to demonstrate the phases of the solar cycle. At solar minimum, a higher proportion of sunspot area occurs at higher latitudes, and closer to solar minimum, sunspots appear closer to the equator. Image from `https://solarscience.msfc.nasa.gov/images/bfly.gif`.

next is $\approx$11 years. The numbering of solar cycles began in 1755, and at the time of writing this thesis, solar cycle 24 is approximately at its end (having begun in 2008 and reached its maximum in 2014).

Magnetic flux is observed to emerge through the photosphere in two latitudinal bands, with one each in the northern and southern hemispheres. The latitude of these so-called active bands depends on the stage of the solar cycle, with active regions emerging between roughly $\pm 20^\circ - 40^\circ$ at the start of a new solar cycle, but tending to emerge closer to the equator around solar minimum (Carrington, 1858). This phenomenon is known as Spörer's Law, and can be seen in 'the butterfly diagram', shown in Figure 1.7.

As introduced in Section 1.1.2.1, individual sunspot regions are normally oriented in the roughly east-west direction with 'leading' and 'trailing' spots. This approximate east-west alignment is the manifestation of the toroidal field component introduced to the solar magnetic field by differential rotation at the base of the convective zone (Section 1.1.1). Hale's law (Hale and Nicholson, 1925) states that,

during a given solar cycle, the polarity of leading sunspots in active regions is correlated with the hemisphere they are in. In solar cycle 24, by Hale's law, active regions in the northern hemisphere would have leading sunspots of negative polarity and trailing spots of positive polarity, whereas the southern hemisphere would feature leading sunspots of positive polarity and trailing spots of negative polarity. This hemispheric polarity trend reverses every cycle at solar minimum, and the sign of the magnetic poles reverse at solar maximum. For example, in solar cycle 25, leading sunspots in the northern hemisphere are expected to have positive polarity, and leading spots in the southern hemisphere are expected to be negative.

Hale's law is based on observations, but there are exceptions to the trend. 8.4% of active regions observed during cycles 21, 22, and 23 were anti-Hale, *i.e.* the polarities of leading spots opposed the hemispheric trend (McClintock et al., 2014).

Joy's law describes the trend of active regions to deviate from exact east-west alignment. Leading sunspots are often closer to the solar equator than their trailing counterparts, such that active regions are tilted with respect to the equator by $3^\circ - 5^\circ$ (McClintock and Norton, 2013). However, anti-Joy active regions are observed with leading polarities being further from the equator than their trailing counterparts.

Magnetic field with left-handed twist (negative chirality) emerges more often in the northern hemisphere, and right-handed twist (positive chirality) emerges more frequently in the southern hemisphere. This (weak) hemispheric helicity preference was first noted by Seehafer (1990), who determined 11 out of the 12 northern-hemisphere active regions they studied were left-handed, and 3 of 4 southern hemisphere active regions were right-handed. More recently, studies have included larger numbers of active regions and found varying levels of support for the trend (*e.g.*, Pevtsov et al., 2001 found $66\% \pm 3\%$ of 263 regions matched the preferred helicity sign for their hemisphere and Liu et al., 2014 found $75\% \pm 7\%$ of 151 regions followed the trend).

1.3.1.2 Polarity Inversion Lines (PILs)

Since active regions are systems of connected positive and negative magnetic polarities, we may introduce the concept of a polarity inversion line (PIL). PILs are the

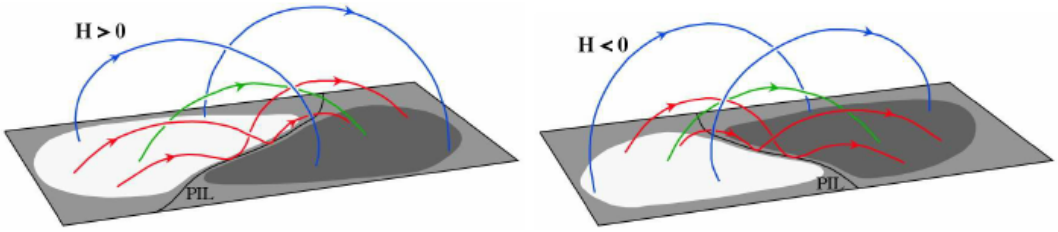

Figure 1.8: Figure from Luoni et al. (2011). On the left, the leading (dark) polarity extends to the south of the trailing (white) polarity. This is expected during the emergence of right-handed twisted flux (positive helicity). On the right, the leading polarity extends to the north of the trailing polarity. This is seen during the emergence of left-handed twisted flux (negative helicity).

fictitious boundaries that separate opposing magnetic polarities, and they are generally considered 2-dimensionally in the photosphere using line-of-sight or radial magnetic field measurements.

Features along PILs can be used as one method of observationally determining the chirality of magnetic flux that emerges through the photosphere. The polarities in an emerging active region may be elongated such that the leading polarity overlaps with the trailing polarity either to its north or south. These overlapping elongations are sometimes called 'magnetic tails' (*e.g.* Archontis and Hood, 2010), or, as in the rest of this thesis, 'magnetic tongues'. As illustrated in Figure 1.8, the observation of a leading tongue that overlaps to the south (north) of its trailing polarity can be reconciled with the emergence of a right-handed (left-handed) system of twisted magnetic flux through the photosphere (López Fuentes et al., 2000; Luoni et al., 2011).

1.3.1.3 Arcades of Magnetic Loops

Where strong magnetic fields puncture the surface and enter the solar atmosphere, closed loops with plasma following along them are formed in the corona. This plasma emits EUV and X-ray light, and so coronal loops (and active regions overall) appear bright in these wavelengths. The feet of coronal loops are "line-tied" to the high-β photosphere/chromosphere, and so surface motions can shear coronal loops, storing free magnetic energy in them. Collections of many loops are referred to as arcades. In some cases, highly-sheared arcades of coronal loops may appear as

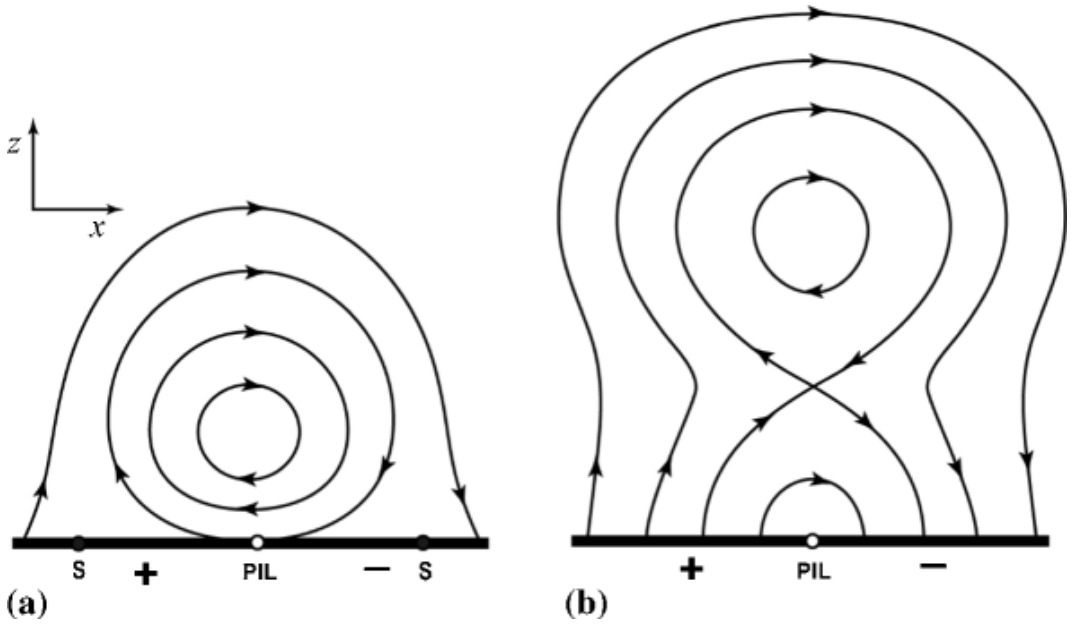

Figure 1.9: Figure from (Filippov et al., 2015). The thick black line at the bottom of each panel represents the photosphere. (a) A BPSS flux rope that intersects the photosphere at its lowest point. (b) A flux rope in an HFT configuration, including an 'X-point' beneath the rope that is above the photosphere.

J-shapes when viewed from above.

1.3.1.4 Magnetic Flux Ropes

In this work, a magnetic flux rope is defined as a structure consisting of an axial magnetic field line with at least one off-axial field line wrapped around it with at least one full turn (2π) of twist from end to end. This is the same definition as outlined by Savcheva et al. (2012). In practice, then, magnetic flux ropes are bundles of twisted magnetic field.

It can be useful to categorise flux ropes in to two groups based on their magnetic field configuration. These are bald patch separatrix surface (BPSS) flux ropes and hyperbolic flux tube (HFT) flux ropes. BPSS flux ropes are those that are sufficiently low down in the solar atmosphere that their lower sections intersect the photosphere and are "line-tied" by the relatively dense plasma of the photosphere and chromosphere (Figure 1.9a). HFT flux ropes are those that are sufficiently high in the solar atmosphere that their undersides do not intersect the photosphere (Figure 1.9b).

Both BPSS and HFT flux rope configurations feature a quasi-separatrix layer (QSL; Priest and Démoulin, 1995). QSLs are surfaces that separate regions of different magnetic connectivities, and therefore may be found *e.g.* between a flux rope and the more-potential field that surrounds it. Since local magnetic field gradients are sharp between separate connectivities, electric currents are relatively strong and magnetic reconnection may occur at QSLs.

The QSL at the periphery of a BPSS flux rope will intersect the photosphere, and therefore any magnetic reconnection beneath such a low flux rope will form small, low-lying loops. Magnetic tension causes sufficiently-small loops to submerge beneath the photosphere, and this is observed as flux cancellation (van Ballegooijen and Martens, 1989; see Section 1.3.3.1). The toroidal field of a BPSS flux rope is almost horizontal at its underside and is oriented such that it crosses its local PIL from negative to positive (see Figure 1.9a). Therefore, observations of the photospheric magnetic field beneath a low-altitude flux rope may show a 'bald patch' in vertical field and an 'inverse crossing' in horizontal field.

The QSL around an HFT flux rope does not intersect the photosphere at the underside of the flux rope, and as such, HFT flux ropes do not exhibit bald patches or inverse crossings in the photospheric magnetic field. However, HFT flux ropes do have an 'X-point' beneath them (in 2-D at least; see Figure 1.9b) that is above the photosphere. Magnetic reconnection at this X-point can cause an arcade of loops to form beneath the flux rope that are too large to submerge under tension. For some time after their formation, these loops will be hot, appearing as bright flare arcades that eventually cool and fade (see Section 1.3.2 for more about solar flaring).

1.3.1.5 Sigmoids

Sigmoids are continuous S-shaped (or inverse-S-shaped) plasma structures that appear strongly in soft X-ray bands, but also at hot EUV wavelengths. Sigmoid formation has been observed as a transition from two J-shaped sets of coronal loops in soft X-ray images (*e.g.*, Green and Kliem, 2014; Figure 1.10). Magnetic reconnection occurs between the Js, causing their reconfiguration into a continuous S. Canfield et al. (1999) found that sigmoidal active regions are highly likely to produce

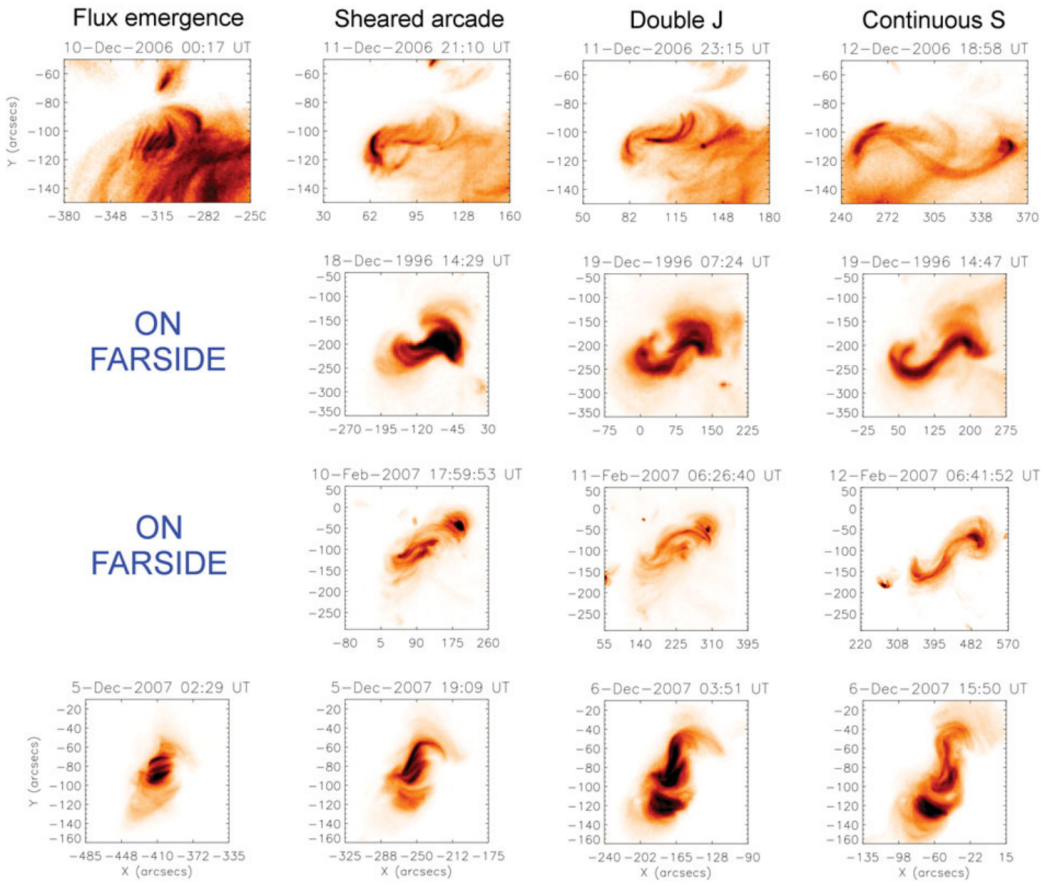

Figure 1.10: The formation of sigmoids in 4 active regions (one per row). First, magnetic flux emerges in to the solar atmosphere, and arcades of magnetic loops are sheared. These sheared arcades sometimes take a 'double J' configuration, and magnetic reconnection between the J-shaped aracades forms a continuous-S sigmoid. Observations from the *Hinode X-ray Telescope* (XRT). (Green and Kliem, 2014).

eruptions, so sigmoids are great targets for studies aimed at learning about solar magnetic activity. A weak hemispheric trend (77% – 82%; Zhang et al., 2010) for right-handed sigmoids in the south and left-handed in the north follows the similar trend for hemispheric helicity of active regions introduced in Section 1.3.1.1.

Sigmoids may be interpreted as bundles of magnetic field lines with approximately one turn of twist along their length, viewed from above. In this way, sigmoids may correspond to magnetic field lines at the periphery of magnetic flux ropes, perhaps where electric currents are strong (Kliem et al., 2004; Fan and Gibson, 2004; cf. Section 1.3.1.4 regarding QSLs). Following this logic, sigmoids are used as observational indicators of magnetic flux rope presence (*e.g.* in Green and Kliem,

2009).

1.3.1.6 Filaments

Filaments are dark, elongated structures consisting of relatively cool, dense chromospheric plasma observed against the bright solar disc. Flux ropes can form at low-altitudes in the solar atmosphere via magnetic flux cancellation (described in Section 1.3.3.1). The low-altitude magnetic reconnection in the flux cancellation scenario can cause relatively-cool, dense chromospheric plasma to become suspended in the dips of a forming helical flux rope along a PIL. On this basis, filaments can be used to observationally suggest the presence of low-altitude magnetic flux ropes. On the other hand, filaments may not form when the magnetic reconnection that forms a flux rope occurs higher up in the corona. In this way, the lack of a filament (in the presence of other flux rope signatures, *e.g.* a sigmoid) can be used to probe the altitude at which a flux rope formed in the solar atmosphere, and therefore whether the flux rope may have a BPSS or HFT configuration.

1.3.2 Solar Flares

Solar flares are bursts of high-energy particles and radiation. Flares are especially bright at EUV and X-ray wavelengths. The "standard model" of solar flares, otherwise known as the CSHKP model after those who worked to develop it (Carmichael, 1964; Sturrock, 1966; Hirayama, 1974; Kopp and Pneuman, 1976), is summarised by a 2.5-D cartoon that uses magnetic reconnection as the mechanism for producing the observed signatures of an eruptive flare. For an illustration, see Figure 1.11.

Magnetic field lines pinch together beneath a rising plasma structure (cf. an erupting flux rope; see Section 1.3.3 for more on solar eruptions). Magnetic reconnection may occur in the current sheet that forms between the inflowing oppositely-directed field lines, reconfiguring the magnetic field and accelerating particles away from the reconnection site (see Section 1.2.3 for more on magnetic reconnection). Above the magnetic reconnection site, magnetic flux may be built in to the overlying flux rope structure. Beneath the reconnection site, an arcade of relatively compact magnetic loops is formed.

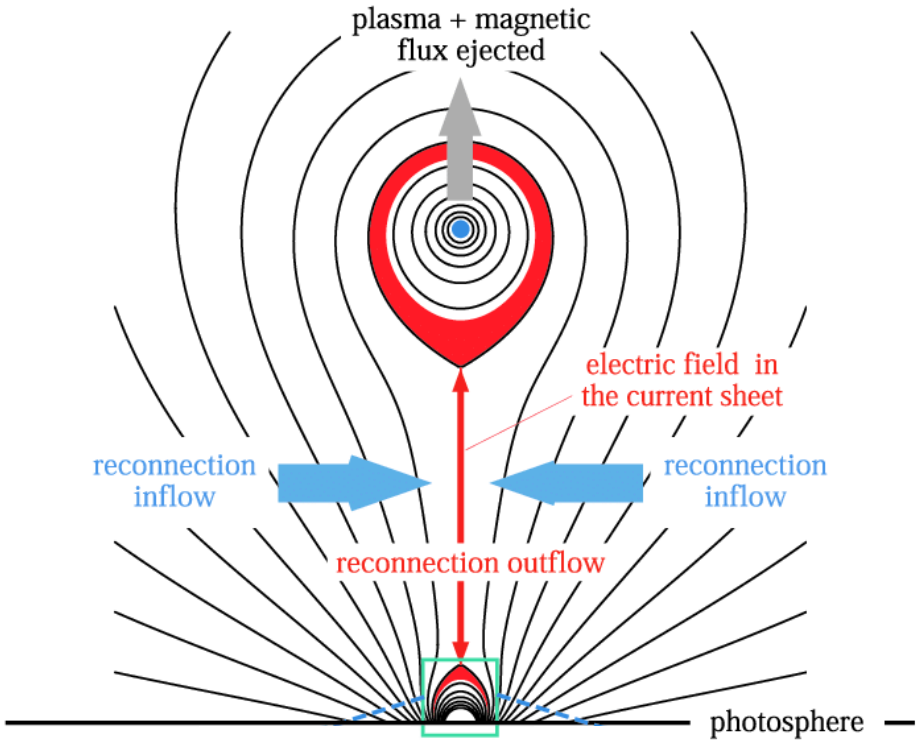

Figure 1.11: 2-D schematic of the standard model of a solar flare. There is an inflow of magnetic field lines beneath a rising plasma structure (*e.g.* an erupting flux rope), and a current sheet forms. Magnetic reconnection in this current sheet adds magnetic flux to the rising plasma structure and forms closed flare loops underneath. Image adapted from Ko et al. (2003) which was based on the model of Lin and Forbes (2000).

If the inflowing magnetic field moves in the horizontal direction, the reconnection outflows will move vertically to conserve momentum. The downward-jet of accelerated particles bombards the high-density chromosphere, depositing their kinetic energy. This heats plasma that then rises up along magnetic loops (known as chromospheric evaporation). The hot plasma in the loops radiates at EUV and X-ray wavelengths, and we observe a bright, flaring arcade.

The photospheric/chromospheric footpoints of the reconnected loops appear bright where the accelerated particles impact. On the real Sun, magnetic reconnection does not occur simply in 2-D, but along 3-D surfaces called QSLs (Figure 1.12; QSLs introduced in Section 1.3.1.4). In a continuous, 3-D case, the flaring footpoints will be elongated, appearing as "flare ribbons". In the case of a simple, bipolar configuration, as in Figure 1.12, the ribbons will manifest as two J-shapes

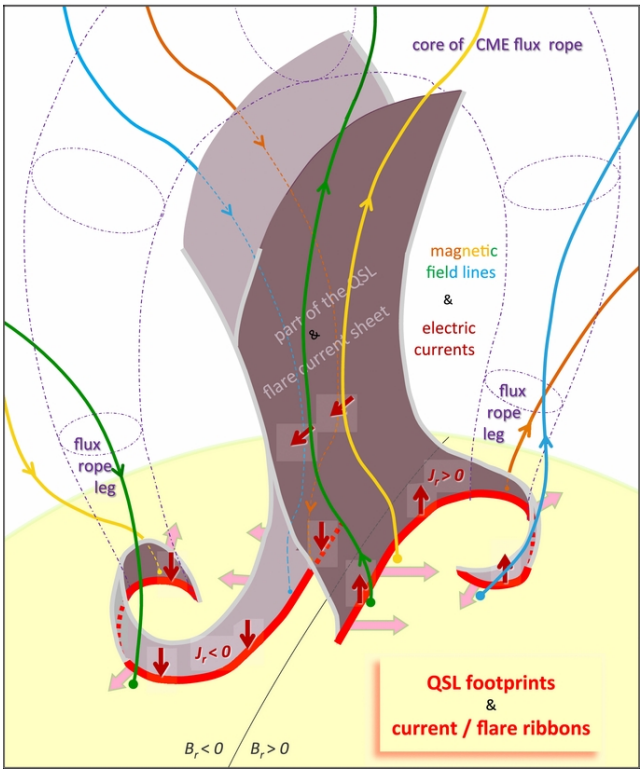

Figure 1.12: 3-D schematic of a solar flare by (Janvier et al., 2014). A QSL (current sheet, in grey) separates an overlying flux rope from an underlying arcade. The photospheric imprint of the QSL is seen as J-shaped flare ribbons that hook around the feet of the flux rope.

with their hooks around the feet of the overlying flux rope. As more and more magnetic reconnection occurs, the underlying arcade and overlying structure will grow, and the footpoints of newly-reconnected loops will appear to sweep apart from each other. Practically, the amount of magnetic flux that is built in to an overlying flux rope can be estimated by examining the magnetic flux contained in the area the flare ribbons sweep over in the photosphere (*e.g.* Fletcher and Hudson, 2001), and the hooks of flare ribbons can be used to locate the feet of the flux ropes.

1.3.3 Coronal Mass Ejections (CMEs)

Coronal mass ejections (CMEs) are eruptions of billions of tonnes of magnetised plasma from the Sun that require large amounts of energy ($\approx 10^{32}$ ergs). The only coronal energy source large enough to produce CMEs is magnetic energy, as kinetic, gravitational and thermal energy fall short by orders of magnitude (Forbes, 2000). Many CME models describe processes by which an increasing amount of energy is

stored in the corona and then suddenly released (Forbes, 2000). However, there is currently no consensus regarding their cause.

CMEs that are able to escape the Sun and propagate through the heliosphere are often referred to as interplanetary coronal mass ejections (ICMEs). When ICMEs are Earth-directed, they can drive phenomena that affect the Earth and the near-Earth environment, and these effects are known collectively as space weather. Space weather impacts include geomagnetically induced currents (GICs) that can cause strong voltage fluctuations and heating in power grid transformers, and solar energetic particles (SEPs) that can damage satellites. Therefore, sufficiently-early space weather forecasts are needed to allow preparation for the effects of Earth-directed ICMEs. To achieve this, we must be able to predict eruptions, which requires a better understanding of the processes by which eruptive structures form and lose stability.

Spacecraft measuring the solar wind *in situ* detect signatures of ICMEs. ICMEs appear as strong magnetic field fluctuations that sometimes display a smooth rotation in field direction as the ICME passes the spacecraft. Such observations are called "magnetic clouds" (Burlaga et al., 1981) and are consistent with the presence of a flux rope.

It is unclear whether all CMEs have internal magnetic flux ropes that are just sometimes undetected due to the geometry of the spacecraft crossing (as shown can happen by *e.g.* Kilpua et al., 2011) or have had their structure modified in transit (see Manchester et al., 2017), or whether there is a fundamental difference between the formation mechanisms of CMEs with and without detected flux ropes (as supported by *e.g.*, Owens, 2018).

Regardless, all models of CME initiation account for the presence of a magnetic flux rope after the onset of the eruption so that they may be detected by the time an eruption has reached interplanetary space. Where models differ is in the coronal magnetic field configuration before the onset of eruption, and this is explored next.

Theories regarding the pre-eruptive magnetic field configuration can be organised in to two groups (Forbes, 2000; Forbes et al., 2006; Aulanier et al., 2010). One

of these involves the presence of a sheared arcade (introduced in Section 1.3.1.3). Sheared arcades are non-potential and are therefore a store of magnetic energy that may be able to power an eruption. In these sheared arcade eruption models, a flux rope may form during the onset of eruption (*e.g.*, via internal tether-cutting reconnection; cartoon by Moore et al., 2001) or after the onset of eruption (*e.g.*, via reconnection in a sheared arcade following 'magnetic breakout'; Antiochos et al., 1999; Lynch et al., 2008 — see Section 1.3.3.1). The other group of theories requires that the pre-eruptive configuration is a magnetic flux rope (introduced in Section 1.3.1.4). Field lines that are less twisted than a flux rope (*i.e.* $< 2\pi$) are classified as belonging to a sheared arcade.

Understanding the pre-eruptive structure of the corona is crucial for identifying the processes involved in CME initiation because certain eruption mechanisms may only be relevant to specific configurations. We must also be aware about the ways eruptive structures form.

1.3.3.1 Triggers and Drivers

In this thesis, the mechanisms involved with CME initiation are classified as triggers and drivers, following the convention of Aulanier et al. (2010). *Triggers* can create eruptive structures (such as magnetic flux ropes) and/or evolve them to the point where they may erupt. Another process may then *drive* the erupting structure away from the Sun. In order to predict a CME, we need to look for triggers to recognise when and where eruptive structures may form, and identify whether eruptions of those structures could be successfully driven.

A wide range of processes have been identified as CME triggers in the solar atmosphere, including sunspot rotation (*e.g.*, Yan et al., 2012; Chapters 4 & 6), magnetic reconnection (*e.g.*, flux cancellation; van Ballegooijen and Martens, 1989, and tether-cutting; Moore et al., 2001), and the helical kink instability of a flux rope (Hood and Priest, 1979; Török and Kliem, 2005). Some triggers that are relevant to this thesis are described next, and more proposed mechanisms can be found with references in Table 1 of Green et al. (2018).

Some eruption triggers involve the formation of an initially stable flux rope that

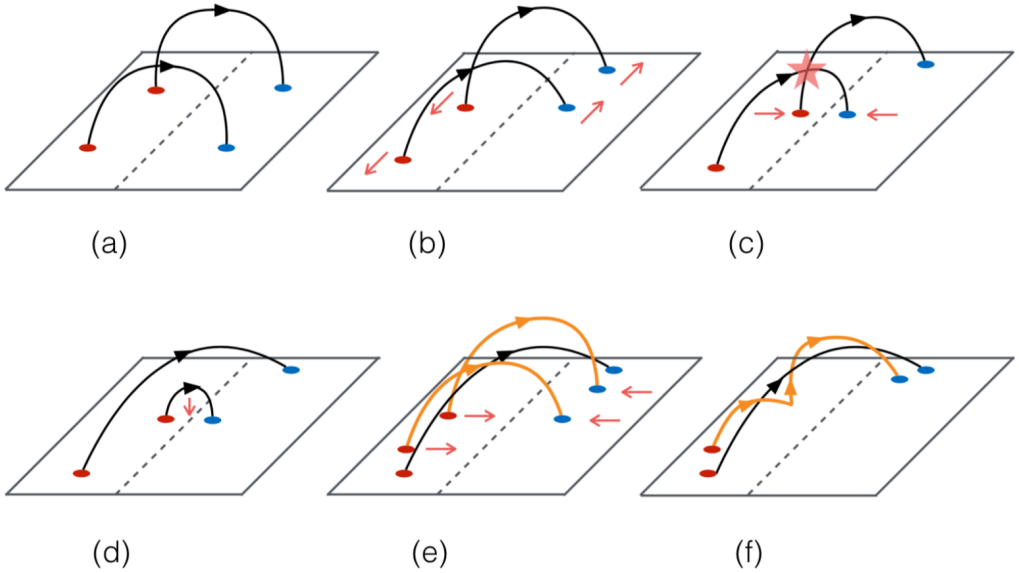

Figure 1.13: Schematic of magnetic flux cancellation by Yardley (2017), which was adapted from van Ballegooijen and Martens (1989). Magnetic loops (a) are sheared by motions in the photosphere (b), bringing their footpoints together and enabling magnetic reconnection (c). The small loops that form beneath the reconnection site submerge beneath the photosphere under tension (d), which is observed as a decrease in magnetic flux. As more loops are sheared and reconnected (e), a magnetic flux rope can form (f).

may then later lose stability. Magnetic flux cancellation describes how this can happen via a series of magnetic reconnection events low down in the solar atmosphere. For example, van Ballegooijen and Martens (1989) described how the shearing, convergence and reconnection of magnetic field driven by photospheric flows may form a flux rope (illustrated in Figure 1.13). As low-lying, small-scale loops that are formed by reconnection submerge beneath the photosphere due to magnetic tension, a decrease in magnetic flux is observed in the photosphere. Therefore, this process is called flux cancellation. A flux rope formed by flux cancellation should form low down with its underside in the photosphere or chromosphere due to the low altitude of the reconnection, and may therefore contain filament material. The observed flux cancellation can occur over timescales of hours to days (Yardley et al., 2018).

Mechanisms have also been proposed by which a flux rope may be formed after the onset of the eruption of a sheared arcade. One such method is via 'tether-cutting' reconnection between the internal footpoints of two J-shaped sheared arcades, that

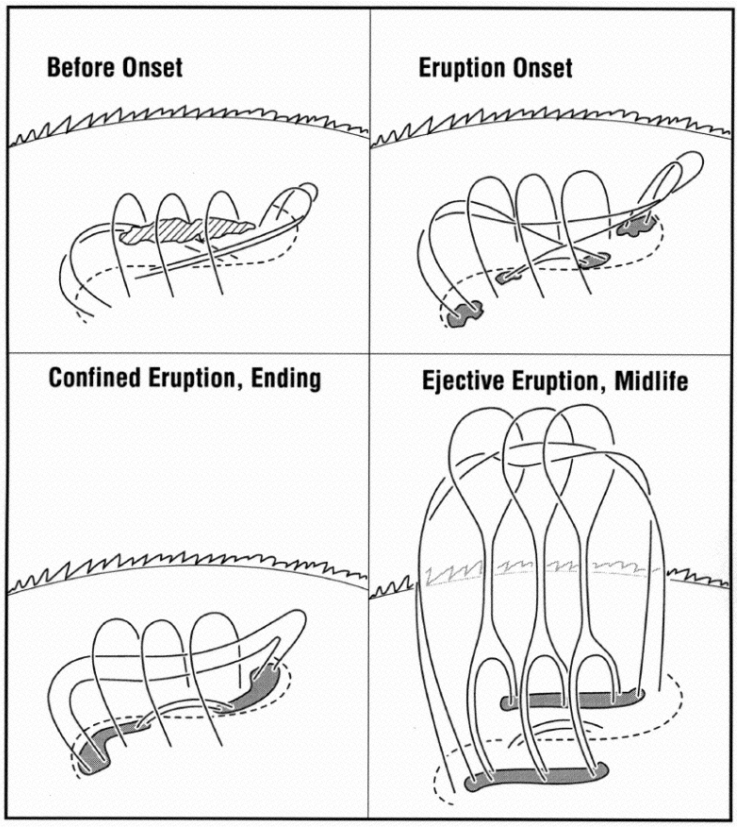

Figure 1.14: The tether-cutting cartoon of Moore et al. (2001). The internal footpoints of sheared J-shaped arcades are rooted in dense plasma. Magnetic reconnection between these internal footpoints 'cuts' this tethering effect, enabling a rising flux rope to form. This erupting flux rope may be either confined by overlying field or successfully ejected from the atmosphere.

forms a flux rope and an underlying arcade (Moore et al., 2001; Figure 1.14). The J-shaped arcades have their footpoints in relatively dense plasma, and are therefore 'tethered' to the photosphere. These tethers are cut during magnetic reconnection, marking the onset of eruption and enabling the forming flux rope to rise higher in the corona. The erupting flux rope may either be successfully ejected, or confined.

The helical kink instability is an ideal MHD instability (*i.e.* no resistivity and therefore no magnetic reconnection) that occurs when the twist of a flux rope exceeds a critical value (Hood and Priest, 1979; Török and Kliem, 2005). Török and Kliem (2003) examined a Titov and Démoulin (1999) flux rope topology and found a critical twist of 3.5π (1.75 turns). Simulations have successfully reproduced the observed kinking of an erupting filament (Török and Kliem, 2005). The kink instability can function as the initial process in the eruption of a flux rope, raising the

axis of a flux rope to the height where a driving process (*e.g.* the torus instability; Kliem and Török, 2006, see the next paragraph) can take set in. In this way, the kink instability may be considered to be a trigger.

There are two main groups of theories pertaining to how the rapid expansion of CMEs is driven. One group assumes that CMEs are driven by flare reconnection, *e.g.* in the 'breakout' model (Antiochos et al., 1999; Temmer et al., 2010; Karpen et al., 2012). Reconnection above a sheared arcade enables that arcade to erupt, and further reconnection beneath the erupting arcade can cause a flux rope to form and drives its accelerating eruption. The other set of theories assumes that CMEs are driven by an ideal MHD instability involving a flux rope, such as the torus instability (van Tend and Kuperus, 1978; Kliem and Török, 2006; Démoulin and Aulanier, 2010). The torus instability is an ideal MHD instability that occurs when there is a sufficiently-rapid drop-off in poloidal magnetic field strength above an arched (toroidal) flux rope (Kliem and Török, 2006). The rate of change of magnetic field strength with height may be quantified by the decay index, n, defined as

$$n = -\frac{d\ln B_{\mathrm{ext},p}}{d\ln R}, \tag{1.36}$$

where $B_{\mathrm{ext},p}$ is the strength of the poloidal component of the magnetic field external to the flux rope (non current-carrying), and R is the major radius of the torus. The value of the critical decay index required for the torus instability of a symmetric torus with a large aspect ratio is 1.5 (Bateman, 1978; Kliem and Török, 2006), and a number of studies have found similar values in MHD simulations (Török and Kliem, 2007; Aulanier et al., 2010; Kliem et al., 2013; Zuccarello et al., 2015, 2016). However, some studies have also found lower and higher critical decay indices (*e.g.*, $n_{crit} = 1.1 - 1.3$; Démoulin and Aulanier 2010, and $n_{crit} \approx 2$; Fan 2010).

Chapter 2

Instrumentation

A number of different observational techniques have been employed throughout this thesis to gain information about the evolution of CME source regions. This chapter contains details of the numerous spacecraft, instruments, and data products that have been used.

2.1 The Solar Dynamics Observatory (SDO)

The *Solar Dynamics Observatory* (SDO; Pesnell et al., 2012) was launched on 11 February 2010, and its instruments began taking measurements on 1 May of the same year. The spacecraft operates in a geosynchronous orbit that is inclined by 28° to the equator, such that SDO remains above the longitude of its ground station in New Mexico. This allows SDO to obtain and downlink a continuous 24 hours of solar observations per day.

The purpose of SDO is to study the continual variability of the Sun. Data from two of the instruments onboard SDO have been used in this work, and these are described subsequently.

2.1.1 The Atmospheric Imaging Assembly (AIA)

The *Atmospheric Imaging Assembly* (AIA; Lemen et al., 2012) is an instrument onboard SDO that makes high-cadence, high-resolution, full-disc observations of the Sun in the ultraviolet (UV) and EUV to study variation in the corona.

AIA features four main telescopes, each with a filter wheel so that every telescope can be used to observe multiple channels (see Figure 2.1). Three of the tele-

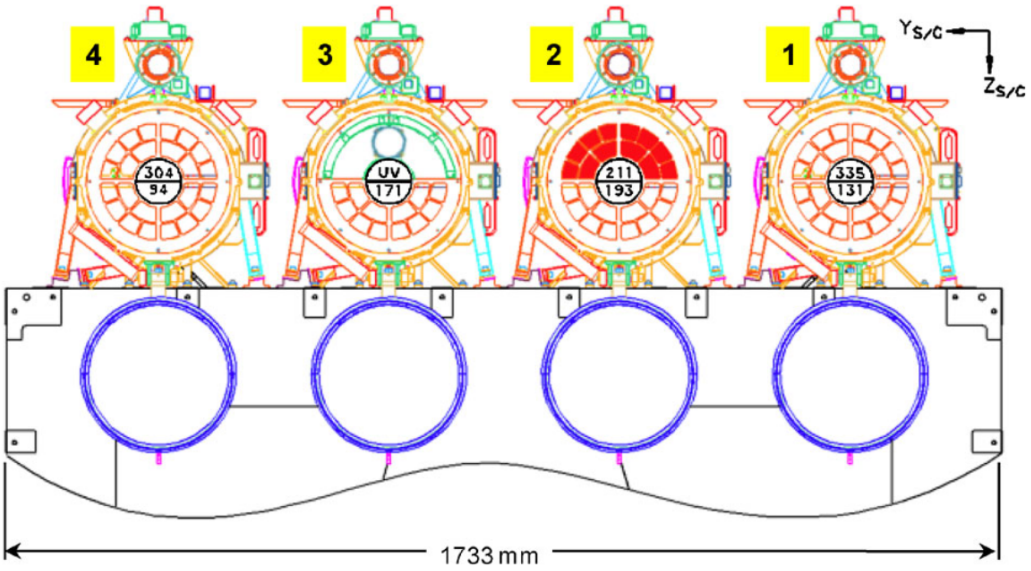

Figure 2.1: The four main telescopes of AIA. Each telescope is capable of making observations in multiple channels using a filter wheel to switch between them. Telescopes 1, 2 and 4 are used to observe two EUV channels each, whereas telescope 3 observes one EUV channel as well as one of three UV channels at a time. Telescope 2 utilises an aperture blade to ensure that only one of its filters is used at a time. Each main telescope also has a guide telescope on top of it for image stabilisation. This is Figure 2 of Lemen et al., 2012.

scopes are used to observe two EUV channels each (telescopes 1, 2 and 4 in Figure 2.1), while the remaining telescope observes one EUV channel and one of three channels in the UV at any time. Telescope 2 requires an aperture selector blade to control which channel is used in each exposure, because its two filters are similar to each other. The EUV observations are made using filters that are each centred on one of seven different spectral lines, corresponding to observations around 94 Å, 131 Å, 171 Å, 193 Å, 211 Å, 304 Å and 335 Å, and the UV observations are centred at 1600 Å, 1700 Å and 4500 Å (see Figure 2.2 for example images made by AIA). The filters each cover a range of plasma temperatures, and, in some channels, this can introduce ambiguity into the observations with regards to which plasma temperature is dominating the observation. For example, the 131 Å pass-band is strongly double-peaked about temperatures of $10^{5.6}$ K and $10^{7.0}$ K (see Figure 2.3 and Table 2.1 for the temperature responses of the filters).

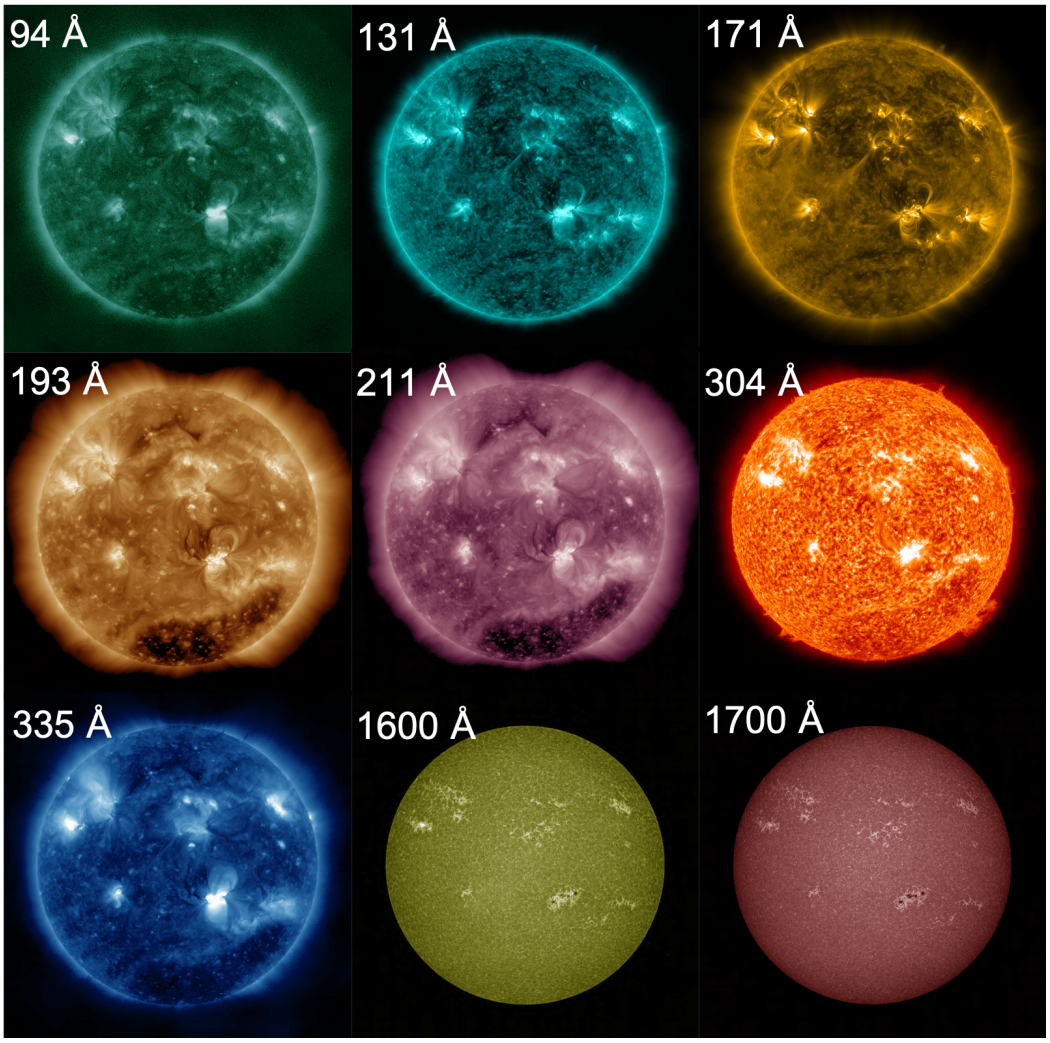

Figure 2.2: Example images produced by AIA in nine of its ten channels, showing the full solar disc. Not pictured is the 4500 Å channel. These images were all taken on the 15 February 2011.

AIA uses four charge-coupled devices (CCDs), with the light that enters each telescope directed to one of the CCDs via two mirrors. Each main telescope also has an associated guide telescope for image stabilisation purposes. Variations in the position of the solar limb, as seen by the guide telescopes, are corrected for by actuating the secondary mirrors accordingly to produce stable images. The CCDs each consist of 4096×4096 pixels, meaning that for the 2460″ diameter instrument field-of-view, each pixel corresponds to an angular diameter of 0.6″ on the Sun. Images are produced in all seven of the EUV channels and one of the UV channels every 12 seconds.

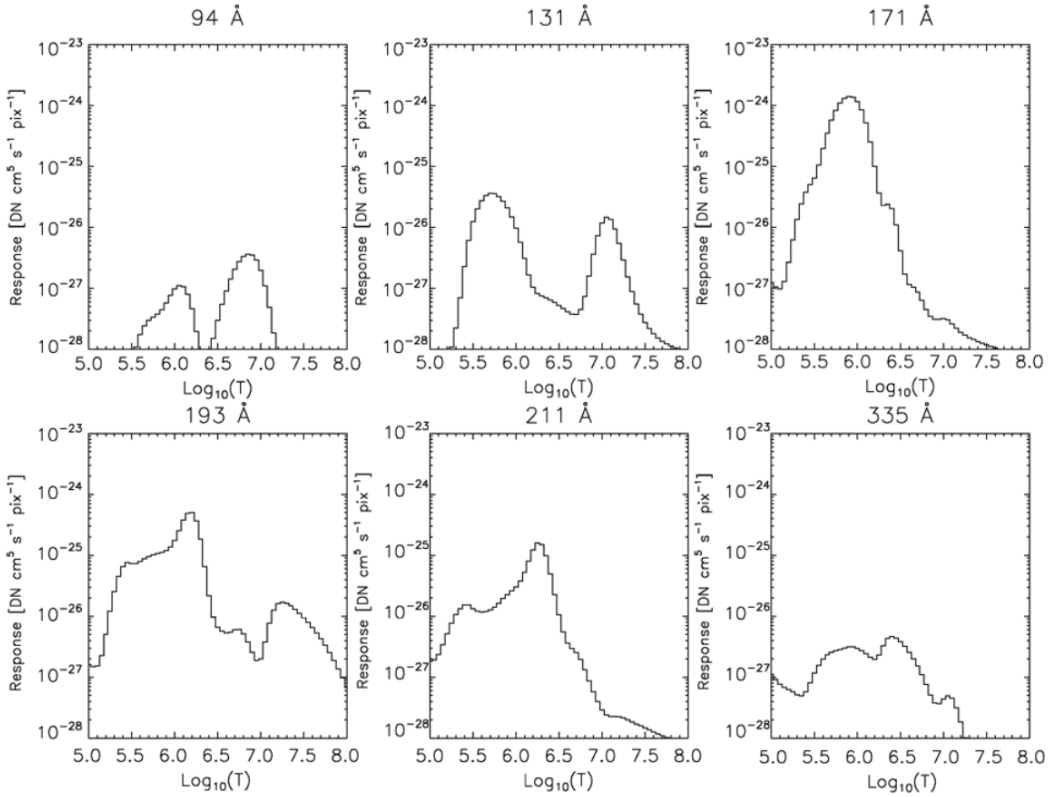

Figure 2.3: Response functions at different plasma temperatures for six of the EUV channels used by AIA. Some channels are strongly double-peaked in response (*e.g.* 94 Å, 131 Å). Adapted from Figure 11 of Boerner et al., 2012.

Channel	Primary ion(s)	Region of atmosphere	Char. $\log(T)$
4500 Å	continuum	photosphere	3.7
1700 Å	continuum	temperature minimum, photosphere	3.7
304 Å	He II	chromosphere, transition region	4.7
1600 Å	C IV + cont.	transition region, upper photosphere	5.0
171 Å	Fe IX	quiet corona, upper transition region	5.8
193 Å	Fe XII, XXIV	corona and hot flare plasma	6.2, 7.3
211 Å	Fe XIV	active-region corona	6.3
335 Å	Fe XVI	active-region corona	6.4
94 Å	Fe XVIII	flaring corona	6.8
131 Å	Fe VIII, XXI	transition region, flaring corona	5.6, 7.0

Table 2.1: Each AIA channel corresponds to one or more primary ion and therefore has associated characteristic temperatures. This means different channels can be used to examine plasma at different heights in the solar atmosphere, from the photosphere to the corona. This is Table 1 of Lemen et al., 2012.

The raw, 'level 0' data received at the SDO ground station from AIA are subsequently corrected for CCD noise, dark current, bad pixels and flat-field effects. Images are also rotated by 180° so that solar North is at the top of the images, because in the raw data, solar South is at the image top. Once the data have undergone these corrections, they are labelled as 'level 1' data, and it is at this stage the data can be accessed by users.

2.1.2 The Helioseismic and Magnetic Imager (HMI)

The *Helioseismic and Magnetic Imager* (HMI; Scherrer et al., 2012) is another instrument onboard SDO. Similarly to AIA, HMI captures full-disc images of the Sun, but instead of imaging the corona, HMI makes narrow-band measurements called filtergrams around a photospheric line that can be used to derive the photospheric magnetic field and give pseudo continuum images. Knowledge of the photospheric magnetic field is useful for studying the behaviours that drive phenomena observed in the corona.

2.1.2.1 Filtergram Construction

Magnetograms (images of the Sun's magnetic field) can be made using knowledge of the Zeeman effect. The Zeeman effect refers to the slight shifts in energy that occur in spectral lines in the presence of a magnetic field. In the simplest case, a spectral line is split into three components: one with a slightly increased energy, one with slightly decreased energy of the same amount, and one that is not shifted. The components of the line that either increase or decrease in energy are each polarised in different ways, with one component right-hand circularly polarised and the other left-hand circularly polarised. The component that is not shifted is linearly polarised.

The degree of the splitting (the value of the energy shift) is correlated with, and therefore representative of, the strength of the magnetic field that is present. Therefore, examining the polarisation state across a spectral line allows the determination of the strength and direction of the field in the line-of-sight direction. The transverse component of the magnetic field can be found by also examining the un-displaced

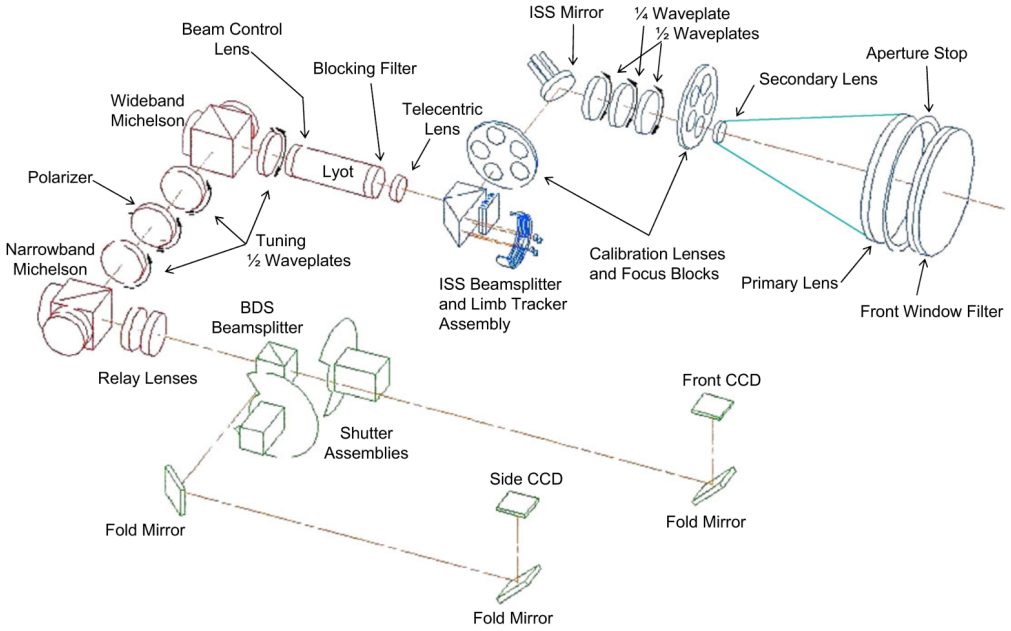

Figure 2.4: The design of the HMI instrument. This is Figure 1 of Scherrer et al., 2012.

line. Since this component is linearly polarised, by measuring the polarisation state of all of the incoming light, the full, vector magnetic field can be determined via an inversion process, albeit with a 180° ambiguity in the transverse field direction (the inversion process and the implications of this ambiguity are discussed in Section 2.1.2.3, along with an attempted disambiguation solution).

HMI takes narrow-waveband 'filtergram' images at six wavelengths and in various polarisation states, and it is these filtergrams that are combined to make magnetic field observations.

2.1.2.2 The HMI Instrument

HMI consists of a telescope, a system of filters and waveplates, an image stabilisation system (ISS; an actuatable mirror connected to four detectors), a beam disruption system, two shutters, and two CCDs. For a visual layout of the instrument components, see Figure 2.4. The light first enters the telescope, which consists of a 14 cm objective lens and an enlarging lens. For calibration purposes, the light then passes through the first of two calibration focus wheels that are together used to image the front window onto the CCD with sunlight falling on every pixel. Three rotatable waveplates (two half-wave plates and one quarter-wave plate) are located

between the first calibration wheel and the ISS mirror in HMI. These allow for the selection of the polarisation state to be examined and allow for redundancy, since only two of the three waveplates are required to be in the correct position for any polarisation state. The light from the telescope then reflects from the actuatable mirror of the ISS and is passed through the second calibration focus wheel. A polarising beam splitter then creates two primary images, with the light of the rejected polarisation from the beamsplitter imaged on to the detectors of the ISS. The ISS mirror is then actuated accordingly to ensure the data images of the Sun eventually produced at the CCDs are stabilised based on the position of the Sun's limb in the ISS images.

Light of the desired polarisations is directed to the filters. The filters of the instrument are housed inside an oven because of the required narrow passbands of the filter system. Even small variations in temperature can alter the passband, affecting the measurements. The light heading for the filters must pass through a telecentric lens that images the light to infinity for its journey through the filters. In this way, all of the light passing through the filters arrives at each CCD pixel with the same angular distribution. The filter system works to produce a narrow passband of wavelengths around the 6173 Å line, which is a visible light wavelength representative of the photospheric Fe I absorption line. The central wavelength of this narrow band is tunable by design of the Lyot filter and Michelson interferometers, so that 6 wavelengths around the 6173 Å centre may be sampled when making the narrow-waveband filtergram images that are used to make magnetograms. The optics package of HMI is surrounded by 'Multi-Layer Insulation', to help keep the filters warm while reducing the amount of power required by the oven.

Inside the oven, the light passes into a Lyot filter, which has an 8 Å-wide blocking filter at its entrance to limit the light and heat input. A Lyot filter consists of a number of birefringent plates, meaning the refractive index of each plate depends on the polarisation and path of the light passing through it. Each successive plate in a Lyot filter is also half the thickness of the previous plate, such that successive plates have a passband half as thick as the one before. HMI has five of these elements,

with the final element being tunable via a rotating waveplate. The result of passing through the Lyot filter is that only a narrow band of wavelengths are transmitted. The HMI Lyot filter has a full width at half maximum (FWHM) of 612 mÅ.

Next, the light enters the first of two Michelson interferometers. This has a lower FWHM than the Lyot filter, of 172 mÅ, to narrow the width of transmitted wavelengths even further. Michelson interferometers require an already small range of input wavelengths, so it makes sense to use both types of filter with the Lyot filter placed before the Michelson interferometers to primarily reduce the passband that will enter the interferometers. Two rotating waveplates and a polariser between the interferometers allow for the tuning of the central wavelength in the vicinity of the 6173 Å photospheric absorption line with a three-for-two redundancy. The second Michelson interferometer then reduces the bandwidth of the light even further, with a FWHM of 86 mÅ. The combined filter system produces a 76 mÅ-wide band centred around a tuned peak in the vicinity of 6173 Å. This range of wavelengths was chosen because it reduced the contributions of continuum intensity. As the light leaves the oven, two lenses refocus the telecentric beam to the CCDs. A beam splitter then separates the light in to two beams — one for each CCD.

HMI has two 4096×4096 pixel CCDs. One of these CCDs is used for producing the line-of-sight observables, while the other produces the vector field information. The light passes through the instrument in the same way for both measurements and is only split before reaching the CCDs, instead of using different tuning settings for each set of images. Constantly adjusting the tuning of the instrument back and forth for each image in turn would put a significant stress on the mechanisms of the instrument. Using separate CCDs also allows for a higher image cadence. HMI sends all of the data it gathers back to Earth, where the observables are then later computed.

2.1.2.3 Data Products

The HMI data products used in this work are the continuum intensity, line-of-sight magnetic field, and vector magnetic field (for examples, see Figure 2.5). The CCD that is used to produce the so-called ‘line-of-sight’ observables (which include the

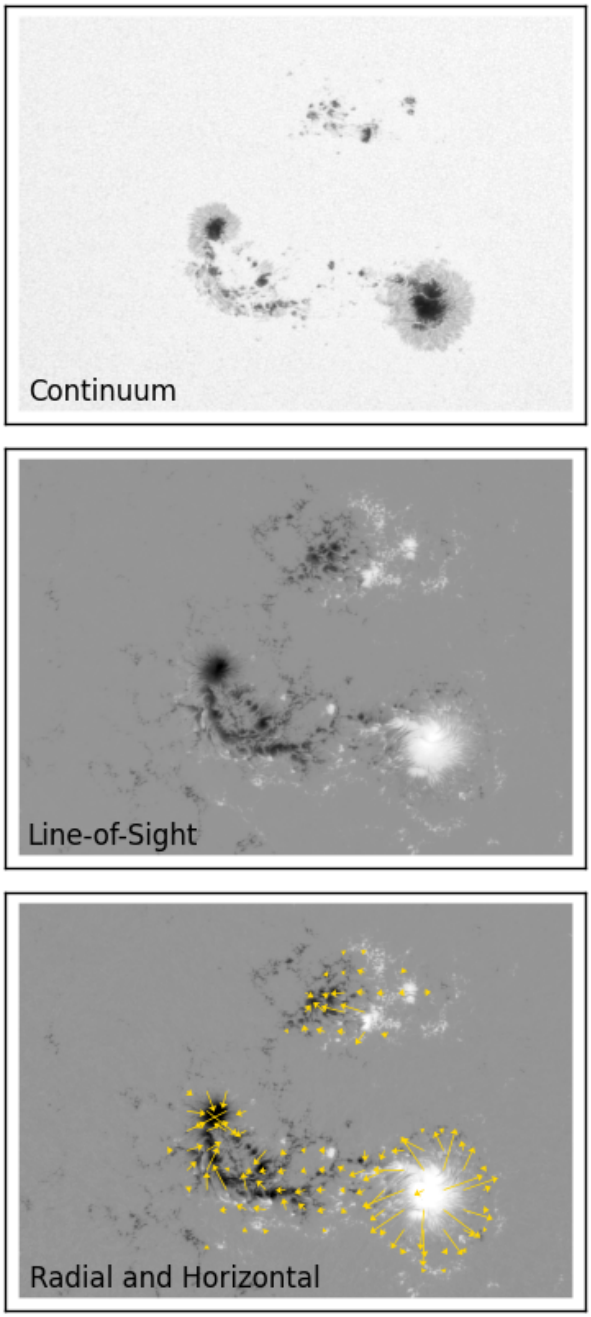

Figure 2.5: Example images of the HMI observables used in this work. *Top*: a continuum intensity image. *Middle*: a line-of-sight magnetogram. *Bottom*: a composite 'vector field' image consisting of an image of the radial magnetic field component with gold arrows representative of the horizontal field component where values exceed 100 G. All three images are from the *hmi_sharp_cea_720s* data series, and therefore also demonstrate the field-of-view selection of a HARP box, which in this case contains two active regions.

continuum intensity images and line-of-sight magnetograms), produces the observables at a cadence of 45 seconds. Each line-of-sight magnetogram is constructed from 12 filtergrams (left and right circularly polarised light at each of the 6 wavelengths that HMI observes). All filtergrams produced by HMI are corrected for overscan, dark current and flat-field effects to science level 1.0 before being used to produce the level 1.5 observables that are downloaded by the user.

The second CCD is used to produce the vector observables. Measurements of the four Stokes parameters that describe the complete polarisation state of the observed light are required to compute the vector field. These parameters are the integrated intensity (I), linear polarisations (Q and U) and circular polarisation (V). Filtergrams are combined to construct each full Stokes vector (for a review on remote sensing magnetic fields, see Lites, 2000), and HMI uses 36 filtergrams; six polarisation states (I$\pm$Q, I$\pm$U, I$\pm$V) at each of the six observed wavelengths. To reduce noise, 360 filtergrams are averaged together when producing science data, resulting in an overall 720 second cadence.

The 3-dimensional magnetic field vector is derived from the Stokes vector via an inversion process, in which spectral measurements are compared to synthetic values from a model solar atmosphere. HMI vector data products are inverted using the Very Fast Inversion of the Stokes Vector (Borrero et al., 2011) method. This inversion outputs the magnitude of the magnetic field (B), and the inclination (θ) and azimuth (ϕ) angles that describe its orientation. However, the azimuth angles obtained via inversion are subject to a 180° ambiguity, and are only given as values $0 < \phi \leq 180$, which means the resulting field vector will also be subject to ambiguity (see Figure 2.6). One effective way to resolve the ambiguity is to apply a 'minimum energy' disambiguation algorithm to the azimuth angles (ME0; described in Hoeksema et al., 2014 and based on ME1 of Metcalf, 1994). The algorithm visits each pixel in a magnetogram a number of times and selects the azimuth orientation there that results in the lower global cost-function defined in terms of gradients of the magnetic field (*i.e.*, whether ϕ or $\phi + 180°$ locally contributes to minimising the global quantity $\sum(|\nabla \cdot \mathbf{B}| + |\mathbf{J}|)$). Methods that work in this way are referred to as

"simulated annealing" techniques (see also the pre-processing method described in Section 3.6.4). The result of the disambiguation process is a set of azimuth angles, $0 < \phi \leq 360$, that describe the magnetic field vector.

One limitation of the minimum energy disambiguation method is that it may have the tendency to select coronal field configurations that are actually less non-potential than the 'true' field, if compatible with minimising the cost-function. Furthermore, simulated annealing techniques can be very computationally expensive. For example, in HMI data, the area of an active region typically covers tens or hundreds of thousands of pixels, and each pixel is visited ~ 100 times. However, the ME0 algorithm was shown to be the best-performing disambiguation method in a series of comparative tests on both idealised and observational conditions (Metcalf et al., 2006; Leka et al., 2009).

It is often useful to convert the observed magnetic field vector from the observed line-of-sight field component (unambiguous) and the transverse component (ambiguous; perpendicular to the line-of-sight) in to components that are radial and tangential (horizontal) to the solar surface. However, both the resulting radial and horizontal field components will be affected by the 180°, since the transverse component is required to determine them both. This is illustrated in Figure 2.6.

The end-user may download the HMI vector data products in a number of formats. Full-disc images are available in the *hmi.B_720s* data series in the form of the magnetic field strength, the inclination and the azimuth angles that describe the magnetic field vector, and information regarding the azimuthal disambiguation. The vector field data is also available in the form of the *hmi_sharp_cea_720s* dataset, which have had two further processing steps applied (see `http://jsoc.stanford.edu/doc/data/hmi/sharp/sharp.htm`; Bobra et al., 2014). Firstly, smaller field-of-view cut-outs of active regions are taken, called HMI active region patches (HARPs; see Figure 2.5 for examples). These are produced by tracking areas of strong magnetic flux as they pass across the observed solar disc, and a field-of-view large enough to encompass the area at its largest point is used for the cut-out. Such a HARP may contain more than one NOAA-designated active region,

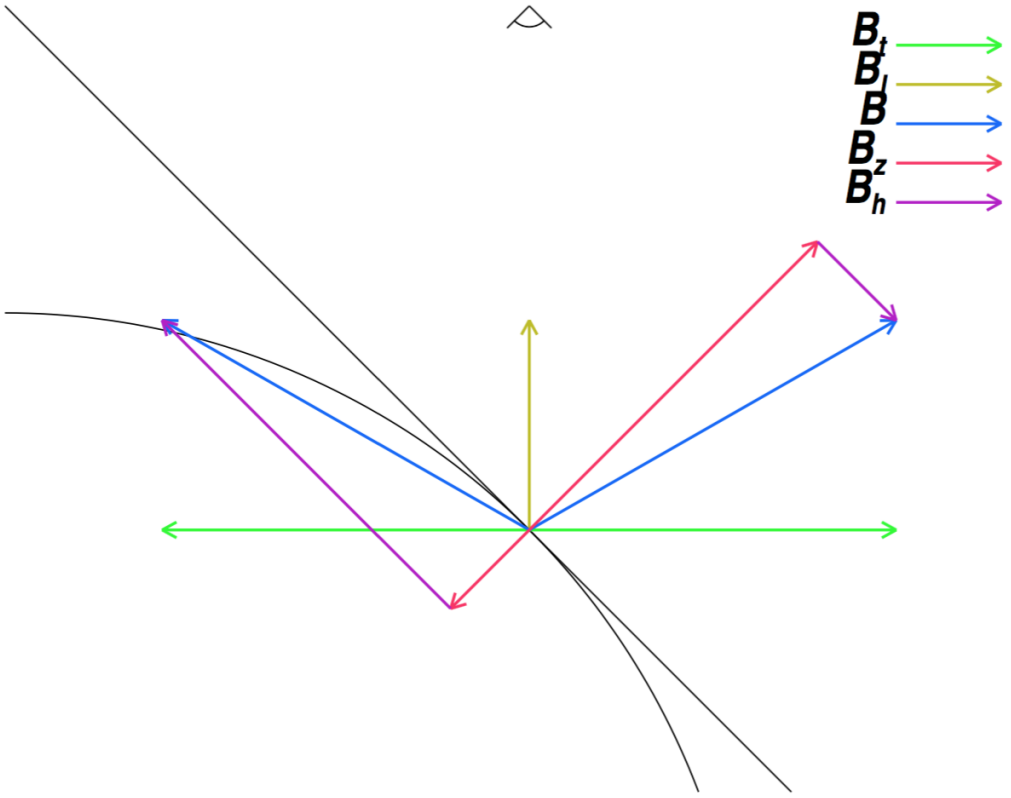

Figure 2.6: Figure by K.D. Leka. Both possibilities of the ambiguous transverse field component (B_t, shown in green) are perpendicular to the unambiguously measured line-of-sight component of the magnetic field (B_l, shown in gold). Either value of B_t results in a different total magnetic field-vector (B, shown here in blue). In the case pictured here, one field-vector has a radial field component (B_z, pink) that is positive and pointing out of the Sun, while the other results in a small, negative radial component pointing in to the Sun. The horizontal field components (B_h, purple) also differ in magnitude and direction.

and so a unique HARP number is assigned to each patch. Quantities useful for space weather analysis (such as the total unsigned flux) are calculated within each HARP box, and so the data are referred to as Spaceweather HMI Active Region Patches (SHARPs). Secondly, the SHARP data are remapped into a Lambert cylindrical equal-area (CEA) projection, so that every pixel contains an equal area of the solar surface (see Section 3.6.3.2). The projected coordinate system is centred on each HARP, reducing line-of-sight projection effects by projecting such that it is as if the observer is looking down on the centre of the HARP throughout its passage across the disc. The line-of-sight and transverse magnetic field components

are remapped into the components that are parallel to the radial direction of the Sun (radial component) and tangential to its surface (horizontal component).

2.1.2.4 Known Instrumental Issues

There is a variation in the orbital velocity of SDO relative to the Sun of ± 3 km s^{-1} every 12 hours that introduces a Doppler shift to the spectral line that is measured by HMI (Hoeksema et al., 2014). The varying Doppler shift thereby affects the filtergrams, causing variations in the determined magnetic field strength that are both time-dependent and spatially-dependent across the solar disc. The extent of the periodic variation in measured field strength is dependent on the value of the field itself, with smaller fractional variations observed in strong-field pixels and larger fractional variations in quiet-sun areas (see Figure 2.7).

There may also be pixels with saturated values present in processed HMI data, which are most often an erroneous result of the inversion process in pixels with large field strengths.

2.2 *Hinode*

The *Hinode* spacecraft (Kosugi et al., 2007) was launched in September 2006 and its instruments had all begun operating by 28 October 2006. *Hinode* operates in a circular, sun-synchronous polar orbit that takes 98 minutes and enables continuous observations of the Sun for nine months of the year. During the remaining months, *Hinode* observations are eclipsed by the Earth for up to 20 minutes[1] of each *Hinode* orbit (so called 'eclipse season'). Data are stored onboard the spacecraft and down-linked to ground stations in Japan (Uchinoura Space Center) and Norway (Svalbard) a number of times per day.

The primary aims of the *Hinode* mission are to investigate the origin and transport of solar magnetic fields, the transfer of energy from the photosphere to the corona, heating in the chromosphere and the mechanisms behind flares and CMEs. In this work, data from the *EUV Imaging Spectrometer* (EIS; Culhane et al., 2007) onboard *Hinode* are used to study plasma composition and Doppler velocities.

[1] Source: '*Where is Hinode?*', `https://www.nasa.gov/mission_pages/hinode/where.html`

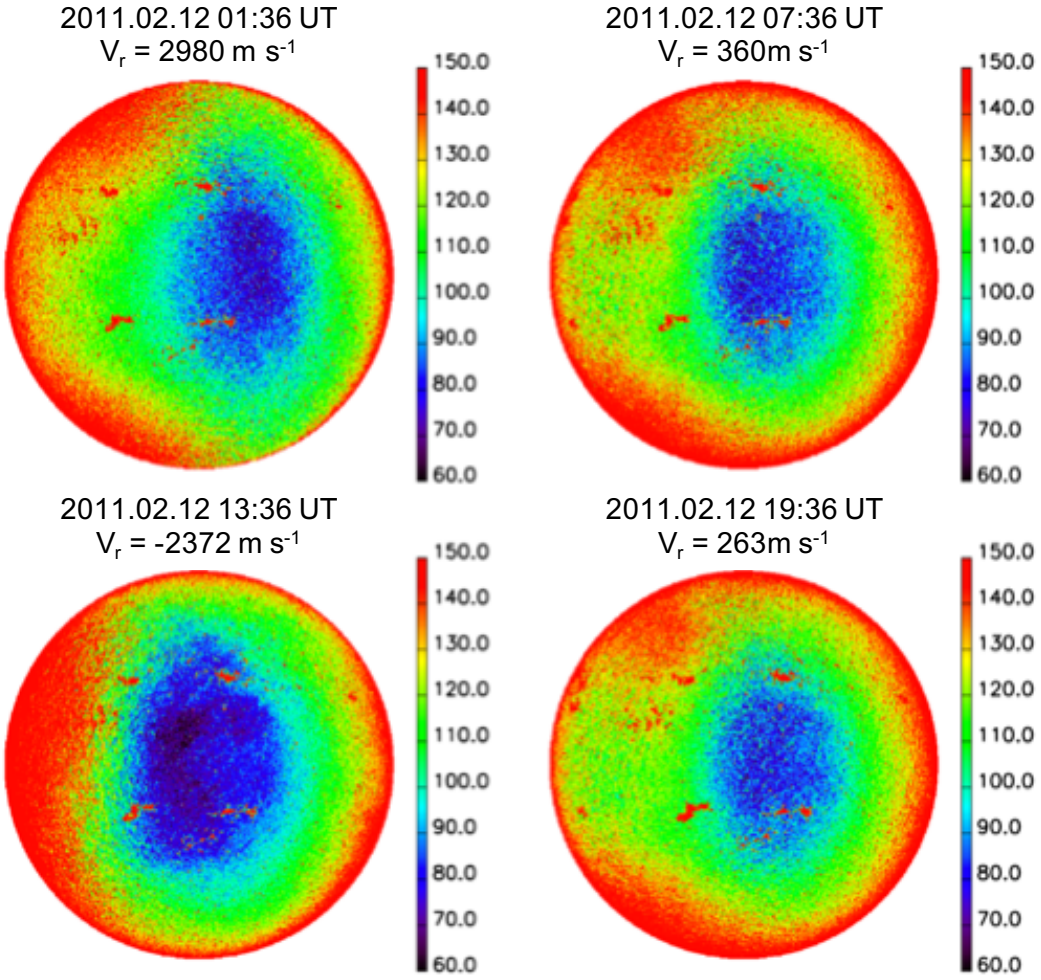

Figure 2.7: HMI observations of line-of-sight magnetic field strength (in Gauss) taken at four times when the spacecraft was moving with different velocities relative the the Sun. The quiet-Sun magnetic field strength should be uniform, but it is seen to vary across the disc. Additionally, the magnitude of this spatial variation depends on the relative velocity of the spacecraft. Adapted from Hoeksema et al., 2014.

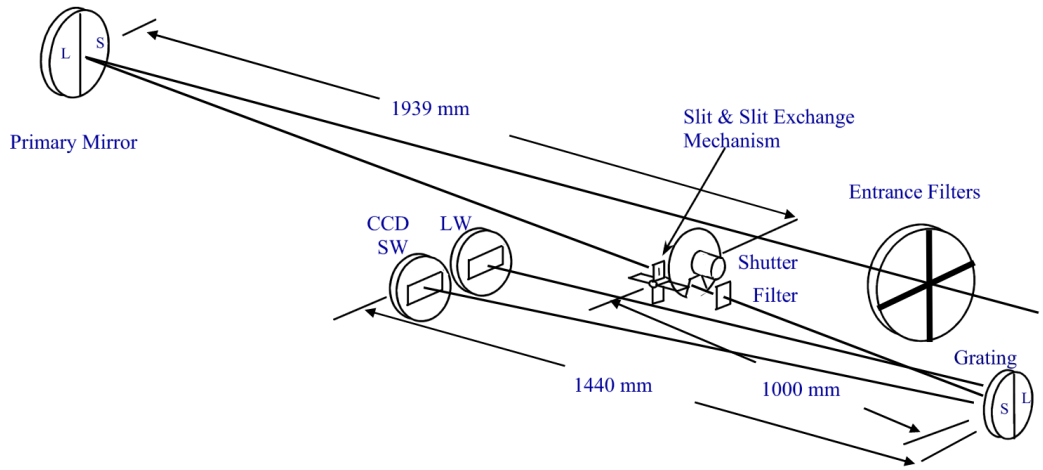

Figure 2.8: The design of EIS. This is Figure 1 of Culhane et al., 2007.

2.2.1 The EUV Imaging Spectrometer (EIS)

The EIS onboard *Hinode* is capable of observing spectral lines at wavelengths in the ranges 170 – 210 Å and 250 – 290 Å using a slit that can be moved to build up images, as well as producing spectra. Separate CCDs are used for the lower and higher wavelength ranges — both of which consist of 1024×2048 pixels — and diffraction gratings are used to produce spectra on these CCDs (see Figure 2.8). EIS features four sizes of aperture that can be used when making observations, and these are categorised as either 'slits' or 'slots'. The two slit apertures are the $1''$ slit and the $2''$ slit, and they can be used to make images of intensity as well as Doppler velocity measurements with a typical error of 5 km s^{-1} (see Figure 2.9 for examples of these image types). The two slot apertures are the $40''$ and $266''$ slots, which can be used to produce high-cadence images. EIS images can be produced via either the 'sit-and-stare' mode, in which the aperture remains in the same location during each exposure, or by moving the aperture from west to east between exposures in a raster scan, which builds up a larger field-of-view over time. The aperture can scan to produce a 6 arcmin × 8.5 arcmin field-of-view. Coarse rasters are those in which the aperture is moved by a larger distance than the width of the slit itself. For example, the $1''$ slit may undergo a $2''$ coarse raster, in which the slit pointing is moved by $2''$ between each $1''$-wide measurement.

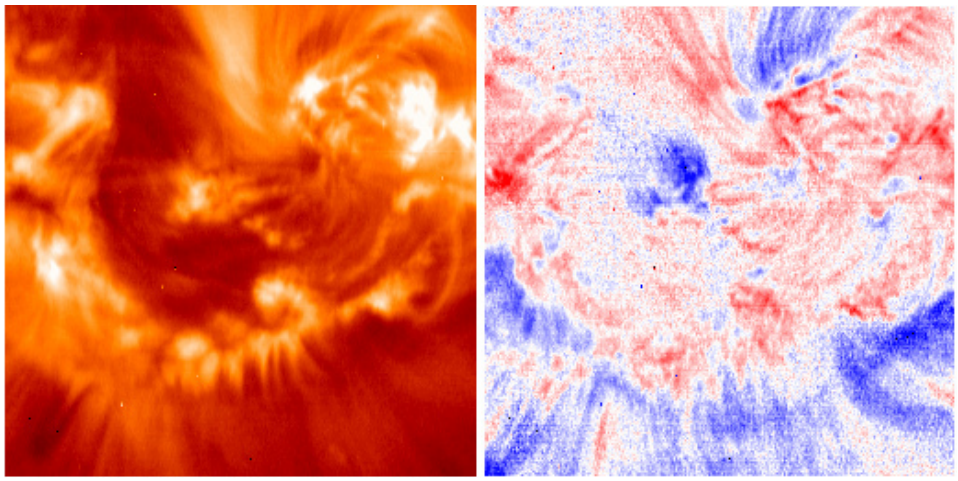

Figure 2.9: Example *Hinode*/EIS images. *Left*: Intensity map in the Fe XII line. *Right*: Doppler velocity map. Credit Dere 2007.

2.3 The Nançay Radioheliograph (NRH)

The Nançay Radioheliograph (NRH; Kerdraon and Delouis, 1997) is a ground-based telescope array located in Nançay, France and operated by Paris Observatory. The purpose of NRH is to produce observations of solar radio activity that can be used in conjunction with other solar and space-weather missions. The instrument is made of 44 total antennae across two 'arms'; the 'North-South' array and the 'East-West' array, that together, form a 'T'-shape (see Figure 2.10). The NRH can observe at up to ten radio frequencies simultaneously in the range 150 – 450 MHz, with a spatial resolution between 0.3 – 6 arcminutes that depends on the frequency and season. The NRH is designed to produce images with a very fast cadence, and can take up to 200 images per second. Figure 2.11 shows an example of an image produced by NRH.

2.4 The Geostationary Operational Environmental Satellite (GOES) System

The *Geostationary Operational Environmental Satellite* (GOES) system is a network of satellites that function together to monitor terrestrial weather, such as hurricanes, but also measures solar X-ray activity. Each GOES satellite is designated an identifying letter prior to its launch and is renamed with a sequential number if it

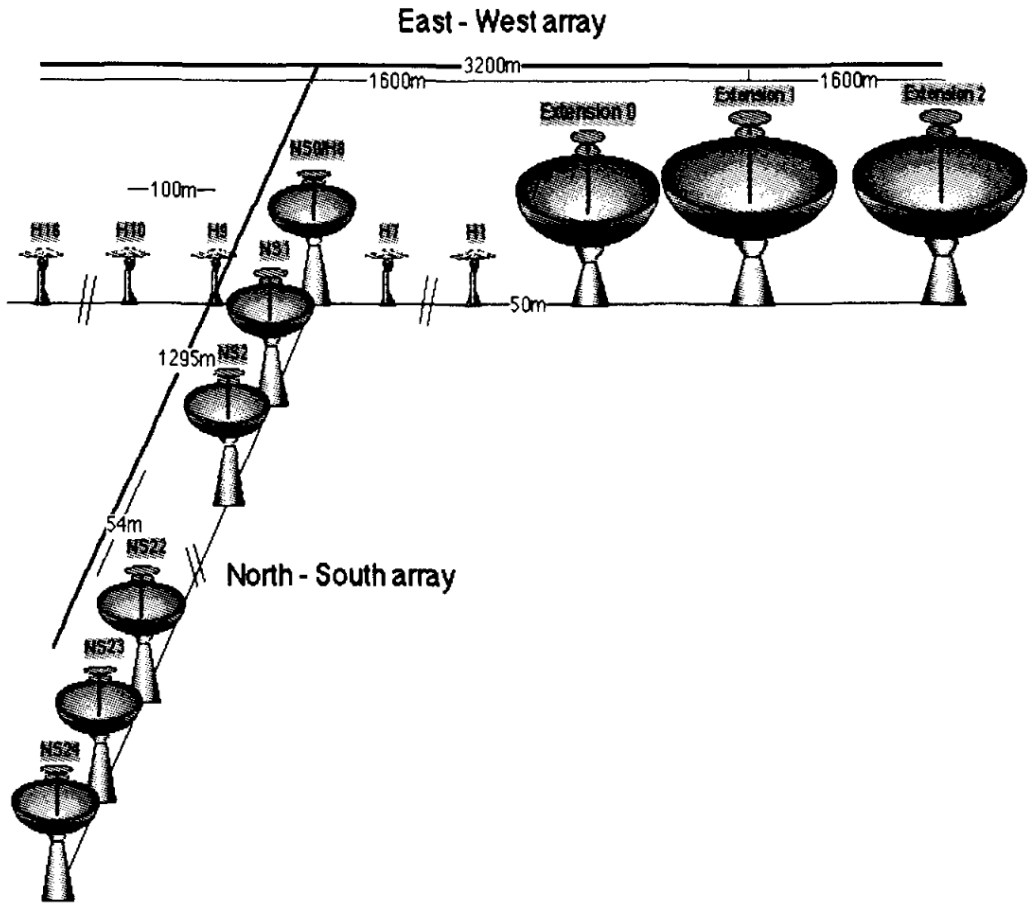

Figure 2.10: The 'T'-shape configuration of the Nançay Radioheliograph, in which the East-West and the North-South 'arms' combine for a total of 44 antennae. This is Figure 1 of Kerdraon and Delouis (1997).

successfully reaches orbit. For example, GOES-A was the name of the first satellite of the mission during its construction and it was renamed GOES-1 once in orbit, but the rocket carrying GOES-G exploded soon after launch, so GOES-H went on to become GOES-7 in its stead. GOES-15 launched in March 2010 and has been operational since December 2011.

2.4.1 X-ray Sensor (XRS)

In this work, measurements of full-Sun integrated X-ray flux taken by the *X-ray Sensor* (XRS) instrument onboard GOES-15 are used to give context to EUV and photospheric observations of active region evolution. The XRS is one of the instruments in the GOES-15 *Space Environment Monitor* package, and it provides

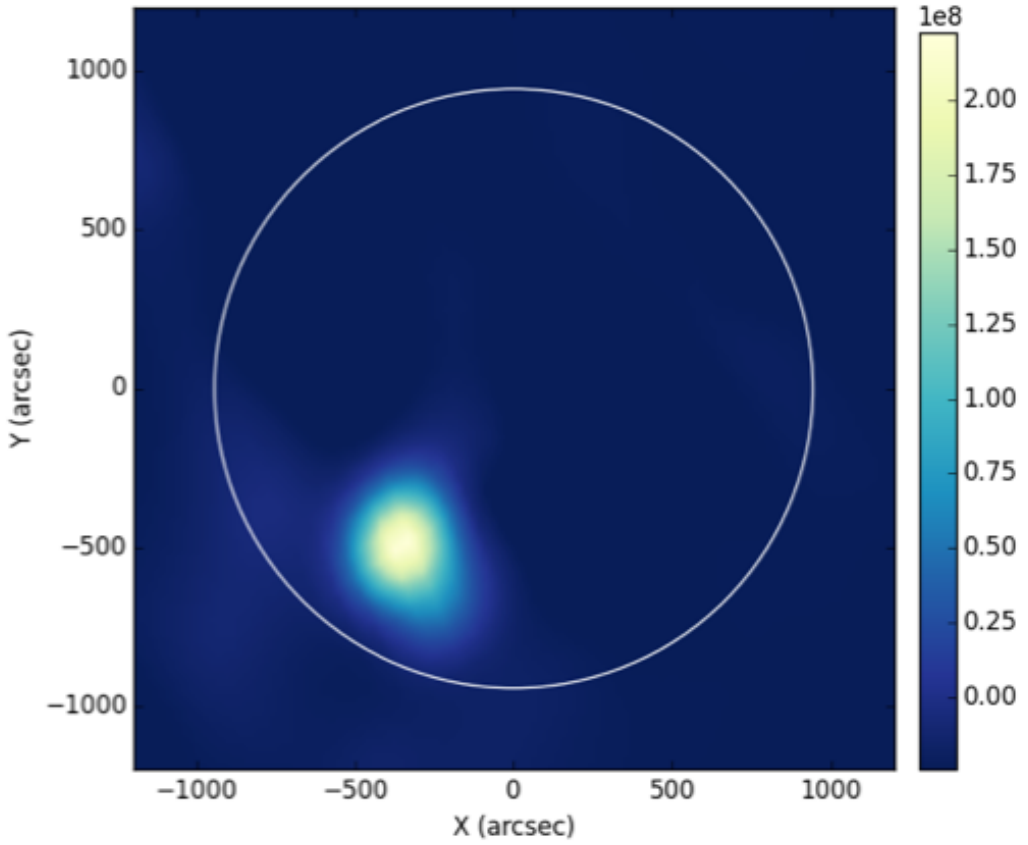

Figure 2.11: An example of an image produced by NRH. This image was taken at around 10:00 UT on the 14th June 2012 at 150 MHz, and the brightest regions correspond to the largest intensities of radio emission. The position of the limb of the Sun has been added in white for reference.

full-disc integrated X-ray flux measurements in the wavelength ranges 0.5 – 4.0 Å and 1.0 – 8.0 Å (see Figure 2.12 for an example of lightcurves produced by GOES). Data from the XRS are relayed to the Space Weather Prediction Center in Boulder, Colorado, where they are used for space weather forecasting purposes. In particular, solar flares are classified according to their peak integrated X-ray flux measured by GOES in the 1 – 8 Å wavelength range. Each successive class of flare corresponds to an order of magnitude increase in X-ray flux, from the weakest class-A flares ($<10^{-7}$ W m^{-2}) through B, C, M and X-class flares ($>10^{-4}$ W m^{-2}; see Table 2.2). Further to the letter of its class, each flare is designated a number to delineate the value of the peak intensity. For example, a flare with a peak intensity of 2×10^{-4} W m^{-2} is designated X2, and a flare of 6×10^{-5} W m^{-2} will be M6.

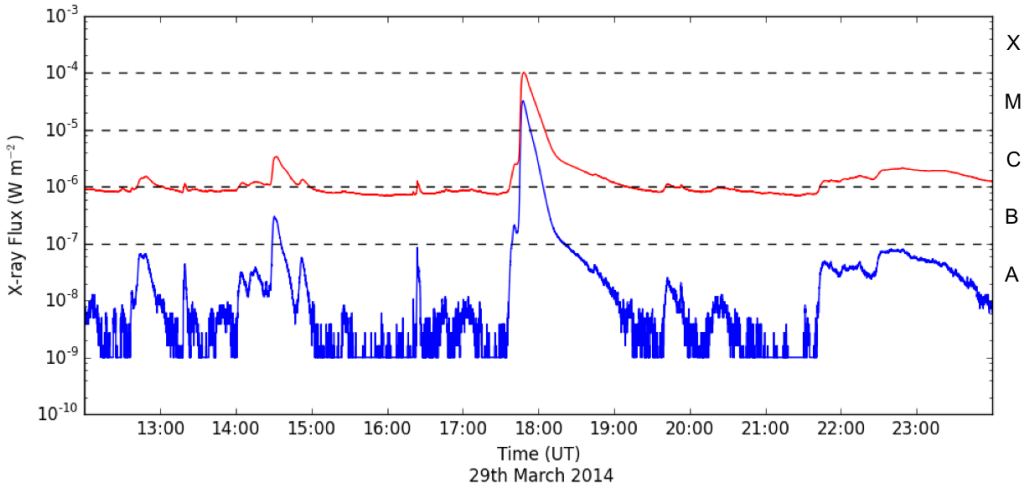

Figure 2.12: An example of lightcurves obtained by GOES-15. The blue curve represents integrated X-ray flux measurements in the 0.5 – 4.0 Å range and the red curve shows the 1.0 – 8.0 Å range.

Class	X-ray Flux (W m^{-2})
A	$< 10^{-7}$
B	$10^{-6} - 10^{-7}$
C	$10^{-5} - 10^{-6}$
M	$10^{-4} - 10^{-5}$
X	$> 10^{-4}$

Table 2.2: Flares are classified according to their peak intensity of X-ray flux integrated over the 1.0 – 8.0 Å wavelength range.

2.5 The Solar and Heliospheric Observatory (SOHO)

The *Solar and Heliospheric Observatory* (SOHO; Domingo et al., 1995) was launched on 2 December 1995 and operates in a halo orbit about the Earth-Sun L1 point. SOHO has a comprehensive instrument payload for taking *in situ* measurements and remote-sensing observations.

2.5.1 The Large Angle and Spectrometric Coronagraph (LASCO) Experiment

One of the remote-sensing instrument packages onboard SOHO is the *Large Angle and Spectrometric Coronagraph* (LASCO; Brueckner et al., 1995). LASCO consists of three coronagraphs with different fields-of-view: C1 which images from 1.1 – 3 $R_\odot$, C2 which images from 1.5 – 6 $R_\odot$, and C3 which images from 3.7 – 30

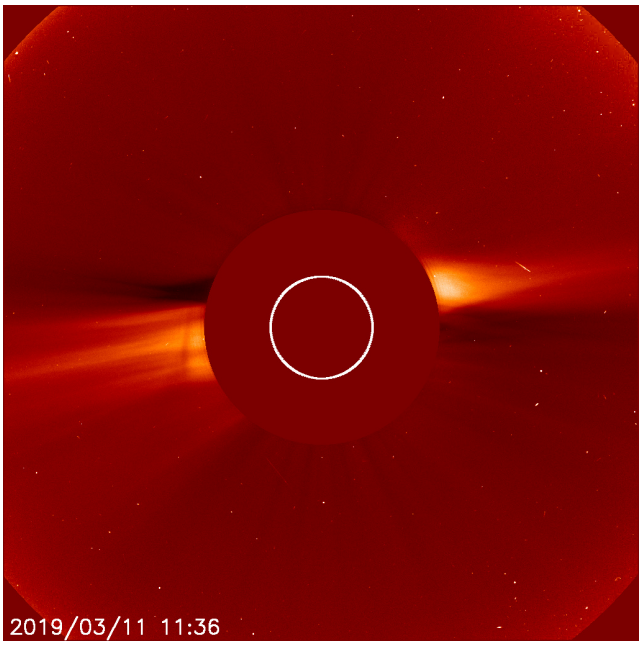

Figure 2.13: Image from SOHO/LASCO C2. The brightest regions in this image are where the electron density is highest. The location of the solar surface is indicated by the central white circle.

$R_\odot$ (all distances measured from the centre of the Sun).

Occulting discs block photons from the bright solar disc to enable better imaging of the faint corona. Light from the Sun is Thomson-scattered by electrons in the corona, so the observed intensity is proportional to the electron density (Figure 2.13).

2.6 The Solar Terrestrial Relations Observatory (STEREO)

The *Solar Terrestrial Relations Observatory* (STEREO; Kaiser et al., 2008) mission consists of two satellites: STEREO-A and STEREO-B, that were launched in October 2006. Both spacecraft orbit the Sun at approximately 1 AU, but STEREO-A is slightly closer to the Sun and therefore orbits slightly faster than the Earth does, and STEREO-B is slightly farther from the Sun and therefore orbits slightly slower than the Earth does. The effect of this is that the separation of the STEREO satellites varies over time, as STEREO-A moves 'Ahead' of the Earth and STEREO-B lags 'Behind' (see Figure 2.14).

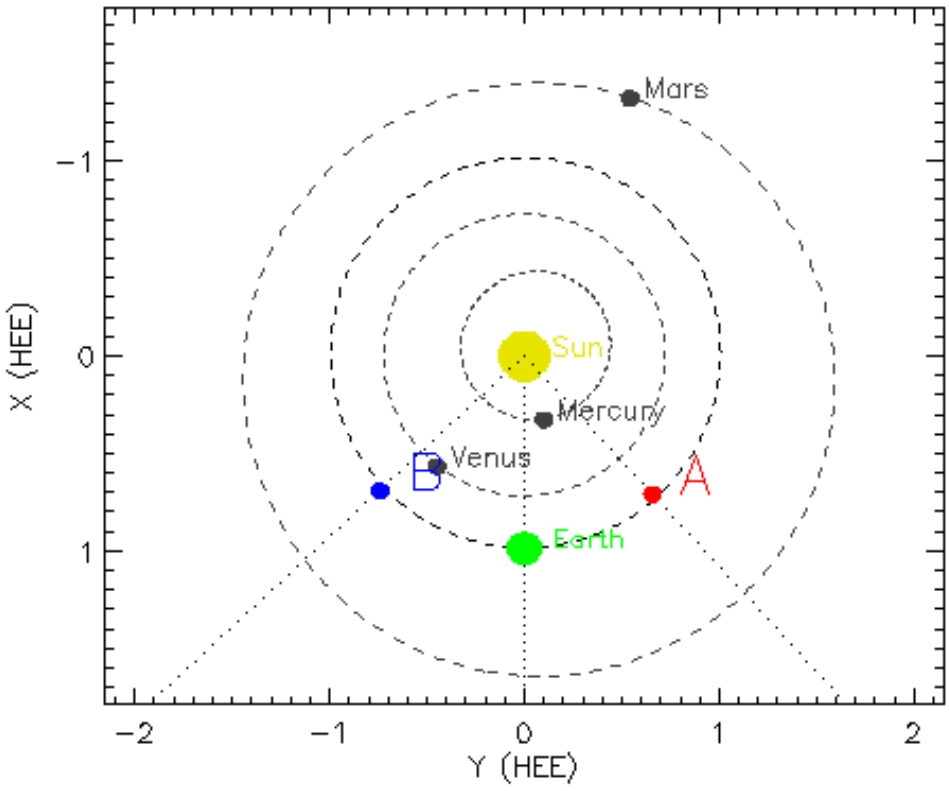

Figure 2.14: The positions along their orbits of the STEREO-A and STEREO-B spacecraft on 24 January 2009. On this date, the spacecraft were at quadrature. Made using the 'Where Is STEREO' tool at `https://stereo-ssc.nascom.nasa.gov/cgi-bin/make_where_gif`.

Contact was lost with STEREO-B on 1 October 2014, and no scientific data has been obtained from it since. However, STEREO-A is still functional and providing data at the time of writing this thesis.

Each of the STEREO spacecraft contains a package of instruments called the *Sun Earth Connection Coronal and Heliospheric Investigation* (SECCHI). SECCHI consists of the *Extreme-Ultraviolet Imager* (EUVI) for the solar disc (with 171Å, 195Å, 284Å, and 304Å channels), two coronagraphs (COR1; 1.5 – 4 $R_\odot$ and COR2; 2 – 15 $R_\odot$), and two heliospheric imagers. To distinguish between data from each spacecraft, the name of each instrument may be appended with an 'A' or 'B' (*e.g.*, COR2-A vs COR2-B).

Chapter 3

An Introduction to Magnetic Field Modelling

3.1 Why Do We Need Magnetic Field Modelling?

Although CMEs are a way of releasing energy and magnetic helicity from the Sun, no relationship has been found between the amount of available magnetic energy and helicity in the corona and the likelihood that an eruption will occur. Connections have been made between the structure of the coronal magnetic field and the occurrence of eruptions, such as critically-twisted fields becoming kink-unstable, and decreasing field gradients in height causing the torus instability (see Section 1.3.3.1 for an introduction to these instabilities). Furthermore, simulations suggest that a specific magnetic helicity quantity may be a predictor for eruptions (the ratio of the current-carrying field helicity and the total-volume helicity, $\frac{H_J}{H_V}$; Pariat et al., 2017). To investigate processes such as these, we need to study the structure of the coronal magnetic field in detail.

However, we are currently unable to make sufficiently accurate measurements of the magnetic field in the corona due to its high temperature, low density, and low field strength. In lieu of magnetic field measurements in the corona, we can use our knowledge of coronal conditions to create models of the coronal magnetic field. For example, techniques have been developed to extrapolate the coronal magnetic field from photospheric magnetic field measurements, which are readily available

(for example, produced by HMI; Section 2.1.2.2). From these models of the solar atmosphere, we are able to study twisted coronal fields and obtain quantitative results, for example identifying flux ropes and their twist, computing the decay index, and evaluating magnetic helicity.

3.2 Extrapolating the Corona From Photospheric Measurements

Although the corona evolves dynamically, we can assume that the coronal field at any point in time is in quasi-static equilibrium with the photosphere. This is possible because of the sharp contrast in density between the photosphere and the corona ($n_{ph}/n_{cor} \sim 10^8$), whilst the magnetic field strength only changes by one order of magnitude (Gary, 2001). This difference in density means that magnetic disturbances travel at different speeds in the photosphere and the corona. For an order-of-magnitude estimation, we can consider that magnetic waves travel at the Alfvén speed, defined in Equation 1.18. In the corona, typical magnetic field strengths and densities can be $B \sim 100$ G (above sunspots) and $\rho \sim 10^{-12}$ kg m^3 (from $\rho \approx m_p n$, where number density, $n \sim 10^{15}$ m^{-3}, and the mass of a proton, $m_p = 1.67 \times 10^{-27}$ kg), giving a typical Alfvén speed $v_A \sim 10^6$ m s^{-1}. In the photosphere, typical magnetic field strengths and densities can be ~ 1000 G and $\rho \sim 10^{-7}$ g cm^3 ($n \sim 10^{23}$ m^{-3}), giving a typical Alfvén speed $v_A \sim 10^3$ m s^{-1}.

The difference in local velocities means that changes to the coronal magnetic field occur on a much shorter dynamic timescale than in the photosphere. By choosing typical length scales, l, in the photosphere and the corona, we are able to define the Alfvén time,

$$t_A = \frac{l}{v_A}, \tag{3.1}$$

as the timescale on which variations in the magnetic field propagate. For $l \sim 10$ Mm, we see that the Alfvén time in the corona and photosphere are of the order of seconds and hours, respectively. Since the corona evolves on a much faster timescale, the coronal field will adapt relatively instantly to any evolution of the photo-

spheric magnetic field beneath, and can therefore be considered in equilibrium with respect to the photospheric evolution. This allows us to extrapolate snapshots of the photospheric magnetic field to construct series of the corresponding quasi-static coronal field equilibria.

The approximation that the corona is quasi-static is not always valid. For example, during the onset of a CME, the coronal field may become unstable and no longer be in equilibrium with the photosphere. This means that changes in the large-scale coronal magnetic field occur on a timescale defined by the development of instability in the field, not based on the speed at which small magnetic disturbances can travel across a length-scale in the photosphere.

3.3 Forces in the Corona

In Section 1.2.2.1, the relative importance of terms in the ideal MHD momentum equation (Equation 1.13) was analysed. In the corona, the Lorentz force term on the RHS of Equation 1.13 dominates the pressure and velocity terms on the LHS. Since the Lorentz force cannot be balanced by the relatively negligible pressure and velocity forces, the Lorentz force must vanish to a first order approximation. This leads to the force-free condition in the corona:

$$\mathbf{J} \times \mathbf{B} = 0, \tag{3.2}$$

which means that, within the validity of the assumptions given above, electric currents must be aligned with the magnetic field in coronal equilibrium. This, together with the solenoidal condition ($\nabla \cdot \mathbf{B} = 0$; Equation 1.8) defines the force-free system of nonlinear partial differential equations for the coronal field. These are therefore the conditions that must be solved when producing a force-free model of the corona. For a review of force-free field modelling in the corona, see Wiegelmann and Sakurai (2012).

3.4 Satisfying a Force-Free Corona

The force-free condition (Equation 3.2) can be satisfied in two ways: either by $\mathbf{J} = 0$, or with $\mathbf{J} \parallel \mathbf{B}$.

3.4.1 Potential Field

In the case of $\mathbf{J} = \nabla \times \mathbf{B} = 0$, the magnetic field $\mathbf{B}$ can be defined as the gradient of a scalar function, ϕ:

$$\mathbf{B} = \nabla \phi. \tag{3.3}$$

By using the solenoidal condition (Equation 1.8), we obtain

$$\nabla \cdot \mathbf{B} = \nabla \cdot (\nabla \phi) = \Delta \phi = 0. \tag{3.4}$$

Here, we see that ϕ is a scalar potential, and therefore Equation 3.3 describes a potential magnetic field, and a unique solution can be determined for given boundary conditions (Seehafer, 1978).

Laplace's Equation 3.4 can be solved using Neumann boundary conditions

$$\frac{\partial \phi}{\partial \hat{n}} = \hat{n} \cdot \mathbf{B} \tag{3.5}$$

where $\hat{n}$ is the external normal to the bounding surface. In this case potential fields can be extrapolated without knowledge of the full-vector magnetic field at the photosphere; only the component normal to the boundary is needed (which is the radial field component in spherical coordinates). Some large-scale features on the sun can be well-described by a potential field, such as coronal holes and the quiet Sun (Wiegelmann and Solanki, 2004), however, potential field models can not explain all observations of active regions (Schrijver et al., 2005).

In general, the corona must not be in the minimum-energy state. We know this because magnetic eruptions are observed without dramatic changes to the normal field component (that determines the potential field in the photosphere), and free energy is required to power these events. This free energy is provided by electric currents.

3.4.2 Non-potential Field

The second case that satisfies a force-free corona is where the electric current density is parallel (or anti-parallel) to magnetic field. This means the magnetic field and current density vectors differ only in magnitude and orientation, and we can therefore write that

$$\mathbf{J} = \alpha \mathbf{B}, \tag{3.6}$$

where α is a scalar function called the force-free parameter that can be positive or negative and relates the current density to the field strength. Larger magnitudes of α describe fields with stronger currents, *i.e.*, fields that are further from the potential configuration (note that $\alpha = 0$ describes a potential field).

Taking the divergence of Equation 1.12 (and using Vector Identity A.3) gives

$$\nabla \cdot \mathbf{J} = 0, \tag{3.7}$$

and, by substituting Equation 3.6, we see that

$$\nabla \cdot \mathbf{J} = \nabla \cdot (\alpha \mathbf{B}) = \alpha (\nabla \cdot \mathbf{B}) + \mathbf{B} \cdot (\nabla \alpha) = 0. \tag{3.8}$$

Utilising Equation 1.8 ($\nabla \cdot \mathbf{B} = 0$), this simplifies to

$$\mathbf{B} \cdot \nabla \alpha = 0, \tag{3.9}$$

which states that the gradient of α is zero in the direction of the magnetic field, or in other words, α is constant along the length of individual field lines. Equations 3.6 and 3.9 are a set of force-free equations equivalent to equations 1.8 and 3.2.

3.4.2.1 Linear Force-Free Fields (LFFF)

A linear force-free field (LFFF) is a field that satisfies Equations 3.6 and 3.9 with constant α throughout the specified volume (such that every modelled field line has the same value of α). In this linear case, a Helmholtz equation is found by taking

the curl of Equation 3.6:

$$\Delta\mathbf{B} + \alpha^2\mathbf{B} = 0, \tag{3.10}$$

Numerous solutions to this condition have been provided, for example, by using Fourier analysis (Alissandrakis, 1981).

The approximation of using a constant α everywhere throughout a region can be adequate for modelling certain aspects of simple magnetic regions (*e.g.,* Green et al., 2002), but in general, the distribution of α in the photosphere is not uniform. For LFFF extrapolation, an input value of α is required. In the same way as for a potential field (which is recovered when $\alpha = 0$), the only magnetic field component needed to make a linear extrapolation is the component normal to the photospheric boundary.

There are a number of ways to determine the appropriate α to use in a linear field approximation. Firstly, the sign of α can be inferred from solar observations. As described in Chapter 1, magnetic flux can show a 'magnetic tongue' pattern as it emerges through the photosphere that indicates its sense of twist. Furthermore, methods have been developed to determine the appropriate magnitude (and sign) of α for the desired case by iteratively comparing to observations, *e.g.*, by minimising the difference between the linearly-extrapolated B_x and B_y components at the photosphere and the corresponding observed components (which requires the 3-D vector field at the photosphere, Pevtsov et al., 1995), or by comparing field lines of different α values with soft X-ray observations of an active region (Green et al., 2002).

The linear force-free problem can be solved using any of a number of methods (Seehafer, 1978; Alissandrakis, 1981), and these can yield real and imaginary solutions. In order to build an LFFF with finite energy (*i.e.*, one that is physical), the real solutions must be taken, and there are therefore constraints on the values of α that may be taken. This is discussed, for example, by Alissandrakis (1981), but it is worth noting the interesting result that the allowed magnitude of α is defined by the dimensions of the extrapolation volume, *i.e.*, the size of the magnetogram used

as the lower boundary condition. In the Alissandrakis method,

$$|\alpha| \leq \alpha_{max} = \frac{2\pi}{L}, \tag{3.11}$$

where L is the length of the longest side of the magnetogram. Since there is an upper limit to α, the maximum value of twist that can be reproduced by a linear extrapolation is therefore constrained by the size of the input magnetogram, rather than any physical constraints. Under the constraint of α, the linear field has a unique solution for given boundary conditions (including the five non-photospheric boundaries).

3.4.2.2 Nonlinear Force-Free Fields (NLFFF)

In the nonlinear case, the force-free parameter, α, varies for different field lines in a volume. This is necessary when attempting to accurately model complex structures in the corona. The nonlinear force-free field (NLFFF) approximation is the simplest method that can reproduce the constraints of an observed photospheric vector magnetogram in terms of electric currents and complex distributions of twist associated with a flux rope (*i.e.*, with a finite value of α) embedded in a (relatively potential; $\alpha \simeq 0$) arcade.

The distribution of α in a force-free field can be found using a rearranged form of Equation 3.6:

$$\alpha(x,y,z) = \frac{\mathbf{J}(x,y,z)}{\mathbf{B}(x,y,z)}, \tag{3.12}$$

where $\mathbf{J}(x,y,z)$ and $\mathbf{B}(x,y,z)$ are the electric current density and magnetic field strength in the volume, respectively. However, in reality, we see from Equation 1.12 that it is not possible to compute the full 3-dimensional $\mathbf{J}(x,y,z)$ without the knowledge of $\mathbf{B}(x,y,z)$ in the same volume. Equation 1.12 shows that electric current density, $\mathbf{J}$, is related to the curl of $\mathbf{B}$, and so we can compute the components of $\mathbf{J}$ with the spatial derivatives of $\mathbf{B}$ as follows:

$$\mu_0 \mathbf{J}_x = \left(\frac{\partial B_z}{\partial y} - \frac{\partial B_y}{\partial z} \right) \hat{\mathbf{x}}, \tag{3.13}$$

$$\mu_0 \mathbf{J}_y = \left(\frac{\partial B_z}{\partial x} - \frac{\partial B_x}{\partial z} \right) \hat{\mathbf{y}}, \tag{3.14}$$

$$\mu_0 \mathbf{J}_z = \left(\frac{\partial B_y}{\partial x} - \frac{\partial B_x}{\partial y} \right) \hat{\mathbf{z}}. \tag{3.15}$$

Here, we see that $\mathbf{J}_x$ and $\mathbf{J}_y$ require information about how $\mathbf{B}$ varies in the z-direction. In application to solar observations, we can not currently compute these two quantities because we do not routinely have measurements of how $\mathbf{B}$ varies with height; we only have knowledge of the magnetic field in a 2-dimensional plane in the form of magnetograms. However, we can compute $\mathbf{J}_z$ using a photospheric magnetogram (*i.e.*, at $z = 0$), and therefore, assuming the magnetogram is compatible with the force-free condition such that the current density and magnetic field are parallel (discussed next), we can get α over the magnetogram by

$$\alpha(x, y, z = 0) = \frac{J_z(x, y, z = 0)}{B_z(x, y, z = 0)}, \tag{3.16}$$

where $J_z(x, y, z = 0)$ and $B_z(x, y, z = 0)$ are the vertical components of the electric current density and magnetic field strength in the lower-boundary magnetogram, respectively. Fortunately, because α is constant along magnetic field lines (Equation 3.9), knowing α in the photosphere is, in principle, sufficient to extrapolate the magnetic field in to the corona within the force-free approximation. Unfortunately, photospheric magnetograms are not force-free, since typically $\beta > 1$ in the photosphere (Gary, 2001; see Figure 1.4). A technique called pre-processing is often used to modify magnetograms within sensible constraints to improve their compatibility with the force-free condition (described in Section 3.6.4).

3.5 Extrapolation by Magnetofrictional Relaxation

There are a number of methods for performing NLFFF extrapolations. In the work of Chapter 5, a magnetofrictional relaxation method is used to produce an NLFFF model of the corona. This procedure is described in detail by Valori et al. (2005, 2007, 2010), but an overview is given in the rest of this chapter.

To summarise, an initial potential coronal field is constructed using the radial field component of a photospheric magnetogram as a lower boundary condition, and then the horizontal potential field components in the lower boundary are overwritten

by the measured, non-potential values. This operation introduces a sharp gradient in the vector field between the lower boundary and the field above it, adding electric current and thereby forces and finite divergence to the field used as the initial condition. The field is then relaxed towards a force-free equilibrium state by propagating the currents upwards and throughout the field volume.

The magnetofrictional relaxation (Chodura and Schlueter, 1981; Yang et al., 1986; Valori et al., 2005, 2007, 2010) works by adding an artificial viscosity term to Equation 1.13

$$\rho(\frac{\partial}{\partial t} + \mathbf{v}\cdot\nabla)\mathbf{v} + \nabla p = \mathbf{J}\times\mathbf{B} - \nu\mathbf{v}, \tag{3.17}$$

where ν is the viscosity. Under the same coronal approximations used to reduce Equation 1.13 to Equation 3.2, and assuming the friction term to be of the same order as the Lorentz force, Equation 3.17 reduces to

$$\mathbf{J}\times\mathbf{B} = \nu\mathbf{v}, \tag{3.18}$$

which prescribes the magnetofrictional velocity, $\mathbf{v}$. A quasi-static coronal equilibrium can be obtained by using Equation 3.18 in the induction equation (Equation 1.7), thereby reducing Lorentz forces with friction (Yang et al., 1986). In reality, friction forces are far smaller than Lorentz forces in the largely collisionless corona, but this unrealistic assumption is used only to pseudo-temporally counter flows resulting from an initially-constructed non-force-free coronal field as it relaxes towards a more realistic force-free equilibrium, not to study the physical evolution of the corona over time. On the other hand, magnetofrictional extrapolations of near-continuous series of (interpolated) photospheric boundary conditions have successfully approximated the observed time-evolution of the coronal field to some extent (*e.g.*, Mackay et al., 2011).

To modify the magnetic field, the relaxation uses a modified version of the MHD induction equation,

$$\frac{\partial\mathbf{B}}{\partial t} = \nabla\times(\mathbf{v}\times\mathbf{B}) + c_L\nabla(\nabla\cdot\mathbf{B}). \tag{3.19}$$

Equation 3.19 differs from the usual MHD induction equation (Equation 1.7) in the addition of the second term on the RHS, which functions as a "divergence cleaner", since the pre-relaxation field will not satisfy $\nabla \cdot \mathbf{B} = 0$ because of the discontinuity in the transverse field components at the bottom boundary, and the relaxed equilibrium should satisfy it as closely as possible. In order to show the effect of the additional term, the divergence of Equation 3.19 is taken (applying Vector Identity A.3), resulting in a diffusion equation for $\nabla \cdot \mathbf{B}$:

$$\frac{\partial (\nabla \cdot \mathbf{B})}{\partial t} = c_L \nabla^2 (\nabla \cdot \mathbf{B}). \tag{3.20}$$

Equation 3.20 demonstrates that finite $\nabla \cdot \mathbf{B}$ contributions will diffuse out of the extrapolation volume as the magnetic field is relaxed (Marder, 1987). The scaling number c_L regulates the diffusion velocity of the "divergence cleaner", and the velocity, $\mathbf{v}$, is defined from Equation 3.18 as

$$\mathbf{v} = c_Y \frac{\mathbf{J} \times \mathbf{B}}{B^2}, \tag{3.21}$$

where c_Y is another parameter that determines the speed of the relaxation (see Section 3.6.1 for more about this parameter).

After a sufficient number of computational steps, the field will have relaxed to a configuration that matches the observed photospheric boundary conditions by construction, and will have been evolved to satisfy the other enforced criteria, such as having a minimal divergence in the magnetic field and minimal Lorentz forces, whilst generally still containing currents, and therefore free energy.

3.6 Numerical Implementation and Boundary Conditions

3.6.1 Space and Time Discretisation

The relaxation must evaluate a number of partial derivatives (*e.g.*, in Equation 3.19). The spatial derivatives are computed using a fourth-order central difference method,

meaning that quantities in one pixel are computed using the differences between neighbouring values that are up to two pixels away on either side (inclusive). Valori et al. (2007) performed a number of extrapolations to compare the use of second-order and fourth-order central differencing, and found that the fourth-order method reproduced a test-equilibria more accurately.

The iteration of quantities is handled with discrete, single time-steps (*i.e.*, using an Euler method). The size of these time-steps, Δt varies to ensure that numerical instability is avoided. To ensure this, the so-called heuristic Courant criterion is adopted: the maximum velocity that is representable on the grid ($v_{courant}$) must be greater than the fluid (magnetofrictional) velocity and wave velocity anywhere across the grid, *e.g.*,

$$v_{courant} = \frac{\Delta x}{\Delta t} \geq \max_{grid}(v_{plasma}, v_{wave}), \tag{3.22}$$

where Δx is the space discretisation. To satisfy this condition, each time step is chosen as

$$\Delta t = c_Y \frac{\Delta x}{\max_{grid}(v_{plasma}, v_{wave})}. \tag{3.23}$$

Here, $0 < c_Y \leq 1$ controls the size of the time step and is tuned experimentally for stability (for diffusion processes, as used here, a typical value is $c_Y = 0.5$.) Smaller time steps give results with smaller errors, but make the computation take longer. A Runge-Kutta-Chebyshev acceleration technique (super-time-stepping; Alexiades et al. 1996; Evje and Karlsen 2000) is used to increase the efficiency of the chosen time steps.

To improve performance, the relaxation is performed over a number of stages, each at different resolutions (referred to as multi-gridding). For example, the first stage of relaxation may be performed on a grid at 1/4 the resolution of the photospheric boundary magnetogram. Once the extrapolated field has reached a fairly stable state at this resolution, the resolution is doubled through trilinear interpolation (*i.e.*, now to 1/2 of the magnetogram resolution), and another stage of relaxation is performed. Finally, the extrapolation resolution can then be increased to the full

magnetogram resolution for a final relaxation. This speeds up the relaxation process by allowing the larger-scale features of the NLFFF field to efficiently propagate to the entire volume before increasing the resolution and allowing smaller-scale adjustments to the field, and also helps to prevent numerical instabilities from developing (Yang et al., 1986).

3.6.2 Initial and Boundary Conditions

The extrapolation volume is defined by the area of the input magnetogram (see Section 3.6.3) and the user-specified height. Then, as introduced in Section 3.5, an initial potential field is extrapolated using only the B_z component of the magnetogram (the component of the magnetic field in the radial direction from the Sun remapped into Cartesian coordinates — see Section 3.6.3.2), resulting in a 3-dimensional potential field vector throughout the extrapolation volume. The potential B_x and B_y components at the photosphere (horizontal to the solar surface) are overwritten by the corresponding non-potential components from the vector magnetogram (see Section 3.6.3 for details on boundary vector magnetograms), and these are kept fixed for the full duration of the relaxation process.

Boundary conditions that the coronal field must satisfy need to also be specified on each of the other five non-photospheric faces of the extrapolation volume. At the side and top boundaries, we impose that the normal component of the field must satisfy $\nabla \cdot \mathbf{B} = 0$. The transverse component is specified at the boundaries by extrapolating from inside the field volume. Valori et al. (2007) found that using a fourth-order polynomial gave the best extrapolated transverse boundary values.

3.6.3 Photospheric Boundary Conditions

The lower boundary condition, which is kept fixed during the extrapolation, is a disambiguated photospheric vector magnetogram with magnetic field components in Cartesian coordinates, *i.e.*, components in the plane of the photosphere (horizontal; B_x and B_y), and perpendicular to the photosphere (vertical; B_z). Furthermore, each pixel in the magnetogram should represent the same area of the solar surface. In this section, the steps taken to obtain such magnetograms are described.

3.6.3.1 Disambiguation

As discussed in Section 2.1.2.3, the azimuth angles used to describe the magnetic field vector are subject to a 180° ambiguity. This must be resolved as best as possible before the photospheric field is used as a boundary condition, because any inaccuracy in the disambiguation will cause inaccuracy in the injected currents (or α) and, therefore, in the final extrapolated field.

There are a number of ways to attempt to resolve the 180° ambiguity. One commonly-used method is the computationally-expensive but effective 'minimum energy' method discussed in Section 2.1.2.3.

When necessary to reduce computation time, the minimum energy method may be used to only disambiguate pixels where the magnetic field is stronger than the noise threshold (≈ 150 G; Liu et al., 2017), since applying the method to potentially-noisy pixels may result in a noisy solution anyway. For weaker-field pixels, less-intensive methods may be used to estimate the correct field orientation. Examples of such methods include choosing the orientation of the transverse field component as the orientation that is closest to the potential field configuration, hand-selecting the orientation that is closest to the "expected" orientation (*e.g.* selecting the most-radial direction outwards from a sunspot), or simply selecting randomly. The downside of the potential and radial methods are that they may select against real areas of non-potentiality by choosing the most-potential orientation. By its nature, the random method will only produce an accurate result in $\approx$50% of the pixels it is used on, but it avoids introducing systematic error in the way that the other two methods do, and is therefore often the method that is used for disambiguating pixels below the noise threshold.

3.6.3.2 Transformation and Remapping

The two-dimensional plane-of-sky images we take of the three-dimensional spherical Sun result in an observed disc. The pixels across these images correspond to different surface areas of the Sun, and must be remapped into a spherical or, as in our case, Cartesian projection before extrapolation. Typically, and for the purposes of the work in this thesis, the Lambert cylindrical equal-area (CEA) projection is

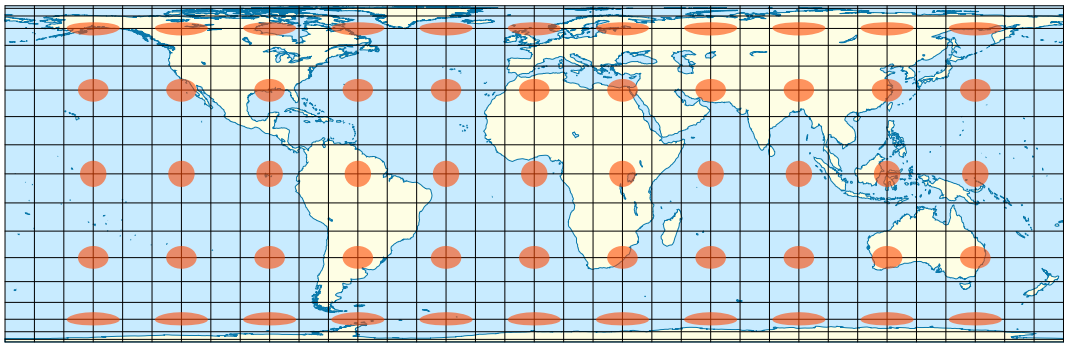

Figure 3.1: A map of the Earth in the Lambert cylindrical equal-area (CEA) projection. Every grid square (image pixel) contains an equal surface area of the planet. The shape of circles are preserved when translated longitudinally, but not in latitude. Image by Eric Gaba, Creative Commons BY-SA 4.0.

used (introduced in Section 2.1.2.3). When applied to a sphere, this projection preserves the shape of features in longitude, but there is distortion with latitude (see Figure 3.1). When applied to an observed disc (*e.g.* solar observations), there will be some amount of foreshortening with longitude away from central meridian as well. Therefore, magnetograms of regions close to the centre of the solar disc are the best targets for extrapolation.

Furthermore, the implementation of the magnetofrictional relaxation employed in the work of this thesis requires the magnetogram to use a Cartesian coordinate system. The description of the magnetic field vector is transformed from field strength, inclination, and azimuth (B, θ, ϕ), to field components that are vertical and horizontal to the solar surface (B_x, B_y, B_z).

3.6.3.3 Available Photospheric Data Products

The *hmi_sharp_cea_720s* data series (as introduced in Section 2.1.2.3), provides magnetograms in a format suitable for extrapolation. SHARP magnetograms are cut-out from full-disc data to contain at least one active region, remapped into the Lambert CEA projection (Section 3.6.3.2), disambiguated with the minimum energy method (Section 3.6.3.1), and transformed to Cartesian coordinates with the same, constant resolution in x and y (Section 3.6.3.2). Since the SHARP images contain far fewer pixels than a full-disc image, the minimum energy disambiguation method is applied to all pixels.

Alternatively, using the Joint Science Operations Center Data Export web tool[1], the user can produce their own magnetograms suitable for extrapolation by taking cut-outs of B, θ, and ϕ from the full-disc vector data (the *hmi.B_720s* data series), remapping into an equal-area projection, disambiguating ϕ, and transforming the field vector to Cartesian coordinates. This may be required if, for example, the magnetograms in the SHARP data series are too small to sufficiently reconstruct the coronal field, as was the case in the work of Chapter 5 (see Section 5.2). Information regarding the full-disk vector data and routines for disambiguating and transforming it to Cartesian coordinates can be found at `http://jsoc.stanford.edu/jsocwiki/FullDiskDisamb`.

3.6.4 Pre-processing

To produce a force-free field, the boundary magnetogram must be force-free. However, the force-free condition does not hold generally in the photosphere because plasma pressure there is comparable-to or greater-than the magnetic pressure ($\beta \gtrsim 1$, except perhaps in sunspots; see Figure 1.4). Further forces are introduced to magnetograms through errors in the filtergram measurements and/or inversion process that are used to make the magnetograms (see Chapter 2.1.2 for details on how magnetograms are made). These errors produce small-scale but sharp gradients in the observed photospheric field. Transverse magnetic field components are particularly subject to such error. This is because the transverse components are derived from the Q and U components of the Stokes vector (these describe linear polarisation), and $Q, U \sim \sin^2(\psi)$, where ψ is the angle between the magnetic field vector and the line-of-sight (Jefferies et al., 1989). Therefore, when a magnetic field is closely aligned with the line-of-sight, the observed linear polarisation is small, and the transverse field component that is inverted from Q and U will be as well. Conversely, Stokes $V \sim \cos(\psi)$, so observed circular polarisation is strong for small ψ, and the measured longitudinal field is strong (Jefferies et al., 1989). For these reasons, magnetograms are often "pre-processed" to reduce total Lorentz forces (both real and error-induced) before they are used as boundary conditions.

[1] `http://jsoc.stanford.edu/ajax/lookdata.html`

In the work of this thesis, the pre-processing method used was that described by Fuhrmann et al. (2007). The method works by defining a functional, L, that quantifies the total magnetic force and torque exerted by the magnetogram on the boundaries of the extrapolation volume, as well as the smoothness of the magnetogram.

The Lorentz force, $\mathbf{F}$ in a volume, V, is

$$\begin{aligned}
\mathbf{F} &= \int \mathbf{J} \times \mathbf{B} \, \mathrm{d}V \\
&= \frac{1}{\mu_0} \int_V (\nabla \times \mathbf{B}) \times \mathbf{B} \, \mathrm{d}V \\
&= \frac{1}{\mu_0} \int_V \left[(\mathbf{B} \cdot \nabla)\mathbf{B} - \frac{1}{2} \nabla B^2 \right] \, \mathrm{d}V \\
&= \frac{1}{\mu_0} \int_V \nabla \cdot \left[\mathbf{B}\mathbf{B} - \frac{1}{2} \mathbf{I} B^2 \right] \, \mathrm{d}V \\
&= \frac{1}{\mu_0} \oint_S (\mathbf{B}\mathbf{B} - \frac{1}{2} \mathbf{I} B^2) \cdot \mathrm{d}\mathbf{S}
\end{aligned} \tag{3.24}$$

where $\mathbf{I}$ is the identity tensor and $\mathrm{d}\mathbf{S}$ is an infinitesimal surface element. If we assume that the lateral and top boundaries do not contribute significantly to the surface integral, then we can restrict the surface integral to only the lower boundary. This implies that the positive and negative flux in the boundary magnetogram are balanced, and any field lines that originate in the photosphere should also eventually terminate there. Dropping the factor μ_0 for convenience, and rewriting $\mathrm{d}\mathbf{S} = -\mathrm{d}x\mathrm{d}y\hat{\mathbf{z}}$, the components of the Lorentz force can then be computed as

$$\begin{aligned}
F_x = \hat{\mathbf{x}} \cdot \mathbf{F} &= -\int_{mgm} B_x B_z \, \mathrm{d}x\mathrm{d}y \\
F_y = \hat{\mathbf{y}} \cdot \mathbf{F} &= -\int_{mgm} B_y B_z \, \mathrm{d}x\mathrm{d}y \\
F_z = \hat{\mathbf{z}} \cdot \mathbf{F} &= \frac{1}{2} \int_{mgm} (B_x^2 + B_y^2 - B_z^2) \, \mathrm{d}x\mathrm{d}y,
\end{aligned} \tag{3.25}$$

and, finally, the functional for the the Lorentz force is

$$L_{force} = F_x^2 + F_y^2 + F_z^2. \tag{3.26}$$

Similarly, for the magnetic torque

$$\mathbf{T} = \int \mathbf{r} \times (\mathbf{J} \times \mathbf{B}) \, \mathrm{d}V, \tag{3.27}$$

components may be written as

$$\begin{aligned} T_x &= \frac{1}{2} \int_{mgm} y(B_x^2 + B_y^2 - B_z^2) \, \mathrm{d}x\mathrm{d}y \\ T_y &= \frac{1}{2} \int_{mgm} x(-B_x^2 - B_y^2 + B_z^2) \, \mathrm{d}x\mathrm{d}y \\ T_z &= \int_{mgm} (yB_xB_z - xB_yB_z) \, \mathrm{d}x\mathrm{d}y, \end{aligned} \tag{3.28}$$

and a functional is defined as

$$L_{torque} = T_x^2 + T_y^2 + T_z^2. \tag{3.29}$$

Another functional, L_{smooth}, describes the smoothness of the magnetogram using a windowed-median around each pixel:

$$L_{smooth} = \sum_{i=x,y,z} \sum_{mgm} (M_{n,B_i}(x,y) - B_i(x,y))^2, \tag{3.30}$$

where $M_{n,B_i}(x,y)$ is the median of B_i values in a $(2n+1)^2$ window centred on pixel (x,y) of a magnetogram, where the window size, n is to be chosen by the user. L_{smooth}, therefore, quantifies the difference between field strength components in one pixel and the median of its neighbours.

An overall functional can be defined as the weighted sum of the others

$$L = \mu_1(L_{force} + L_{torque}) + \mu_2 L_{smooth}, \tag{3.31}$$

where the values of μ_i quantify the importance given to minimising the Lorentz force and magnetic torque, or achieving maximum smoothness ($\mu_i \geq 0$). Only the ratio of the μ_i to each other is important, so μ_1 may be taken as unity, with μ_2 to be chosen. In testing, Fuhrmann et al. (2007) found that $\mu_2 = 0.1$ produced a good balance between lowering the magnetic force and torque whilst still smoothing the magnetogram well. When pre-processing was used during the work contained in this thesis (see Chapter 5), $\mu_2 = 0.01$ was used to give slightly more emphasis to reducing the force and torque.

The pre-processing uses a simulated annealing technique (similar to the method used to disambiguate magnetograms described in Section 2.1.2.3) that makes local, random changes to the components of **B** in the magnetogram with the aim of reducing L. These changes are not completely arbitrary, but rather the user defines limits by which B_x, B_y, and B_z may vary. For each component, the maximum allowed variation per-pixel is given as both as an absolute value and as a relative error, with whichever is largest in each pixel being used by the algorithm. One way to define these limits is to base them on the measurement error, so that the flux densities are only varied within their uncertainty range. In this way, the vertical flux densities are typically allowed to vary less than the horizontal components (if at all), since, as described earlier in this section, transverse field components are subject to larger uncertainties.

The minimisation technique used to reduce L over a magnetogram is named "simulated annealing" due to its resemblance to the metallurgical annealing process, by which a metal is cooled slowly to control its physical properties. A pixel is chosen at random and the field components are changed by a random amount within the specified limit. If this change decreases L, the change is accepted, but if it does not decrease L, the change is given a probability of acceptance. The assigned probability is proportional to $\exp\left(-\frac{\Delta L}{T}\right)$, where ΔL is the difference in L due to changing any of the field components and T is a factor that controls the probabilities, representing a "temperature" for the process. This process is repeated until every pixel in the magnetogram has been visited once, and then the process begins again

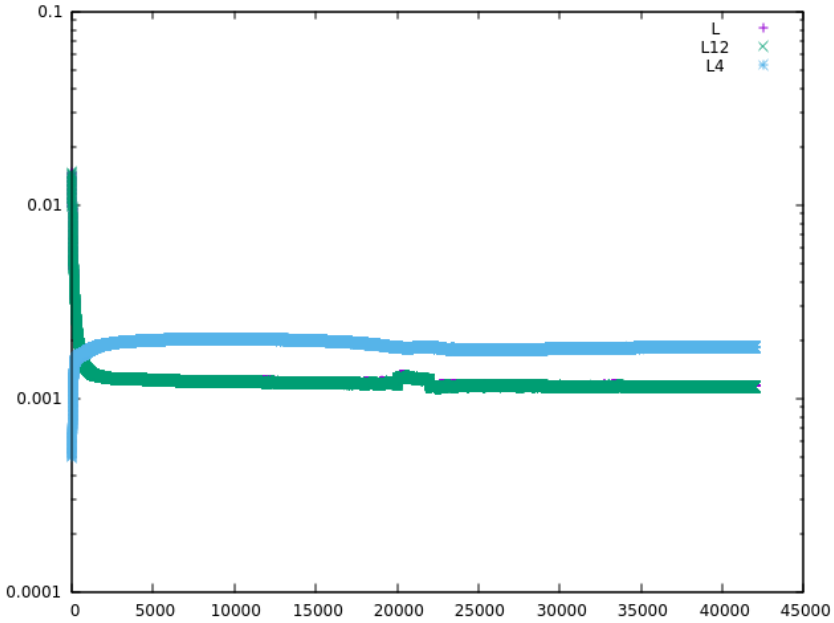

Figure 3.2: An example of the minimisation of the functional, L, (and its individual components, L_{12} and L_4) via simulated annealing. Here, L (purple) approximately follows the same evolution of L_{12} (green, such that it is difficult to see L beneath L_{12}) and reaches a local minimum at ≈20000 iterations. The 'temperature' is raised, and after a few thousand more iterations, a new minimum of L is found that is lower than the previous one.

with the edited magnetogram. Eventually, L will reach a local minimum, but this may not be the global minimum. At this point, T is increased to enable the algorithm to try and leave the local minimum by assigning larger probabilities of acceptance to the changes that increase L. T is decreased again to "cool" the system into the (possible) new minimum. Figures 3.2 and 5.2 show examples of the minimisation of L, demonstrating the way the L is allowed to increase temporarily in order to leave a local minimum.

The effectiveness of the method was tested on an artificially-constructed NLFFF magnetogram with added noise. Starting from the noisy data, preprocessing was able to reproduce a smooth magnetogram that largely resembled the original force-free magnetogram (see Figure 3.3).

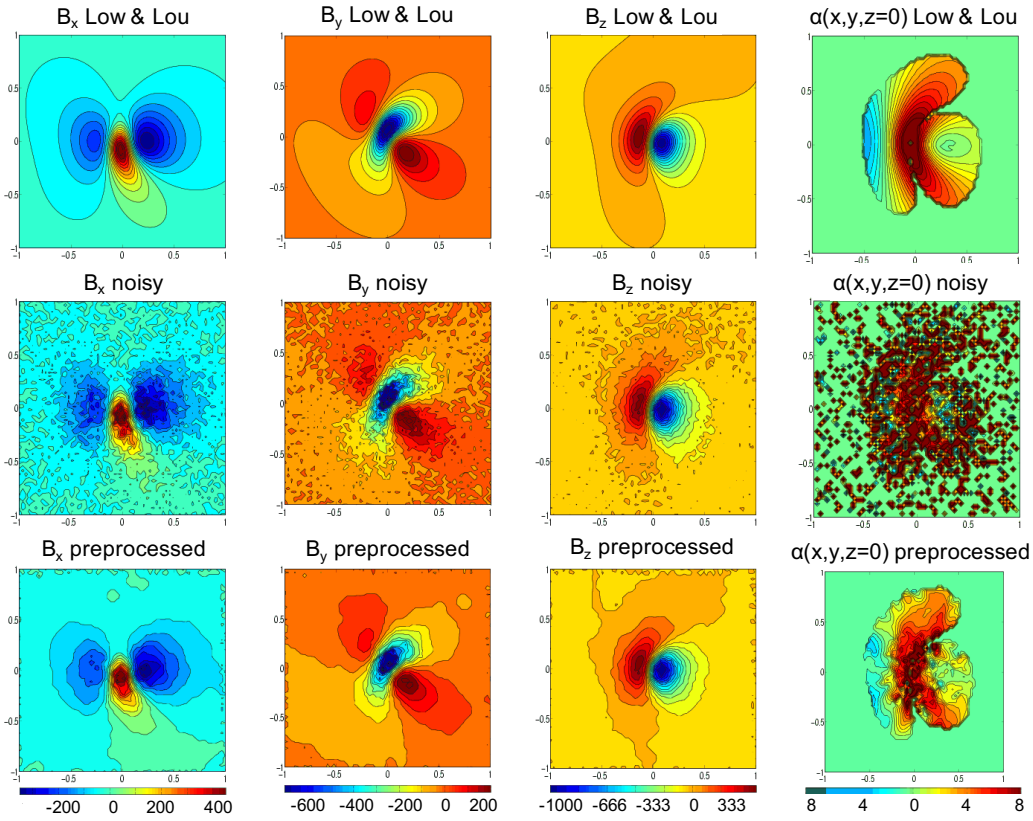

Figure 3.3: Adapted from Figures 1 and 3 of Fuhrmann et al. (2007). The top row shows the constructed Low & Lou test-magnetograms of the three magnetic field vector components, B_x, B_y, and B_z, as well as a map of the force-free parameter, α, in the magnetogram. The middle row shows the same maps with artificial noise added to them. A "white noise" of 35 G was added to all three components of B as well as an additional field-relative noise of 30% in horizontal field components (B_x, B_y) and 5% in the vertical component (B_z). The difference in relative noise was chosen to resemble real data, since in observations, the vertical magnetic field component is generally measured with higher accuracy than the horizontal components. The bottom row shows the results after pre-processing was applied to the noisy maps.

3.7 A Critical Overview of the Coronal Field Extrapolation Procedure

Currently, there is no method of producing an NLFFF that is mathematically well-posed (*i.e.*, a unique solution that depends smoothly on the boundary conditions) for arbitrary large values of α. In addition, specific difficulties are encountered in applying extrapolation to solar observations. Here, the steps used to produce the NLFFF extrapolation in this thesis are summarised whilst highlighting the stages that contribute to the challenging nature of the exercise.

The first task in coronal field extrapolation is to obtain spectropolarimetric measurements. Various instruments provide such measurements, albeit it each to their own limits and specifications. The space-based telescopes SDO/HMI and the *Solar Optical Telescope* (SOT) onboard *Hinode* both make spectropolarimetric measurements, but where HMI makes measurements of the full disc of the Sun almost continuously, SOT targets smaller regions at better spatial and spectral resolutions than HMI. Furthermore, ground-based spectropolarimetric telescopes can benefit from even smaller spatial resolutions, due to lesser restrictions on the size of mirrors that can be used. However, measurements from ground-based telescopes are subject to atmospheric effects and limited observing time due to the Earth's rotation. Anyone that wants to produce a coronal magnetic field extrapolation must first choose the source for their spectropolarimetric measurements depending on the image size, temporal coverage, and measurement quality they need. Each of these factors will eventually affect the magnetic field extrapolation.

Secondly, the spectropolarimetric measurements must be inverted to get the magnetic field strength, B and the inclination and azimuth angles, θ and ϕ, that describe the magnetic field vector. To do this, spectral measurements are compared to a synthetic model of the solar atmosphere, and therefore the inverted solution is affected by both the quality of the measurements (*e.g.*, by the spectral resolution of the instrument used and by errors from overlooked modifications to the polarisation-state of the observed light between the source and the detector) and the choice of model atmosphere. Hence, the inversion procedure is not unique, and in this sense,

is not mathematically well-posed.

The azimuth angles determined by the inversion process are subject to a 180° ambiguity ($0 < \phi \leq 180$). This ambiguity must be resolved to give a representative vector field. One implementation, the so-called minimum energy method (Section 3.6.3.1), uses a simulated annealing routine to disambiguate the azimuth based on the solution that minimises a global energy functional. By the nature of the simulated annealing process, the final state of the disambiguated field vector, *i.e.*, the energy minimum that the algorithm arrives at, may be a local minimum rather than the global minimum.

The field strength, inclination, and unambiguous azimuth can then be projected in to Heliographic magnetic field components, B_x, B_y, and B_z, and re-binned on to a Cartesian grid (see Section 3.6.3.2). These are well-posed geometrical transformations, however, different de-projection methods modify the magnetic field in different ways.

To produce a force-free coronal field, the boundary magnetogram must also be force-free (or at least, as close to it as possible). Pre-processing is used to improve compatibility of magnetograms with the force-free condition, but the degree to which magnetograms should be manipulated is not well-defined. Thus, different choices of pre-processing parameters will result in different processed boundary magnetograms, and therefore different extrapolated fields. Moreover, the simulated annealing method used in this thesis may reduce forces to a local-minimum state instead of the global minimum in the same way as the minimum energy field-azimuth disambiguation method.

The initial state of the coronal field is a potential field extrapolated from the boundary magnetogram (Section 3.6.2). Potential field extrapolation is mathematically well-posed, so that any input magnetogram (together with the chosen lateral and top boundary conditions) has a unique potential field solution. However, the subsequent NLFFF relaxation (Section 3.5) is not well-posed, and therefore may not yield a unique solution.

In summary, the numerous stages between making initial spectropolarimet-

ric measurements and obtaining an NLFFF field are not all mathematically well-defined and can introduce both systematic and random errors. In order to begin to draw conclusions from such an extrapolated field model, one must first validate the accuracy of the model. One way to achieve this is to compare the extrapolated magnetic field to solar observations. There are numerous examples of NLFFF extrapolations that have successfully reconstructed observed coronal field features (e.g. Valori et al., 2012; Polito et al., 2017; Green et al., 2017), demonstrating that the method can produce valuable results.

In Chapter 5 of this thesis, an NLFFF extrapolation of the coronal magnetic field one hour before a CME is presented that matches a range of observations very well. The model is then used to investigate the processes that triggered the formation of the pre-eruptive magnetic structure and drove its eruption.

Chapter 4

On-Disc Observations of Flux Rope Formation Prior to Its Eruption

This chapter contains results that have been published in Solar Physics (James et al., 2017 *Sol. Phys.* 292, 71). Under the supervision of Lucie Green, Gherardo Valori and Lidia van Driel-Gesztelyi, this work was carried out in collaboration with Erika Palmerio and Emilia Kilpua (University of Helsinki), who focused on the data analysis and interpretation of *in situ* aspects. David Brooks (George Mason University) made computations of the first-ionisation potential (FIP) using spectroscopic measurements provided by Deborah Baker (University College London MSSL), and both contributed insightful expertise. Hamish Reid (University of Glasgow) provided and helped with the interpretation of solar radio data. Special thanks are given to Yang Liu (Stanford University) for processing and providing additional HMI SHARP data that were important for this work.

While the work of this chapter was in progress, it was presented as a contributed talk at the 2016 Solar Physics Division meeting in Boulder, Colorado, and twice as a seminar; firstly at NorthWest Research Associates (Boulder), and then at Stanford University. It has since been presented as a poster at the 7$^{\text{th}}$ *Solar Orbiter* Workshop in Granada, and as part of a talk at the 2017 Flux Emergence Workshop in Budapest.

4.1 Introduction

Many aspects of CME formation and eruption remain unclear, including the processes by which magnetic flux ropes form, whether flux ropes are present before the onset of eruption, and what the key mechanisms that cause CMEs are.

Measurements of the 3-D photospheric magnetic field can be produced by exploiting the Zeeman effect (described in Section 2.1.2.1), but there are difficulties in measuring the full coronal magnetic field vector. This is because temperatures in the corona can be more than 1000 times higher than in the photosphere (Gary, 2001; see Figure 1.4 of this thesis), so thermal and non-thermal broadening have a much larger effect than Zeeman splitting in the corona. Furthermore, because the corona is optically thin, it is difficult to determine the altitude from which observed photons originate, and various magnetic field directions and strengths may occur along the line of sight. Therefore, direct, 3-D magnetic field measurements of flux ropes in the corona have not been made.

However, the presence of flux ropes can be inferred without directly measuring the coronal magnetic field. Photospheric vector magnetic field observations can exhibit inverse crossings and bald patches, which are signatures of BPSS flux ropes (see Section 1.3.1.4). EUV signatures of flux ropes include sigmoids (Section 1.3.1.5), filaments (Section 1.3.1.6), and plasmoids. Plasmoids are hot, globular plasma structures that may be interpreted as cross-sections of coronal flux ropes (for examples, see Shibata et al., 1995; Reeves and Golub, 2011). Plasmoids (and therefore coronal flux ropes) have been most commonly observed at the solar limb, where they are away from the much brighter solar disc and any flaring that may occur beneath them (*e.g.* Nindos et al., 2015). The altitude of such coronal flux ropes and the existence of underlying flare arcades implies an HFT configuration.

The formation of BPSS flux ropes can be explained by the flux cancellation scheme of van Ballegooijen and Martens (1989, see Section 1.3.3.1), in which magnetic reconnection occurs in the photosphere/chromosphere. Quantitative observational studies have found that flux ropes form via flux cancellation on timescales of hours to days (*e.g.*, Yardley et al., 2018).

The processes and timescales involved in HFT flux rope formation are less clear. Previous studies have used observations of plasmoids above the limb to infer that pre-eruption flux ropes can form via magnetic reconnection in the corona (*e.g.*, Reeves and Golub, 2011; Patsourakos et al., 2013). In some studies coronal flux ropes erupted ≈10 minutes after they first appeared (Cheng et al., 2011; Zhang et al., 2012), whereas Patsourakos et al. (2013) observed a coronal flux rope that appeared and grew larger over 17 minutes, but did not erupt until ≈7 hours later. Magnetic reconnection in the corona requires the convergence of magnetic field lines in the corona, and this may be driven by motions in the photosphere. However, since coronal flux rope signatures have so-far been primarily observed at the limb, the evolution of the photospheric magnetic field beneath the forming coronal flux ropes has not been studied.

One potential way to distinguish between flux ropes that formed at different heights is to examine their plasma composition. Plasma composition can be determined by studying the intensity of emission lines from elements that each have a different first-ionisation potential (FIP; Brooks and Warren, 2011). Low-FIP elements are more abundant in the corona than in the photosphere. Baker et al. (2013) observed photospheric plasma in the core of a sigmoidal active region, and suggested this could correspond to part of a flux rope that formed via reconnection low-down in the solar atmosphere by flux cancellation along the polarity inversion line (*i.e.*, a BPSS flux rope). Following this hypothesis, an HFT flux rope that forms as a result of coronal reconnection should contain coronal plasma, but no previous study has investigated this.

In this chapter, the solar origin of a magnetic cloud studied by Palmerio et al. (2017) is investigated to determine the pre-eruptive configuration of the corona. EUV observations from SDO/AIA are used to study the evolution of NOAA AR 11504 before, during, and after it produced a CME on 14 June 2012. These are supplemented with photospheric line-of-sight and vector magnetic field measurements from SDO/HMI, as well as spectroscopic measurements from *Hinode*/EIS and radio observations from the NRH. The various data products used are outlined in Section

4.2. Section 4.3 begins by describing the *in situ* magnetic cloud detection and how the active region of origin is identified. The magnetic field, EUV, spectroscopic and radio observations of the active region are also presented in Section 4.3, and their implications are discussed in Section 4.4. Finally, the key conclusions are given in Section 4.5.

4.2 Data Analysis

SOHO/LASCO coronagraph data are used to identify the CME that formed the magnetic cloud and determine the plane-of-sky CME speed. The two STEREO satellites were used to give opposing perspectives of the CME to confirm it was Earth directed.

Low-coronal EUV observations from SDO/AIA are used to study the source active region of the CME. The aia_prep routine in SolarSoft is used to prepare the AIA data to level 1.5, correcting for the slight difference in viewing angle, focal length, and alignment between each of the four AIA telescopes.

White-light continuum images as well as line-of-sight and vector magnetograms from SDO/HMI were used to characterise the evolution of the photosphere. The line-of-sight data are processed using the aia_prep routine, changing the image scale to $0.6''$ per pixel to match AIA for easier comparison between the two data sets. The vector magnetograms are from the '*hmi.sharp_cea_720s* series' (see Section 2.1.2.3). HMI SHARP data were not available during 13 June 2012 (the day before the eruption), so instead, cutouts were taken from the full-disk vector magnetic field series and transformed into the CEA projection (see Section 3.6.3.2) to produce SHARP-style magnetograms. Electric currents were computed from the x- and y-components of the magnetic field vector using Equation 3.15.

The GOES/XRS system is used to provide a full-Sun integrated X-ray flux light curve over the hours before, during, and after the eruption to identify flares in the source active region.

Spectroscopic data are obtained from *Hinode*/EIS. The data used are $1''$ slit coarse ($2''$) raster scans of a $120''\times512''$ field of view, taking 60-second exposures

at each position. They are processed and calibrated using standard routines available in SolarSoft that remove the dark current pedestal, account for hot, warm, and dusty pixels, and correct the orbital drift of the spectrum on the CCD. The data are then calibrated to physical units. The EIS calibration shows an on-orbit evolution with time (Del Zanna, 2013; Warren et al., 2014), so the data are re-calibrated using the method of Del Zanna (2013). The EIS scans used here are manually aligned with AIA images to enable the comparison of observed features between data sets.

Finally, radio images are used from the NRH at nine frequencies between 150 MHz and 445 MHz using a 10-second integration time.

4.3 Observations

4.3.1 The Magnetic Cloud

An *in situ* observation of a magnetic cloud was made by the *Wind* satellite on 16 June 2012. The shock preceding the magnetic cloud was first detected at ≈19:30 UT on 16 June, and the passage of the magnetic cloud lasted from ≈22:00 UT on 16 June until ≈12:30 UT on 17 June. The measured magnetic field vector rotated from north to south in the geocentric solar ecliptic coordinate system as the cloud passed the spacecraft, and an eastern field component was measured throughout the cloud (see Figure 6 of Palmerio et al., 2017). This is consistent with a right-handed flux rope that has eastward axial field with helical field wrapped around it. The helical field at the leading edge of the flux rope is northward and at the trailing edge it is southward, so the measured rotation from north to south is produced as it passes over the spacecraft. The *in situ* flux rope detection is discussed in more detail by Palmerio et al. (2017) in addition to another event, whereas this chapter focuses on the pre-eruptive coronal field that generated the magnetic cloud.

The magnetic cloud has previously been associated with a halo CME that was observed by LASCO on 14 June 2012 at 14:12 UT (Richardson-Cane "Near-Earth Interplanetary Coronal Mass Ejections" list;[1] Kubicka et al., 2016; Palmerio et al., 2017. For the method used in creating the ICME list, see Cane and Richardson,

[1] See `http://www.srl.caltech.edu/ACE/ASC/DATA/level3/icmetable2.htm`

2003 and Richardson and Cane, 2010). Here the validity of this association is checked. Halo eruptions manifest when CMEs travel along the line-of-sight of an observer, either towards the Earth or away from it. Images from the STEREO A and B satellites confirm that the halo CME originated on the Earth-facing side of the Sun, and the magnetic cloud speed was measured to be ≈500 km s^{-1} by *Wind* at 1 AU. Assuming the ICME had a constant speed between the Sun and L1 suggests that the source eruption took place at ≈08:30 UT on 13 June 2012. However, since the speed of the solar wind preceding the ICME was lower than the ICME speed (solar wind speed ≈400 km s^{-1} measured by *Wind*), it is likely the ICME had been decelerating before reaching L1. This means that 08:30 UT on 13 June is an earliest estimate of the eruption time, and the eruption likely took place somewhat later than this.

There are six eruptions listed in the SOHO/LASCO ICME catalog that occurred between 08:30 UT on 13 June and the halo eruption on 14 June (see `https://cdaw.gsfc.nasa.gov/CME_list/`). One of the six other eruptions was a partial-halo CME, but that eruption is associated with a small, low-speed CME that was detected by *Wind* 12 – 14 hours prior to the magnetic cloud referenced in this work. This association is made because the 13 June partial-halo eruption was determined to have a slower speed than the full-halo eruption of the 14 June by SOHO/LASCO. Therefore, the 16 June magnetic cloud is associated with the 14 June halo CME.

Once the LASCO CME associated with the magnetic cloud has been identified, the next step is to locate the CME source region. Given the time the halo CME was first seen in LASCO C2 and the size of the occulting disc, a CME with plane-of-sky speed of ≈ 980 km s^{-1} should have left the low corona at ≈ 13:45 UT. The full-disc EUV data from AIA show that only one eruption occurred on the Sun from 13:00 UT – 14:00 UT: a CME that originated from NOAA AR 11504 at ≈ 13:30 UT (see Section 4.3.3 for details of the eruption). Therefore, the origin of the considered magnetic cloud is associated with NOAA AR 11504.

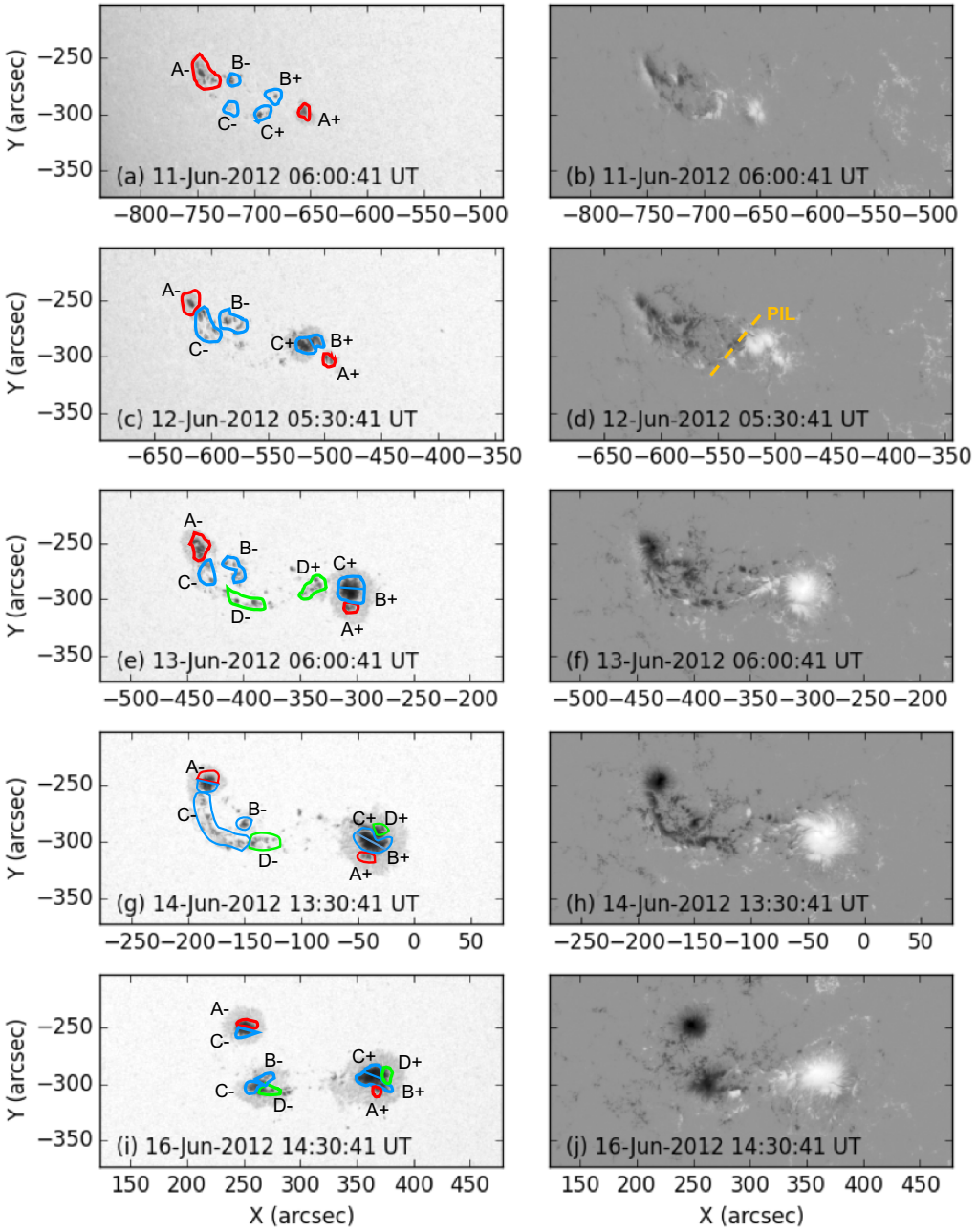

Figure 4.1: Annotated continuum intensity images (left) and line-of-sight magnetograms (right) from HMI showing the evolution of NOAA AR 11504. The magnetograms are saturated to ±2000 G, with positive flux shown in white and negative in black. In the continuum images, distinct fragments of magnetic flux are highlighted and labelled ±A, ±B, ±C, and ±D. The evolution of these fragments is described in Section 4.3.2.

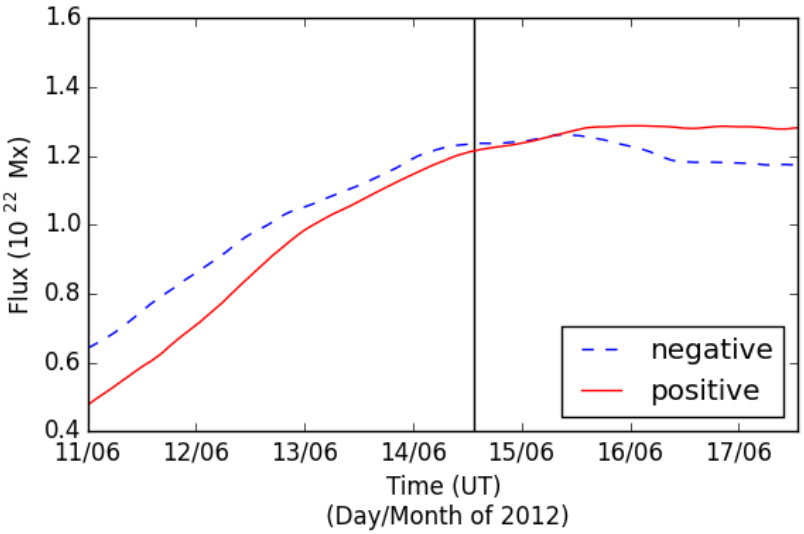

Figure 4.2: Integrated magnetic flux of NOAA AR 11504 during its disk passage. Vertical field-component HMI SHARP images are smoothed over 15×15 pixel boxes and then only pixels with a magnetic field strength greater than ± 400 G are included in order to exclude the majority of quiet-Sun field. This therefore fails to count some small-scale serpentine flux emergence, and so these values of magnetic flux should be regarded as lower limits. 24-hour moving-average smoothing has been applied to the curve to remove short-timescale variations. The vertical black line is drawn at 13:30 UT on 14 June to represent the time at which the eruption of the sigmoid is observed to begin.

4.3.2 Photospheric Evolution

NOAA AR 11504 rotates onto the solar disc as seen by SDO on 8 June 2012 and rotates off on 21 June 2012. The region initially contains two small sunspots, a leading positive polarity spot and a trailing negative polarity spot (labelled A+ and A- in Figure 4.1a). New magnetic flux emergence occurs between the two spots and they separate (labelled $\pm$B and $\pm$C in Figure 4.1c). Figure 4.2 shows that $\approx 7 \times 10^{21}$ Mx cm^{-2} (with an estimated error of $\approx$5% based on the 2.3 Mx cm^{-2} noise-per-pixel value of Liu et al., 2012) of magnetic flux emerges in the active region from 11 June until around noon on 15 June, at which time emergence ceases.

The positive flux that emerges during 11 – 13 June ($\pm$B and $\pm$C) moves towards the north of the positive sunspot (A+) and is distinguished as two sections of umbra in Figure 4.1e. The southernmost section (C+) moves northward and clockwise around the northern emerged umbra (B+), such that it (C+) eventually

comprises the northernmost part of the positive sunspot. However, rather than fully coalescing with the pre-existing positive sunspot umbra, the newly emerged flux remains somewhat separate from the pre-existing flux, existing as distinct umbrae within one penumbra (see Figure 4.1e). Further emergence of positive flux from 13 – 15 June (D+) forms another separated area of umbral field within the positive sunspot penumbra to the north of the previous sections (see Figure 4.1g). As it (D+) approaches the positive sunspot, it is observed to orbit the sunspot clockwise. This continues, displaying an $\approx 120^{\circ}$ movement about the sunspot in 24 hours before stopping (compare panels e and i of Figure 4.1). This orbit of newly emerged flux around separate areas of magnetic flux seen in the photosphere suggests that regions of magnetic field in the corona may be wrapping around each other — increasing stored energy and creating more favourable conditions for magnetic reconnection between the different magnetic flux regions. The implications of this are discussed in full in Section 4.4.

The negative flux that emerges during 11 – 15 June forms a magnetic tongue to the south of the pre-existing negative sunspot (B-, C-, and D- in Figure 4.1g). In this active region, the negative polarity tongue extends to the north of the positive emerging flux (see Figure 4.1d), indicating that the emerging flux tube has right-handed twist (explained in Section 1.3.1.2). The sheared negative polarity tongue develops into a third sunspot, becoming cohesive on 16 June (see Figure 4.1i/j). From 15 June until the active region leaves the disc, the positive sunspot moves eastward towards the third sunspot. This motion is observed in the line-of-sight data, but also in the CEA-projected vector data that remove some of the foreshortening near the limb (Section 3.6.3.2). This suggests that the convergence is not just a foreshortening effect near the limb. Additionally, when the converging motion begins on 15 June, the active region is still quite far from the western limb, with the leading sunspot only $\approx 250''$ west of central meridian.

The horizontal component of the magnetic field extends radially from the southern section of the positive sunspot (A+ in Figure 4.1), but the field extending out to its north (C+, D+) is sheared by $\approx 45^{\circ}$ relative to the radial direction

(see Figure 4.3a). Furthermore, the pre-existing negative sunspot (A-) exhibits horizontal field that is mostly radial outwards from the sunspot, but the elongated tongue to its south (C-, D-) features shear to a similar degree as seen to the north of the positive sunspot. The positive and negative magnetic flux locations that exhibit horizontal field components without shear (A$\pm$) both pre-exist the flux emergence that is observed here, and the positive and negative field areas that do show shear in their horizontal field components emerge at around the same time as their opposing-polarity counterparts (C$\pm$, D$\pm$). The negative polarity tongue is associated with a region of relatively strong vertical electric current density, seen in Figure 4.3b, and the same is seen to the north of the positive sunspot. The vertical current density is proportional to gradients in the horizontal field component (see Equation 3.15), and so the vertical current is strongest in areas where shear is strongest. Finally, no inverse crossings are found along the central part of the polarity-inversion line in the HMI vector data (see Section 1.3.1.4 for an introduction to inverse crossings).

4.3.3 Coronal Evolution

Figure 4.4 depicts a timeline of coronal events, such as flares and sigmoid development, observed in NOAA AR 11504 during the hours prior to the eruption on 14 June 2012. For the remainder of this section, all stated times refer to activity on 14 June 2012.

A C5.0 flare that produces a bright arcade in the centre of the active region begins at 11:05 UT and reaches its peak intensity at 11:12 UT (as measured by GOES). At 11:20 UT, loops appear to the west of the positive sunspot in the 131 Å images of AIA (see Figure 4.5b). Other AIA channels were studied, but the coronal features described in this section appear only in the 94 Å channel and, most prominently, in the 131 Å channel ($\approx$6 MK and $\approx$11 MK respectively; Lemen et al., 2012). These western loops briefly brighten before fading out of view by 11:40 UT, by which time the intensity of the flare arcade has also decreased. Data from the *X-ray Telescope* (XRT) onboard *Hinode* were also studied, but there was a gap in observations from 11:12 UT – 11:43 UT.

At 12:20 UT, loops that span from one sunspot to the other begin to brighten,

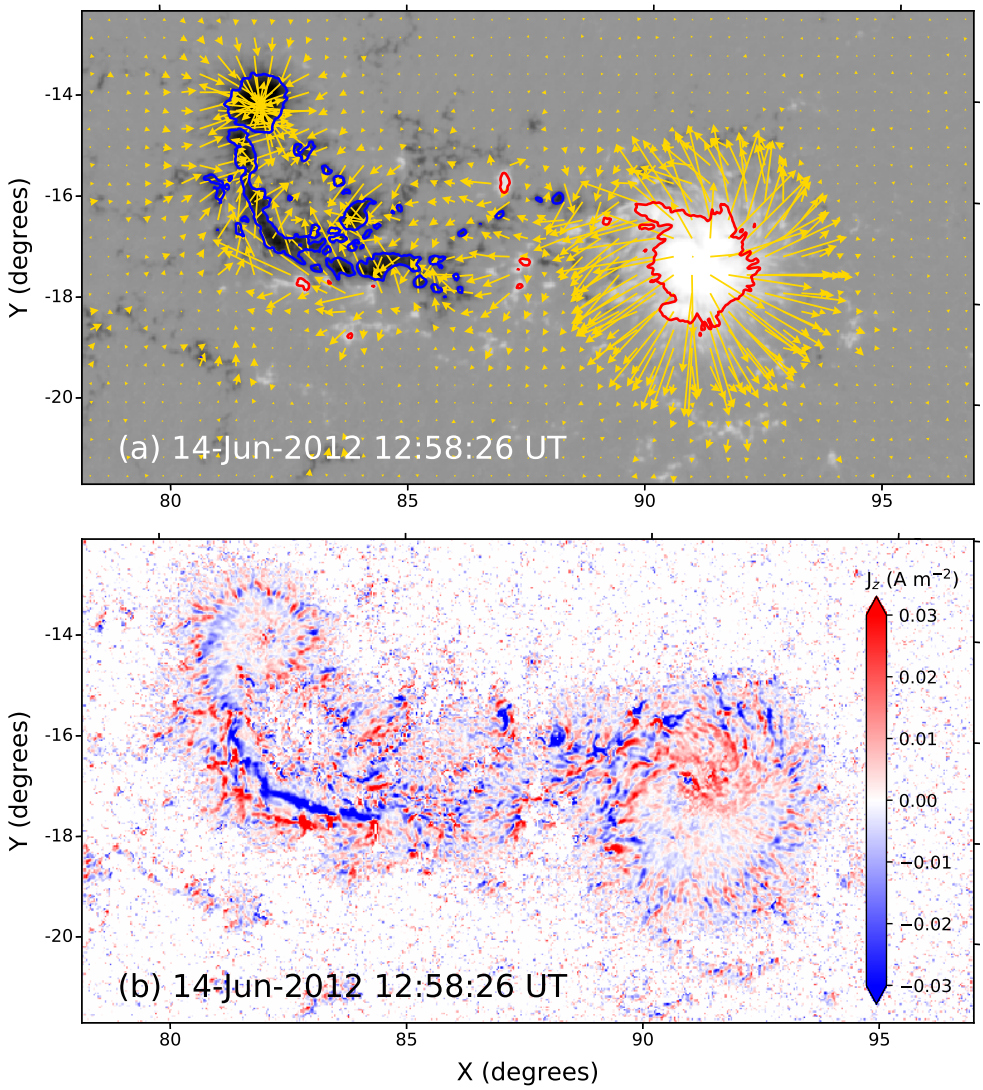

Figure 4.3: (a): The vertical component of the vector magnetic field, with positive polarity in white and negative polarity in black. Red and blue contours outline regions of $\pm$1000 G. Gold arrows represent the direction and magnitude of the horizontal field component for horizontal field strengths of 100 G or higher. The horizontal field component is sheared to the north of the positive sunspot and in the negative magnetic tongue. (b): A map of vertical current density (J_z) in units of A m^{-2} (red=positive, blue=negative) with the same field-of-view as panel (a), demonstrating locations of strong gradients in the horizontal magnetic field component. The calculation of current densities in these units relies on the assumption that each pixel represents an equal area in square metres. Here, the relation is used that the width of one 0.03° pixel represents 0.5″ (strictly only true at disc centre), which corresponds to 362.635 km at a distance of 1 AU. To remove noise, it is set that $J_z = 0$ in pixels where the horizontal field strength is weaker than 100 G.

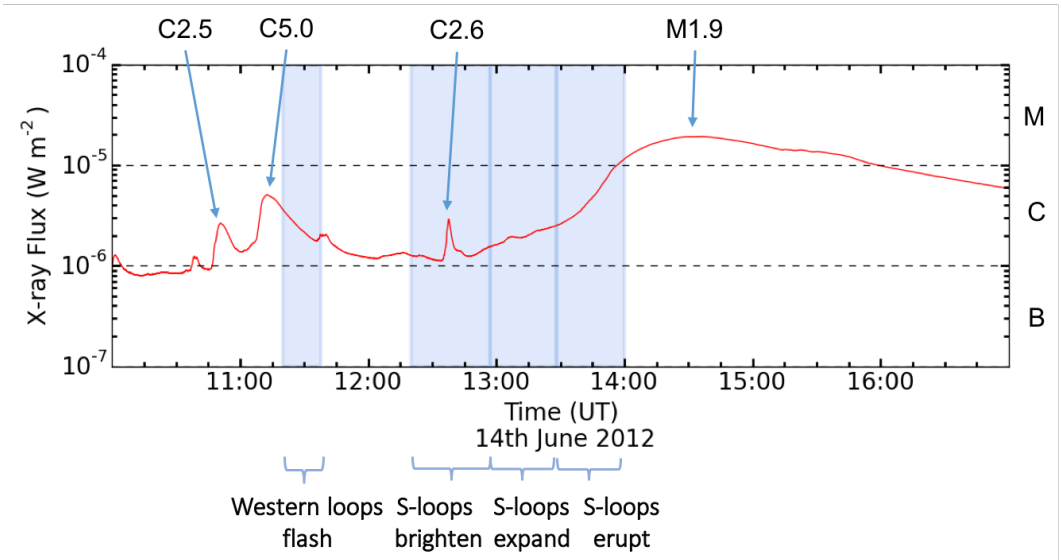

Figure 4.4: The full-disc integrated X-ray flux (1.0 – 8.0 Å) as measured by GOES-15. Flares observed in NOAA AR 11504 are labelled and the durations of observations from the 131 Å EUV data described in Section 4.3.3 are shown by the blue boxes. There is a two-stage rise in X-ray flux leading up to the CME, with a slow rise from ∼13:00 UT – 13:30 UT, and a fast rise from 13:30 UT – 14:00 UT.

seen best to the south of the centre of the active region. A C2.6 flare begins at 12:33 UT and peaks at 12:37 UT. Throughout this time, the loops increase in brightness and size while remaining in the same location, and continue like this until 13:00 UT. As they brighten, loops once again appear to the west of the positive sunspot in the same location as those that appear at 11:20 UT (from Figure 4.5b), and it becomes clear that they are part of a common structure with the southern brightening. In fact, together they form a continuous S-shape that traces along the polarity inversion line and has its ends rooted near each sunspot: a forward-S sigmoid (see Figure 4.5c). This continuous sigmoid cannot be identified in *Hinode*/XRT data because the field-of-view does not cover the whole active region.

At 12:52 UT, an M1.9 flare begins, although it does not reach peak intensity until 14:35 UT. The rise in X-ray intensity of this flare exhibits a two-stage increase (see Figure 4.4). From 12:52 UT until ≈13:30 UT, there is a relatively steady rise in intensity. During this time, the central flare arcade increases in brightness and the sigmoidal loops expand. However, from ≈13:30 UT until ≈14:00 UT, the X-

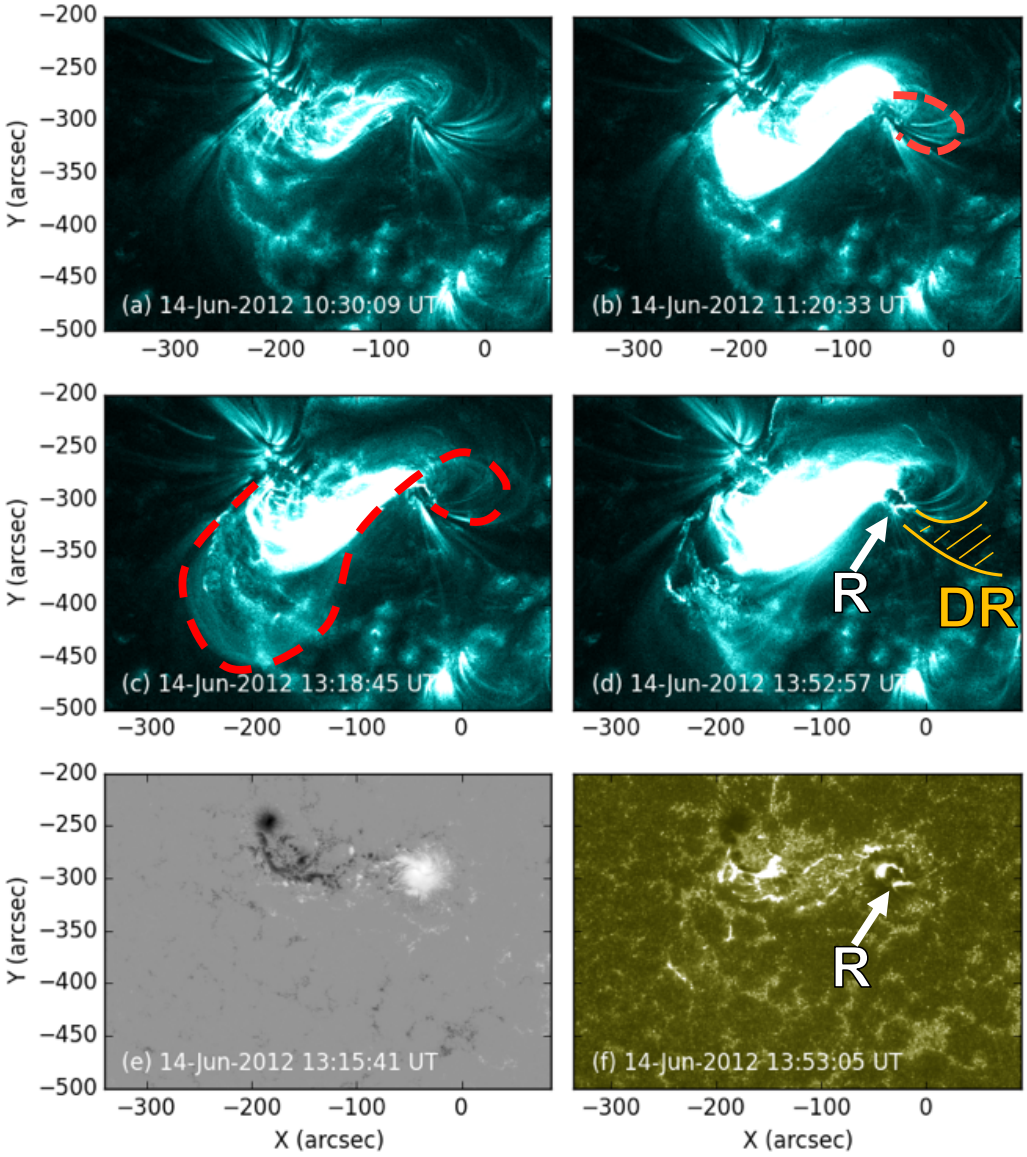

Figure 4.5: Four EUV images at 131 Å showing coronal evolution over the hours before, during and after the eruption, a line-of-sight magnetogram of the active region and an EUV image at 1600 Å showing flare ribbons. (a) NOAA AR 11504 ≈3 hours before eruption. (b) Loops become visible to the west of the western sunspot (dashed line). (c) The full S shape is visible (dashed line). (d) The eruption is occurring, producing a hooked flare ribbon to the south of the western sunspot (annotated R). A dimming region (see Figure 4.6a) that appears dark in EUV compared to surrounding plasma is outlined and hatched in gold, marked DR. (e) An HMI line-of-sight magnetogram of the active region. (f) The hooked flare ribbon (annotated R) is also visible at 1600 Å. The AIA 131 Å images are saturated to 200 DN s^{-1} $pixel^{-1}$, the magnetogram is saturated to ±2000 G and the AIA 1600 Å image is saturated to 800 DN s^{-1} $pixel^{-1}$.

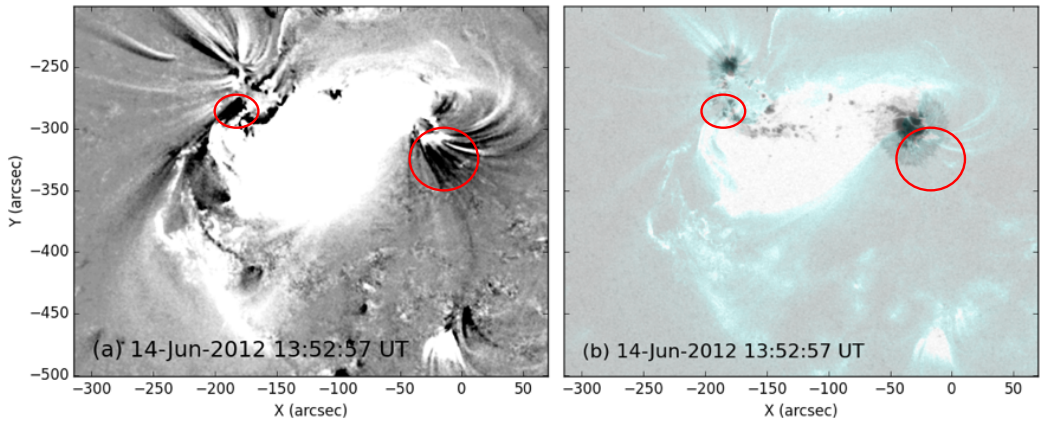

Figure 4.6: (a) Base difference image of NOAA AR 11504 showing the difference in intensity between AIA 131 Å images taken at 10:30 UT and 13:53 UT on 14 June 2012. Black areas correspond to decreases in intensity between the image times, and white represents brightenings (saturated to ± 50 DN s^{-1} pixel^{-1}). The red circles indicate the areas near the east and west sunspots that undergo dimming around the time of eruption. (b) An HMI continuum white-light image of the active region with a semi-transparent 131 Å AIA image overlaid. The AIA image is saturated to 500 DN s^{-1} pixel^{-1}, as in Figure 4.5. The dimming locations from panel (a) are included.

ray intensity increases more rapidly. This coincides with a growth in the size and brightness of the flare arcade, as well as the eruption of the sigmoid, and the erupting sigmoid material is seen to move southward from the active region in the plane of the image. It is concluded that the flare arcade forms beneath the sigmoid because the arcade is not disrupted by the upward motion and eruption of the sigmoid.

A flare ribbon is observed to brighten at the western footpoint of the flare arcade in every AIA channel from 13:45 UT. It is difficult to identify a flare ribbon on the eastern side due to the brightness of the arcade and the complex photospheric flux distribution, but the ribbon on the western side is particularly prominent, tracing around the group of positive sunspot umbrae. After extending out and around the sunspot, the flare ribbon turns back on itself to produce a hook-shape at 13:53 UT (see Figure 4.5d).

At the same time as the flare ribbon on the western side traces out the hook, twin dimmings are observed in the EUV data, with one occurring on either side of the active region (marked with red circles in Figure 4.6). These are most apparent when taking base difference images of the region, because these show increases and

decreases in intensity relative to the chosen time of origin (10:30 UT on 14 June). The western dimming is located within the hook of the western ribbon (where the dark region labelled DR in Figure 4.5d extends from), and the eastern dimming appears over a small patch of negative magnetic field to the south of the eastern sunspot. The locations of the dimmings and their significance to the pre-eruptive coronal configuration are discussed in Section 4.4.

4.3.4 Plasma Composition

Composition analysis is performed using data from an EIS raster that began at 11:42 UT on 14 June 2012 to investigate whether features observed in the EUV data have photospheric or coronal plasma composition. The method of Brooks and Warren (2011) is followed, which uses Fe lines to measure the electron density and compute a differential emission measure (DEM) distribution. The density and temperature are then used to model the Si X 258.375 Å / S X 264.223 Å line ratio, which is sensitive to the difference in compositional fractionation of silicon and sulfur due to the FIP effect. The method has been tested extensively in many studies (see Brooks and Warren, 2011, 2012; Baker et al., 2013, 2015; Culhane et al., 2014; Brooks et al., 2015; Edwards et al., 2016, for specific examples). The CHIANTI database v.8 was used to compute the contribution functions needed for this analysis (Dere et al., 1997; Del Zanna et al., 2015).

The study is performed on loops that extend to the north-west of the positive sunspot, and also on an area to the south-west of the positive sunspot (see the red and blue boxes in Figure 4.7). It is inferred that these locations correspond to the periphery and leg of the flux rope, respectively, so that plasma composition in the flux rope can be probed. The red box is located at the western part of the sigmoid, where faint loops had appeared from 11:20 UT (as described previously, — see Figure 4.5b). However, at the time of the EIS raster scan, these loops have faded from the AIA 131 Å observations, and the EIS data show that the box covers a set of loops that exhibit a red-shift (Figure 4.7). There will be a contribution along the line-of-sight from photons of arcade plasma beneath the flux rope as well as plasma in the flux rope itself. It is concluded that the blue box samples plasma within the

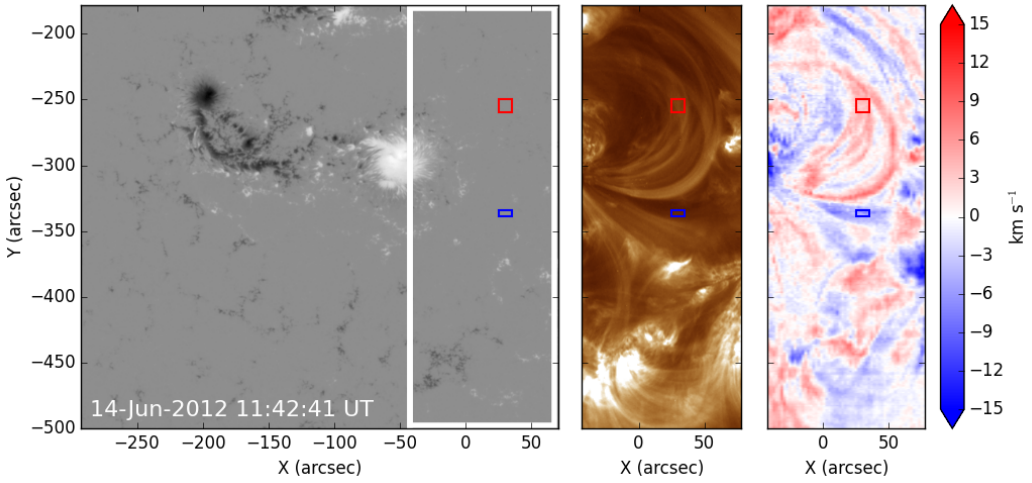

Figure 4.7: HMI line-of-sight magnetogram (left), 193 Å AIA image (middle) and an EIS Doppler-velocity image produced at 195.12 Å (Fe XII, right). The AIA and EIS images show an area to the west of the positive sunspot, and this field-of-view is marked on the HMI image. Downflows (red) are observed by EIS in loops that extend to the north-west of the positive sunspot and upflows (blue) are observed to the south-west of the sunspot. The composition analysis is performed on these flow areas in locations shown by red and blue boxes. Since these EIS images are produced via a raster that began at 11:42 UT, the red and blue boxes sample plasma that is observed at ≈12:00 UT. Doppler velocities are saturated to ± 15 km s^{-1}.

western leg of the flux rope because it is within the western EUV dimming region that is later seen (marked DR in Figure 4.5d and shown in Figure 4.6a) that traces back to the hooked flare ribbon (Figure 4.5f). Photons from this plasma are blue-shifted, revealing that in this location there is a plasma flow toward the observer along the line-of-sight (Figure 4.7).

The analysis returned a FIP bias of 3.1 at the northern loops and 1.9 for the southern region. FIP biases of the order 1.0 are representative of photospheric plasma, whereas FIP biases of the order of 2 – 3 correspond to coronal plasma composition (for a review of the FIP effect including the interpretation of FIP biases, see Laming, 2015). Therefore, these values both suggest plasma that is coronal in composition rather than photospheric. Uncertainties in the FIP bias factors are difficult to quantify, since errors in the radiometric calibration and atomic data are likely to be systematic in nature. Here the standard deviation from a distribution of values calculated from 1000 Monte Carlo simulations is used, where the intensities

are randomly perturbed within the calibration error. This produces an uncertainty of $\approx$0.3, which is much smaller than the difference between photospheric abundances (FIP bias $\approx$1) and the range of coronal abundances ($\approx$2 – 3).

4.3.5 Coronal Radio Observations

Solar radio emission originates from the acceleration of particles, which can occur during magnetic reconnection. The coherent mechanism that can cause radio emission from the accelerated particles results in lower frequencies of radio emission from source regions of lower-density plasma, and higher frequencies from higher-density plasma (see *e.g.*, McLean and Labrum, 1985; Pick and Vilmer, 2008; Reid and Ratcliffe, 2014, as reviews). Therefore, observing the Sun at a number of different frequencies enables the probing of radio emission from different plasma densities. Plasma density generally varies with altitude in the solar atmosphere (with lower plasma density at larger heights), so radio emission at lower frequencies generally originates from higher altitudes, whilst high-frequency emission generally originates lower down. However, this is not strictly true because plasma density also varies between different structures, *e.g.*, coronal loops and coronal holes.

Radio observations taken at nine frequencies between 150 MHz and 445 MHz from 10:00 UT on 14 June 2012 show strong emission across all frequencies to the east of the active region until 13:30 UT (Figure 4.8a – f). The emission at different frequencies appears to form a column, suggesting radio emission from different coronal heights. The sources of emission appear progressively farther to the south as frequency decreases, likely because the emission at lower frequencies originates from higher altitudes, and is therefore subject to stronger projection effects. This is a type I noise storm, which corresponds to acceleration of electrons in the corona over a continuous period. During this same time period, the *Wind* spacecraft observed many successive individual type III radio bursts at lower frequencies (from 14 MHz down to 0.1 MHz), indicative of a type III noise storm. Frequencies of 0.1 MHz imply that the accelerated electrons generate coherent radio emission from rarefied plasma as far out as 0.3 AU (*e.g.*, Leblanc et al., 1998; Mann et al., 1999). The type III bursts therefore indicate that the accelerated electrons have access to

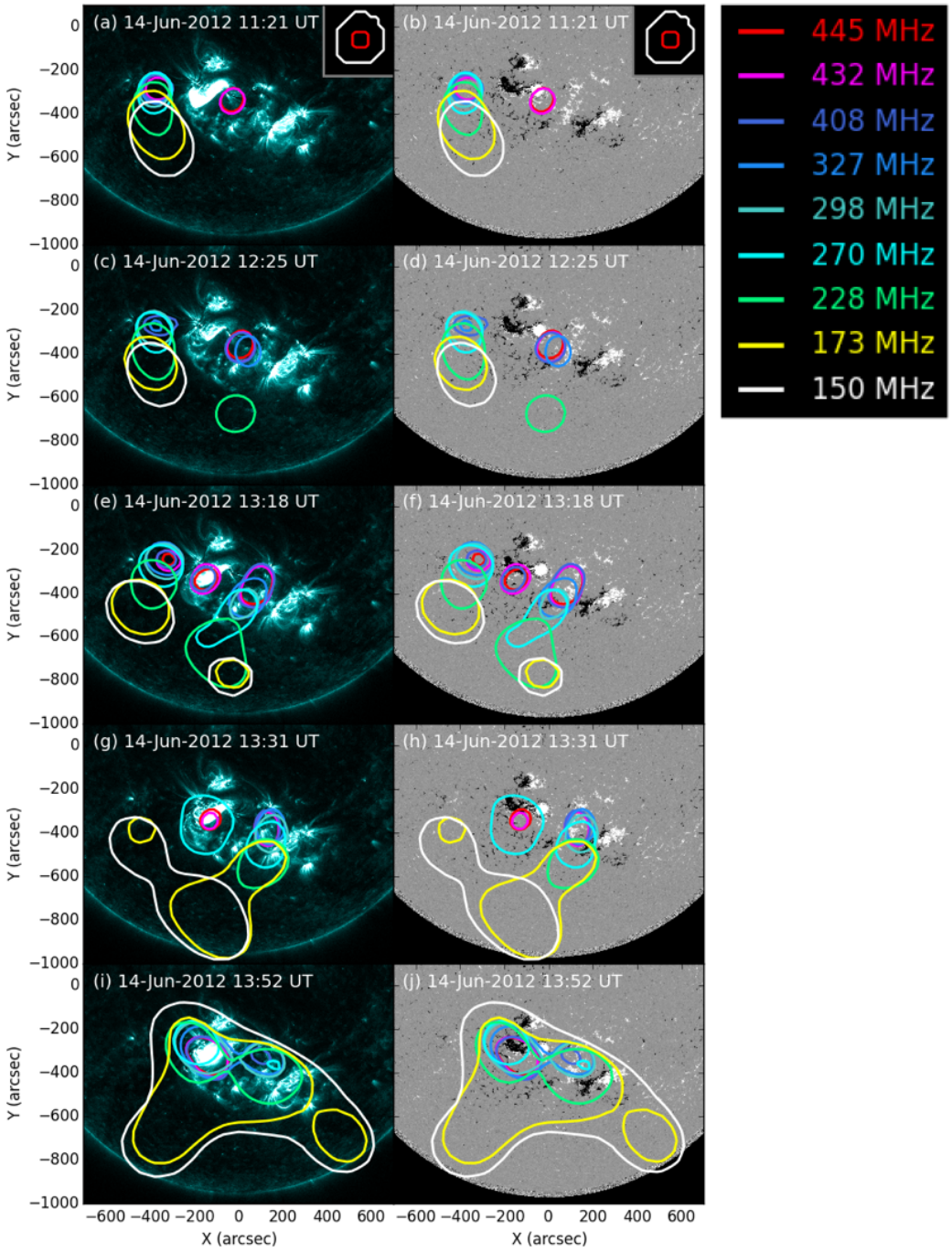

Figure 4.8: Contours representing locations of radio emission at different frequencies around NOAA AR 11504. Contours are drawn at 50% of the maximum radio intensity at each frequency and time. The beam sizes of NRH at 150 MHz (largest) and 445 MHz (smallest) at 11:21 UT on 14 June 2012 are indicated in the top right corners of panels a and b, to show that all sources are resolved. The contours are overlaid on 131 Å images taken by AIA (left) and line-of-sight magnetograms taken by HMI (right) at the closest available times to the radio data.

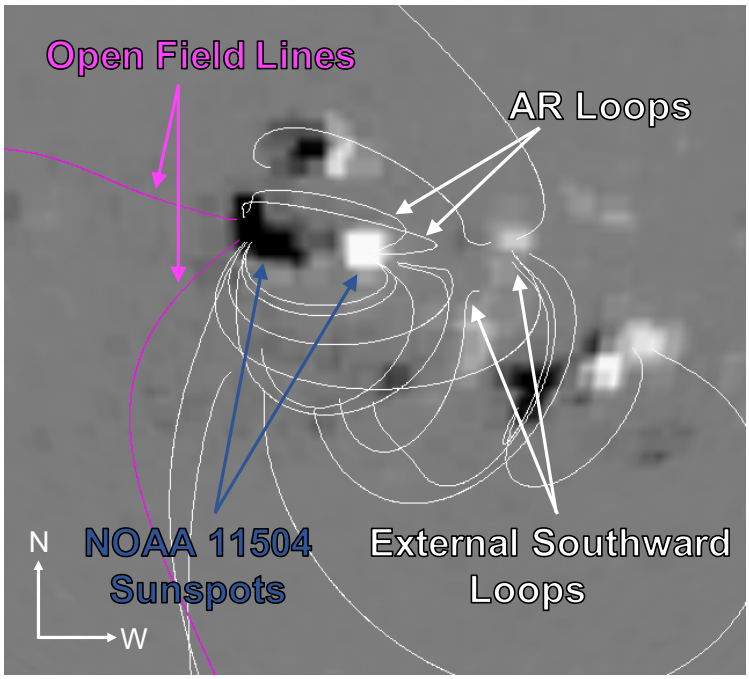

Figure 4.9: A PFSS extrapolation of the solar magnetic field at 12:04 UT on 14 June 2012 produced using the '*pfss*' package of SolarSoft. Field lines are plotted on an image of the photospheric magnetic field and extend from positive polarities (white) towards negative (black). The sunspots that comprise NOAA AR 11504 are indicated with blue arrows. Closed field lines are shown in white and field lines that are open to the heliosphere are magenta. The extrapolated field lines originate from a height of 1.15 $R_\odot$ with a uniform grid spacing and the viewing perspective is from that of Earth. The extrapolation suggests the presence of open field lines to the east of NOAA AR 11504, active region loops that initially curve north-westward from the positive sunspot ("AR loops") and loops that originate from an area of positive magnetic polarity to the west of the active region and connect to negative field to the south of the sunspots ("External Southward Loops").

magnetic fields that extend out of the corona, and can subsequently travel through interplanetary space.

To further investigate the coronal magnetic field, a potential field source surface (PFSS) extrapolation is performed using line-of-sight photospheric magnetic field data at 12:04 UT on 14 June 2012 (see Figure 4.9). Although PFSS extrapolations have limitations, since they necessarily produce a potential field (see Section 3.4.1), they are useful in probing the global magnetic field configuration. This extrapolation suggests the presence of a region of magnetic field that is open to the heliosphere prior to the eruption. This open field is situated to the east of the active

region and corresponds to the location of the radio noise storm seen in the NRH images. Open field allows particles accelerated at different altitudes (plasma densities) to escape into the heliosphere, which is commensurate with the observation of radio emission at all of the NRH frequencies.

A faint radio source is also present at the west of the active region in the higher NRH frequencies (*e.g.*, 445 MHz, see Figure 4.8a/b). From 11:20 UT (around the same time as the C5.0 soft X-ray flare and the initial brightening of loops that later comprise the western portion of the sigmoid), the western radio source brightens, indicating increased particle acceleration. Higher radio frequency type I emission corresponds to higher density plasma, and so the increased particle acceleration is likely occurring low-down in the solar atmosphere. The eastern noise storm remains present and type III bursts continue to appear in the interplanetary data, but at 12:25 UT, the lower-frequency sources begin to move farther eastward, giving the appearance that the column is being deflected away from the active region. Also around 12:25 UT, relatively low-frequency radio emission is briefly observed centrally to the south of the active region before reappearing and remaining from 13:08 UT. With projection effects, this could represent high-altitude emission above the centre of the active region, and the lack of spread in frequency implies that emission originating only from a certain height in the solar atmosphere is being observed.

Beginning at around 13:18 UT, a new radio source appears centred on the active region at frequencies above 327 MHz (Figure 4.8e/f). This emission is interpreted to originate from the core of the active region because it is localised to the higher frequencies. From this time, the eastern noise storm begins to disappear, completely vanishing around 13:30 UT. Meanwhile, the western signatures extend into lower frequencies, developing to show a column of emission from different frequencies (Figure 4.8g/h). The lower-frequency sources extend southward until they reach the same location as the central high-altitude emission. The sources of this emission move outwards to the west of the active region (see Figure 4.8c-h).

After 13:30 UT, the central high-altitude radio emission begins to move farther southward, consistent with a moving type IV radio burst (accelerated electrons

within plasma that is erupting into interplanetary space, *e.g.*, Bain et al., 2014 — see Figure 4.8g/h). The moving type IV source is observed to move from (-125″,-875″) to (-225″,-1050″) in 8 minutes, and so, assuming radial expansion from the active region latitude of 17°, the speed of the source is $\approx$ 1040 km s^{-1}. This speed is of the same order as the 980 km s^{-1} plane-of-sky CME speed estimated by LASCO.

After the eruption, at around 13:52 UT, low-frequency (high altitude) radio signatures are observed over the active region core and western external polarities, as well as to the south-east and south-west of the active region (Figure 4.8i/j). The southern sources at 150 MHz move away from the active region to the south-east and south-west before fading after 15 minutes. Finally, from 14:00 UT onwards, emission continues in all frequencies to the east and west of the active region, and then only from the eastern location after 14:13 UT.

4.4 Discussion

Here, the wide range of observations presented in this chapter are brought together. The aim is to build a coherent interpretation of how the magnetic field in NOAA AR 11504 evolved in the hours leading up to the eruption on 14 June 2012. The studied data cover plasma emitting across a range of temperatures and altitudes from the photosphere to the corona, as well as emission from particle acceleration.

The AIA observations strongly support an interpretation that part of the magnetic field in NOAA AR 11504 transforms from a sheared arcade to a flux rope before the CME occurs. This is illustrated by a cartoon shown in Figure 4.10, where two sets of sheared loops are indicated on a 171 Å image at 07:37 UT on 14 June 2012. Then, by 13:18 UT, a full S-shaped (sigmoidal) emission structure is observed, most prominently in the AIA 131 Å channel along with a flare arcade. The earliest signature of the forming sigmoid is seen at 11:20 UT (see Figure 4.5b), although this then fades and becomes visible again at around 12:20 UT. The sheared loops are connected to the areas of magnetic flux that emerge between 11 – 13 June, labelled B$\pm$ and C$\pm$ in Figure 4.1, and the footpoints of the subsequently formed sigmoid and flare arcade are in approximately the same locations. A pro-

cess similar to the tether-cutting magnetic reconnection described by Moore et al. (2001) could explain this transition from sheared loops to a sigmoid and flare arcade with conserved footpoints. However, in contrast to the Moore et al. (2001) scenario, the reconnection did not apparently lead to the immediate ejection of the flux rope. Simulations by Aulanier et al. (2010) support the scenario of a flux rope that forms by tether-cutting reconnection and only later becomes unstable (to the torus instability).

The large extent of the sigmoid, particularly its extension to the south of the active region, allows the central section of the sigmoid to be identified, which is otherwise difficult due to the bright emission from the underlying flare arcade along the same sight-line. The magnetic tongues in the emerging photospheric magnetic field in the active region indicate that the sigmoid forms in a flux region that is of right-handed chirality, consistent with the weak trend for active region magnetic fields in the southern hemisphere. In addition, the sense of the S-shape (forward-S) also indicates right-handed chirality (Pevtsov et al., 1997). A stable forward-S sigmoid in a positive-chirality field is consistent with the presence of helical field lines that have a dip in their central section (Török et al., 2010a), which is interpreted here as a flux rope with at least one turn in the field lines (according to our definition in Section 4.1). Previous work has shown that sigmoidal emission can be produced by plasma trapped on S-shaped field lines that pass through a quasi-separatrix layer underneath a flux rope (Titov and Démoulin, 1999). Furthermore, the hooked shape of the western flare ribbon is considered a signature of energy deposition along field lines at the periphery of a flux rope (Démoulin et al., 1996; Janvier et al., 2014, see Figure 1.12). Our interpretation of the presence of a flux rope in the active region by the time of the CME is matched by the *in situ* data, which find the ICME to contain a flux rope with a chirality and axial orientation matching that observed at the Sun (Palmerio et al., 2017).

The location of the footpoints of the erupting flux rope are determined using EUV dimmings and the curved end of a hooked flare ribbon. The eastern EUV dimming is located over a patch of negative magnetic polarity to the south of the

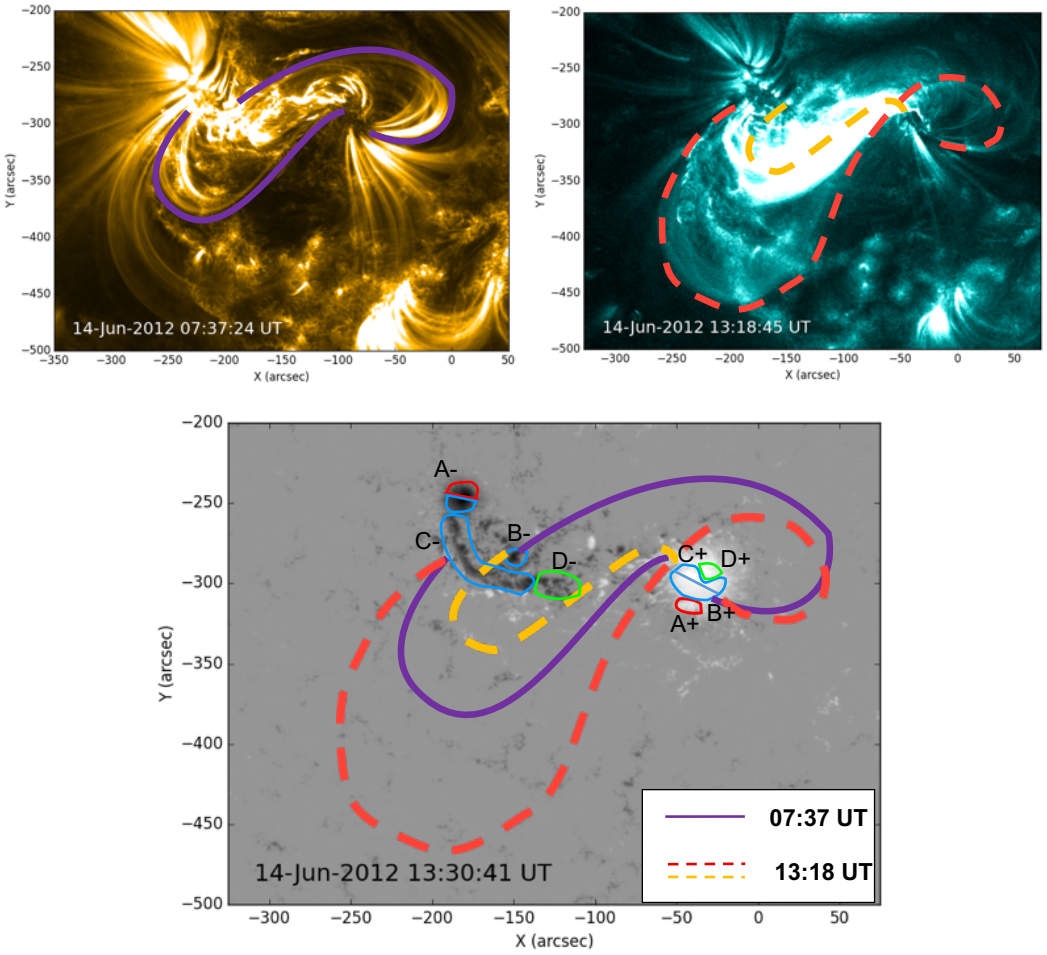

Figure 4.10: Schematic to illustrate the formation of the sigmoid and arcade. Initially, sheared loops (seen here in 171 Å and indicated with purple lines) connect B+ to B- and C+ to C-, using the nomenclature of Figure 4.1. Later, a flare arcade and a sigmoid (shown in dashed gold and red respectively) are observed. The sigmoid connects B+ to C-, and the arcade footpoints are at C+ and B-. The sigmoid footpoints are consistent with the footpoint locations inferred from the EUV dimmings shown in Figure 4.6. The transition from sheared loops to an arcade and sigmoid is consistent with tether-cutting-like reconnection, although it differs from that described by Moore et al. (2001) in that the flux rope that forms (evidenced by the sigmoid) is stable for at least two hours. The background image of the lower panel corresponds to the line-of-sight magnetic field distribution shown in Figure 4.1g with the annotated coloured contours of Figure 4.1h that show which areas of the flux distribution emerge at the same time and are therefore connected.

pre-existing eastern sunspot in the extended magnetic field region. The western EUV dimming and flare ribbon indicates that the western flux rope footpoint is located in the southern penumbra of the pre-existing positive sunspot. These footpoint locations are displayed in Figure 4.6.

The sigmoidal structure that first partially appears in the 131 Å images around 11:20 UT is co-temporal with the brightening of high-frequency (low-altitude) radio emission produced on the western side of the active region. The sigmoidal emission fades and then appears again at around 12:20 UT on 14 June 2012 — just over an hour before the eruption and ≈30 minutes before the slow rise in the X-ray flux begins. Whilst the 131 Å channel of AIA does include contributions from cooler plasma at ≈0.4 MK, images taken in this channel are largely representative of coronal plasma temperatures ≈11 MK during flares or high-temperature sigmoid formation. This indicates that the sigmoidal structure contains hot plasma. Both appearances of the S-shaped emission structure are associated with increases in soft X-ray emission detected by GOES and an enhancement in intensity and extent of the central arcade of the active region as seen by AIA. These observations are interpreted as an indication that magnetic reconnection occurs in two phases, and that these two phases are predominantly responsible for building the flux rope. The first phase of reconnection, around 11:20 UT, heats plasma and accelerates electrons, which leads to the radio emission at the western end of the flux rope. The second phase of magnetic reconnection, around 12:25 UT, then further builds the flux rope structure. The flare arcade brightens and grows simultaneously with the overlying sigmoid, suggesting they both develop as a result of the same episode of magnetic reconnection, and therefore that the flux rope builds during the times the flare arcade is seen to brighten. Furthermore, little photospheric flux cancellation is observed, there are no photospheric inverse crossings seen along the central section of the polarity-inversion line, and the sigmoid formation is best observed in the 131 Å channel of AIA (≈11 MK; representative of flaring plasma in the corona). Together, these observations suggest that the flux rope does not form in a BPSS configuration via reconnection in the photosphere or chromosphere via the flux cancellation form-

ation process described by van Ballegooijen and Martens (1989), but rather that the flux rope forms at a higher altitude in an HFT configuration by reconnection in the corona (see Section 1.3.1.4).

The interpretation that magnetic reconnection in the corona builds the flux rope is further supported by the plasma composition in the flux rope. In a previous study, Baker et al. (2013) used plasma composition to investigate the altitude at which magnetic reconnection occurs. In that work, a sigmoidal active region was observed with a core channel of plasma that had a FIP-bias of order 1.0. This signified that the channel contained plasma of a photospheric composition. The conclusion of Baker et al. (2013) was that a flux rope formed via magnetic reconnection in the photosphere associated with flux cancellation along the polarity-inversion line of an active region. However, in our study, a photospheric plasma composition is not observed in the sigmoidal structure. Instead, the composition analysis indicates that plasma in the initial sigmoid loops that begin to brighten around 11:20 UT and plasma within the western leg of the flux rope is of coronal composition, with FIP biases of 3.1 and 1.9 respectively, with errors $\approx$0.3. This supports our interpretation that the flux rope forms in the corona. Coronal flux ropes, formed via coronal reconnection, have previously been observed in other works as the appearance of diffuse emission structures in the hottest AIA channels above brightening flare arcades (*e.g.*, Reeves and Golub, 2011; Zhang et al., 2012; Patsourakos et al., 2013). In these cases, flux ropes were viewed along their axes when the structure was at the limb. Here, the sigmoid is observed close to disc centre, viewing the flux rope from above and allowing the photospheric magnetic field evolution to also be studied. So, now the role that photospheric flows might have played in the evolution of the magnetic field in the corona is examined.

As discussed previously, NOAA AR 11504 was in its emergence phase at the time the CME studied here erupted. The flux emergence proceeded in stages with different bipoles emerging in sequence. On 11 June, there are already two small sunspots present, and the emergence of further bipoles, some of which coalesce with the pre-existing field, develops these sunspots. The HMI data show that the

photospheric horizontal magnetic field component is sheared in the locations of the emerged flux, *i.e.*, to the north of the positive sunspot and in the negative elongated flux region, which manifests as strong concentrations of vertical electric current. There are domains of positive emerged flux that remain distinct from the main positive sunspot (leading spot) as well as a region of negative magnetic flux that forms an elongated structure to the south of the main negative sunspot (trailing spot). As the flux emergence proceeds, there are 'orbital' and shearing motions between the bipoles. The positive magnetic flux that emerges between 13 June and 15 June moves westwards towards the pre-existing positive sunspot and then moves clockwise around the pre-existing sunspot umbra as separate umbrae. This suggests that, in the days leading up to the eruption, the coronal magnetic field emanating from this strongly moving and shearing positive region wraps around the magnetic field of the pre-existing sunspot. Yan et al. (2012) also observed one umbra orbiting around another in another active region, and associated the anti-clockwise motion they observed with the formation of a left-handed sigmoid (whereas here, clockwise orbiting and the formation of a right-handed sigmoid are seen). Yan et al. (2012) concluded that the twisting of magnetic field from the rotational motion in the photosphere led to a non-potential field configuration in the corona. Similarly, it is concluded here that the clockwise wrapping of twisted and sheared emerging magnetic flux facilitates the reconnection that leads to the formation of the flux rope in this study.

Observational support is found that the collision of the two newly-emerged sheared flux domains drove the magnetic reconnection in the corona that subsequently builds the sigmoidal structure (and inferred flux rope). As discussed previously, this magnetic reconnection is likely to be of tether-cutting type (Moore and Labonte, 1980; Moore et al., 2001) that forms a flux rope through episodes of magnetic reconnection between two sets of sheared loops (illustrated in Figure 4.10), but which here initially produces a stable flux rope that only later erupts rather than runaway reconnection that both builds the flux rope and facilitates the eruption. Numerical studies have shown that a thin current layer can be formed in an arcade that

is subject to shearing, and that in the presence of resistivity, magnetic reconnection can proceed in this current layer (Mikic and Linker, 1994; Roumeliotis et al., 1994; Amari et al., 1996). Furthermore, the combined rotational and inward motion of a pore around a sunspot has been shown to lead to a strong build up of current that is needed for reconnection (Gerrard et al., 2003). Here, it is proposed that the shearing and orbiting motion of the positive magnetic field elements around each other in NOAA AR 11504 leads to magnetic reconnection in the sheared arcade and the formation of a magnetic flux rope in the corona.

The photospheric motions are likely to also play a role in the occurrence of the CME beyond the formation of the flux rope itself. The orbiting motion seen here in the western sunspot of NOAA AR 11504 could drive the twisting of field rooted in and around the sunspot, causing it to rise and inflate (Török et al., 2013). Furthermore, the field that overlies the forming flux rope may also twist and inflate until it is no longer able to contain the underlying flux rope due to decreased tension. Evidence of this expanding magnetic field configuration is seen in the form of deflected radio emission to the east and west of the active region before the eruption (see Section 4.3.5 and Figure 4.8). The radio emission is interpreted as a signature of magnetic reconnection, and its motion outward from the edges of the active region suggests that reconnection is occurring further and further away from the centre of the active region as the active region magnetic field expands and pushes against external magnetic field.

The increase in radio emission and the production of emission at lower frequencies to the western side of the active region in the lead-up to the eruption suggests that magnetic reconnection is ongoing, with electrons being accelerated at increasing altitudes, perhaps a consequence of the flux rope and active region magnetic field inflating. The increase in low-frequency emission takes place during the slow-rise phase of the eruption. From 13:18 UT — as the slow-rise phase continues — low frequency (high-altitude) radio emission is observed directly above the active region. The high-altitude radio emission source appears stationary at first, indicating that the expanding flux rope and active region field is pushing against

and reconnecting with field above the active region.

After 13:30 UT, the eruption moves into the fast-rise phase, the flux rope escapes, and more impulsive flare reconnection sets in. This is consistent with previous work that has shown that the slow-rise and fast-rise phases are common to CMEs (Zhang and Dere, 2006). In this study, the first phase (the slow-rise phase) lasts for around 30 minutes and shows a steady increase in soft X-ray flux which is co-temporal with the brightening and expansion of the sigmoid in 131 Å and the radio emission. The second phase is a sharp rise phase that occurs during the eruption of the sigmoid that involves more impulsive flare reconnection below and above the flux rope. It is important to note that the flux rope was already present before the onset of eruption, as evidenced by early, partial-sigmoid loops at 11:20 UT. However, additional magnetic flux will likely have been built in to the flux rope by magnetic reconnection during the slow and fast rise phases.

As the fast rise phase continues, the previously-stationary central high-altitude radio emission moves southward in the plane of the NRH images. This is interpreted as a type IV radio burst, corresponding to the acceleration of energetic electrons within the plasma of the moving CME as it erupts.

It is interesting to note the timescale over which the flux rope appears to be stable. From the SDO/AIA observations and the appearance of the sigmoid, it is inferred that the flux rope forms at least 2 hours prior to its eruption. Few studies have been carried out to probe when flux ropes form prior to their eruption, and the timescales over which they are stable. Previous studies of flux ropes that form through magnetic reconnection in the corona, as in this event, suggest they might be stable for a few hours. For example, Patsourakos et al. (2013) studied an event where the flux rope formed 7 hours prior to eruption and Cheng et al. (2014) investigated the eruption of a flux rope that formed 2 hours beforehand. In contrast, a small survey by Green and Kliem (2014) found that flux ropes that formed by photospheric magnetic reconnection associated with flux cancellation were stable in their active regions for between 5 and 14 hours. This is an area where further research is needed (see Chapter 6). Flux ropes formed by reconnection in the corona

will be of the HFT type, whereas flux ropes formed through flux cancellation may be of BPSS type with their underside line-tied to the photosphere. The altitude and specific topology of the flux rope may affect the timescale over which it is stable, but no parametric numerical study of this has yet been conducted.

4.5 Conclusions

The pre-eruptive configuration of a flux rope that is detected *in situ* is investigated to determine whether a flux rope was present before the onset of eruption at the Sun, or if it formed at a later time. It is concluded that a flux rope forms via reconnection in the corona at least 2 hours before the onset of eruption on 14 June 2012. This is evidenced by a flux rope of coronal composition associated with a sigmoid in 131 Å images. The sigmoid first partially flashes into view between 11:20 UT and 11:40 UT before fully appearing from 12:20 UT. The EUV sigmoid grows and brightens from 13:00 UT to 13:30 UT, and there is an accompanying slow rise in soft X-ray emission. Finally, the sigmoid begins to erupt at 13:30 UT, and a fast rise in soft X-ray intensity is observed.

The CME occurs when NOAA AR 11504 is still in its emergence phase. Positive areas of emerging flux move towards and then clockwise around the leading positive sunspot, facilitating tether-cutting-type reconnection in the corona that forms a flux rope and an underlying flare arcade, but does not initially cause the flux rope to erupt. Photospheric motions may cause the inflation of the global active region magnetic field. Simulations have previously shown that vortical motion at the footpoints of magnetic loops can cause the loops to rise, leading to weaker magnetic field overlying an active region (Török et al., 2013). If the magnetic field overlying the pre-eruption flux rope was weakened sufficiently, the eruption of the flux rope could have been driven by the torus instability. This possibility is tested in Chapter 5.

Chapter 5

An Observationally-Constrained Model of a Flux Rope that Formed in the Corona

This chapter contains work that has been published in The Astrophysical Journal Letters (James et al., 2018 *ApJL* 855 L16). This work was performed under the supervision of Gherardo Valori, Lucie Green, and Lidia van Driel-Gesztelyi. Yang Liu (Stanford University) provided a custom-made photospheric magnetogram that was necessary for the successful extrapolation of the flux rope, Mark Cheung (Lockheed Martin Space and Astrophysics Laboratory) performed a DEM inversion of the active region and provided interpretation on this topic, and Yang Guo (Nanjing University) provided the code used to compute the twist and writhe of the extrapolated flux rope.

This work was presented at the 2017 Flux Emergence Workshop in Budapest and at the 2018 SDO Science Workshop in Ghent.

5.1 Introduction

In Chapter 4, a variety of observations were used to conclude that a magnetic flux rope formed in the corona above NOAA AR 11504 before it erupted on 14 June 2012. It was suggested that the same 'orbiting' motions of emerging magnetic flux that enabled the flux rope to form via magnetic reconnection in the corona could

have inflated and weakened the active region magnetic field to the point where the pre-eruption flux rope became torus-unstable. However, the conclusions of Chapter 4 were based on indirect indications of the flux rope, because presently no direct measurements of the full coronal magnetic field vector have been made.

In lieu of coronal magnetic field measurements, techniques have been developed to extrapolate the coronal magnetic field from complex (but routinely available) photospheric observations under the assumption that the corona is in a force-free state (see Chapter 3 for details on these models and assumptions). A valid model of the coronal magnetic field can provide quantitative information regarding the pre-eruptive magnetic field, further supporting the conclusions inferred in Chapter 4 and enabling the investigation of the processes that may have caused the CME.

In this work, a nonlinear force-free field (NLFFF) extrapolation (see Section 3.4.2.2) is used to test the hypothesis of Chapter 4 — that a flux rope formed before the CME that occurred at ≈13:30 UT on 14 June 2012 — and investigate the cause of the eruption. The data and specific parameters used in this work are described in Section 5.2, and the validity of the extrapolated coronal fields are checked by comparison to EUV images of the active region. The properties of the extrapolated coronal field, including the relevance of instabilities in causing the observed eruption, are analysed in Section 5.3, and the conclusions are summarised in Section 5.4.

5.2 Data, Method, and Validation of the Model

The NLFFF extrapolation of NOAA AR 11504 was performed using a photospheric vector magnetogram produced by SDO/HMI. The chosen magnetogram was taken at ≈12:24 UT on 14 June 2012: approximately one hour after the first observational indication that a flux rope was present, and one hour before the CME began (see Chapter 4). The episode of magnetic reconnection associated with the formation of the flux rope had ended (as determined by the duration of the C5.0 flare, see Figure 4.4) and therefore the flux rope could manifest in the NLFFF extrapolation. Fur-

thermore, the observed eruption-onset would not begin for another hour, suggesting the flux rope was stable and could therefore be modelled with NLFFF extrapolation (see Section 3.2 for a discussion of the validity of coronal NLFFF extrapolation).

The observations in Chapter 4 show that the EUV sigmoid was extended to the south of NOAA AR 11504 before the CME occurred (see Figure 4.5c). Since the active region occupied a large coronal volume, a lower-boundary magnetogram with a large area was required. The field-of-view of a publicly available HMI SHARP series magnetogram (see Section 2.1.2.3) was too small to use as a lower-boundary for an extrapolation that would accurately reproduce the sigmoidal field. Therefore, a bespoke SHARP-style magnetogram was required, and Yang Liu of the HMI instrument team produced one with an area more than large enough to form the base of volume that could accommodate the size of the sigmoid ($\approx 400'' \times 600''$; the right-hand panel of Figure 5.1). However, the presence of a dispersed patch of negative magnetic flux to the south of the active region caused the final extrapolated magnetic field configuration to depend strongly on the chosen input photospheric magnetogram area. The area of the boundary magnetogram for extrapolation was chosen to be small enough to exclude as much of the dispersed negative magnetic flux to the south of the active region as possible, whilst still being large enough to accommodate the extent of the sigmoid as described above. The chosen boundary magnetogram area is represented by the red boxes in Figure 5.1.

The magnetogram was re-binned to 1/6th resolution such that each pixel in the CEA projection represents an angular diameter of 0.18° (equivalent to $3''$ or $\approx$2.18 Mm at disc centre when viewed from 1 AU). This was done because lower resolution extrapolations are less computationally-demanding, and a $3''$ resolution should still be sufficient to resolve the feet of the flux rope inferred by observations in Chapter 4 (Figure 4.6 shows EUV footpoint dimmings with an area of $\approx 20'' \times 20''$). The magnetogram was then smoothed using the median of a 7-pixel boxcar.

Despite the effort to choose a magnetogram area that avoided as much of the dispersed negative magnetic flux as possible, there was still an imbalance of 13.6% between the positive and negative magnetic flux in the magnetogram. To alleviate

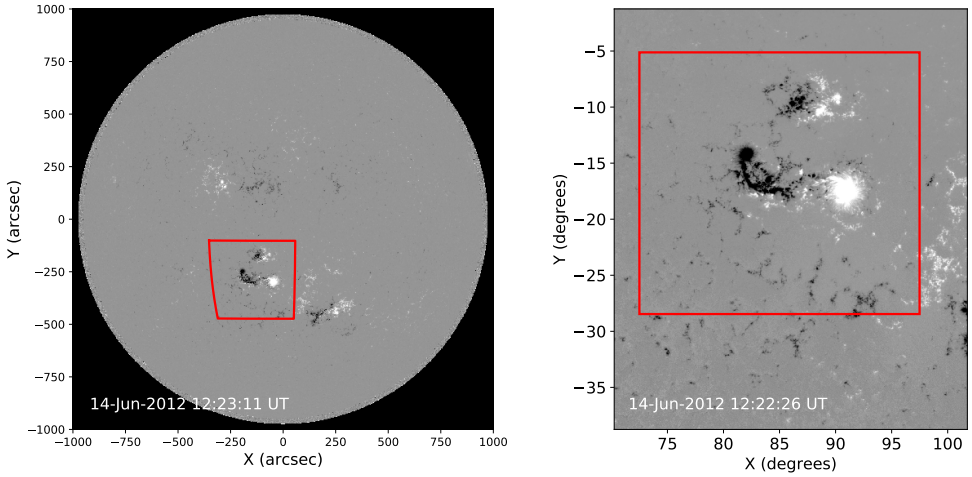

Figure 5.1: HMI magnetograms of the Sun taken on 14 June 2012. Positive (negative) magnetic flux is shown in white (black), and saturated at $\pm$1000 G. The left panel is a line-of-sight magnetogram for context, and the right panel shows the radial magnetic field component in CEA projection. The red boxes show the boundary of the SHARP-style magnetogram that was used for the NLFFF extrapolation, containing NOAA AR 11504.

the impact that this unblanaced flux would have on the extrapolated field, the balance of positive and negative magnetic flux was enforced over the magnetogram. This was achieved by modifying the magnetic flux density in every pixel by +5.2 G, which is far smaller than the 100 G per pixel error estimation suggested by Hoeksema et al. 2014.

The magnetogram was then pre-processed using the method of Fuhrmann et al. (2007) to reduce the total Lorentz force by applying variations to the horizontal and vertical magnetic field components (explained in Section 3.6.4). Modifications to the observed horizontal (vertical) field component in each pixel were limited to 80 G or 30% (30 G or 10%) of its initial value — whichever was largest. Figure 5.2 shows the relative reduction in the total Lorentz force over the course of the pre-processing.

The height of the extrapolation volume was chosen to more than doubly accommodate the height of a semi-toroidal flux rope that has a footpoint separation as indicated by the EUV dimmings observed in Chapter 4 (Figure 4.6). The coronal magnetic field was extrapolated in this volume from the pre-processed magnetogram using the magnetofrictional NLFFF method detailed in Chapter 3, yielding a

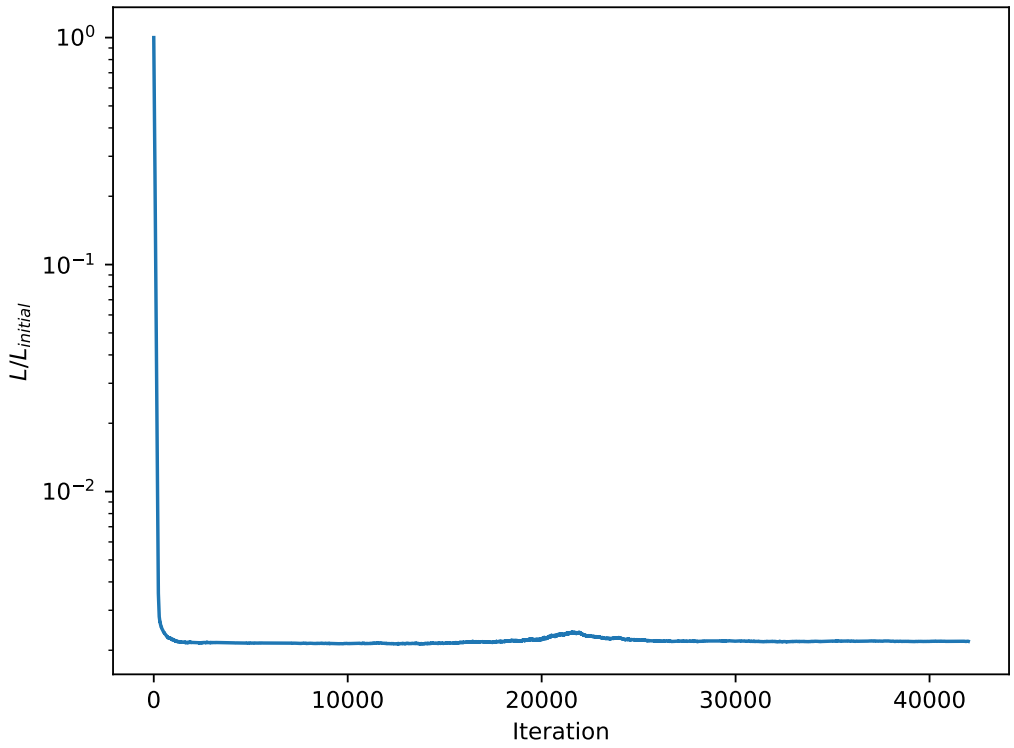

Figure 5.2: Minimisation of the functional, L, in the pre-processing of the magnetogram used. The simulated annealing ran for over 40000 iterations and L was reduced by a factor ≈500.

model of the active region.

The validity of the extrapolated magnetic field can be examined in several ways. Previous studies have quantified how well the magnetic field satisfies the force-free ($\mathbf{J} \parallel \mathbf{B}$; from Equation 3.2) and solenoidal ($\nabla \cdot \mathbf{B} = 0$; Equation 1.8) conditions (Wheatland et al., 2000; Valori et al., 2013). 75% of the current in the extrapolated field presented in this chapter is parallel to the magnetic field, and 9% of the energy in the extrapolated field is associated with non-solenoidal magnetic field. The degree to which these values are satisfactory is debatable, but next, a qualitative test of how well the extrapolated field reproduces observations of the corona — which is the ultimate goal of the model — is described.

The extrapolated magnetic field is compared to EUV observations produced by SDO/AIA that were taken at the same time as the boundary magnetogram. The AIA data are processed using standard techniques (*i.e.*, to level 1.5 using the aia_prep

routine available in SolarSoft). A direct comparison would not be immediately correct because AIA images show the Sun projected in the plane-of-sky, whereas the extrapolation is based on a vector magnetogram in a CEA projection (introduced in Sections 2.1.2.3 and 3.6.3.2). Therefore, the NLFFF extrapolated field lines must be re-projected and aligned with an AIA plane-of-sky image to enable a direct comparison. The re-projection is achieved by tilting the CEA-projected magnetogram (and thereby the extrapolation volume) to give the same viewing angle of the active region as AIA had. Since the active region was 10° east and 19° south of disc-centre as observed by AIA, these were the tilt angles used. Once the re-projection is complete, the alignment is achieved in two steps. Firstly, the CEA HMI magnetogram is aligned with a plane-of-sky (line-of-sight) HMI magnetogram, and secondly the plane-of-sky magnetogram is aligned with the plane-of-sky AIA EUV image. In doing this, the CEA image is thereby aligned with the EUV image (a few more details about this method are given in Polito et al. 2017).

Figure 5.3 shows that the extrapolation reproduces the large-scale active region emission structures seen in the 193 Å channel of AIA, including field lines that fan out from the edges of the active region and the sheared arcade in the core of the active region (shown by the southern group of white field lines in the left panel of Figure 5.3).

5.3 The Pre-eruptive Flux Rope

The NLFFF model is used to study the coronal magnetic field of NOAA AR 11504 before a CME that occurred at ≈13:30 UT on 14 June 2012. In particular, a magnetic flux rope is searched for, since it was concluded observationally in Chapter 4 that one was present prior to eruption (with footpoint locations shown in Figure 4.6).

The magnetic field strength (B), electric current (I), and force-free parameter (α) are all studied in a vertical slice through the extrapolation volume in order to identify whether a flux rope is present in the extrapolation volume (see Figure 5.4). Examining Figure 5.4, the left panel shows that there is no clear signature of a flux

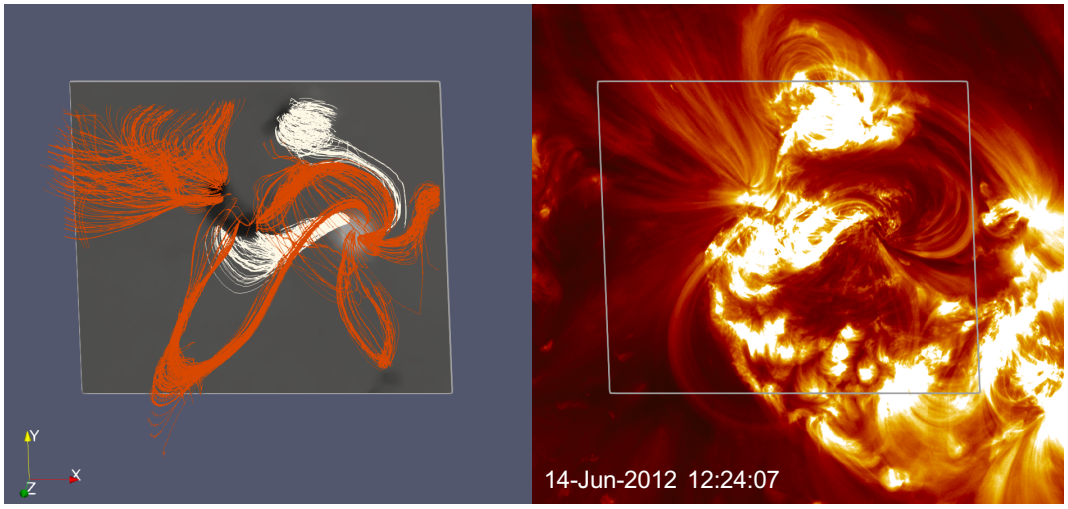

Figure 5.3: The extrapolated coronal magnetic field (left) closely matches a number of active region features observed in the 193 Å channel of AIA (right). The AIA image is saturated at 2500 DN s^{-1} $pixel^{-1}$.

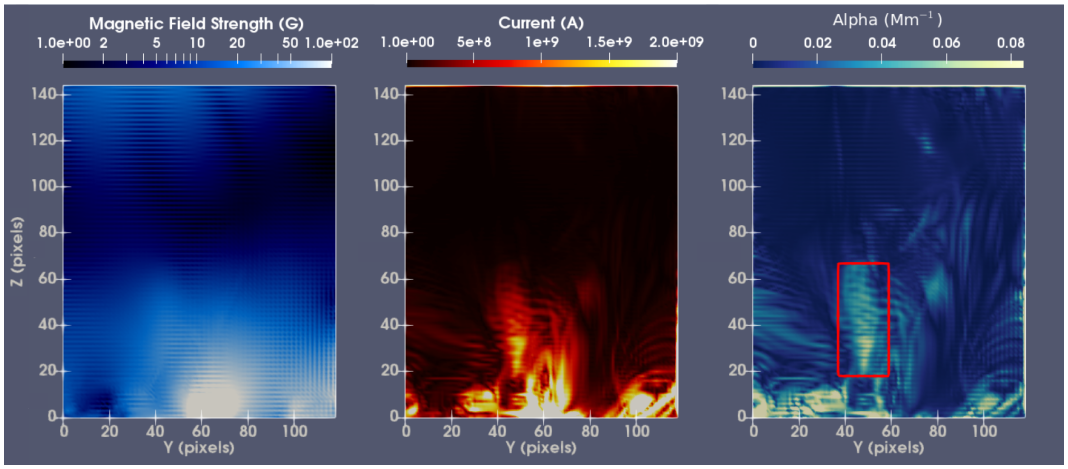

Figure 5.4: A vertical slice taken through the extrapolation volume at $x = 67$ pixels (see Figure 5.5 for scale) that shows the magnetic field strength (*left*), the electric current (*middle*), and the magnitude of the force-free parameter, α (*right*). A region of large α (outlined by a red box) is used to define the extent of the flux rope shown in Figure 5.5.

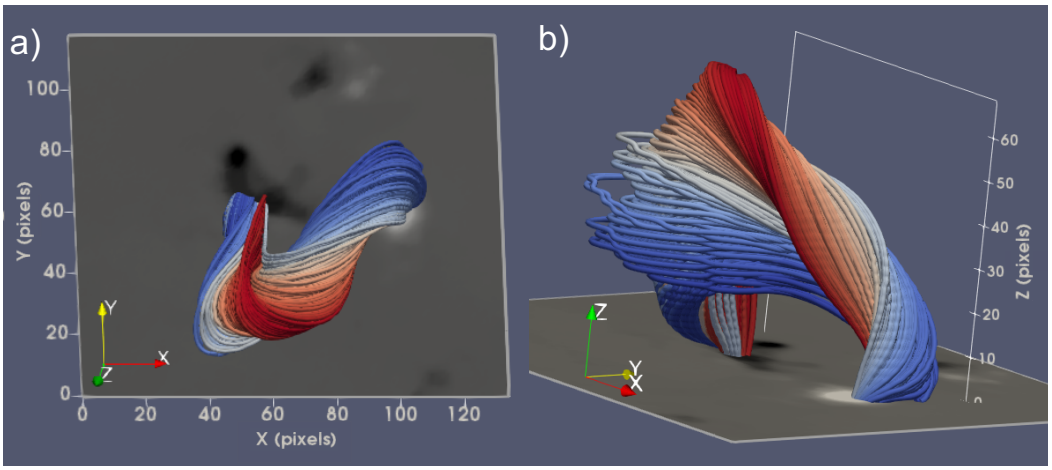

Figure 5.5: Stream lines are drawn through the region of strong α shown in the right panel of Figure 5.4, revealing a flux rope. Each stream line is given a fixed colour along its length. (a) The flux rope in the extrapolated field as seen from the same perspective as SDO. (b) Side-on view of the extrapolated flux rope.

rope in the magnetic field strength, and the middle panel shows many regions of strong electric current. However, a distinct region where the α parameter is strong can be seen in the right-hand panel (outlined in red). From Equation 3.12, the force-free parameter α is the ratio of magnetic field strength and electric current density, representing a proxy for twist in the extrapolated magnetic field.

Within the red box shown in Figure 5.4, the region of strong α was selected by hand. By visualising magnetic field lines that pass through the region of strong α, a flux rope is revealed (see Figure 5.5). The average value of α in the flux rope is ≈ 0.07 Mm^{-1}. The location and shape of the flux rope matches most, if not all, of the observational constraints identified in Section 4.4 remarkably well, and these similarities will be discussed in the remainder of this section.

The flux rope extends high in the corona, with its highest point reaching ≈ 150 Mm (≈ 0.2 R$_\odot$) above the photosphere. The axis of the flux rope is not planar, but is oriented roughly eastward and inclined to the south with respect to the vertical. The axis is ≈ 350 Mm long and reaches up to ≈ 120 Mm above the photosphere. The flux rope is highly asymmetric and has a strongly inhomogeneous distribution of right-handed twist. The vaguely elliptical flux rope cross-section shown in the right panel of Figure 5.4 has a major diameter of $\approx$105 Mm and a minor diameter

of ≈35 Mm.

The footpoints of the extrapolated flux rope are located in the north-western penumbra of the positive sunspot and to the south of the negative sunspot. EUV observations, however, suggest that the western footpoint of the flux rope was rooted in the south-western penumbra of the positive sunspot during the eruption (see Figure 4.6). This difference of approximately half the sunspot diameter could be due to modification of the magnetogram induced by pre-processing, to the difference in time between the pre-eruptive extrapolation and observations during the dynamic phase of the eruption, or to projection effects in the coronal EUV data.

In addition to the set of observations presented in Chapter 4, a DEM inversion was performed using the method of Cheung et al. (2015) to study the thermal emission of the active region. At the time of the extrapolation, the sigmoid and underlying flare arcade observed in the active region emitted most strongly in the temperature range $\log(T/K) = 6.85 - 7.15$. This is consistent with their observation in the 131 Å channel of AIA, which has a peak in temperature response at 11 MK (Lemen et al., 2012), and confirms flux rope temperatures from previous DEM studies (*e.g.*, Cheng et al. 2012). The shape of the sigmoid in the EUV observations and DEM closely matches extrapolated field lines that pass through the strong region of current density in the bottom-third of the flux rope (see Figure 5.6).

Field lines that reproduce the observed sheared arcade were also found to pass through a region of strong current beneath the flux rope (see the green field lines in Figure 5.6c and 5.6d). The average value of α in the sheared arcade is $\approx 0.07\ \mathrm{Mm}^{-1}$, which is the same as that of the flux rope, as mentioned previously. In addition to the many observational details summarised above, the similarly hot temperatures and high current densities of the sigmoid and the arcade support the hypothesis of Chapter 4 that the flux rope and flare arcade form as the products of magnetic reconnection in the corona, driven in particular by the orbiting motion of satellite sunspot fragments.

The flux rope contains 4×10^{20} Mx of magnetic flux, which is $\approx 3\%$ of half the unsigned active-region flux computed in Chapter 4 (see Figure 4.2). The total

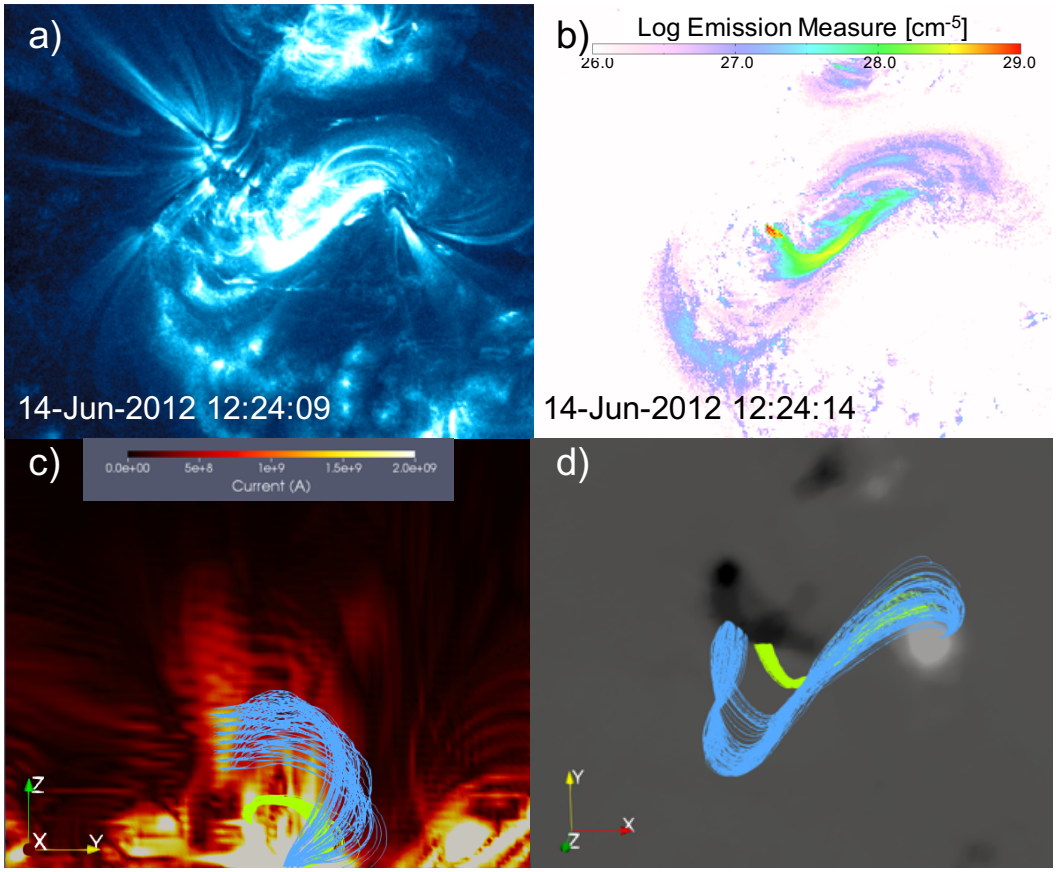

Figure 5.6: (a) EUV image of NOAA AR 11504 in the 131 Å channel of AIA showing the bright central flare arcade and the faint sigmoid. The image is saturated at ± 200 DN s^{-1} pixel^{-1}. (b) DEM of NOAA AR 11504 in the temperature range $\log(T/K) = 6.85 - 7.15$ shows the flare arcade and sigmoid. (c) Electric current in a vertical slice taken through the extrapolation volume. The flux rope appears as a region of relatively high current, which is particularly strong at the bottom of the flux rope. Stream lines are drawn through regions of strong current that match the EUV observations of the sigmoid (blue) and the flare arcade (green). (d) The extrapolated sigmoidal and flare arcade stream lines from panel (c) as viewed from the perspective of SDO, imposed on the extrapolated magnetogram.

electric current, I, is given by

$$I = \int \mathbf{J} \cdot \mathrm{d}\mathbf{S}, \tag{5.1}$$

where d$\mathbf{S}$ is the surface through which the current passes and the current density, $\mathbf{J}$, is defined in Equation 1.12. The total electric current within the flux rope is 2.3×10^{11} A, with an average current density of 9.9×10^{-5} A m^{-2}. These values are similar in magnitude to previous estimations of currents in prominences (Filippov et al. 2015, and references within).

5.3.1 Twist and Writhe

According to the test in Section 4.3 of Valori et al. (2010), attempting to extrapolate an unstable coronal magnetic field equilibrium with the magnetofrictional method would result in an uncommonly long computational time, which did not occur when producing the extrapolation in this work. However, the flux rope in this study is clearly twisted and extends very high in the atmosphere, so it is investigated whether the flux rope is indeed stable to the ideal MHD kink and torus instabilities.

The helical kink instability will occur if the flux rope twist exceeds a critical value (see Section 1.3.3.1). To quantify the twist in our very asymmetric case, the twist of individual field lines in the flux rope was calculated around an axis, and the average was taken (*e.g.* Guo et al., 2010, 2013). Following Guo et al. (2017), the axial field line is defined as the field line with the smallest ratio of tangential-to-normal magnetic field components with respect to a plane roughly perpendicular to the body of the flux rope.

The determination of the axis is therefore dependent on the chosen slice through the flux rope. Given the marked asymmetry of the flux rope, three slices were taken through the flux rope with different inclinations, resulting in three axes and therefore three values of the average twist. Firstly, a slice was taken in the y-z plane of the extrapolation volume through the centre of the flux rope (as in Figure 5.4). This gives an axis seen in Figure 5.7a and the average twist around it is 1.35. The second slice was rotated about the z-axis with respect to the first slice, with the axis shown in Figure 5.7b and the average twist around it is 1.61. The third slice

was inclined downward with respect to the second slice, to be perpendicular to the central part of the flux rope. This is shown in Figure 5.7c and the average twist around it is 1.88. The axes are similar in height and length (for reference, the first axis is ≈350 Mm long and reaches up to ≈120 Mm above the photosphere). The same set of flux rope field lines were used to determine the twist around each of the three axes. Two of the values obtained for the twist of the asymmetric, non-uniform flux rope in this work are comparable to the critical threshold of 1.75 turns (see Section 1.3.3.1).

The observations detailed in Chapter 4 show no significant sign of the flux rope kinking before or during the eruption. In fact, the axis of the flux rope changed so little that the CME configuration measured *in situ* closely matched the pre-eruptive configuration (Palmerio et al., 2017). Therefore, the critical twist required for this flux rope to become kink unstable seems not to have been reached.

The writhes of the three axes were 0.29, 0.09, and -0.07 turns. The axis that resulted in the largest value of average twist was the one with the smallest writhe, and vice versa. Therefore, the sum of the twist and writhe is closer to being independent from the choice of the plane used to determine the axis (as expected; Török et al. 2010b).

Guo et al. (2017) concluded that a good proxy of the magnetic helicity in the current-carrying field inside a finite volume is

$$H_{TW} = \Phi^2(Twist + Writhe), \tag{5.2}$$

where Φ is magnetic flux. In our case, using the total magnetic flux in the flux rope, this method gives a maximum helicity estimate of $\approx 3 \times 10^{41}$ Mx^2. On the other hand, using the extrapolated field and Equation 1.35, the helicity of the closed, current-carrying field, H_J, in the extrapolation volume is $\approx 4 \times 10^{42}$ Mx^2, which is 14 times larger than H_{TW}. Part of this discrepancy may originate from underestimating the magnetic flux in the flux rope when defining the boundary of the flux rope using the force-free parameter, α. However, because H_{TW} scales with Φ^2, there would need to be a factor of $\sqrt{14} \approx 3.7$ error in the magnetic flux to fully explain

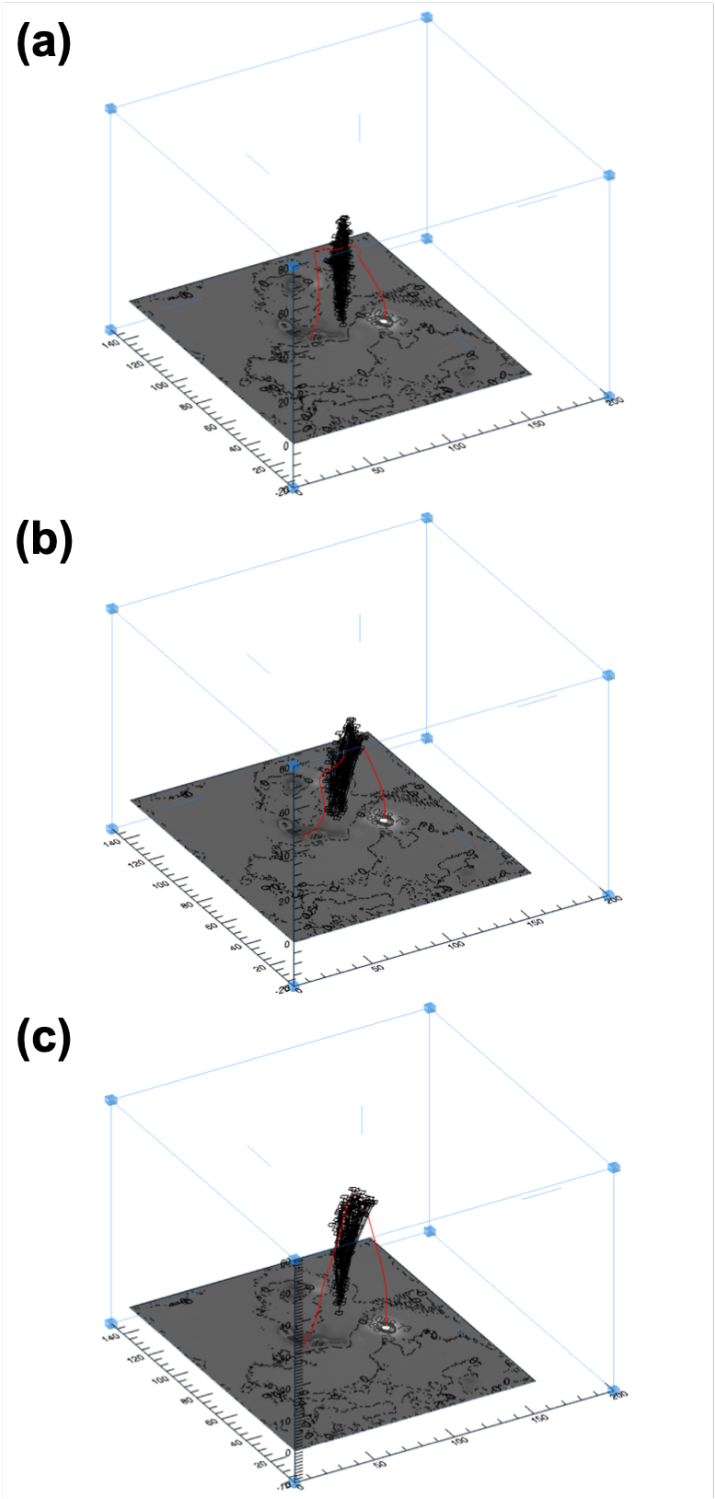

Figure 5.7: Three different cross-sections (the collections of black points) are taken through the flux rope at different angles, and the best choice of axial field line (red) is taken from each one using the method of Guo et al. (2017). The grey square at the base is a contoured photospheric magnetogram.

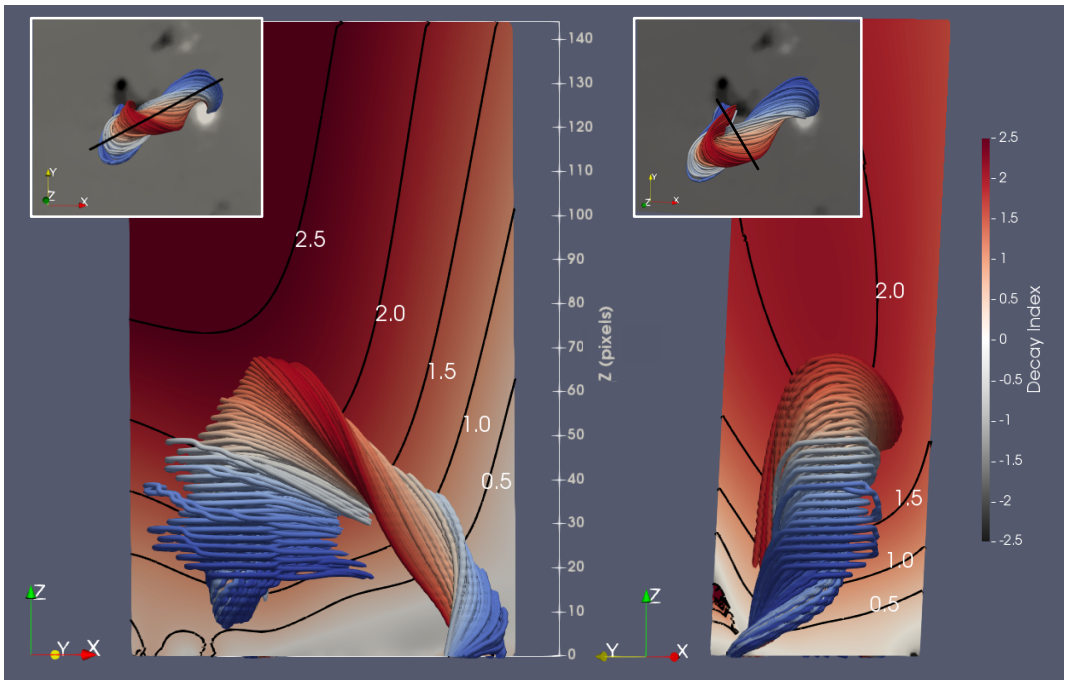

Figure 5.8: The decay index is computed in slices along and perpendicular to the flux rope axis. The decay index at the centre of the flux rope is ≈1.8.

the difference, which is unreasonable to assume is the case. Instead, the difference may originate from strong currents elsewhere in the active region (*i.e.* external to the flux rope), since H_J is computed in the whole volume and H_{TW} is counted only in the flux rope. Regions of strong electric current external to the flux rope are observed in the middle panel of Figure 5.4.

The helicity of the threading part of the field, related to both the potential field and current-carrying field (as defined, *e.g.*, by Equation 11 in Pariat et al. 2017), $H_{PJ} \approx 1 \times 10^{43}$ Mx^2. The total helicity in the extrapolation volume is then $H = H_J + 2H_{PJ} \approx 2.4 \times 10^{43}$ Mx^2. In this chapter, the first estimation of the eruptivity proxy recently introduced by Pariat et al. (2017) for an NLFFF extrapolation of an active region is given, equal to $H_J/H = 0.17$.

5.3.2 Decay Index

A toroidal magnetic structure, such as a flux rope, may be torus-unstable to perturbations if the overlying magnetic field strength decreases too rapidly with height, *i.e.*, if the decay index is critical (see Section 1.3.3.1 for an introduction to the torus instability and the decay index).

In order to estimate the decay index at the height of the flux rope, a potential field extrapolation is performed using the method of Alissandrakis (1981) to approximate magnetic field external to the flux rope. The poloidal field component is taken as the component perpendicular to the central section of the flux-rope axis. Then, following Equation 1.36, the gradient of the poloidal field component is used to compute the decay index in two planes: one inclined parallel with the flux rope axis, and one perpendicular to the axis (shown in Figure 5.8).

The decay index near the centre of the extrapolated flux rope is equal to 1.8, and closer to the axis apex is equal to 2.0. The extrapolated asymmetric flux rope therefore lays above the critical decay index for a symmetric torus of $n_{crit} = 1.5$, but as stated before, the extrapolation method used here should have produced a stable equilibrium field configuration. Other studies have suggested higher (and lower) values of n_{crit} ($1.1 < n_{crit} < 2.0$; see Section 1.3.3.1). The scenario of the flux rope in this work being very close to being torus unstable is compatible with the eruption of the flux rope occurring just one hour after the extrapolation time. A triggering process may act during this hour that can modify the decay index and/or raise the flux rope until the decay index at the axis is critical.

5.4 Conclusions

In this study, the hypothesis from Chapter 4 that a magnetic flux rope formed in the corona of NOAA AR 11504 before erupting as a CME is tested. An NLFFF extrapolation of the coronal magnetic field is produced from a photospheric magnetogram one hour before the onset of eruption, and a close match is found with the observational conclusions of Chapter 4. Firstly, a flux rope is indeed found in the extrapolated field before the eruption. Secondly, the flux rope is relatively high up in the corona, with its axis reaching $\approx$120 Mm above the photosphere ($\approx$150 Mm at the top of the flux rope). A sheared arcade is found beneath the flux rope in an HFT configuration, supporting the hypothesis that the flux rope formed via reconnection in the corona.

The altitude of the flux rope is comparable to that of the pre-eruptive configura-

tions of several reported stealth CMEs (Robbrecht et al., 2009; Ma et al., 2010). The eruption studied in this chapter is certainly not a stealth CME, as it exhibits numerous strong low-coronal signatures (outlined in Chapter 4). The CME studied here originates from an active region with strong magnetic field, whereas many identified stealth CMEs originate from regions of weaker magnetic field. This difference in field strength may explain the contrast in observed eruption signatures, such that stealth CMEs are simply the weaker-field limit of high-altitude (HFT configuration) flux rope eruptions.

The flux rope found in this chapter is different in a number of ways to sigmoid-associated flux ropes that form via magnetic flux cancellation. Flux cancellation can form flux ropes over a few days, building magnetic flux in to a flux rope. Yardley et al. (2018) studied a sample of four active regions that produced low-altitude flux rope eruptions, and found that an average of 36% of the peak fluxes of the regions was cancelled over the days before the eruptions. Other studies have found higher quantities of flux cancellation than this, and also suggest that only $50\% - 70\%$ of cancelled flux is built in to flux ropes (Green et al., 2011; Savcheva et al., 2012). The reconnection involved in flux cancellation occurs low down in the solar atmosphere, so the flux ropes that form may have BPSS configurations. In contrast, the flux rope found in this chapter formed via magnetic reconnection in the corona with an HFT configuration, was only stable for $\approx$2 hours, and contains 3% of the active region flux.

The decay index near the centre of the flux rope is $\approx$1.8, which is comparable to the critical value for the torus instability onset determined in other works. However, the extrapolated magnetic field equilibrium must represent a stable configuration, so the flux rope modelled in this work is stable (although a proper verification of the latter statement requires an MHD numerical evolution starting from the extrapolated field). Therefore, it is concluded that, at the time of the extrapolation (1 hour before eruption), the flux rope was close to becoming torus unstable.

During the hour between the extrapolation and the eruption, a triggering process may have further evolved the coronal magnetic field towards instability. Any

perturbation could have caused the QSL around the HFT flux rope to collapse and form a current sheet, enabling magnetic reconnection to occur and thereby modifying the decay index and/or raising the flux rope.

In another study, Vemareddy et al. (2017) used observations to conclude that the helical kink instability caused a highly twisted prominence (flux rope; 2.96 turns) to rise to the point at which the torus instability set in. The flux rope modelled in this chapter has an average twist in the range of 1.35 – 1.88 turns, which is similar to estimates of the critical twist needed for the onset of the kink instability. However, the observations presented in Chapter 4 suggest that kinking did not occur. Therefore, the kink instability did not trigger the CME studied here, and another trigger mechanism is required to explain how the magnetic field evolved before the eruption.

In Chapter 4, it was suggested that the 'orbiting' motion of emerging sunspot fragments around each other drove magnetic reconnection in the corona that formed an HFT flux rope, but also inflated magnetic field above the flux rope. The results of the modelling in this chapter very closely match the observational conclusions of Chapter 4, lending support to the hypothesis that the flux rope formation was triggered by photospheric motions. By extension, there is now further support for the scenario in which these same photospheric motions may also have inflated and therefore weakened magnetic field above the flux rope, explaining how the torus instability developed and drove the eruption.

Since only one event has been studied in this thesis so far, more cases of HFT flux rope formation are studied in Chapter 6. The aim of this extended study is to reveal how common the pre-eruptive processes identified in Chapters 4 and 5 are.

Chapter 6

Magnetic Flux Emergence and the Formation of Coronal Flux Ropes

The work contained in this chapter was performed under the supervision of Lucie Green, Gherardo Valori, and Lidia van Driel-Gesztelyi. The results have been presented as a contributed talk at the 2018 SDO Science Workshop in Ghent, Belgium.

6.1 Introduction

Different processes are required to describe the slow build-up of electric currents in the corona before eruptions and the onset and acceleration of CMEs (Aulanier et al., 2010). In this thesis, these initiation mechanisms are classified as triggers and drivers. *Triggers* create stable structures before eruptions, such as magnetic flux ropes, and evolve them to the point where they may lose stability. Then a *driving* process is responsible for the loss of stability and the fast dynamical phase of eruption. For further discussion of triggers and drivers with examples, see Section 1.3.3.1.

In order to predict CMEs, relevant triggers must be identified so that pre-eruptive structures can be recognised, and knowledge of whether eruptions of these structures can be successfully driven must be obtained.

A number of observational studies have used EUV, X-ray, and radio observations to find evidence supportive of flux ropes that formed high up in the corona

before eruptions, seen best when close to the solar limb (*e.g.*, Reeves and Golub, 2011; Patsourakos et al., 2013; Nindos et al., 2015). However, since these studies identified coronal flux ropes at the limb, they were unable to observe the evolution of the photosphere beneath the forming flux ropes. Photospheric observations can provide crucial information about the triggering mechanisms that cause flux ropes to form in the corona and evolve towards the brink of eruption.

The work contained in Chapter 4 builds on previous studies by inferring the presence of a coronal flux rope that is close to the centre of the solar disc. The observational conclusions of Chapter 4 are supported by an extrapolated magnetic field model in Chapter 5 which reveals a flux rope that matches the observations well. The modelled flux rope has its axis ~ 0.2 $R_{\odot}$ above the photosphere, and spectroscopic measurements in Chapter 4 confirmed that the flux rope had a coronal plasma composition, supporting the conclusion that the flux rope formed in an HFT configuration via magnetic reconnection in the corona.

Since the flux rope studied in Chapters 4 and 5 was close to disc-centre as viewed by SDO, the photospheric behaviour of the host active region could be studied to identify the processes that drove reconnection in the corona and formed the flux rope. The active region was in a phase of ongoing magnetic flux emergence, with emerging flux fragments moving towards — and then around — previously-emerged sunspots of the same magnetic polarities. It was concluded that this 'orbiting' motion of emerging flux caused the footpoints of two J-shaped sets of magnetic field loops to wrap around each other, forcing magnetic reconnection to occur in the corona. This reconnection caused the observed transition in the active region from the two J-shaped structures to a flux rope and an underlying flare arcade (see Figure 4.10).

Furthermore, the observed orbital motion of emerging magnetic flux around the sunspot could have injected magnetic energy in to the field that overlies the flux rope (Török et al., 2013). This would have inflated the overlying field, weakened its confining effect on the underlying flux rope, and therefore enabled the flux rope to rise. This is consistent with the model in Chapter 5 that suggested the flux rope

eruption was driven by the torus instability due to a critical magnetic field gradient above the rope.

The scenario of emerging flux that 'orbits' pre-existing magnetic flux explains the observed formation and eruption very well. However, Chapters 4 and 5 represent only a case-study of one active region. A natural extension of this previous work is therefore to ask how common this process is, and investigate whether these processes are observed in other eruptive active regions.

The motion of magnetic flux fragments around each other may be framed in the broader observational context of sunspot rotation. The causal connection between rotational motions of sunspots and the onset of solar activity has been well-studied. The rotation of sunspots has been linked to the the formation of sigmoids, flaring, and CMEs (*e.g.*, Gerrard et al., 2003; Brown et al., 2003; Yan et al., 2012; Vemareddy et al., 2016). The sunspots in each of these studies feature multiple umbrae within one rotating sunspot, and may therefore be similar to the 'orbiting' scenario described above. The relative energetic contribution of the solid-body rotation (spin) of a sunspot has been compared to that of shearing individual fragments around each other, concluding that the energy budgets of flares can be powered by either one, or both, in different cases (Longcope et al., 2007; Kazachenko et al., 2009, 2010). In summary, sunspot rotation and the relative motion of sunspot fragments are known to correlate with energy storage and release in flares and CMEs. However, the physical processes that cause these motions and create the magnetic field configurations that ultimately erupt require further investigation.

Specifically, relatively few studies have focused on the formation and eruption of structures high up in the corona (*e.g.* HFT flux ropes). In the rest of this chapter, the formation of five HFT flux ropes in four active regions is studied. Photospheric motions are quantified in each active region to identify whether the same processes that formed the flux rope in Chapters 4 and 5 are systematic in HFT flux rope formation. The criteria used to select events are given in Section 6.2. The method used to quantify photospheric motions is described in Section 6.3.1, and the method used to estimate the height of structures in the corona is explained in Section 6.3.2. Sec-

tion 6.4 contains the observations of each eruption and the measured motions. The results are interpreted and discussed in Section 6.5, and conclusions are presented in Section 6.6.

6.2 Data and Event Selection

For this study, events were selected from the SDO-era in which flux ropes formed in the corona before erupting. It was also required that observations of the photospheric evolution during the days before eruption were available.

Events were selected by following one of two procedures. Some events were chosen by identifying halo CMEs in the SOHO LASCO CME catalogue, using the STEREO spacecraft to check that the CMEs originated from the SDO-facing disc of the Sun, and then identifying signatures of flux ropes in the corona before the eruptions (*e.g.* sigmoids and plasmoids). Other events were chosen by identifying pre-eruption signatures of flux ropes in the corona first, and then using SOHO/LASCO observations to confirm that the flux ropes erupted as CMEs.

The coronal configuration before each CME was studied using EUV observations from SDO/AIA (AIA data were processed to level 1.5 using the aia_prep routine available in SolarSoft). Sigmoids and plasmoids are observational signatures of flux ropes corresponding to hot plasma and can therefore be observed using the 94 Å and 131 Å channels of AIA. However, the temperature response functions of the 94 Å and 131 Å channels of AIA are 'double-peaked' (see Figure 2.3), and therefore the images they produce contain contributions of photons from both hot and cold plasma. To ensure that only hot signatures were identified, images from the relatively cool 171 Å channel was used for comparison. Any feature that appears in the 94 Å and 131 Å images but does not appear in the 171 Å channel must correspond to hot plasma, and therefore may be a flux rope signature.

Additionally, observations from the 193 Å and 211 Å channels of AIA were used to identify EUV dimmings, and images from the 304 Å and 1600 Å channels were used to locate flare ribbons. EUV dimmings and flare ribbons manifest at the footpoints of erupting flux ropes, and are therefore useful for determining the

locations in the CME source regions where photospheric motions should be studied.

In order to study the evolution of the photosphere before the eruptions, accurate observations of the photospheric magnetic field over a number of days were required. To ensure these observations were available, any CME that did not originate from within $\pm 60^{\circ}$ of disc-centre was ruled out. From the initial sample, 18 CMEs were identified that occurred within $\pm 60^{\circ}$ of disc-centre and showed signatures of pre-eruptive flux ropes. However, to serve as a continuation of the work in Chapters 4 and 5, this selection was narrowed further to include only flux ropes that formed high up in the corona, *i.e.* flux ropes with an HFT configuration, not a BPSS configuration (see Section 1.3.1.4).

When a flux rope forms with an HFT configuration, an arcade of magnetic loops is also created beneath the rope. Alternatively, when magnetic reconnection forms a BPSS flux rope, flux cancellation can be observed when newly-formed loops submerge beneath the photosphere. EUV observations from SDO/AIA were used to identify whether arcades of magnetic loops had developed beneath the flux ropes, and observations of the radial photospheric magnetic field (B_r) from the SDO/HMI SHARP data series (see Section 2.1.2.3) were used to check for flux cancellation.

Using the above method, it was found that 12 of the 18 candidate CMEs showed no arcades forming beneath their pre-eruptive sigmoids/plasmoids, and exhibited significant magnetic flux cancellation, suggesting BPSS configurations. In the other 6 events, sheared arcades were seen to simultaneously brighten beneath the forming flux ropes, and little-to-no flux cancellation was observed along their central polarity inversion lines. The observations of these 6 events suggest that HFT flux ropes formed via magnetic reconnection in the corona. The dates of the 6 CMEs are given in Table 6.1, along with information about the source active regions.

The sigmoid that erupted on 17 July 2016 spanned two active regions: NOAA ARs 11585 and 11587. The photospheric magnetic field configuration of this event was determined to be too complex for the scope of this work, and this event was therefore excluded from the rest of this study. The observations and analysis presen-

Date of CME	NOAA AR	Lat.	Long.	Hale	Chirality	Orbiting
13 March 2012	11429	N18°	W59°	No	Left	Anticlockwise
13 June 2012	11504	S17°	E23°	Yes	Right	Clockwise
14 June 2012	11504	S17°	E10°	Yes	Right	Clockwise
08 October 2012	11585	S19°	W33°	Yes	Left	Anticlockwise
17 July 2016*	11585/7	N5°	E8°	Yes	Both	Both
14 July 2017	12665	S6°	W34°	Yes	Left	Anticlockwise

Table 6.1: The identified events that feature HFT flux ropes that form in emerging active regions that go on to erupt as CMEs. Latitude (Lat.) is specified in either the northern (N) or southern (S) hemisphere. Longitude (Long.) is specified east (E) or west (W) of central meridian. All values from the Debrecen Photoheliographic Data sunspot catalogue `http://fenyi.solarobs.csfk.mta.hu/en/databases/DPD/`. *The CME on 17 July 2016 spans two active regions: NOAA ARs 11585 and 11587, so the given latitude and longitude is the average of the two regions. These two regions have opposite chiralities and observed orbiting motions to each other, so taken overall, both are observed. This event is not selected for further study.

ted in the rest of this chapter are of the remaining five events.

The evolution of the photosphere before each CME was studied using white-light continuum images and radial magnetic field strength observations from the SDO/HMI SHARP data series. The magnetic flux of the CME source regions was computed by integrating the radial magnetic flux densities in each HMI SHARP magnetogram. In events where the SHARP magnetograms contained more than one region of strong magnetic flux, such as multiple active regions, the data were cropped to contain only the desired source active region. Pixels with magnetic flux densities lower than 30 G were excluded from the flux calculations to reduce the effect of noise. The method used to quantify photospheric motions is described in Section 6.3.1.

Full-Sun integrated X-ray light curves are obtained from the GOES XRS system and used in combination with EUV images from SDO/AIA to identify flares in the CME source active regions.

6.3 Methods

6.3.1 Quantifying the 'Orbital' Motion of Emerging Magnetic Flux Fragments

In Chapter 4, the orbital motion of a magnetic flux fragment around a sunspot was estimated by-eye using two white-light continuum images that were taken 24 hours apart. However, in this chapter, a more systematic method is used to track the motion of individual magnetic flux fragments, as explained in this section.

HMI continuum images from the SHARP data series were used to study the motion of magnetic flux fragments in the photosphere. Roughly 12 days of data were used to follow the full passage of each active region across the solar disc at an image cadence of 6 hours.

Contours were set on each HMI SHARP continuum image to encircle individual umbral fragments, and the flux-weighted centre of each fragment was found using the radial magnetic field strength inside each contour (see Figure 6.1). In the first image of a sequence (at time t_1), two fragments were selected by hand: one as the "central" fragment and one as the "orbiting" fragment, and a vector ($\mathbf{v}_1$) was drawn between the flux-weighted centroids of the two fragments. In the next image in the sequence (at time t_2), the orbiting fragment had moved relative to the central fragment, and a new vector ($\mathbf{v}_2$) was drawn between the new flux-weighted fragment centroids. By comparing the vectors in successive images (illustrated in Figure 6.2), the angle the orbiting fragment had moved around the central fragment by was calculated using the relation

$$\theta_{21} = \arccos \frac{\mathbf{v}_1 \cdot \mathbf{v}_2}{|\mathbf{v}_1|\,|\mathbf{v}_2|}. \tag{6.1}$$

This gives $0 \leq \theta_{21} \leq 180$, and therefore does not distinguish between rotation in the clockwise and anticlockwise directions. In order to obtain a signed orbit angle,

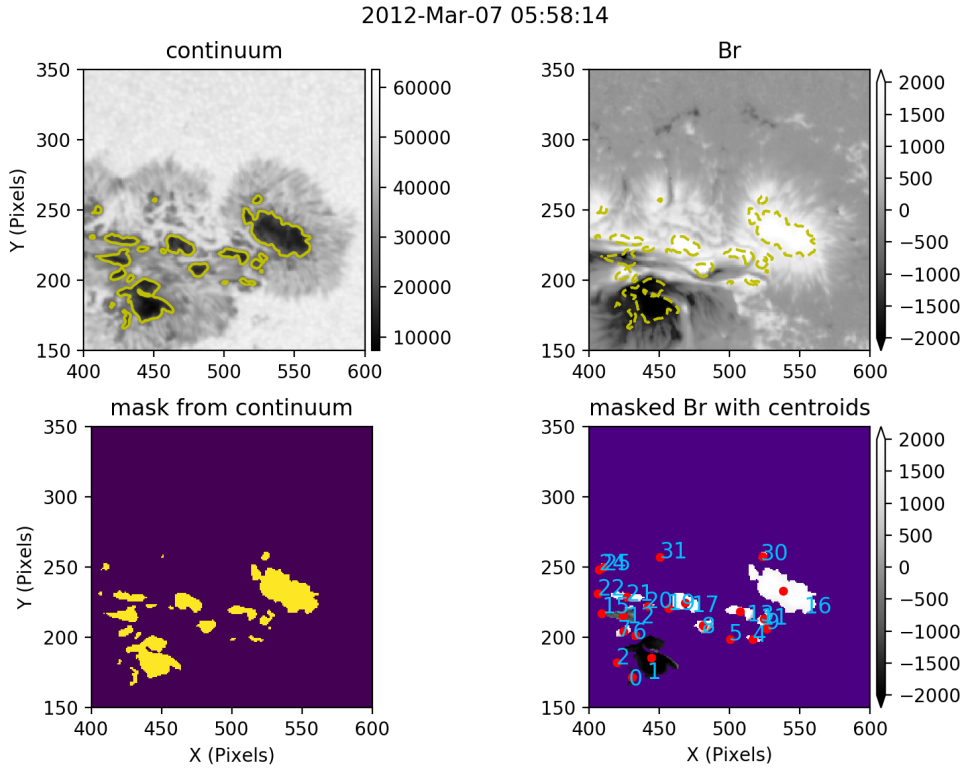

Figure 6.1: a) Contours are drawn at fixed intensity levels on HMI continuum images to enclose individual umbral fragments. b) The radial magnetic field component, B_r, shows the polarity and strength of magnetic flux. c) Masks of the pixels within the continuum contours. d) Flux-weighted centroids (red) of the fragments are computed using B_r within the masked pixels. Each centroid (and therefore fragment) is assigned a unique number so they can be hand-selected to quantify orbiting.

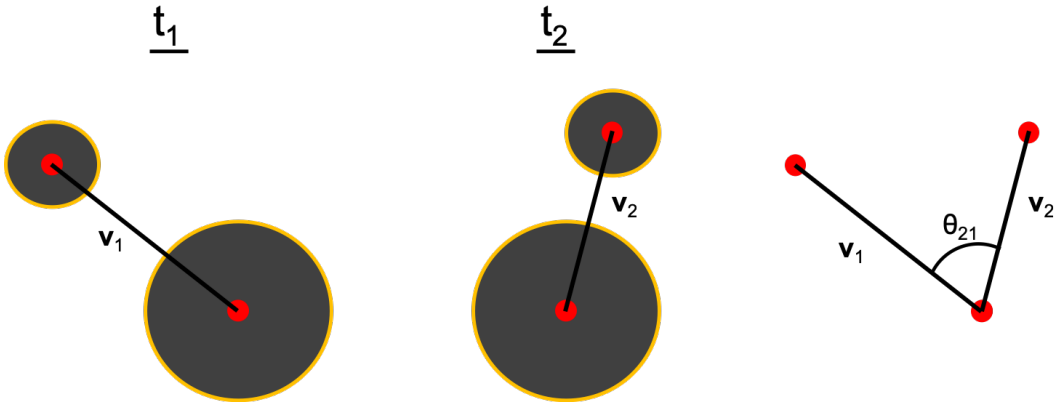

Figure 6.2: Illustration of the method used to track the relative orbital motion of a magnetic flux fragment.

$-180 \leq \theta_{21} \leq 180$, the relation

$$\begin{aligned} (\mathbf{v}_1 \times \mathbf{v}_2) \cdot \mathbf{v}_n > 0 \rightarrow \quad & 0 < \theta_{21} < 180 \\ (\mathbf{v}_1 \times \mathbf{v}_2) \cdot \mathbf{v}_n < 0 \rightarrow \quad & -180 < \theta_{21} < 0 \end{aligned} \tag{6.2}$$

may be used, where $\mathbf{v}_n$ is the vector normal to $\mathbf{v}_1$ and $\mathbf{v}_2$, oriented positively towards the observer. This process was repeated for every image in the time sequence to track the orbital rotation over time.

At some points in the time sequence, different pairs of fragments were tracked to best quantify the observed motions. The vectors between different pairs of tracked fragments are colour-coded in *e.g.* Figure 6.4, and the corresponding orbit angles of different fragments are colour-coded in *e.g.* Figure 6.5.

Occasionally, it was not possible to distinguish two fragments, for example after they had merged together. In these cases, the solid-body rotation of the merged sunspot was quantified. This was done by linearly fitting a vector to the major axis of the elliptical sunspot umbra to best describe the orientation of the sunspot. The rotation of this vector is then followed through time in the same way as described above by Equations 6.1 and 6.2. The assumption here is that the previously-distinguishable fragments still comprise different parts of the now-elliptical sunspot, and this is confirmed by the observation of light bridges in some events.

6.3.2 Estimating Heights in the Corona

Unlike in Chapter 5, models of the coronal magnetic field are not produced for the events studied in this chapter. Therefore, the heights of structures in the corona are estimated from observations using geometrical considerations and assumed symmetry. Throughout the rest of this section, the middle of a sigmoid is used as an example of a point in the corona where the height above the photosphere is estimated.

The assumption is made that the middle of the chosen sigmoid lies radially above the centre of a photospheric PIL, via symmetry. In reality, the middle of a sigmoid does not necessarily lie radially above the centre of a PIL, as the symmetry

of the system is affected by many factors (*e.g.*, the spatial flux distribution at the photosphere, the distribution of currents in the active region, the dynamical evolution of the sigmoid, etc.). Due to the nature of the assumptions being made, any resulting heights should only be taken as order-of-magnitude estimations.

From plane-of-sky solar observations, two coordinates are taken: the coordinate of a point at the centre of the coronal sigmoid (x_{sig}, y_{sig}) and the point at the middle of the photospheric PIL (x_{pil}, y_{pil}). In addition, the heliocentric longitude (ϕ) and latitude (θ) of (x_{pil}, y_{pil}) is required. Then, the height of the sigmoid above the photospheric PIL can be estimated using either the difference in x coordinates or the difference in y coordinates:

$$h_x = \frac{x_{sig} - x_{pil}}{cos(\theta)sin(\phi)}, \tag{6.3}$$

$$h_y = \frac{y_{sig} - y_{pil}}{sin(\theta)}. \tag{6.4}$$

If the assumption that the coronal point lies radially above the photospheric point is correct, then $h_x = h_y$, but otherwise these two equations will give different height estimates. Whenever this method is applied later in this chapter, both h_x and h_y are computed and the average is taken to give a qualitative estimate of height. The calculated values of h_x and h_y are found to differ by no more than a factor of 2.5.

6.4 Observations

6.4.1 13 March 2012

6.4.1.1 Coronal Evolution

A CME occurred on 13 March 2012 at ∼17:10 UT in NOAA AR 11429 with an accompanying M7.9 flare that spanned the active region. The white-light CME was first observed by LASCO C2 at 17:36 UT (Figure 6.3a). An inverse-S (left-handed) sigmoid brightened in the active region shortly before the onset of the eruption along with a clear underlying flare arcade, suggesting that an HFT flux rope was

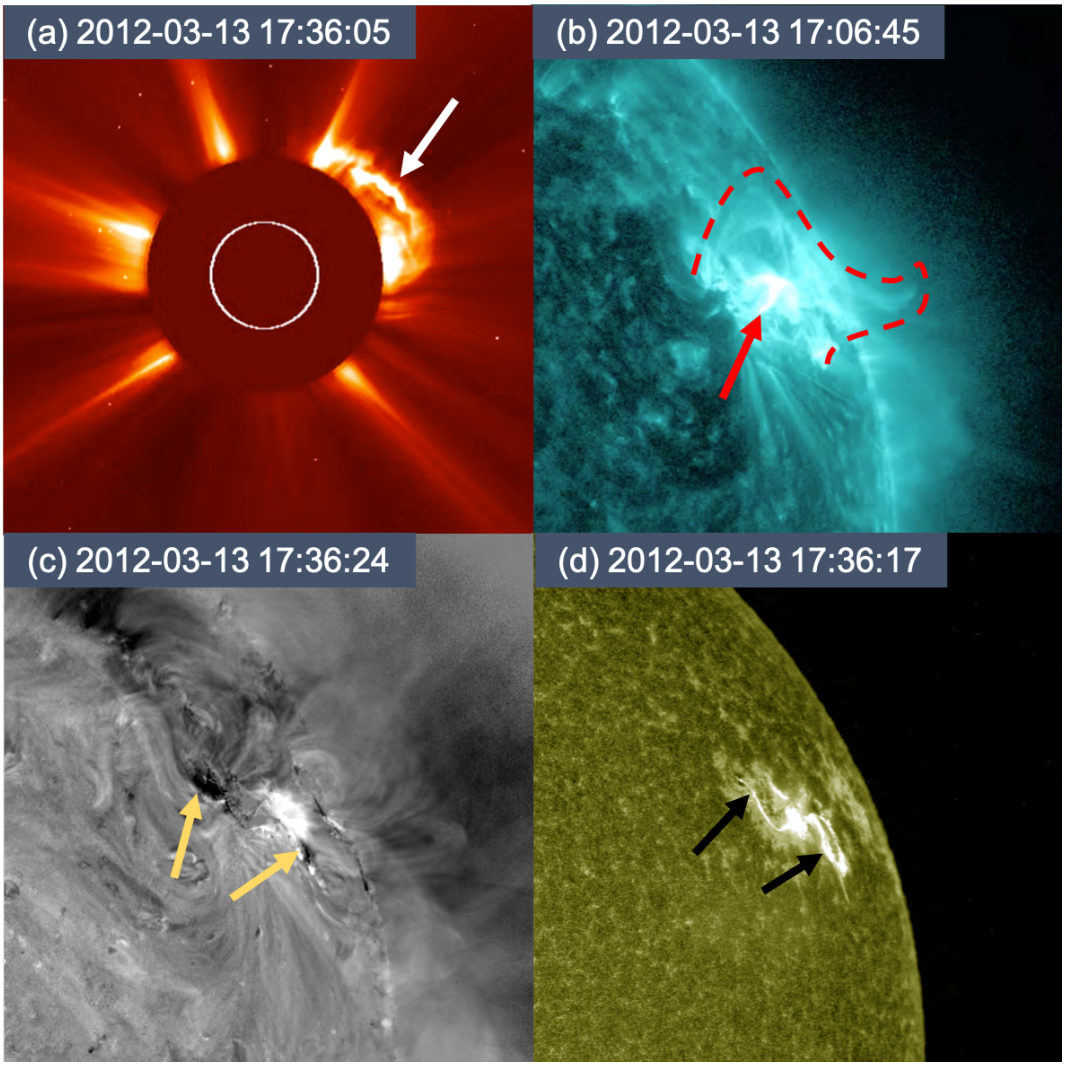

Figure 6.3: Observations of the 13 March 2012 eruption. (a) A white-light CME (indicated by the white arrow) seen by LASCO C2. (b) AIA 131 Å image of a sigmoid (highlighted by a dashed red line) brightening above a flaring arcade (indicated by a red arrow). (c) AIA 211 Å base difference image showing twin EUV dimmings (marked by two yellow arrows). (d) AIA 1600 Å image showing hooked flare ribbons (indicated by two black arrows).

forming via reconnection in the corona (see Figure 6.3b). The middle of the sigmoid is estimated to be at an altitude of 68 Mm above the footpoints of the flaring loops at 16:47 UT (using the method described in Section 6.3.2). The ends of the sigmoid appear rooted in the east and west parts of the active region, and twin EUV dimmings and hooked flare ribbons are also observed in these locations during the eruption (Figures 6.3c and 6.3d respectively). These observations suggest that a flux rope formed with footpoints in the east and west parts of the active region and later

erupted during the CME.

The previous CME from NOAA AR 11429 occurred on 10 March (3 days before the CME mentioned above), and was associated with an M8.4 flare at 17:44 UT. A white-light CME with a bright front and cavity was seen at 18:18 UT in LASCO C2 images, suggesting that the CME had a flux rope structure at the time of the coronagraph observations (as described by Vourlidas et al., 2013 and the references within). Much like the M7.9 flare associated with the CME on 13 March, the M8.4 flare on 10 March spanned the full width of the active region, suggesting both eruptions originated from the same major PIL at the centre of the active region. Assuming any pre-eruptive structure (*e.g.* a flux rope) was fully-ejected from the active region during the 10 March CME, the flux rope that erupted on 13 March must have formed at some time during the 3 days between eruptions.

The specific time(s) of flux rope formation can be inferred by identifying solar flares that occurred in the active region during the 3 days between CMEs. This is because solar flares are produced by magnetic reconnection, and the same episode of reconnection could simultaneously build a flux rope.

Four of the flares detected by GOES between the CMEs on 10 and 13 March 2012 occurred in NOAA AR 11429. On 11 March, a C2.3 flare began at 03:18 UT and a B8.8 flare began at 14:06 UT. Both of these flares were highly-localised to small areas of the active region and lasted for only 10s of minutes. Then, a C4.1 flare began on 12 March at 22:20 UT, and a C3.1 flare began on 13 March at 06:55 UT. These latter two flares brightened across the whole active region, lasting for 2.5 hours and 1.5 hours respectively, and hot plasma structures were observed above the flaring arcades with shapes similar to — and in the same location as — the sigmoid that appeared before the 13 March CME. The C3.1 flare was only partially-observed because the view of the Sun from SDO and GOES was eclipsed from 06:30 – 07:30 UT on 13 March, but the fading flare loops are seen after this time. STEREO-A had an uninterrupted view of the active region, and observations from EUVI-A and COR2-A confirm that no eruption was associated with the flare.

6.4.1.2 Photospheric Evolution

The active region was 59° west of central meridian around the time of the eruption, giving a clear perspective of the brightening sigmoid and underlying arcade. This also means that the evolution of the photospheric magnetic field can be studied for 10 days before the CME, as the active region moved across the solar disc. This means the photospheric motions that facilitated the coronal reconnection, and therefore flux rope formation, can be characterised.

NOAA AR 11429 rotated on to the solar disc on 3 March 2012, as observed by SDO, and it contained two pre-existing sunspots. The leading sunspot had positive polarity and the trailing spot was negative, which means the active region does not follow Hale's law for a northern-hemisphere region in solar cycle 24. On 4 March 2012, magnetic flux emergence began at two sites between the pre-existing sunspots. The emerging active region exhibited left-handed magnetic tongues, showing that it had left-handed twist (negative chirality).

Positive and negative fragments of emerging flux moved westward and eastward respectively in the active region, towards the pre-existing sunspots of the same polarities. As the fragments approached the sunspots, they orbited around them in an anti-clockwise sense. The strongest orbiting was observed around the leading sunspot (see Figure 6.4), and the EUV dimmings (shown in Figure 6.3c) suggest that the flux rope had a footpoint in the leading spot. Therefore, the leading sunspot was chosen as the location to quantify orbiting motion.

The motion of positive magnetic flux around the leading sunspot was tracked by following distinct fragments using the method described in Section 6.3.1. The orbiting motion is quantified in Table 6.2 and also represented in Figure 6.5, with different fragments colour-coded in the same way as the corresponding vectors in Figure 6.4. In addition, Figure 6.5 also contains the GOES X-ray lightcurve over the duration of the orbiting for comparison and the evolution of the positive and negative magnetic flux of the active region. Measurements of magnetic flux when the active region was close to the solar limb should be treated cautiously. In particular, noise increases in HMI measurements past 60° of central meridian (Hoeksema

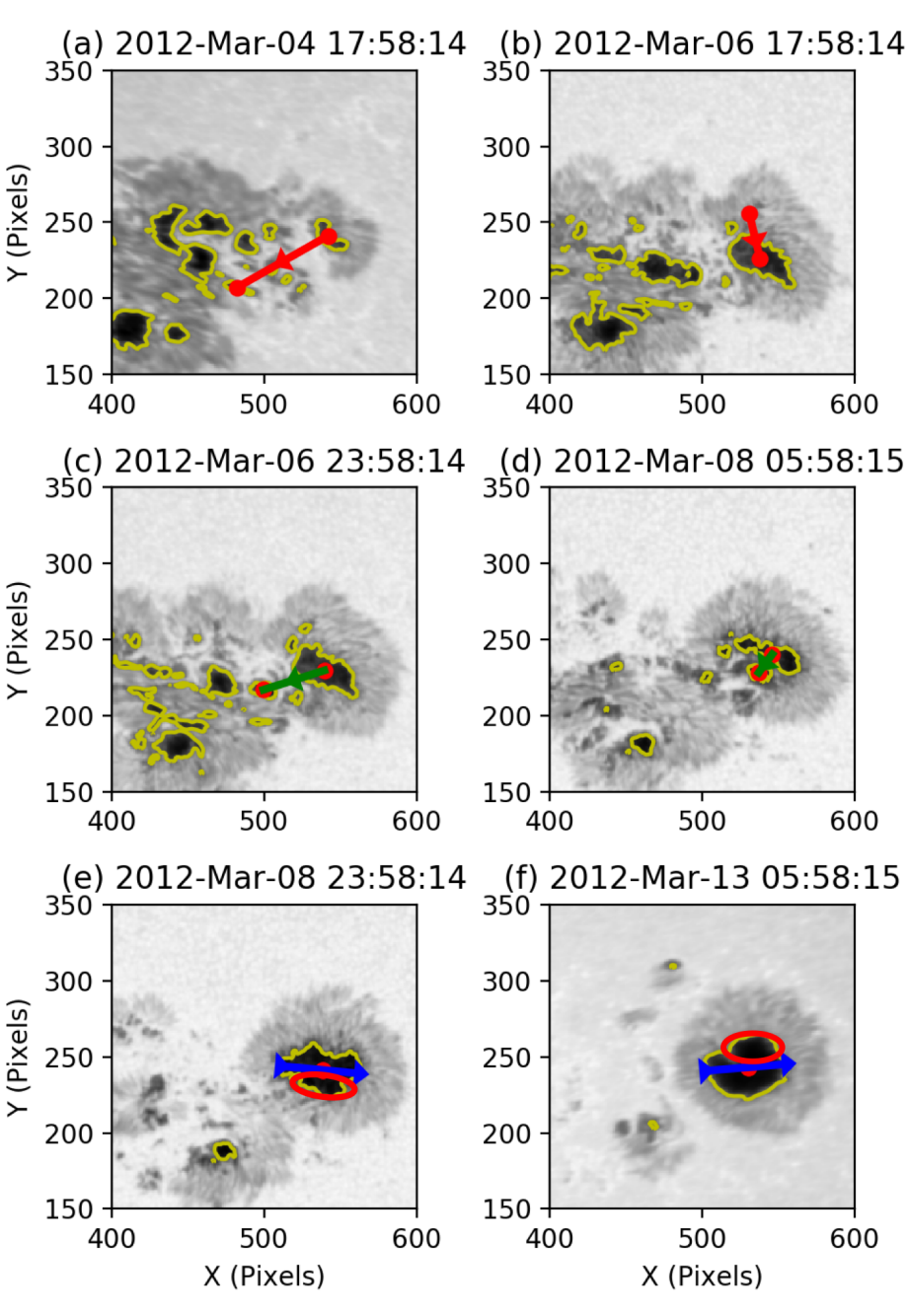

Figure 6.4: The anticlockwise motion of newly-emerged flux around the pre-existing positive (leading) sunspot in NOAA AR 11429. In each image, vectors are drawn either to connect the flux-weighted centroids of two orbiting fragments (panels a-d) or to best-fit the major axis of merged fragments (panels e-f). In the bottom two panels, red circles highlight the position of a fragment whose $\approx 180^{\circ}$ orbit from the south of the sunspot to the north between panels was not successfully tracked using the vector method.

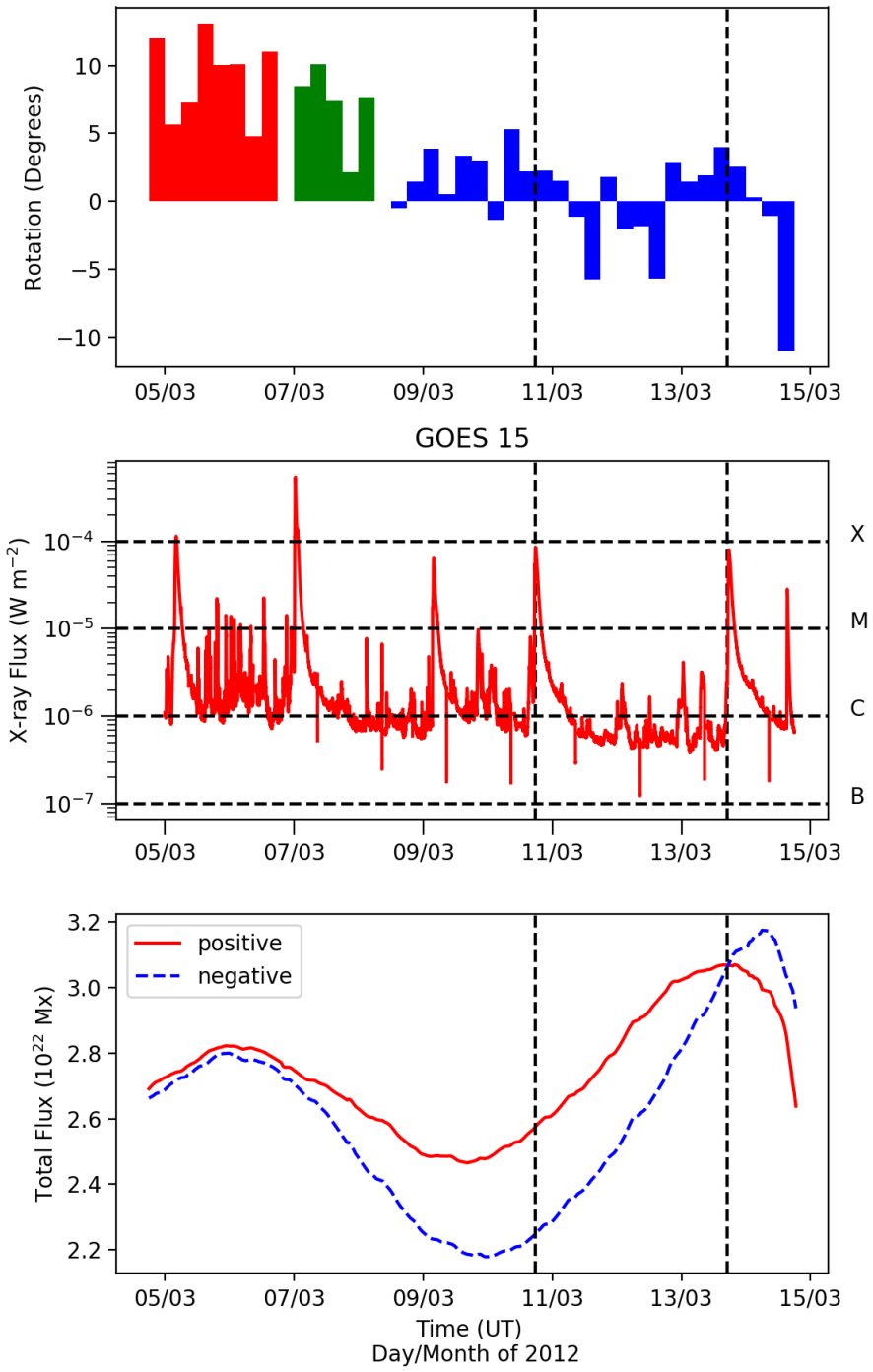

Figure 6.5: Top: The measured orbital motion of chosen magnetic flux fragments in 6-hour intervals. The colours correspond to different choices of fragments (see Figure 6.4). Middle: Full-disc integrated GOES soft X-ray lightcurve. Bottom: The evolution of magnetic flux in NOAA AR 11429, made using the radial magnetic field component, B_r, of the HMI SHARP data series and smoothed with a 24-hour moving average. Vertical dashed lines indicate the times of the CMEs on 10 and 13 March 2012 described in Section 6.4.1.1.

Start Time (UT)	End Time (UT)	Total Orbit (°)	Average Orbit (° day^{-1})
04 March 2012 18:00	06 March 2012 18:00	+73.9	+36.95
07 March 2012 00:00	08 March 2012 06:00	+35.7	+28.56
08 March 2012 12:00	14 March 2012 12:00	+18.9	+3.15
*08 March 2012 12:00	14 March 2012 12:00	+180	+30

Table 6.2: The orbital motion of three subsequently-emerged umbral flux fragments relative to previously-emerged umbrae in NOAA AR 11429. Positive angles are anticlockwise and negative angles are clockwise. The first three rows are the quantities given by the fragment-tracking method, but the orbiting quantified from 8 – 14 March is under-measured compared to observations. *The fourth row contains the values determined by-eye.

et al., 2014; Couvidat et al., 2016), as the active region was until 5 March and from 14 March onward.

For the remainder of this section, the ongoing orbiting motions of the emerging flux fragments is described. One tracked fragment orbited by 73.9° between 5 March and 7 March (an average of $\sim 37°$ per day; Table 6.2). During this time, there was an X-class flare in the the active region (X1.1 on 5 March at 02:30 UT) with an associated halo CME. The total magnetic flux of the active region had begun to decay on 6 March. From 7 March until midday on 8 March, another fragment orbited by 35.7° (an average of $\sim 29°$ per day). During this time, there was another X-class flare from the active region (X5.4 on 7 March at 00:02 UT) with an associated halo CME. The flux ropes involved with the eruptions on 5 and 7 March 2012 were not rooted in the leading, coalescing sunspot, and formed low-down in the atmosphere as a result of shearing motions elsewhere in the active region (Chintzoglou et al., 2015).

On 9 March, all of the emerged fragments had coalesced together as one large sunspot umbra, and on 10 March, the magnetic flux of the active region began to increase again. Little orbiting motion was measured over the remaining time the active region was on the disc using the method described in Section 6.3.1 with a total of 18.9° measured from 9 – 15 March (an average of 3.15° per day). This measured orbiting appears to be noisy, consisting of small rotations $\lesssim 5°$ in each time interval that vary between clockwise and anticlockwise rotations (Figure 6.5).

However, when examining the sunspot by eye, there is significant orbiting occurring in the sunspot that is not detected using the fragment-tracking method (see panels e and f of Figure 6.4). The magnetic flux fragment that arrived at the south of the leading sunspot at 12:00 UT on 8 March orbits almost 180° up to the north of the sunspot by 12:00 UT on 11 March — an average rotation of 60° per day. This is not picked up by the automated orbit-tracking method because the fragments have merged together in to one sunspot (therefore individual fragments cannot be separated by contours) and the sunspot is roughly circular (not elliptical), so its rotation is not identified by the best-fit vector.

6.4.1.3 Interpretation

The flux rope that erupted on 13 March 2012 at 17:10 UT formed at some time after the eruption on 10 March at 17:24 UT. During this 3-day period, the active region was in a phase of emergence after having previously been decaying, with the total unsigned magnetic flux of the region increasing from $\approx 2.4 \times 10^{22}$ Mx to $\approx 3.1 \times 10^{22}$ Mx, and the fragment-tracking method described in Section 6.3.1 measured net clockwise orbiting of 0.7°. This is remarkably small and demonstrates how noisy the measured motions were during this period, with small clockwise and anticlockwise rotations mostly cancelling each other out over time.

However, as explained above, it is clear that more orbiting occurs during this time-frame than can be detected by the tracking method. By eye, the orbiting fragment appears to move anticlockwise from the west of the sunspot on 10 March to the north on 13 March, suggesting an orbit of $\approx 90°$ between eruptions in NOAA AR 11429 (an average of $\approx 30°$ per day).

Between 10 – 13 March, two non-eruptive C-class flares spanned the whole active region, beginning at 22:20 UT on 12 March and at 06:55 UT on 13 March. It is inferred here that the orbiting brought together magnetic loops rooted in the moving fragments, causing the loops to reconnect in the corona. This reconnection caused a twisted flux rope to form and grow in the corona with underlying flare arcades brightening beneath. In this scenario, the times of the observed flares show when the flux rope was forming. This suggests the flux rope had begun to form at

least 19 hours before the onset of the CME on 13 March 2012.

6.4.2 13 & 14 June 2012

6.4.2.1 Coronal Evolution

A CME erupted from NOAA AR 11504 on 13 June 2012 at 13:00 UT. The CME is seen in white-light by LASCO C2 at 14:36 UT (Figure 6.6a). A hot EUV plasma emission feature is seen to grow, brighten, and rise above an M1.2 flaring arcade during the 2 hours leading up to its eruption (Figure 6.6b). The highest point of the growing plasma emission was 376 Mm above the centre of the active region's photospheric PIL at 12:58 UT (using the method described in Section 6.3.2). The hot plasma emission comes from above a flaring arcade in the active region, and is interpreted as a signature of an HFT flux rope forming in the corona. The footpoints of the flux rope are inferred by twin EUV dimmings and hooked flare ribbons that form in the east and west parts of the active region during the eruption (Figure 6.6c and 6.6d).

It is difficult to identify whether a previous CME occurred from the active region before the 13 June eruption. White-light CMEs are seen in LASCO C2 data on 8 June, 10 June, and 12 June, but most of these correspond to filament eruptions on the far-side of the Sun. One of the CMEs on 10 June, seen from 07:30 UT in LASCO C2 images as a faint circular blob, may have originated from NOAA AR 11504. An M1.3 flare began in the active region at ≈06:39 UT on 10 June, and may be associated with this CME. Assuming any flux rope that may have been involved in this eruption was fully-ejected, the flux rope that eventually erupted on 13 June had 3.25 days to form after the 10 June event.

There were 11 flares in NOAA AR 11504 between the CMEs on 10 June and 13 June. These flares were all fairly weak, ranging from C1.1 – C2.7 GOES classes, and all of them illuminated loops that spanned the full width of active region, as the flare associated with the 13 June CME did. Taking these flares as signs that magnetic reconnection was occurring, it is inferred that the flux rope that erupted on 13 June (and had feet on either side of the active region) was forming throughout this 3-day period.

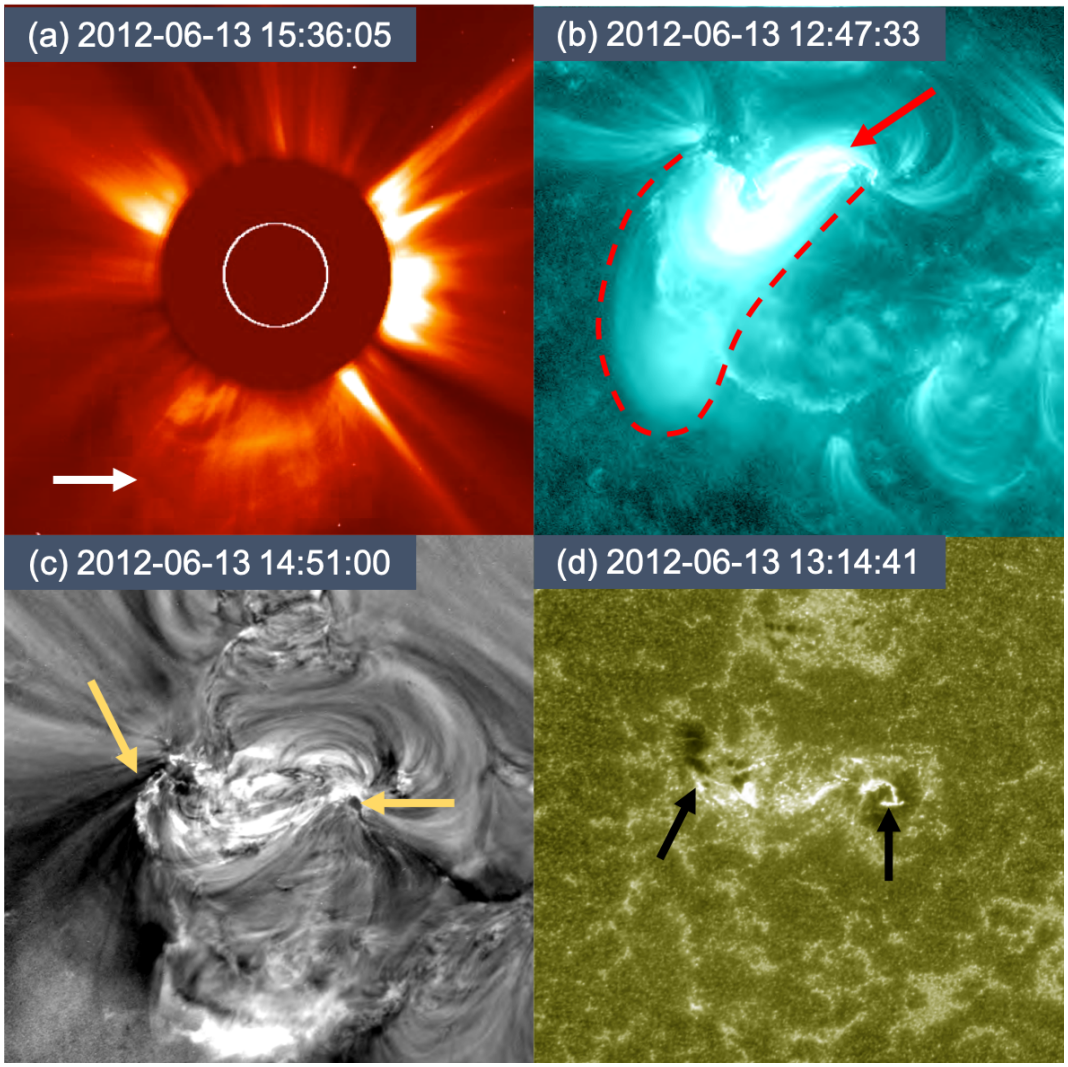

Figure 6.6: Observations of the 13 June 2012 eruption. (a) White-light CME (indicated by the white arrow) observed by LASCO C2. (b) A plasmoid (highlighted by a red dashed line) brightens above a flaring arcade (indicated by a red arrow) in the 131 Å channel of AIA. (c) Twin EUV dimmings (marked by two yellow arrows) seen in base difference 211 Å images. (d) Hooked flare ribbons (indicated by two black arrows) seen in the 1600 Å AIA channel.

After the CME on 13 June 2012, NOAA AR 11504 went on to produce another CME the next day. As described in Chapters 4 and 5, a CME was seen by LASCO C2 on 14 June 2012 at 14:12 UT (Figure 6.7a). To summarise the findings of the previous Chapters, a sigmoid brightened in the active region above an M1.9 flare arcade at least 2 hours before erupting (Figure 6.7b). The sigmoid and its position above the arcade suggests that an HFT flux rope formed in the active region, which is further supported by spectroscopic measurements of coronal plasma and an extrapolated magnetic field model. The middle of the sigmoid was at an altitude of 91 Mm above the footpoints of the flaring loops at 12:24 UT (using the method described in Section 6.3.2). For comparison, the central axis of the extrapolated flux rope in Chapter 5 was 120 Mm above the photosphere at the same time. EUV dimmings and hooked flare ribbons show the footpoint locations of the flux rope during the eruption (Figure 6.7c, and 6.7d).

There were 7 flares in NOAA AR 11504 between the CMEs on 13 June and 14 June. These flares ranged from GOES class C1.2 – C5.0, and all of them illuminated the same region of sheared loops in the centre of the active region that went on to comprise the M1.9 flare associated with the 14 June CME. Therefore, it is inferred that the flux rope that erupted on 14 June was forming throughout this 24-hour period.

6.4.2.2 Photospheric Evolution

NOAA AR 11504 was close to the centre of the solar disc when it erupted on 13 and 14 June. This gives an excellent viewpoint from SDO for examining the corona with minimal projection effects, and for studying the magnetic field in the photosphere from above, since measurements of the vector magnetic field are most accurate at the centre of the Sun.

As detailed in Section 4.3.2, the active region contained two pre-existing sunspots as it entered the solar disc on 8 June. Figure 6.8 shows that the total flux of the active region was increasing throughout the full duration that is studied here, so the active region was undeniably in an emergence phase. The active region showed right-handed magnetic tongues, inferring that the emerging magnetic flux had right-

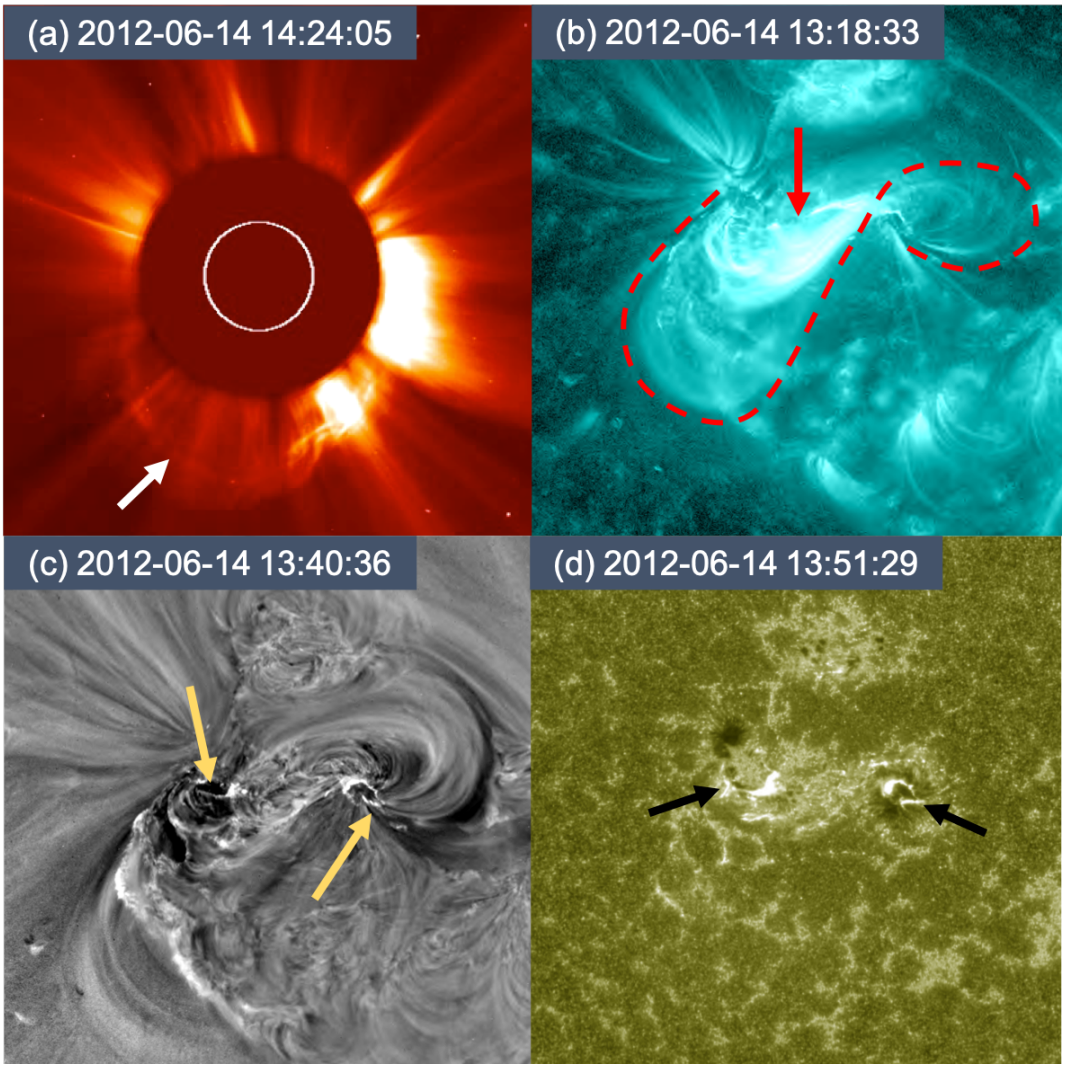

Figure 6.7: Observations of the 14 June 2012 eruption. (a) White-light CME (indicated by the white arrow) observed by LASCO C2. (b) A sigmoid (highlighted by the dashed red line) brightens above a flaring arcade (indicated by the red arrow) in the 131 Å channel of AIA. (c) Twin EUV dimmings (marked by two yellow arrows) seen in base difference 211 Å AIA images. (d) Hooked flare ribbons (indicated by two black arrows) seen in the 1600 Å channel of AIA.

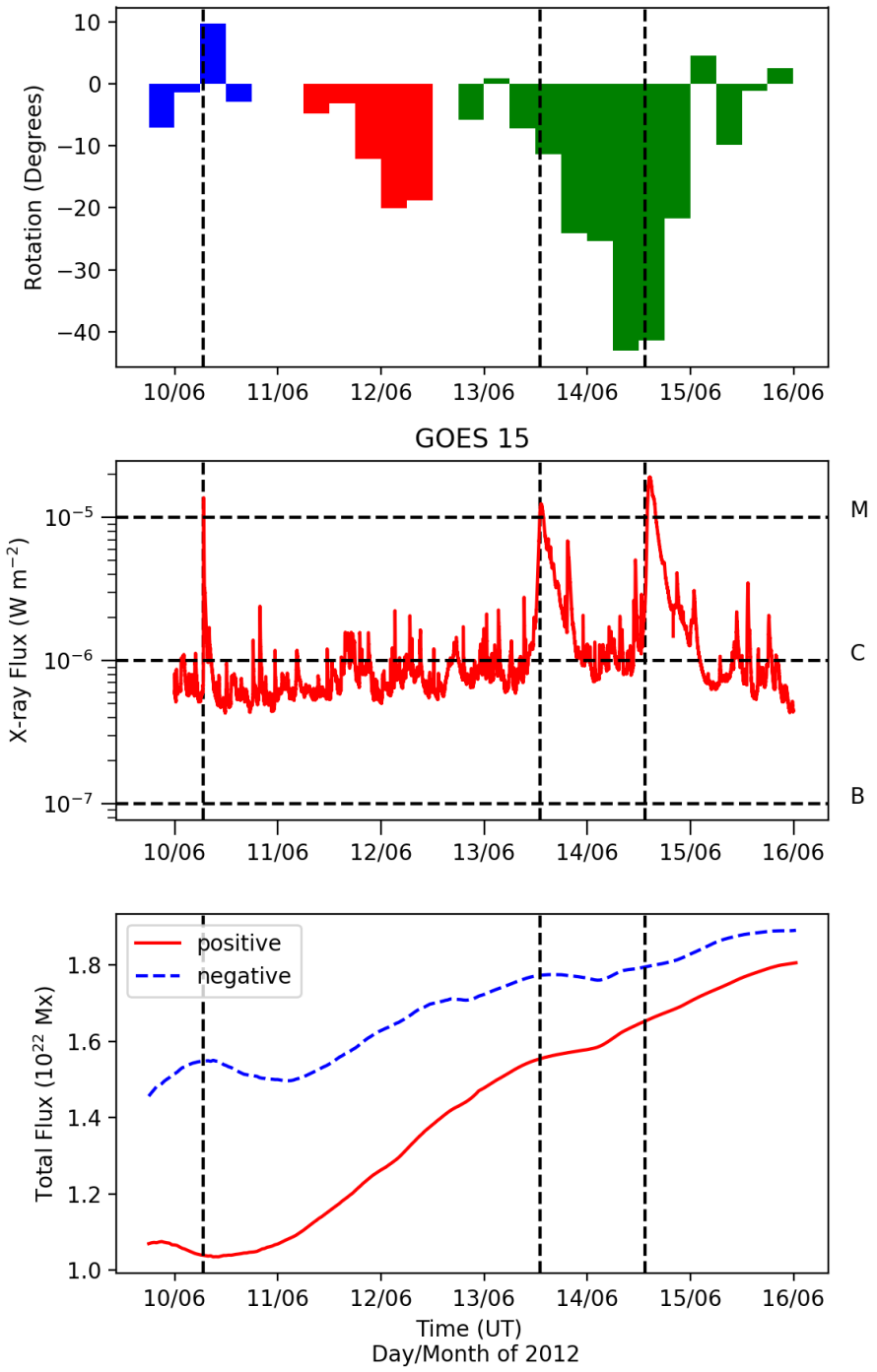

Figure 6.8: Top: The measured orbital motion of chosen magnetic flux fragments in 6-hour intervals. The colours correspond to different choices of fragments (see Figure 6.9). Middle: Full-disc integrated GOES soft X-ray lightcurve. Bottom: The evolution of magnetic flux in NOAA AR 11504, made using the radial magnetic field component, B_r, of the HMI SHARP data series and smoothed with a 24-hour moving average. Vertical dashed lines indicate the times of the CMEs on 10, 13, and 14 June 2012 described in Section 6.4.2.1.

Start Time (UT)	End Time (UT)	Total Orbit (°)	Average Orbit (° day^{-1})
09 June 2012 18:00	10 June 2012 18:00	-1.7	-1.7
11 June 2012 06:00	12 June 2012 12:00	-59.9	-47.12
12 June 2012 18:00	15 June 2012 18:00	-185.6	-61.87

Table 6.3: The orbital motion of three subsequently-emerged umbral flux fragments around the pre-existing leading sunspot in NOAA AR 11504. Positive angles are anti-clockwise and negative angles are clockwise.

handed twist (positive chirality). The magnetic flux emergence occurred in 'episodes' that began on 11 June and continued until 15 June, with distinct fragments of magnetic flux emerging one after the other and moving towards and around the pre-existing sunspots of the same polarities (described in detail in Section 4.3.2). The strongest orbiting was observed in the leading sunspot (see Figure 6.9). Between 11 June 06:00 UT and 12 June 12:00 UT, a fragment of emerged positive magnetic flux moved clockwise around the pre-existing positive sunspot by $\approx 60^{\circ}$ (an average orbital motion of $\approx 47.1^{\circ}$ per day). Then, between 12 June 18:00 UT and 15 June 18:00 UT, another fragment travelled $\approx 186^{\circ}$ around the same, growing sunspot (an average orbital motion of $\approx 61.9^{\circ}$ per day). These quantified orbits are given in Table 6.3 and also represented in the top panel of Figure 6.8. Figure 6.8 shows that the two eruptive M-class flares from the active region occurred during the period of strongest orbiting.

6.4.2.3 Interpretation

The flux rope that erupted on 13 June 2012 at 13:00 UT formed at some time after the eruption on 10 June at 07:00 UT. During this 3.25-day period, the active region was in a phase of emergence (as it had been throughout its disc-passage) with the total unsigned magnetic flux of the region increasing from $\approx 1.3 \times 10^{22}$ Mx to $\approx 1.6 \times 10^{22}$ Mx, and the fragment-tracking method described in Section 6.3.1 measured net clockwise orbiting of 74°.

The flux rope that erupted on 14 June 2012 at 13:30 UT formed at some time after the eruption on 13 June at 13:00 UT. Flux emergence continued during this time, and the fragment-tracking method measured net clockwise orbiting of 145°

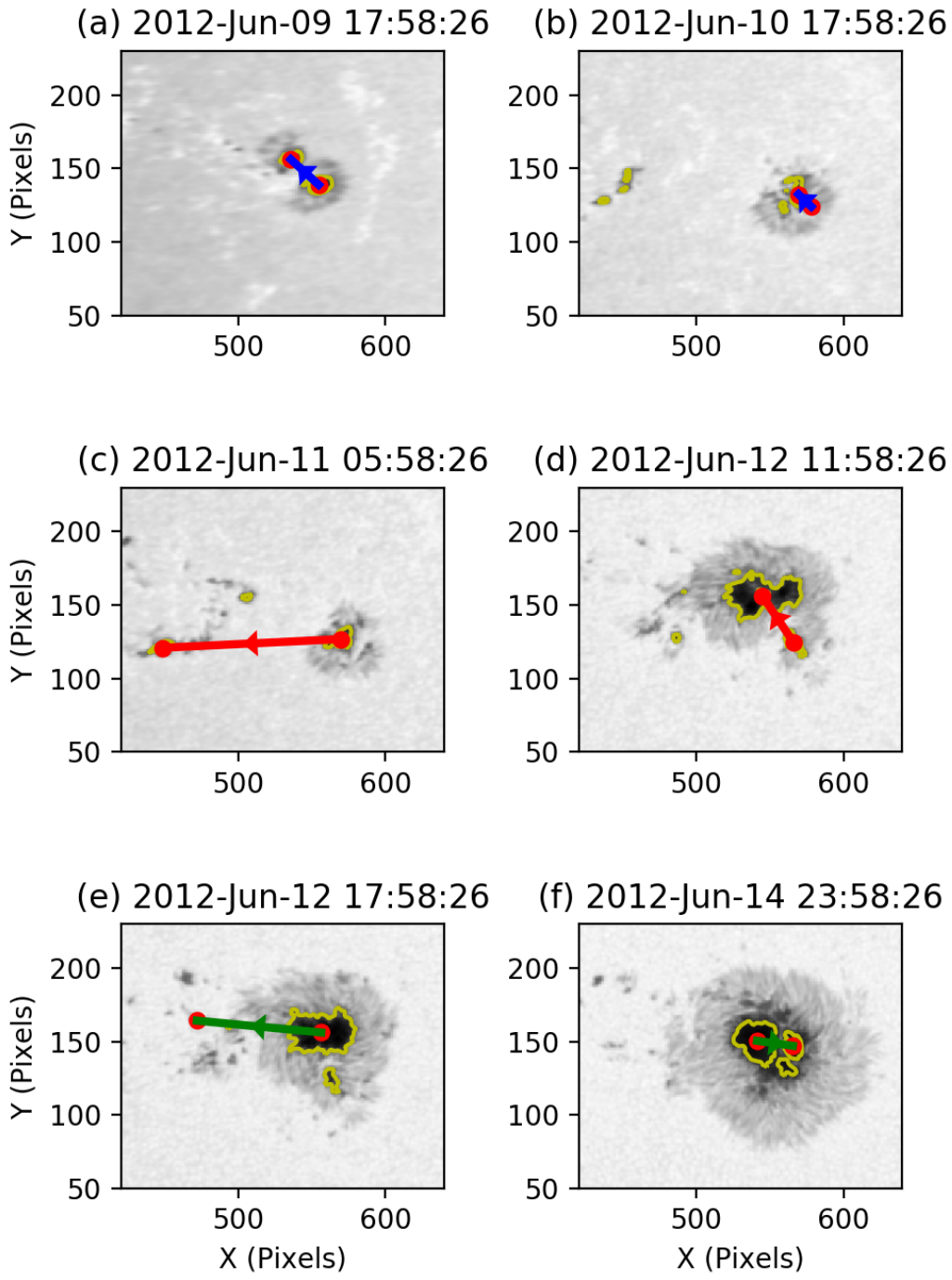

Figure 6.9: The clockwise motion of newly-emerged flux around the pre-existing positive (leading) sunspot in NOAA AR 11504. In each image, vectors are drawn to connect the flux-weighted centroids of two orbiting fragments.

during this 24-hour period.

As the sunspot fragments orbited each other between 10 – 14 June (at an average rate of $\approx 23^{\circ}$ per day), magnetic loops rooted in the fragments were brought together and caused to reconnect with each other in the corona. This reconnection first caused the formation of a flux rope that erupted on 13 June, and further reconnection triggered by the continuing photospheric motions enabled a second flux rope to form that erupted on 14 June. Underlying flare arcades brightened beneath both flux ropes throughout their formation. The times of these major reconnection events can therefore be inferred as the times of the 11 non-eruptive C-class flares that occurred on 10, 12, and 13 June, and the 4 non-eruptive C-flares between the eruptions on 13 and 14 June.

This suggests the first high-altitude flux rope could have formed gradually over 3 days, however, with no major flares observed in the active region on 11 June, formation could have begun with the first flare on 12 June. This gives an upper-limit to the formation timescale of the flux rope of either 1.5 or 3 days. The second flux rope then had less than 24 hours to form, and sigmoid observations suggest it was already present at least 2 hours before it erupted. Therefore, the second flux rope formed much faster than the first. This correlates with the strength of the orbiting motions that were measured in the active region whilst each flux rope formed. Much stronger orbiting was observed in the photosphere during the formation of the second flux rope, which could explain how it formed more quickly than the first, as coronal loops were brought together more rapidly.

6.4.3 8 October 2012

6.4.3.1 Coronal Evolution

A CME erupted from NOAA AR 11585 at $\sim$20:00 UT on 8 October 2012. The eruption is linked to a slow white-light CME seen in STEREO-A coronagraphs: COR1 from 21:15 UT, and COR2 from 23:09 UT (Figure 6.10a). A faint arcade brightened in the active region as the eruption proceeded, but the 1.0 – 8.0 Å X-ray flux measured by GOES did not reach C-class and no flare was registered. Loops that extend from the east and west of the active region appear strongly curved in the

hours before the eruption, but it is difficult to say whether they form a continuous sigmoid across the active region at this time. From 19:30 UT, the curved loops at both ends of the active region begin to expand, giving the sense that there is an expanding sigmoid in the active region (Figure 6.10b), and hot plasma emission is seen near the centre of the active region from 20:19 UT until the eruption, suggesting that a flux rope had formed in the active region. The hot plasma emission was at an altitude of 150 Mm above the centre of the photospheric PIL at 20:39 UT (using the method described in Section 6.3.2) which is consistent with the other HFT flux ropes in this chapter. During the eruption, twin EUV dimmings and hooked flare ribbons develop in the active region, showing that the erupting flux rope had its footpoints in the east and west sides of the region (Figure 6.10c and 6.10d).

No previous CMEs were observed to have originated from NOAA AR 11585 during its passage across the solar disc. Therefore, the entire passage of the region across the disc was analysed to search for the processes that enabled the erupting flux rope to form.

Between 3 October and the eruption on 8 October, there were 7 flares in NOAA AR 11585, ranging from GOES class B3.2 – B5.3. There were 2 flares on 3 October, 3 flares on 6 October, and 2 flares on 7 October. All of these flares occur in the centre of the active region in the same place that the flare arcade later forms during the eruption on 8 October. Therefore, these flares may indicate the times at which the flux rope formed before it erupted on 8 October.

6.4.3.2 Photospheric Evolution

At the time of eruption, the active region was 33° west of central meridian, meaning photospheric magnetic field measurements can be used reliably.

The active region was emerging when it rotated on to the solar disc on 1 October 2012. The leading, positive sunspot had already formed, and a small negative spot briefly coalesced on 2 October before dispersing. The region exhibited left-handed magnetic tongues, implying the emerging flux had left-handed twist (negative chirality). Flux emergence had ceased by 4 October, and the region began to decay (see Figure 6.11).

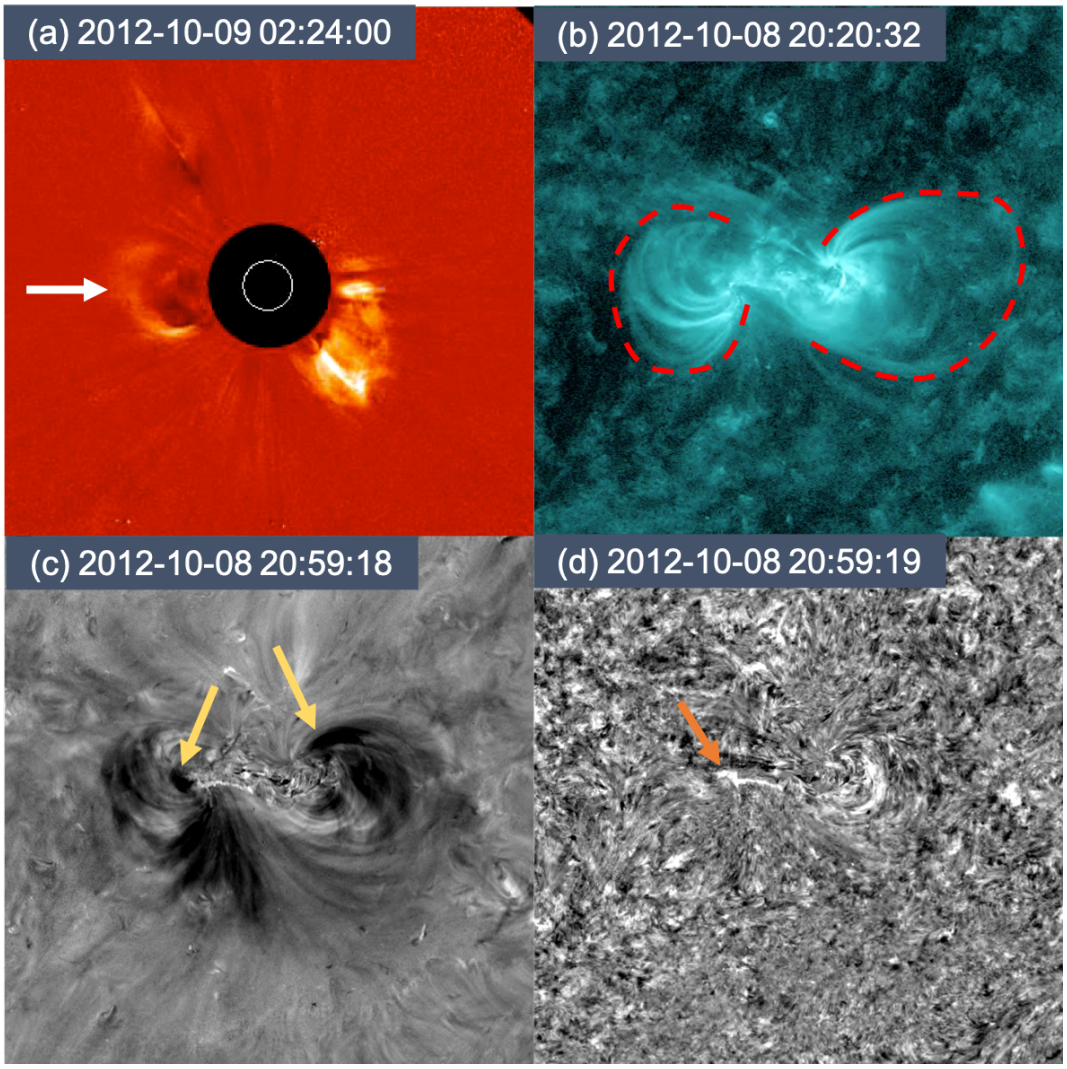

Figure 6.10: Observations of the 8 October 2012 eruption. (a) White-light CME (indicated by the white arrow) observed by STEREO COR2-A. (b) A sigmoid (indicated by the dashed red line) observed in the 131 Å channel of AIA. (c) Twin EUV dimmings (marked by the two yellow arrows) seen in base difference 193 Å images (d) One hooked flare ribbon (indicated by the orange arrow) seen in base difference 304 Å images.

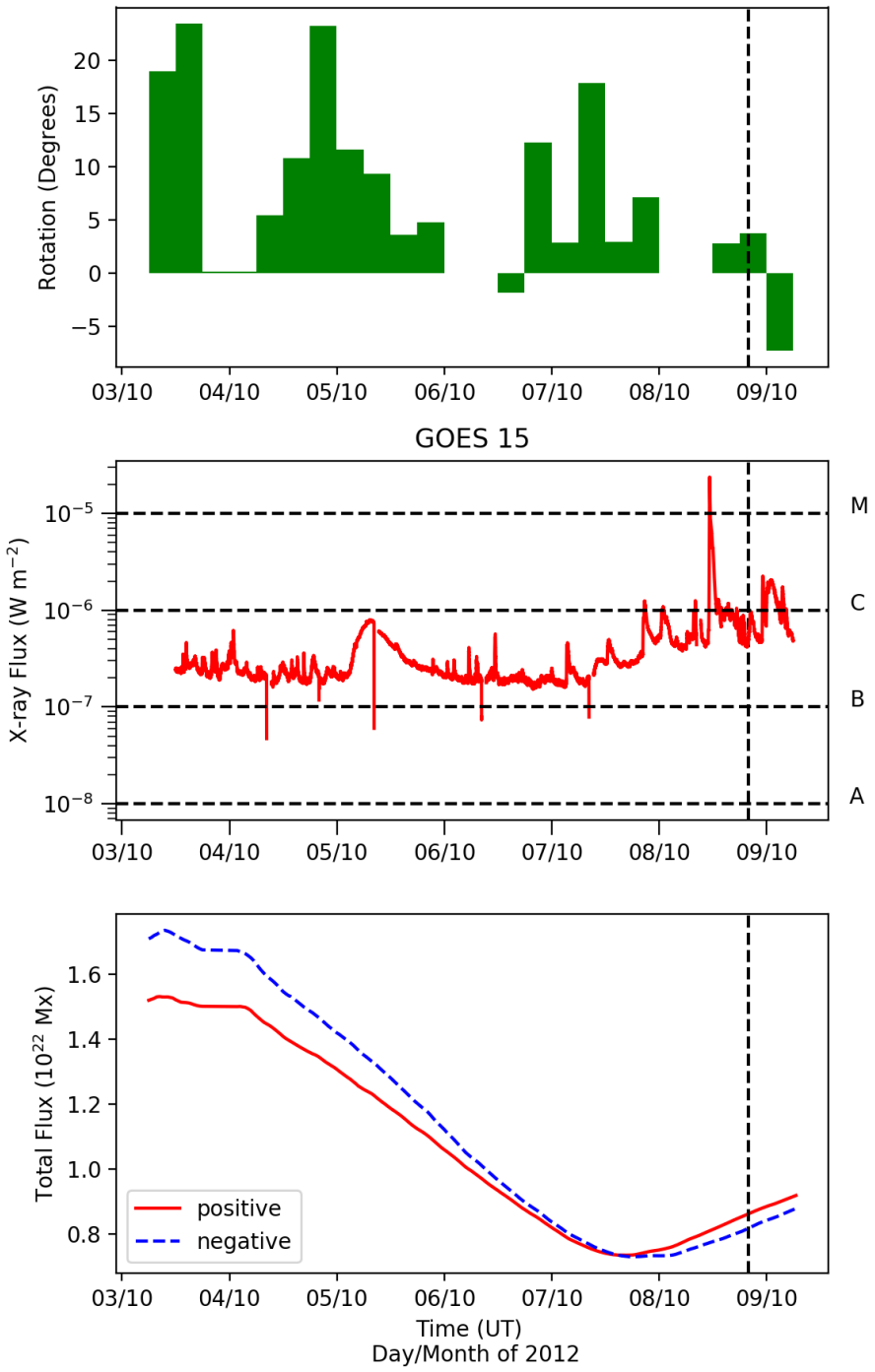

Figure 6.11: Top: The measured orbital rotation of a chosen magnetic flux fragment around another in 6-hour intervals (see Figure 6.12). Middle: Full-disc integrated GOES soft X-ray lightcurve. Bottom: The evolution of magnetic flux in NOAA AR 11585, made using the radial magnetic field component, B_r, of the HMI SHARP data series and smoothed with a 24-hour moving average. The vertical dashed line indicates the time of the CME on 8 October 2012 described in Section 6.4.3.1.

Start Time (UT)	End Time (UT)	Total Orbit (°)	Average Orbit (° day^{-1})
03 October 2012 06:00	06 October 2012 00:00	111.3	40.5
06 October 2012 12:00	08 October 2012 00:00	41.2	27.5
08 October 2012 12:00	09 October 2012 00:00	6.5	13.0

Table 6.4: The orbital motion of umbral flux fragments relative to each other in NOAA AR 11585. Positive angles are anticlockwise and negative angles are clockwise.

The positive sunspot comprised of three subsequently-emerged distinct umbrae that moved around each other within a single penumbra during the week before the eruption (see Figure 6.12). Since the method for quantifying orbiting described in Section 6.3.1 can only follow the motion of one fragment about another, the two fragments that showed the strongest orbiting relative to each other were chosen.

Between 3 October 06:00 UT and 6 October 00:00 UT (2.75 days), the chosen fragment orbited around the other by 111.3° (an average of 40.5° per day). Between 6 October 12:00 UT and 8 October 00:00 UT (1.5 days), the chosen fragment orbited around the other by 41.2° (an average of 27.5° per day). Between 8 October 12:00 UT and 9 October 00:00 UT (0.5 days), the chosen fragment orbited around the other by 6.5° (an average of 13.5° per day). After this time, the three umbrae merged together, making it difficult to discern any further orbiting. These motions are quantified in Table 6.4 and visualised in Figure 6.11 along with the GOES X-ray activity of the Sun during these times.

Between 4 October and midday on 7 October, the total unsigned magnetic flux of the active region decreased from $\approx 1.6 \times 10^{22}$ Mx to $\approx 0.7 \times 10^{22}$ Mx (Figure 6.11). A small magnetic bipole emerged in to the active region on 7 October to the south of the leading sunspot. This led to an increase in the total magnetic flux of the active region until the time of eruption, at which time the total unsigned flux was $\approx 0.9 \times 10^{22}$ Mx.

6.4.3.3 Interpretation

No previous white-light CMEs were identified from NOAA AR 11585 before the flux rope eruption on 8 October 2012 at 20:30 UT. This means no upper-limit can be placed on the timescale of this flux rope's formation. From 3 – 7 October, the active

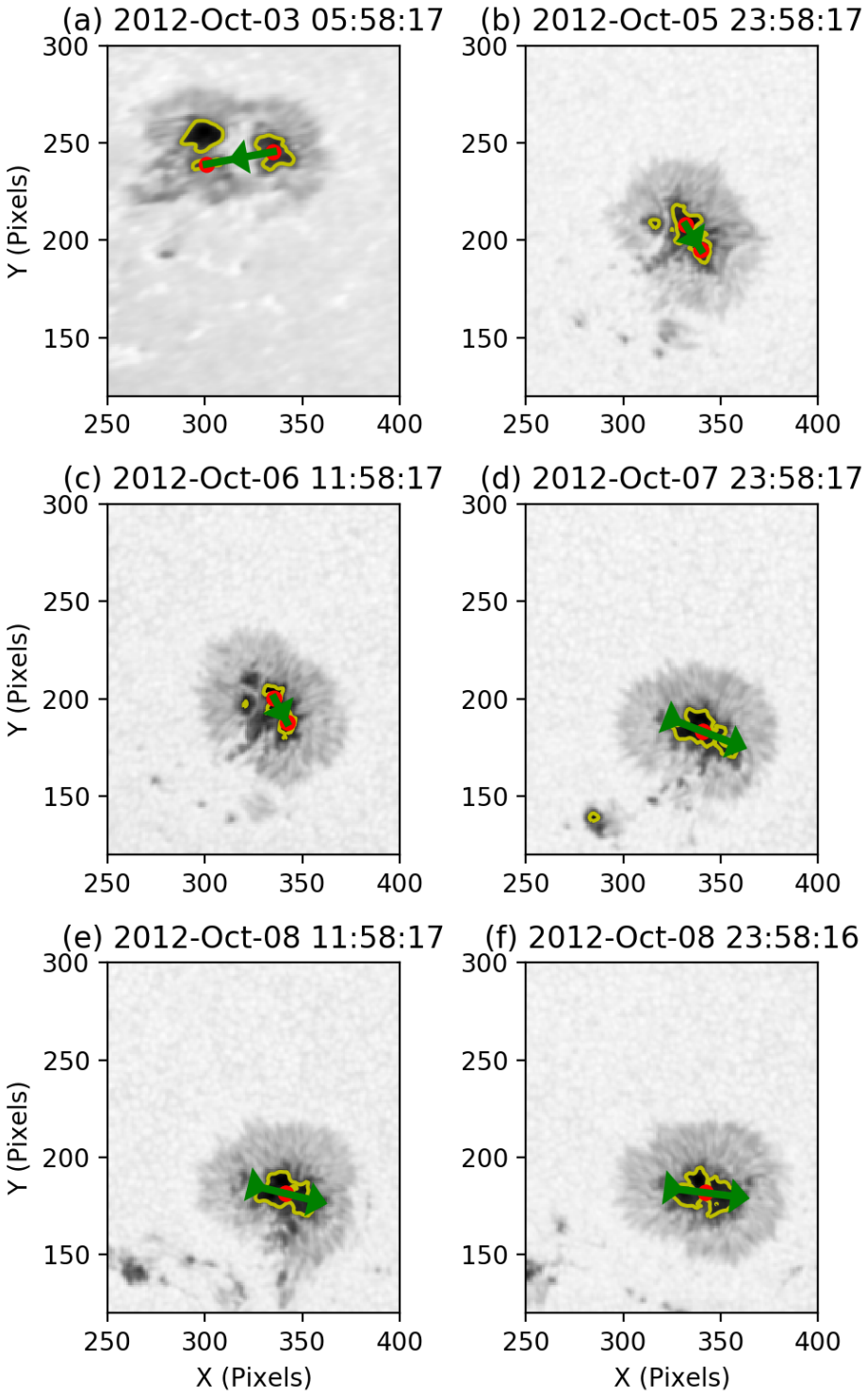

Figure 6.12: The anticlockwise motion of newly-emerged flux around the pre-existing positive (leading) sunspot in NOAA AR 11585. In each image, vectors are drawn either to connect the flux-weighted centroids of two orbiting fragments (panels a-c) or to best-fit the major axis of merged fragments (panels d-f).

region was decaying, but it entered a new phase of emergence from 7 October until past the time of eruption. 159° of anticlockwise orbiting was measured from 3 – 9 October — an average of ≈ 26.5° per day.

Magnetic loops rooted in the orbiting fragments were brought together and reconnected with each other in the corona. This reconnection caused the formation of a flux rope that erupted on 8 October and underlying flare arcades. GOES detected 7 B-class flares in the active region, occurring on 3, 6, and 7 October. This suggests that the flux rope may have been forming on these dates, although there is no upper-limit of the formation timescale since no previous CME is observed.

The orbiting of fragments in this event is weaker in this event than some others, but occurs continuously over a long time. This could explain the lack of flux rope ejections from this active region, because it may have taken a long time to build a flux rope.

6.4.4 14 July 2017

6.4.4.1 Coronal Evolution

On 14 July 2017, a CME erupted from NOAA AR 12665 at ∼ 01:00 UT, accompanied by an M2.4 flare. The corresponding white-light CME is first seen by LASCO C2 at 01:36 UT (Figure 6.13a). The active region appears faintly sigmoidal several hours before the eruption in the 131 Å channel of AIA (Figure 6.13b). A relatively faint flare arcade began to appear beneath the sigmoid from ∼ 00:00 UT, suggesting an HFT flux rope was present in the active region before the CME. The sigmoid began to expand and erupt at 00:30 UT, and the flare arcade brightened and grew in to a cusp shape. At 00:35 UT, the top of the flare arcade was 167 Mm above the photosphere (using the method described in Section 6.3.2). During the eruption, observed twin EUV dimmings and hooked flare ribbons imply that the erupting flux rope has footpoints in the east and west parts of the active region (Figure 6.13c and 6.13d).

It is difficult to confidently identify whether a previous flux rope eruption occurred from NOAA AR 12665 before the 17 July eruption. Multiple white-light CMEs are seen in the LASCO C2 data during the time the active region is on the

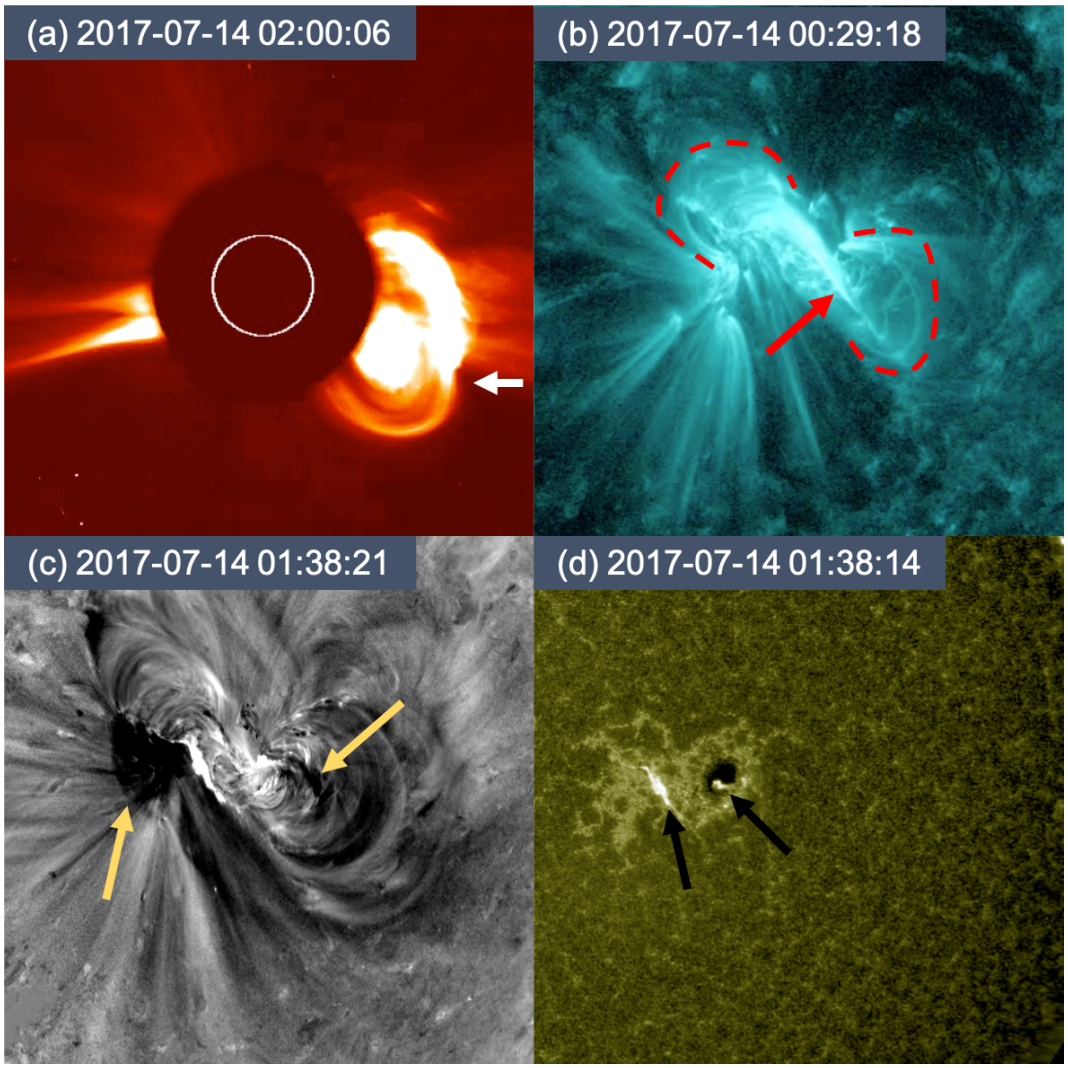

Figure 6.13: Observations of the 14 July 2017 eruption. (a) White-light CME (indicated by the white arrow) observed by LASCO C2. (b) Curved loops (indicated by the dashed red lines) that may belong to a sigmoid above the observed flare arcade (indicated by the red arrow) in the 131 Å channel of AIA. (c) Twin EUV dimmings (marked by the two yellow arrows) seen in base difference 211 Å images. (d) Flare ribbons (indicated by two black arrows) seen in the 1600 Å channel of AIA.

solar disc, but not all of them exhibit a clear three-part structure and some clearly originate from other regions of the Sun. Therefore, the full passage of the active region across the disc before the eruption is used to search for the causes of flux rope formation.

NOAA AR 12665 first rotated on to the solar disc on 5 July 2017 and produced 2 M-class flares, 9 C-class flares, and 48 B-flares between that time and the CME on 17 July 2017 (inclusive). The two largest flares in this period were the M2.4 on 14 July associated with the CME, and an M1.3 flare on 9 July. Notably, 38 of the B-flares occurred before/on 9 July, and 7 of the C-flares occurred on/after 9 July (after the M-flare). To summarise, there were weaker but more frequent flares in the active region until 9 July, and stronger but less-frequent flares from 9 July onwards. By far the most significant flaring occurred on 9 July 2017 (1 M-flare, 4 C-flares, and 16 B-flares), so the flux rope that erupted on 14 July may have undergone a significant portion of its formation on 9 July.

6.4.4.2 Photospheric Evolution

When the CME occurred on 14 July 2017, NOAA AR 12665 was 34° west of central meridian, meaning photospheric magnetic field measurements can be used reliably.

NOAA AR 12665 first rotates on to the east limb of the solar disc viewed by SDO on 5 July 2017. At this time, there are two small pre-existing sunspots; the leading spot is of positive magnetic polarity, and the trailing is negative. The young active region shows left-handed magnetic tongues, meaning that left-handed (negative chirality) magnetic flux is emerging. New magnetic flux is seen to emerge from between the pre-existing sunspots from 6 – 12 July (although the total magnetic flux of the active region is decaying; Figure 6.15). The active region enters a phase of net emergence from 13 – 15 July, and the CME occurs at ≈01:00 on 14 July.

A strong fragment of magnetic flux emerged on 6 July and moved towards the leading sunspot before rotating anticlockwise around the pre-existing sunspot umbra (shown in Figure 6.14). Between 8 July 00:00 UT and 10 July 00:00 UT (2 days), the emerging fragment orbited around the other by 92.0° (an average of 46.0° per day). The strongest orbiting during this period was seen on the evening

Start Time (UT)	End Time (UT)	Total Orbit (°)	Average Orbit (° day^{-1})
08 July 2017 00:00	10 July 2017 00:00	92.0	46.0
10 July 2017 06:00	14 July 2017 00:00	46.5	12.4
14 July 2017 00:00	15 July 2017 00:00	43.2	43.2

Table 6.5: The orbital motion of umbral flux fragments relative to each other in NOAA AR 12665. Positive angles are anticlockwise and negative angles are clockwise.

of 9 July, with the fragments shearing past each other from 18:00 – 00:00 UT for a rotation of 54°. Between 10 July 06:00 UT and 14 July 00:00 UT (3.75 days), the chosen fragment orbited around the other by 46.5° (an average of 12.4° per day). During this time, the umbrae had merged together, making it difficult to discern the full extent of the orbiting. Between 14 July 00:00 UT and 15 July 00:00 UT (1 day), the chosen fragment orbited around the other by 43.2° (an average of 43.2° per day). These values are collected in Table 6.5, and presented in Figure 6.15 with the corresponding X-ray activity measured by GOES.

6.4.4.3 Interpretation

No previous white-light CME were identified from NOAA AR 12665 before the flux rope eruption on 14 July 2017 at 00:30 UT. From 8 – 12 July, the active region was decaying, but it entered a new phase of emergence from 13 July until past the time of eruption. 138° of anticlockwise orbiting was measured from 8 – 14 July — an average of $\approx 20°$ per day.

GOES detected an M-class flare in the active region on 9 July, but no CME was observed. The flux rope that erupted on 14 July may have been forming since this time (or even earlier) as orbiting fragments brought coronal loops together. Magnetic reconnection then occurred in the corona, causing the formation of a high-altitude flux rope.

The average daily orbiting in this active region is weaker than in some events, but since there are no observed prior CMEs from the region, the flux rope may have formed gradually over several days. The main emerging sunspot fragment encountered the pre-existing sunspot on 8 July and showed strong shearing motion clockwise around it throughout 9 July (90° in 24 hours). Most of the strong flares

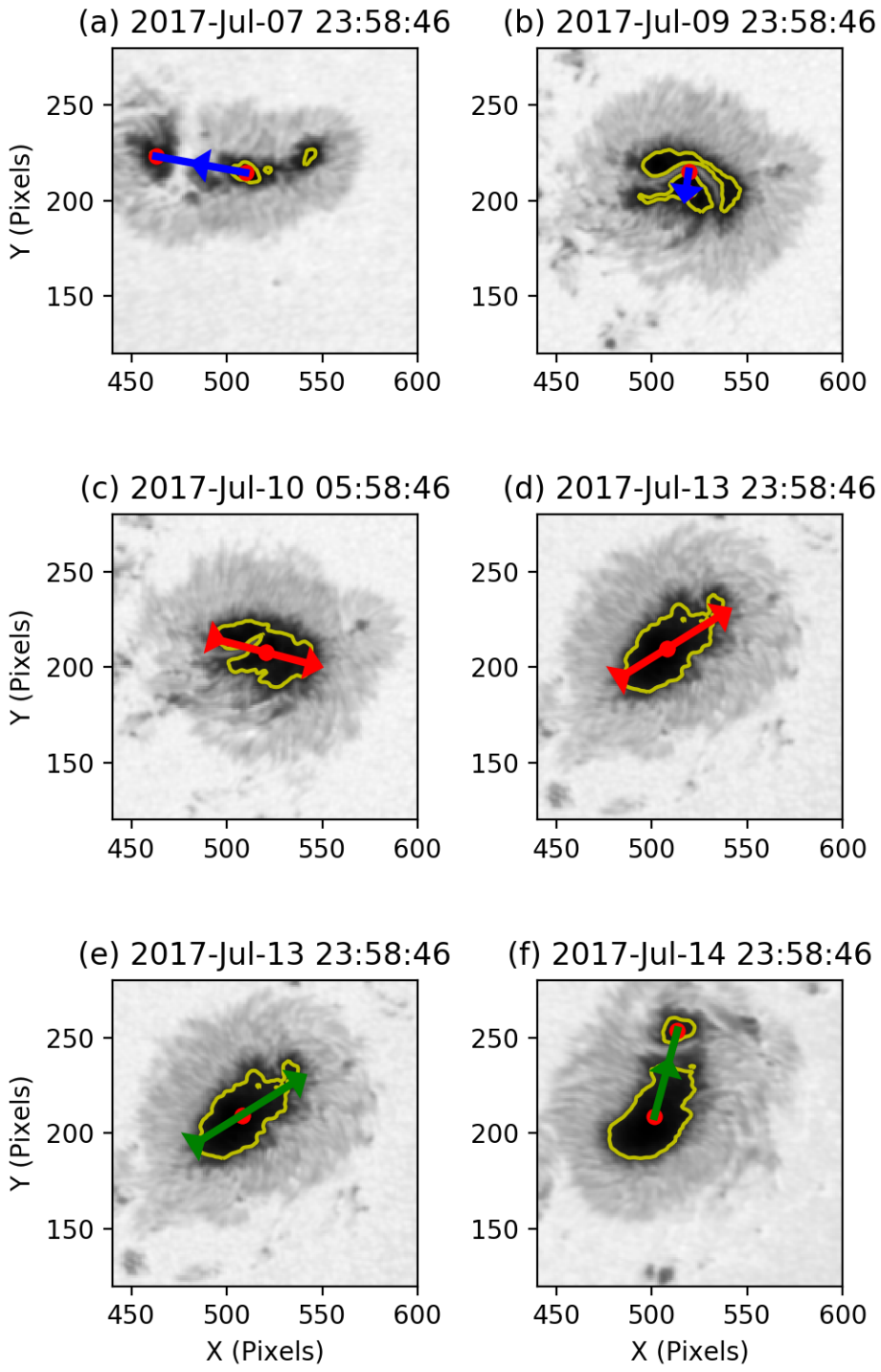

Figure 6.14: The anticlockwise motion of newly-emerged flux around the pre-existing positive (leading) sunspot in NOAA AR 12665. In each image, vectors are drawn either to connect the flux-weighted centroids of two orbiting fragments (panels a, b, and f) or to best-fit the major axis of merged fragments (panels c, d, and e).

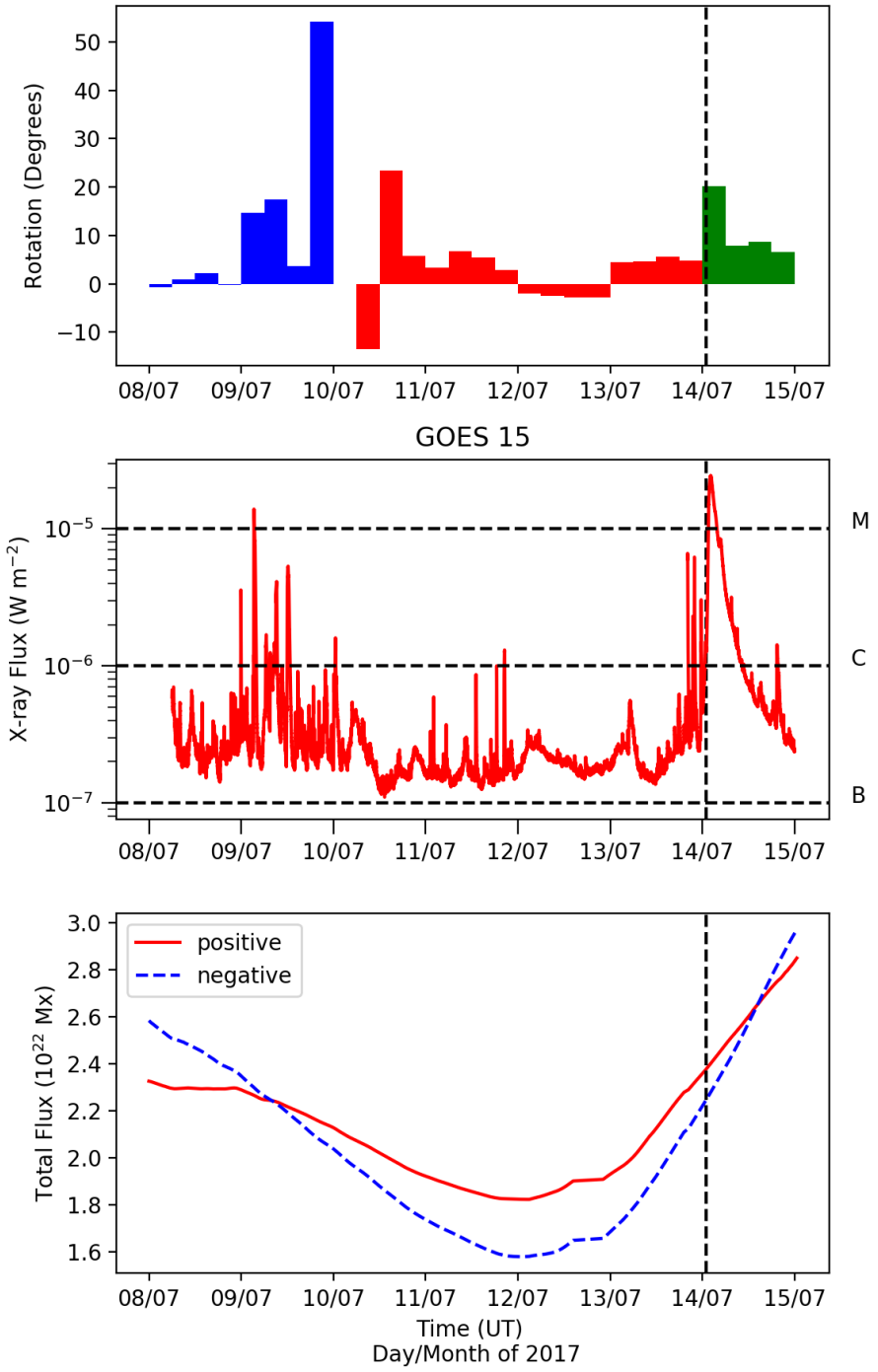

Figure 6.15: Top: The measured orbital motion of chosen magnetic flux fragments in 6-hour intervals. The colours correspond to different choices of fragments (see Figure 6.14). Middle: Full-disc integrated GOES soft X-ray lightcurve. Bottom: The evolution of magnetic flux in NOAA AR 12665, made using the radial magnetic field component, B_r, of the HMI SHARP data series and smoothed with a 24-hour moving average. The vertical dashed line indicates the time of the CME on 14 July 2017 described in Section 6.4.4.1.

from the active region occur during this time, with an M2.4 flare, 4 C-flares, and 16 B-flares. Even if it cannot be said with certainty that a flux rope is forming at this time, there is a clear correlation between strong sunspot shearing orbiting and reconnection in the corona, causing flaring.

6.5 Discussion

CMEs are ultimately the result of a magnetic energy storage and release process that is driven by the emergence of magnetic flux from the solar interior and motions that occur in the photosphere. As introduced in Section 1.3.3.1, there are only two groups of mechanisms that can release energy by 'driving' CMEs: flare reconnection and ideal MHD instabilities. On the other hand, many pre-eruption 'trigger' mechanisms have been identified that cause energy to build up in the solar atmosphere and evolve the coronal magnetic field towards the point where an eruption can occur. One example of a trigger mechanism is magnetic flux cancellation, which can lead to a flux rope forming via magnetic reconnection low down in the solar atmosphere (*e.g.* in the chromosphere). A comprehensive list of identified triggers and drivers with appropriate references can be found in Table 1 of Green et al., 2018.

In this chapter, the hypothesis is tested that a different photospheric process, namely the orbiting motions of emerging magnetic flux, can build a flux rope via reconnection in the corona (see Fig 6.16). This is motivated by the eruption of the flux rope studied in Chapters 4 and 5, which was found to have formed in the corona with an HFT configuration as a consequence of observed orbiting motions in the photosphere before its eruption was driven by the ideal MHD torus instability. The aim of the study in this chapter is to identify additional cases of coronal flux rope formation and investigate the photospheric behaviours that trigger the reconnection in the corona.

In this work, five HFT flux ropes have been identified in four active regions. These five flux ropes erupt as CMEs on 13 March 2012, 13 June 2012, 14 June 2012 (the same event from Chapters 4 and 5), 8 October 2012, and 14 July 2017. In the

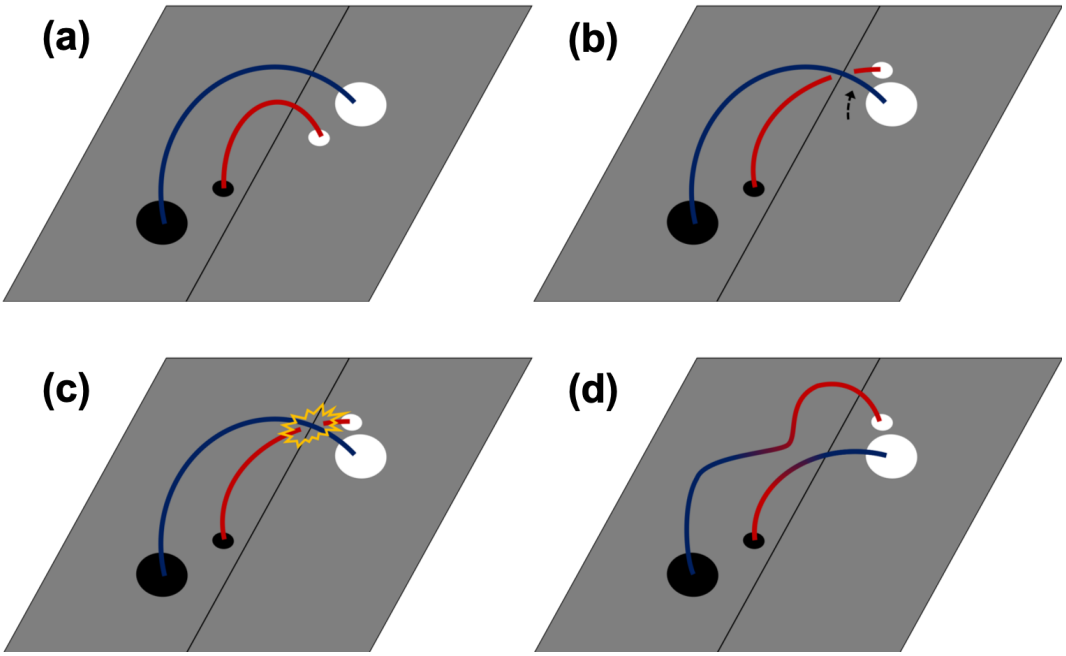

Figure 6.16: Orbiting motions of a magnetic flux fragment around a pre-existing sunspot. (a) A magnetic bipole (red) emerges beneath the pre-existing bipole field of sunspots (blue). (b) A fragment of the emerging flux moves towards and "orbits" around the pre-existing sunspot of the same polarity, wrapping field lines around each other. (c) Component magnetic reconnection occurs in the corona. (d) The products of this reconnection are sheared (twisted) field lines in the form of an overlying flux rope and an underlying arcade.

days before each eruption, magnetic flux emerges in to each source active region and is seen to 'orbit' around previously-emerged sunspots in the photosphere. The observation of this orbiting before each event suggests that the process that forms coronal HFT flux ropes is somewhat systematic, however, since only 5 of the initial 18 candidate eruptions were found to have HFT configurations, these coronal flux ropes appear to be relatively uncommon.

Using EUV images taken before each eruption, the heights of certain flux rope-related structures were estimated. In the 13 June 2012 event, the peak of the observed hot plasma structure was estimated to be 376 Mm above the photosphere, but this is likely to be an overestimate due to significant projection effects. In the cases of the 13 March 2012, 14 June 2012, and 8 October 2012 CMEs, the heights of sigmoids were estimated to be 68 Mm, 91 Mm, and 150 Mm above the photosphere respectively. The peak of the flare arcade in the 14 July 2017 event was likely just

beneath the bottom of the flux rope at the onset of eruption, and had a height of 167 Mm at this time. These estimates are similar to the height of the flux rope modelled in Chapter 5 ($\sim$100 Mm). The estimated heights of the observed structures are in the $\beta < 1$ region of the solar atmosphere (see Figure 1.4), meaning that plasma does not contribute to the stability of these HFT flux ropes in the same way that it would if their underside were line-tied to dense photospheric/chromospheric plasma in a BPSS configuration. In other words, it may be easier for a perturbation to create a current sheet under these HFT flux ropes than in BPSS cases, meaning HFT flux ropes may be less stable to eruption.

The origin of the orbiting motions that form the flux ropes in this chapter is an open and interesting question. Brown et al. (2003) posed two possible explanations for the observed bodily rotation of sunspots, and these may also be relevant for explaining the orbiting motions observed in this chapter. Extending these explanations to the case of orbiting, the first case is that the observed rotation in the photosphere may be caused by one magnetic flux tube being physically moved around another by sub-photospheric flows. Secondly, the orbiting may be an apparent motion caused by the emergence of two flux tubes that are twisted around each other beneath the surface. Building on the work of Brown et al. (2003), Min and Chae (2009) suggest that the case of sunspot rotation they studied was an apparent motion caused by the emergence of twisted flux tube, but were unable to rule out the effect of a torque force from the solar interior. Contrarily, simulations by Sturrock et al. (2015) support the torque scenario for sunspot rotation and rule out the possibility of the rotation being an apparent effect.

To investigate whether the orbiting in this chapter is caused by flux emergence, the evolution of the total unsigned magnetic flux in each active region is studied. The total unsigned flux of one active region (NOAA AR 11504, June 2012) was increasing throughout the full time it was studied, whereas the other three active regions showed phases of decaying magnetic flux followed by new emergence in the lead-up to the CMEs. In all events, the total unsigned flux of each source active region had been increasing for at least 2 days before all five CMEs. However, this

increase in active region flux can not necessarily be linked to the emergence of twisted flux tubes that are causing the orbiting sunspot fragments, because new bipoles are seen to emerge elsewhere in each of the three previously-decaying regions away from the orbiting sunspot fragments. On the other hand, if the apex of a twisted Ω-shaped flux tube has already emerged through the photosphere, no significant increase in magnetic flux would be expected as the mostly-vertical legs continue to emerge. It is therefore difficult to comment on the origin of the observed orbiting motions. The increase in active region flux before each eruption is still an interesting thing to note, as the emerging bipoles may play a role in causing the eruptions (but this is not investigated here).

Regardless of the origin of the orbiting motion of magnetic flux fragments around sunspots, the proposed connection between these motions and the formation of flux ropes in the corona is examined. This requires knowledge of the timescale over which the flux ropes formed. Where possible, upper limits were placed on the formation timescale of each flux rope, determined as the time between the studied flux rope eruptions and the previous eruptions that occurred from the same source active regions. Here, the assumption is made that any flux rope that formed before the previous CME was fully-ejected, meaning the flux ropes studied in this chapter formed purely between eruptions. Previous CMEs occurred roughly 3 days before the 13 March 2012 and 13 June 2012 events, and 1 day before the 14 June 2012 event. For the other two events (8 October 2012 and 14 July 2017), no previous eruptions were observed, so their source regions were studied over the full duration of their disc passage before the studied eruption.

Once these general time intervals were identified during which the five HFT flux ropes likely formed, specific indications of flux rope formation were searched for. The HFT flux ropes studied in this thesis formed via magnetic reconnection with flaring arcades beneath them. By identifying flaring arcades in each active region that form along the same PIL as the eventual CME, the times at which magnetic reconnection occurred (and therefore the times at which the flux ropes could have been built) can be determined. Before the CME that occurred on 13 March at 17:10

UT, homologous C-class flares occurred on 12 March at 22:20 UT and 13 March at 06:55 UT. Taking the time of the first flare in this sequence as the time flux rope formation began, the flux rope was stable for ≈19 hours before erupting. Before the CME on 13 June 2012, multiple C-flares occurred in the same location on 10 and 12 June, giving a formation time of 3.25 days. Then, another CME occurred from the same active region on 14 June, and it has been previously concluded that this flux rope formed at least 2 hours before the eruption, associated with C-class flares (see Chapter 4). There were at least 5 days of B- and C-class flares in NOAA AR 11585 before the 8 October 2012 CME, and no eruptions were observed during this time. This suggests the flux rope may have formed over these 5 days, but since all observational signatures of flaring and eruption in this event are weak, it is important to highlight there is uncertainty in this proposed formation timescale. Finally, strong and frequent flaring occurred in NOAA AR 12665 on 9 July, including an M-class flare with no associated CME, suggesting the flux rope that erupted on 14 July may have begun to form 5 days before erupting. In summary, the timescales between HFT flux rope formation and eruption in this work vary from a couple of hours to five days.

To examine the cause of each flux rope formation, the orbiting motions observed in the photosphere were quantified using the method described in Section 6.3.1. In four of the events, orbital motions ranged from $12-47^{\circ}$ per day between the times the flux ropes were found to have begun forming and the times they erupted. However, before the 14 June 2012 CME, the emerging sunspot fragment orbited the pre-existing sunspot by 100° in one day. This strong orbiting may explain how a flux rope was able to form in NOAA AR 11504 so quickly after the previous CME the day before.

The sense of orbiting appears related to the magnetic helicity sign of the active region field it occurs in. In all of the active regions that emerged with negative helicity (inferred observationally from left-handed magnetic tongues) the emerging flux orbited the pre-existing sunspots in the anti-clockwise direction. Conversely, emerging flux orbited clockwise in the positive-helicity active regions. This con-

nection extends to the chirality of the flux rope that formed in each active region. Left-handed, reverse-S sigmoids formed in the active regions with anticlockwise orbiting, and right-handed forward-S sigmoids formed in the clockwise-orbiting region. Sigmoids are the observational manifestation of magnetic field lines at the periphery of magnetic flux ropes (running beneath them), and therefore the handedness of each sigmoid infers the chirality of the flux rope. The correlation between the chirality of the active regions and the sense of orbiting suggests that the orbiting fragments are part of the same emerging twisted structures as the pre-existing sunspots that they move around. Furthermore, the correlation between the sense of orbiting and the handedness of each flux rope further supports the hypothesis that the orbiting motion of emerging magnetic flux is responsible for triggering the formation of the flux ropes.

6.6 Conclusions

Five HFT flux ropes have been identified in four active regions. The flux ropes formed via magnetic reconnection in the corona at heights $\sim$100 Mm (where it is expected that $\beta < 1$). The reconnection that built the flux ropes occurred in sporadic bursts, as evidenced by solar flares, and by using the timings of these flares, it has been found that the periods these flux ropes were stable for varied from a couple of hours to five days.

In searching for the photospheric process(es) that caused magnetic reconnection to occur in the corona, it was found that all of the active regions exhibit newly-emerged magnetic flux fragments that move towards and then orbit around pre-existing sunspots during the periods of flux rope formation. The studied flux ropes each have one leg rooted in/around the sunspots where the strongest orbiting is observed, and there is consistency between the chirality of the emerging flux, the sense of orbiting, and the chirality of the flux ropes that form (three left-handed sigmoids form in negative chirality active regions that show anticlockwise orbiting and two right-handed sigmoids form in a positive chirality active region that showed clockwise orbiting). Furthermore, the event in which a flux rope formed most quickly

featured the strongest orbiting (100° of motion between the CMEs on 13 and 14 June 2012). Therefore, it is inferred that the orbiting motions of emerging magnetic flux observed in the photosphere are related to the formation of the HFT flux ropes.

It is proposed here that, as the sheared flux tube associated with an orbiting photospheric fragment wraps around pre-existing sunspot field, component magnetic reconnection occurs in the corona. This reconnection forms a magnetic flux rope in the corona in an HFT configuration above a sheared, flaring arcade.

Chapter 7

General Conclusions and Future Work

7.1 Questions and Aims

As established in Section 1.3.3, CMEs can cause a number of space weather effects, such as GICs that (in severe cases) may damage national power networks, and SEPs that may disrupt satellite operations. These effects can be prepared for by allowing for the additional load on electrical networks, by putting satellites into 'safe modes', or by making sure astronauts are safely shielded inside the International Space Station, but all of these actions require time. Long-term forecasting of space weather (for example, forecasting the effects the Sun will have on the near-Earth environment over the next 5 days — as desired by the UK's National Grid; Krausmann et al., 2016), could greatly improve our resilience to the arrival of CMEs and SEP storms. CMEs typically take 1-3 days to reach the Earth at 1 AU, and SEPs can arrive at Earth in minutes, making early warning practically impossible after an eruption has begun. Therefore, in order to be able to produce an effective 5-day forecast of space weather, we need to gain the ability to predict CME occurrence 2-4 days before they happen.

Predicting CMEs first requires an understanding of the mechanisms that cause them, but there is still much debate about what processes may be involved in CME initiation. A wide range of *trigger* mechanisms have been identified that can form

and evolve pre-eruptive structures, and there are two main candidates for *driver* processes by which stability is lost and CMEs are accelerated away from the Sun (see Section 1.3.3.1). Furthermore, deducing which of these mechanisms are relevant to CME initiation depends on the structure of the corona before the onset of eruption, *e.g.* whether a magnetic flux rope forms before or after the onset of eruption. Much of the difficulty in discerning the magnetic structure of the corona before eruptions stems from the present inability to make measurements of the full 3-D magnetic field vector in the corona.

With the open questions raised above in mind, the aims of this thesis are:

- to examine the structure of the corona before CMEs and determine whether magnetic flux ropes form before the onset of eruption;
- to identify triggering processes that are responsible for the formation of pre-eruptive coronal structures;
- to quantify the timescales over which pre-eruptive evolution occurs and discern observational signatures; and
- to determine the mechanisms that drive the eruptions of CMEs.

7.2 Conclusions

In Chapter 4, the pre-eruptive coronal configuration of an active region that produced an interplanetary CME with a clear magnetic flux rope structure at 1 AU is studied. A forward-S sigmoid appears in EUV data two hours before the onset of the eruption, which is interpreted as a signature of a right-handed flux rope that formed prior to the eruption. A flaring arcade formed beneath the brightening sigmoid/flux rope, suggesting the system had an HFT configuration and that the reconnection that formed the flux rope (and arcade) occurred in the corona. Composition analysis suggests that the flux rope had a coronal plasma composition, supporting the interpretation that the flux rope formed via magnetic reconnection in the corona. Flare ribbons and EUV dimmings are used to infer the locations of

the flux rope footpoints. These locations, together with observations of the global magnetic flux distribution, indicate that an interaction between newly emerged magnetic flux and pre-existing sunspot field in the days prior to the eruption may have enabled the coronal flux rope to form via reconnection in the corona. Once formed, the flux rope remained stable for two hours before erupting as a CME. The effective rotational motion of magnetic flux around the sunspots may have inflated and weakened overlying magnetic field, enabling the onset of the torus instability to drive the CME.

In Chapter 5, the coronal magnetic field of the active region studied in Chapter 4 is modelled one hour prior to the eruption using an NLFFF extrapolation. A flux rope is found that remarkably matches the many observational conclusions from Chapter 4, confirming that a flux rope formed before the onset of the CME. The height of the modelled flux rope is also exceptional, with its highest point reaching 150 Mm above the photosphere. To examine whether the eruption of the flux rope could have been triggered by the kink instability, the twist of the flux rope was quantified. Due to the strongly asymmetric nature of the extrapolated flux rope, three choices of axis were used to make three estimations of its average twist, ranging from 1.35 – 1.88 turns. These twist values are in the range of the critical twist required for the onset of the kink instability, but since the erupting structure described in Chapter 4 was not observed to kink, it is concluded that the trigger of the eruption was not the kink instability. The decay index near the apex of the axis of the extrapolated flux rope is comparable to typical critical values required for the onset of the torus instability, supporting the conclusion from Chapter 4 that the eruption was driven by the torus instability.

In Chapter 6, the single-event studies of Chapters 4 and 5 are extended by identifying four more cases of coronal flux rope formation. Each of these events shows similar photospheric motions to those described in Chapter 4, with emerging magnetic flux moving towards and then "orbiting" around pre-existing sunspots in their host active regions. The times at which the flux ropes begin (and continue) to form are determined using observations of solar flares as indications that mag-

netic reconnection is occurring in the corona. In the sample studied, the flux rope formation timescales were found to range from a couple of hours to five days. The difference in formation times appears to be related to the strength of the orbiting motions observed in the photosphere, with flux ropes forming most-quickly in the active regions that show the fastest motions, and vice versa. Additional evidence that the photospheric orbiting motions are connected to the formation of the flux ropes is that there is consistency between the handedness of twist of emerging magnetic flux in the active regions, the sense of the orbiting motions, and the chirality of the flux ropes that form. For example, three left-handed sigmoids (and therefore flux ropes) were found to form in negative-chirality active regions that exhibit anti-clockwise orbiting, and two right-handed sigmoids (flux ropes) formed in positve-chirality active regions that show clockwise orbiting motions.

The work contained in this thesis has provided new insight towards each of the questions it aimed to study. The ways in which the four specific questions listed in Section 7.1 have been addressed are summarised next.

In examining the pre-eruptive magnetic structure of the corona, five cases of flux ropes have been identified that formed before the onset of CMEs. Furthermore, these five flux ropes all formed at relatively high altitudes, $\sim$100 Mm above the photosphere. This is interesting because their HFT configurations suggest they formed via magnetic reconnection in the corona, whereas many flux ropes that have been studied before formed in BPSS configurations via reconnection in the photosphere/chromosphere. Previously-studied HFT flux ropes have generally been identified above the solar limb, where they are easier to discern away from the bright solar disc. This has meant that, until now, the photospheric processes responsible for triggering the formation of these flux ropes in the corona have not been studied. Since the flux ropes studied in this thesis all form and erupt when on the solar disc, the photospheric evolution that caused their formation could be studied.

By inspecting the evolution of the photosphere beneath the forming flux ropes in this thesis, systematic motions have been identified that triggered the flux rope formation. Emerging magnetic flux was seen to move towards and then orbit around

previously-emerged flux during the times when the flux ropes were forming. It is hypothesised that the observed orbiting motions in the photosphere show that magnetic flux tubes are wrapped around each other in the corona, which leads to magnetic reconnection and the formation of a twisted magnetic field structure (flux rope) above a flaring arcade (see Figure 6.16). These orbiting motions of emerging magnetic flux represent a new trigger mechanism by which flux ropes form, adding another trigger to the list of previously-identified processes given in Table 1 of Green et al. (2018).

The timescales of flux rope formation studied in this thesis range from a couple of hours to five days. Observational signatures that suggest a pre-eruptive flux rope may form in the corona include magnetic flux emergence, the relative orbiting motion between emerging photospheric flux fragments, and the appearance of hot ($\sim 10^7$ K) plasma structures such as sigmoids and plasmoids above flaring arcades. The expansion of active region magnetic field in the lead-up to an eruption was also evidenced by radio data.

Using a combination of observations and modelling, it was concluded that the eruption of the flux rope studied in Chapters 4 and 5 was driven by the torus instability. Furthermore, due to the similarities between this event and the other four studied in Chapter 6 (both in their heights in the corona and the observed photospheric motions beneath them), it is plausible that all of the eruptions studied in this thesis may have been driven by the torus instability, However, further modelling work is required to substantiate this claim.

7.3 Future Work

A natural extension of the work contained in this thesis is to produce models of the four flux ropes from Chapter 6 that were not already modelled in Chapter 5. NLFFF models of each event would give additional support to the observational conclusions that stable flux ropes formed in HFT configurations in the corona before the onset of each eruption. Then, in the same way as in Chapter 5, the decay index can be approximated for each event using potential field models to give insight in to

whether the eruptions could have been driven by the torus instability.

Another way to probe the stability of the flux ropes is to use the NLFFF extrapolations as initial states for time-dependent MHD modelling. By evolving the photospheric boundary of extrapolated flux ropes through time, the eruptions of the flux ropes can be simulated. Furthermore, magnetic flux emergence simulations could be used to test the hypothesis given in Chapter 6 that the observed orbiting motions of magnetic flux are the photospheric manifestation of the emergence of magnetic flux tubes that are wrapped around each other beneath the solar surface.

More information can be obtained from the 14 June 2012 CME by further comparing the properties of the pre-eruptive NLFFF flux rope model to the associated magnetic cloud that was measured *in situ*. In Chapter 4, it was noted that the flux rope orientation inferred by pre-eruption observations matched the one measured *in situ* (this result was obtained in collaboration with Palmerio et al., 2017), but this is not always the case (*e.g.* Palmerio et al., 2018), and other properties of the flux rope may also change as it travels through the corona and heliosphere. Understanding the evolution of a flux rope between its pre-eruptive state and its arrival at 1 AU is hugely valuable for forecasting the effects a CME may cause. One avenue for investigation would be to compare the magnetic flux content between the pre-eruption modelled flux rope and the measured magnetic cloud. Magnetic reconnection can occur beneath erupting flux ropes, as evidenced by CME-associated solar flares, implying that magnetic flux may be built in to a flux rope as it erupts. This reconnected flux could explain any discrepancy between the values modelled before eruption and measured *in situ*, and an estimate of the reconnected flux can be quantified by examining the photospheric flux that is 'swept over' by expanding flare ribbons (*e.g.* Fletcher and Hudson, 2001).

One of the motivations behind the studies in this thesis was to work towards the goal of producing accurate, long-term space weather forecasts. As a next step in this direction, it would be an interesting exercise to systematically apply the observational and modelling techniques used in this thesis to CME prediction. NLFFF extrapolations are computationally-expensive (taking days to produce), and are thus

not yet viable for near real-time application to finding pre-eruptive flux ropes in solar active regions. However, the formation and altitudes of flux ropes can be inferred by identifying signatures such as magnetic flux cancellation, magnetic flux emergence, and orbiting motions in routinely-available photospheric observations. Furthermore, computationally-inexpensive potential field extrapolations (that can be performed in a few minutes) can be used to approximate the height above an active region PIL where the decay index becomes critical, and therefore the height at which the successful eruption of a flux rope can be driven by the torus instability. Idealised numerical simulations have shown that the decay index increases more rapidly with height above more complex photospheric flux distributions, *e.g.* in quadrupolar active regions rather than simple bipoles (Török and Kliem, 2007). In future work, I will use a sample of $\approx$50 real-Sun active regions of varying magnetic complexities to test whether the combination of photospheric observations and potential field modelling can effectively predict whether CMEs will occur from active regions. By inferring whether a high-altitude (HFT) or low-altitude (BPSS) flux rope may be forming in an active region, and determining whether the decay index becomes critical at a relatively high or low altitude above that active region, it may be possible to predict whether an eruption could be successfully triggered and driven from that active region.

In addition to space weather forecasting applications, CME prediction is also crucial for the upcoming *Solar Orbiter* mission. Scheduled for launch in 2020, the nominal mission phase of *Solar Orbiter* is set to begin by the end of 2021, and a major objective of the mission is to investigate how solar transients, such as flares and CMEs, drive heliospheric variability. *Solar Orbiter* will not provide continuous observations of the Sun, but rather it will take remote sensing observations during planned 90-day windows throughout each of its orbits. Furthermore, some of *Solar Orbiter's* remote sensing instruments have limited fields-of-view that observe on active region scales. Therefore, to collect the data necessary to address the objectives of *Solar Orbiter*, observation planners will need to be able to recognise likely sites of eruptive activity on the Sun so they can choose when and where to make ob-

servations. My work on using observations and modelling to identify the signs that given active regions may be able to produce eruptions will therefore aid with target selection, allowing the remote sensing windows of *Solar Orbiter* to be utilised efficiently.

Solar Orbiter will provide valuable data that will expand our knowledge of CMEs. By making *in situ* measurements of CMEs as close as 0.3 AU from the Sun, there will be greater opportunities to study the connection between observed pre-eruptive flux ropes and magnetic clouds. Other future missions that will provide opportunities to extend the research of this thesis are the ground-based Daniel K. Inouye Solar Telescope (DKIST) and European Solar Telescope (EST). Scheduled for first light in 2019 and 2026 respectively, DKIST and EST will use mirrors that are > 4 m in diameter to make observations of the photosphere and chromosphere at exceptionally-high spatial resolutions. These telescopes will also provide measurements of the full Stokes polarisation state in the chromosphere and corona for the first time, which can in principle be inverted to provide magnetic field vectors. Accurate, high-resolution maps of the vector magnetic field at the top of the chromosphere are expected to provide boundary conditions for NLFFF extrapolations that are far more compatible with the force-free assumption than photospheric magnetograms. Therefore, to extend the work of this thesis, these chromospheric and coronal magnetic field vector measurements could be used as boundary conditions for magnetic field extrapolations, improving the accuracy of coronal magnetic field models.

Appendix A

Vector Identities and Constants

Vector Dot Gradient

$$\mathbf{A} \cdot \nabla \psi = \nabla \cdot (\psi \mathbf{A}) - \psi \nabla \cdot \mathbf{A} \tag{A.1}$$

The Divergence Theorem

$$\int_V (\nabla \cdot \mathbf{F}) \, \mathrm{d}V = \int_S (\mathbf{F} \cdot \mathbf{n}) \, \mathrm{d}S \tag{A.2}$$

Divergence of Curl

$$\nabla \cdot (\nabla \times \mathbf{B}) = 0 \tag{A.3}$$

Physical Constants

$k_B = 1.38 \times 10^{-23}$ J K^{-1}

$\varepsilon_0 = 8.85 \times 10^{-12}$ F m^{-1}

$\mu_0 = 4\pi \times 10^{-7}$ H m^{-1}

$m_p = 1.67 \times 10^{-27}$ kg

$m_e = 9.11 \times 10^{-31}$ kg

$e = 1.6 \times 10^{-19}$ C

$c = 3 \times 10^{8}$ m s^{-1}

Bibliography

D. J. Acheson. Instability by Magnetic Buoyancy. *Solar Phys.*, 62:23–50, May 1979. doi: 10.1007/BF00150129.

V. Alexiades, G. Amiez, and P.-A. Gremaud. Super-time-stepping acceleration of explicit schemes for parabolic problems. *Communications in Numerical Methods in Engineering*, 12(1):31–42, 1996. doi: 10.1002/(SICI)1099-0887(199601)12:1⟨31::AID-CNM950⟩3.0.CO;2-5.

H. Alfvén. On the Existence of Electromagnetic-Hydrodynamic Waves. *Arkiv for Matematik, Astronomi och Fysik*, 29B:1–7, Jan. 1943.

C. E. Alissandrakis. On the computation of constant alpha force-free magnetic field. *Astron. Astrophys.*, 100:197–200, July 1981.

T. Amari, J. F. Luciani, J. J. Aly, and M. Tagger. Plasmoid formation in a single sheared arcade and application to coronal mass ejections. *Astron. Astrophys.*, 306:913, Feb. 1996.

S. K. Antiochos, C. R. DeVore, and J. A. Klimchuk. A Model for Solar Coronal Mass Ejections. *Astrophys. J.*, 510:485–493, Jan. 1999. doi: 10.1086/306563.

V. Archontis and A. W. Hood. Flux emergence and coronal eruption. *Astron. Astrophys.*, 514:A56, May 2010. doi: 10.1051/0004-6361/200913502.

V. Archontis, F. Moreno-Insertis, K. Galsgaard, A. Hood, and E. O'Shea. Emergence of magnetic flux from the convection zone into the corona. *Astron. Astrophys.*, 426:1047–1063, Nov 2004. doi: 10.1051/0004-6361:20035934.

G. Aulanier, T. Török, P. Démoulin, and E. E. DeLuca. Formation of Torus-Unstable Flux Ropes and Electric Currents in Erupting Sigmoids. *Astrophys. J.*, 708:314–333, Jan. 2010. doi: 10.1088/0004-637X/708/1/314.

H. M. Bain, S. Krucker, P. Saint-Hilaire, and C. L. Raftery. Radio Imaging of a Type IVM Radio Burst on the 14th of August 2010. *Astrophys. J.*, 782:43, Feb. 2014. doi: 10.1088/0004-637X/782/1/43.

D. Baker, D. H. Brooks, P. Démoulin, L. van Driel-Gesztelyi, L. M. Green, K. Steed, and J. Carlyle. Plasma Composition in a Sigmoidal Anemone Active Region. *Astrophys. J.*, 778:69, Nov. 2013. doi: 10.1088/0004-637X/778/1/69.

D. Baker, D. H. Brooks, P. Démoulin, S. L. Yardley, L. van Driel-Gesztelyi, D. M. Long, and L. M. Green. FIP Bias Evolution in a Decaying Active Region. *Astrophys. J.*, 802:104, Apr. 2015. doi: 10.1088/0004-637X/802/2/104.

G. Bateman. *MHD instabilities*. MIT Press, 1978.

M. A. Berger and G. B. Field. The topological properties of magnetic helicity. *Journal of Fluid Mechanics*, 147:133–148, Oct. 1984. doi: 10.1017/S0022112084002019.

M. G. Bobra, X. Sun, J. T. Hoeksema, M. Turmon, Y. Liu, K. Hayashi, G. Barnes, and K. D. Leka. The Helioseismic and Magnetic Imager (HMI) Vector Magnetic Field Pipeline: SHARPs - Space-Weather HMI Active Region Patches. *Solar Phys.*, 289:3549–3578, Sept. 2014. doi: 10.1007/s11207-014-0529-3.

P. Boerner, C. Edwards, J. Lemen, A. Rausch, C. Schrijver, R. Shine, L. Shing, R. Stern, T. Tarbell, C. J. Wolfson, et al. Initial calibration of the Atmospheric Imaging Assembly (AIA) on the Solar Dynamics Observatory (SDO). *Solar Physics*, 275(1-2):41–66, 2012.

A. Bonanno and H. E. Fröhlich. A Bayesian estimation of the helioseismic solar age. *Astron. Astrophys.*, 580, Aug. 2015. doi: 10.1051/0004-6361/201526419.

J. Borrero, S. Tomczyk, M. Kubo, H. Socas-Navarro, J. Schou, S. Couvidat, and R. Bogart. VFISV: Very Fast Inversion of the Stokes Vector for the Helioseismic and Magnetic Imager. *Solar Physics*, 273(1):267–293, 2011.

D. H. Brooks and H. P. Warren. Establishing a Connection Between Active Region Outflows and the Solar Wind: Abundance Measurements with EIS/Hinode. *Astrophys. J. Lett.*, 727:L13, Jan. 2011. doi: 10.1088/2041-8205/727/1/L13.

D. H. Brooks and H. P. Warren. The Coronal Source of Extreme-ultraviolet Line Profile Asymmetries in Solar Active Region Outflows. *Astrophys. J. Lett.*, 760: L5, Nov. 2012. doi: 10.1088/2041-8205/760/1/L5.

D. H. Brooks, I. Ugarte-Urra, and H. P. Warren. Full-Sun observations for identifying the source of the slow solar wind. *Nat. Commun.*, 6:5947, Jan. 2015. doi: 10.1038/ncomms6947.

D. S. Brown, R. W. Nightingale, D. Alexander, C. J. Schrijver, T. R. Metcalf, R. A. Shine, A. M. Title, and C. J. Wolfson. Observations of Rotating Sunspots from TRACE. *Solar Phys.*, 216:79–108, Sept. 2003. doi: 10.1023/A:1026138413791.

G. E. Brueckner, R. A. Howard, M. J. Koomen, C. M. Korendyke, D. J. Michels, J. D. Moses, D. G. Socker, K. P. Dere, P. L. Lamy, A. Llebaria, M. V. Bout, R. Schwenn, G. M. Simnett, D. K. Bedford, and C. J. Eyles. The Large Angle Spectroscopic Coronagraph (LASCO). *Solar Phys.*, 162:357–402, Dec. 1995. doi: 10.1007/BF00733434.

L. Burlaga, E. Sittler, F. Mariani, and R. Schwenn. Magnetic loop behind an interplanetary shock - Voyager, Helios, and IMP 8 observations. *J. Geophys. Res.*, 86:6673–6684, Aug. 1981. doi: 10.1029/JA086iA08p06673.

H. V. Cane and I. G. Richardson. Interplanetary coronal mass ejections in the near-Earth solar wind during 1996-2002. *J. Geophys. Res.*, 108:1156, Apr. 2003. doi: 10.1029/2002JA009817.

R. C. Canfield, H. S. Hudson, and D. E. McKenzie. Sigmoidal morphology and eruptive solar activity. *Geophysical Research Letters*, 26:627–630, Jan 1999. doi: 10.1029/1999GL900105.

H. Carmichael. *A Process for Flares*, page 451. NASA Special Publication, 1964.

R. C. Carrington. On the Distribution of the Solar Spots in Latitudes since the Beginning of the Year 1854, with a Map. *Mon. Not. Roy. Astron. Soc.*, 19:1–3, Nov. 1858. doi: 10.1093/mnras/19.1.1.

X. Cheng, J. Zhang, Y. Liu, and M. D. Ding. Observing Flux Rope Formation During the Impulsive Phase of a Solar Eruption. *Astrophys. J. Lett.*, 732:L25, May 2011. doi: 10.1088/2041-8205/732/2/L25.

X. Cheng, J. Zhang, S. H. Saar, and M. D. Ding. Differential Emission Measure Analysis of Multiple Structural Components of Coronal Mass Ejections in the Inner Corona. *Astrophys. J.*, 761:62, Dec. 2012. doi: 10.1088/0004-637X/761/1/62.

X. Cheng, M. D. Ding, J. Zhang, X. D. Sun, Y. Guo, Y. M. Wang, B. Kliem, and Y. Y. Deng. Formation of a Double-decker Magnetic Flux Rope in the Sigmoidal Solar Active Region 11520. *Astrophys. J.*, 789:93, July 2014. doi: 10.1088/0004-637X/789/2/93.

M. C. M. Cheung and H. Isobe. Flux Emergence (Theory). *Living Reviews in Solar Physics*, 11:3, Jul 2014. doi: 10.12942/lrsp-2014-3.

M. C. M. Cheung, P. Boerner, C. J. Schrijver, P. Testa, F. Chen, H. Peter, and A. Malanushenko. Thermal Diagnostics with the Atmospheric Imaging Assembly on board the Solar Dynamics Observatory: A Validated Method for Differential Emission Measure Inversions. *Astrophys. J.*, 807:143, July 2015. doi: 10.1088/0004-637X/807/2/143.

G. Chintzoglou, S. Patsourakos, and A. Vourlidas. Formation of Magnetic Flux Ropes during a Confined Flaring Well before the Onset of a Pair of Major Coronal

Mass Ejections. *Astrophys. J.*, 809:34, Aug. 2015. doi: 10.1088/0004-637X/809/1/34.

C. Chiuderi and M. Velli. *Basics of Plasma Astrophysics*. Springer, 2015. doi: 10.1007/978-88-470-5280-2.

R. Chodura and A. Schlueter. A 3D Code for MHD Equilibrium and Stability. *Journal of Computational Physics*, 41(1):68–88, May 1981. doi: 10.1016/0021-9991(81)90080-2.

S. Couvidat, J. Schou, J. T. Hoeksema, R. S. Bogart, R. I. Bush, T. L. Duvall, Y. Liu, A. A. Norton, and P. H. Scherrer. Observables Processing for the Helioseismic and Magnetic Imager Instrument on the Solar Dynamics Observatory. *Solar Phys.*, 291:1887–1938, Aug. 2016. doi: 10.1007/s11207-016-0957-3.

J. L. Culhane, L. K. Harra, A. M. James, K. Al-Janabi, L. J. Bradley, R. A. Chaudry, K. Rees, J. A. Tandy, P. Thomas, M. C. R. Whillock, B. Winter, G. A. Doschek, C. M. Korendyke, C. M. Brown, S. Myers, J. Mariska, J. Seely, J. Lang, B. J. Kent, B. M. Shaughnessy, P. R. Young, G. M. Simnett, C. M. Castelli, S. Mahmoud, H. Mapson-Menard, B. J. Probyn, R. J. Thomas, J. Davila, K. Dere, D. Windt, J. Shea, R. Hagood, R. Moye, H. Hara, T. Watanabe, K. Matsuzaki, T. Kosugi, V. Hansteen, and Ø. Wikstol. The EUV Imaging Spectrometer for Hinode. *Solar Phys.*, 243:19–61, June 2007. doi: 10.1007/s01007-007-0293-1.

J. L. Culhane, D. H. Brooks, L. van Driel-Gesztelyi, P. Démoulin, D. Baker, M. L. DeRosa, C. H. Mandrini, L. Zhao, and T. H. Zurbuchen. Tracking Solar Active Region Outflow Plasma from Its Source to the Near-Earth Environment. *Solar Phys.*, 289:3799–3816, Oct. 2014. doi: 10.1007/s11207-014-0551-5.

G. Del Zanna. A revised radiometric calibration for the Hinode/EIS instrument. *Astron. Astrophys.*, 555:A47, July 2013. doi: 10.1051/0004-6361/201220810.

G. Del Zanna, K. P. Dere, P. R. Young, E. Landi, and H. E. Mason. CHIANTI - An atomic database for emission lines. Version 8. *Astron. Astrophys.*, 582:A56, Oct. 2015. doi: 10.1051/0004-6361/201526827.

P. Démoulin and G. Aulanier. Criteria for Flux Rope Eruption: Non-equilibrium Versus Torus Instability. *Astrophys. J.*, 718:1388–1399, Aug. 2010. doi: 10.1088/0004-637X/718/2/1388.

P. Démoulin, E. R. Priest, and D. P. Lonie. Three-dimensional magnetic reconnection without null points 2. Application to twisted flux tubes. *J. Geophys. Res.*, 101:7631–7646, Apr. 1996. doi: 10.1029/95JA03558.

K. P. Dere, E. Landi, H. E. Mason, B. C. Monsignori Fossi, and P. R. Young. CHIANTI - an atomic database for emission lines. *Astron. Astrophys. Suppl.*, 125, Oct. 1997. doi: 10.1051/aas:1997368.

V. Domingo, B. Fleck, and A. I. Poland. The SOHO Mission: an Overview. *Solar Phys.*, 162:1–37, Dec. 1995. doi: 10.1007/BF00733425.

S. J. Edwards, C. E. Parnell, L. K. Harra, J. L. Culhane, and D. H. Brooks. A Comparison of Global Magnetic Field Skeletons and Active-Region Upflows. *Solar Phys.*, 291:117–142, Jan. 2016. doi: 10.1007/s11207-015-0807-8.

T. Emonet and F. Moreno-Insertis. The Physics of Twisted Magnetic Tubes Rising in a Stratified Medium: Two-dimensional Results. *Astrophys. J.*, 492:804–821, Jan 1998. doi: 10.1086/305074.

S. Evje and K. H. Karlsen. Discrete approximations of BV solutions to doubly nonlinear degenerate parabolic equations. *Numerische Mathematik*, 86(3):377–417, Sep 2000. ISSN 0945-3245. doi: 10.1007/s002110000156. URL `https://doi.org/10.1007/s002110000156`.

Y. Fan. On the Eruption of Coronal Flux Ropes. *Astrophys. J.*, 719:728–736, Aug. 2010. doi: 10.1088/0004-637X/719/1/728.

Y. Fan and S. E. Gibson. Numerical Simulations of Three-dimensional Coronal Magnetic Fields Resulting from the Emergence of Twisted Magnetic Flux Tubes. *Astrophys. J.*, 609:1123–1133, Jul 2004. doi: 10.1086/421238.

B. Filippov, O. Martsenyuk, A. K. Srivastava, and W. Uddin. Solar Magnetic Flux Ropes. *Journal of Astrophysics and Astronomy*, 36:157–184, Mar. 2015. doi: 10.1007/s12036-015-9321-5.

J. M. Finn and T. Antonsen Jr. Magnetic Helicity: What is it and What is it Good For? *Comments on Plasma Physics and Controlled Fusion*, 9(3):111–126, 1985.

L. Fletcher and H. Hudson. The Magnetic Structure and Generation of EUV Flare Ribbons. *Solar Phys.*, 204:69–89, Dec 2001. doi: 10.1023/A:1014275821318.

T. G. Forbes. A review on the genesis of coronal mass ejections. *J. Geophys. Res.*, 105:23153–23166, Oct. 2000. doi: 10.1029/2000JA000005.

T. G. Forbes, J. A. Linker, J. Chen, C. Cid, J. Kóta, M. A. Lee, G. Mann, Z. Mikić, M. S. Potgieter, J. M. Schmidt, G. L. Siscoe, R. Vainio, S. K. Antiochos, and P. Riley. CME Theory and Models. *Space Sci. Rev.*, 123:251–302, Mar. 2006. doi: 10.1007/s11214-006-9019-8.

M. Fuhrmann, N. Seehafer, and G. Valori. Preprocessing of solar vector magnetograms for force-free magnetic field extrapolation. *Astron. Astrophys.*, 476:349–357, Dec. 2007. doi: 10.1051/0004-6361:20078454.

H. P. Furth, J. Killeen, and M. N. Rosenbluth. Finite-Resistivity Instabilities of a Sheet Pinch. *Physics of Fluids*, 6:459–484, Apr 1963. doi: 10.1063/1.1706761.

G. A. Gary. Plasma Beta above a Solar Active Region: Rethinking the Paradigm. *Solar Phys.*, 203:71–86, Oct. 2001. doi: 10.1023/A:1012722021820.

C. L. Gerrard, D. S. Brown, C. Mellor, T. D. Arber, and A. W. Hood. MHD simulations of sunspot rotation and the coronal consequences. *Solar Phys.*, 213(1): 39–54, Mar 2003. doi: 10.1023/A:1023281624037.

L. M. Green and B. Kliem. Flux Rope Formation Preceding Coronal Mass Ejection Onset. *Astrophys. J. Lett.*, 700:L83–L87, Aug. 2009. doi: 10.1088/0004-637X/700/2/L83.

L. M. Green and B. Kliem. Observations of flux rope formation prior to coronal mass ejections. In B. Schmieder, J.-M. Malherbe, and S. T. Wu, editors, *Nature of Prominences and their Role in Space Weather*, volume 300 of *IAU Symposium*, pages 209–214, Jan. 2014. doi: 10.1017/S1743921313010983.

L. M. Green, M. C. López fuentes, C. H. Mandrini, P. Démoulin, L. Van Driel-Gesztelyi, and J. L. Culhane. The Magnetic Helicity Budget of a cme-Prolific Active Region. *Solar Phys.*, 208:43–68, July 2002. doi: 10.1023/A:1019658520033.

L. M. Green, B. Kliem, and A. J. Wallace. Photospheric flux cancellation and associated flux rope formation and eruption. *Astron. Astrophys.*, 526:A2, Feb. 2011. doi: 10.1051/0004-6361/201015146.

L. M. Green, G. Valori, F. P. Zuccarello, S. Zharkov, S. A. Matthews, and S. L. Guglielmino. The 2013 February 17 Sunquake in the Context of the Active Region's Magnetic Field Configuration. *Astrophys. J.*, 849:40, Nov 2017. doi: 10.3847/1538-4357/aa8db6.

L. M. Green, T. Török, B. Vršnak, W. Manchester, and A. Veronig. The Origin, Early Evolution and Predictability of Solar Eruptions. *Space Sci. Rev.*, 214:46, Feb 2018. doi: 10.1007/s11214-017-0462-5.

Y. Guo, M. D. Ding, B. Schmieder, H. Li, T. Török, and T. Wiegelmann. Driving Mechanism and Onset Condition of a Confined Eruption. *Astrophys. J. Lett.*, 725:L38–L42, Dec. 2010. doi: 10.1088/2041-8205/725/1/L38.

Y. Guo, M. D. Ding, X. Cheng, J. Zhao, and E. Pariat. Twist Accumulation and Topology Structure of a Solar Magnetic Flux Rope. *Astrophys. J.*, 779:157, Dec. 2013. doi: 10.1088/0004-637X/779/2/157.

Y. Guo, E. Pariat, G. Valori, S. Anfinogentov, F. Chen, M. K. Georgoulis, Y. Liu, K. Moraitis, J. K. Thalmann, and S. Yang. Magnetic Helicity Estimations in Models and Observations of the Solar Magnetic Field. III. Twist Number Method. *Astrophys. J.*, 840:40, May 2017. doi: 10.3847/1538-4357/aa6aa8.

G. E. Hale and S. B. Nicholson. The Law of Sun-Spot Polarity. *Astrophys. J.*, 62: 270, Nov 1925. doi: 10.1086/142933.

P. Higgins. Schematic of the Solar Dynamo, Dec 2012. URL `https://figshare.com/articles/Schematic_of_the_Solar_Dynamo/102094/1`.

T. Hirayama. Theoretical Model of Flares and Prominences. I: Evaporating Flare Model. *Solar Phys.*, 34:323–338, Feb 1974. doi: 10.1007/BF00153671.

J. T. Hoeksema, Y. Liu, K. Hayashi, X. Sun, J. Schou, S. Couvidat, A. Norton, M. Bobra, R. Centeno, K. Leka, et al. The Helioseismic and Magnetic Imager (HMI) Vector Magnetic Field Pipeline: Overview and Performance. *Solar Physics*, 289(9):3483–3530, 2014.

A. W. Hood and D. W. Hughes. Solar magnetic fields. *Physics of the Earth and Planetary Interiors*, 187:78–91, Aug 2011. doi: 10.1016/j.pepi.2011.04.010.

A. W. Hood and E. R. Priest. Kink Instability of Solar Coronal Loops as the Cause of Solar Flares. *Solar Phys.*, 64(2):303–321, Dec 1979. doi: 10.1007/BF00151441.

D. W. Hughes, S. A. E. G. Falle, and P. Joarder. The rise of twisted magnetic flux tubes. *Mon. Not. Roy. Astron. Soc.*, 298:433–444, Aug 1998. doi: 10.1046/j.1365-8711.1998.01622.x.

A. W. James, L. M. Green, E. Palmerio, G. Valori, H. A. S. Reid, D. Baker, D. H. Brooks, L. van Driel-Gesztelyi, and E. K. J. Kilpua. On-Disc Observations of Flux Rope Formation Prior to Its Eruption. *Solar Phys.*, 292:71, May 2017. doi: 10.1007/s11207-017-1093-4.

A. W. James, G. Valori, L. M. Green, Y. Liu, M. C. M. Cheung, Y. Guo, and L. van Driel-Gesztelyi. An Observationally Constrained Model of a Flux Rope that Formed in the Solar Corona. *Astrophys. J. Lett.*, 855:L16, Mar. 2018. doi: 10.3847/2041-8213/aab15d.

M. Janvier, G. Aulanier, V. Bommier, B. Schmieder, P. Démoulin, and E. Pariat. Electric Currents in Flare Ribbons: Observations and Three-dimensional Standard Model. *Astrophys. J.*, 788:60, June 2014. doi: 10.1088/0004-637X/788/1/60.

J. Jefferies, B. W. Lites, and A. Skumanich. Transfer of line radiation in a magnetic field. *Astrophys. J.*, 343:920–935, Aug. 1989. doi: 10.1086/167762.

M. L. Kaiser, T. A. Kucera, J. M. Davila, O. C. St. Cyr, M. Guhathakurta, and E. Christian. The STEREO Mission: An Introduction. *Space Sci. Rev.*, 136: 5–16, Apr. 2008. doi: 10.1007/s11214-007-9277-0.

J. T. Karpen, S. K. Antiochos, and C. R. DeVore. The Mechanisms for the Onset and Explosive Eruption of Coronal Mass Ejections and Eruptive Flares. *Astrophys. J.*, 760:81, Nov. 2012. doi: 10.1088/0004-637X/760/1/81.

M. D. Kazachenko, R. C. Canfield, D. W. Longcope, J. Qiu, A. Des Jardins, and R. W. Nightingale. Sunspot Rotation, Flare Energetics, and Flux Rope Helicity: The Eruptive Flare on 2005 May 13. *Astrophys. J.*, 704:1146–1158, Oct. 2009. doi: 10.1088/0004-637X/704/2/1146.

M. D. Kazachenko, R. C. Canfield, D. W. Longcope, and J. Qiu. Sunspot Rotation, Flare Energetics, and Flux Rope Helicity: The Halloween Flare on 2003 October 28. *Astrophys. J.*, 722:1539–1546, Oct. 2010. doi: 10.1088/0004-637X/722/2/1539.

A. Kerdraon and J.-M. Delouis. The Nançay Radioheliograph. In G. Trottet, editor, *Coronal Physics from Radio and Space Observations*, volume 483 of *Lecture Notes in Physics, Berlin Springer Verlag*, page 192, 1997. doi: 10.1007/BFb0106458.

E. K. J. Kilpua, L. K. Jian, Y. Li, J. G. Luhmann, and C. T. Russell. Multipoint ICME encounters: Pre-STEREO and STEREO observations. *Journal of Atmospheric and Solar-Terrestrial Physics*, 73:1228–1241, Jun 2011. doi: 10.1016/j.jastp.2010.10.012.

M. G. Kivelson and C. T. Russell. Book-Received - Introduction to Space Physics. *Science*, 269:862, Aug 1995.

B. Kliem and T. Török. Torus Instability. *Phys. Rev. Let.*, 96(25):255002, June 2006. doi: 10.1103/PhysRevLett.96.255002.

B. Kliem, V. S. Titov, and T. Török. Formation of current sheets and sigmoidal structure by the kink instability of a magnetic loop. *Astron. Astrophys.*, 413: L23–L26, Jan 2004. doi: 10.1051/0004-6361:20031690.

B. Kliem, Y. N. Su, A. A. van Ballegooijen, and E. E. DeLuca. Magnetohydrodynamic Modeling of the Solar Eruption on 2010 April 8. *Astrophys. J.*, 779: 129, Dec. 2013. doi: 10.1088/0004-637X/779/2/129.

Y.-K. Ko, J. C. Raymond, J. Lin, G. Lawrence, J. Li, and A. Fludra. Dynamical and Physical Properties of a Post-Coronal Mass Ejection Current Sheet. *Astrophys. J.*, 594:1068–1084, Sep 2003. doi: 10.1086/376982.

R. A. Kopp and G. W. Pneuman. Magnetic reconnection in the corona and the loop prominence phenomenon. *Solar Phys.*, 50:85–98, Oct 1976. doi: 10.1007/BF00206193.

T. Kosugi, K. Matsuzaki, T. Sakao, T. Shimizu, Y. Sone, S. Tachikawa, T. Hashimoto, K. Minesugi, A. Ohnishi, T. Yamada, et al. The Hinode (Solar-B) Mission: An Overview. *Solar Physics*, 243(1):3–17, 2007.

E. Krausmann, E. Andersson, M. Gibbs, and W. Murtagh. Space Weather & Critical Infrastructures: Findings and Outlook. Technical Report EUR 28237 EN, European Commission Joint Research Centre, 2016.

M. Kubicka, C. Möstl, T. Amerstorfer, P. D. Boakes, L. Feng, J. P. Eastwood, and O. Törmänen. Prediction of Geomagnetic Storm Strength from Inner Heliospheric In Situ Observations. *Astrophys. J.*, 833:255, Dec. 2016. doi: 10.3847/1538-4357/833/2/255.

J. M. Laming. The FIP and Inverse FIP Effects in Solar and Stellar Coronae. *Living Reviews in Solar Physics*, 12:2, Dec. 2015. doi: 10.1007/lrsp-2015-2.

Y. Leblanc, G. A. Dulk, and J.-L. Bougeret. Tracing the Electron Density from the Corona to 1au. *Solar Phys.*, 183:165–180, Nov. 1998. doi: 10.1023/A:1005049730506.

K. D. Leka, G. Barnes, A. D. Crouch, T. R. Metcalf, G. A. Gary, J. Jing, and Y. Liu. Resolving the 180° Ambiguity in Solar Vector Magnetic Field Data: Evaluating the Effects of Noise, Spatial Resolution, and Method Assumptions. *Solar Phys.*, 260:83–108, Nov 2009. doi: 10.1007/s11207-009-9440-8.

J. R. Lemen, A. M. Title, D. J. Akin, P. F. Boerner, C. Chou, J. F. Drake, D. W. Duncan, C. G. Edwards, F. M. Friedlaender, G. F. Heyman, N. E. Hurlburt, N. L. Katz, G. D. Kushner, M. Levay, R. W. Lindgren, D. P. Mathur, E. L. McFeaters, S. Mitchell, R. A. Rehse, C. J. Schrijver, L. A. Springer, R. A. Stern, T. D. Tarbell, J.-P. Wuelser, C. J. Wolfson, C. Yanari, J. A. Bookbinder, P. N. Cheimets, D. Caldwell, E. E. Deluca, R. Gates, L. Golub, S. Park, W. A. Podgorski, R. I. Bush, P. H. Scherrer, M. A. Gummin, P. Smith, G. Auker, P. Jerram, P. Pool, R. Soufli, D. L. Windt, S. Beardsley, M. Clapp, J. Lang, and N. Waltham. The Atmospheric Imaging Assembly (AIA) on the Solar Dynamics Observatory (SDO). *Solar Phys.*, 275:17–40, Jan. 2012. doi: 10.1007/s11207-011-9776-8.

J. Lin and T. G. Forbes. Effects of reconnection on the coronal mass ejection process. *Journal of Geophysical Research*, 105:2375–2392, Feb 2000. doi: 10.1029/1999JA900477.

B. W. Lites. Remote sensing of solar magnetic fields. *Reviews of Geophysics*, 38 (1):1–36, 2000.

Y. Liu, J. T. Hoeksema, P. H. Scherrer, J. Schou, S. Couvidat, R. I. Bush, T. L. Duvall, K. Hayashi, X. Sun, and X. Zhao. Comparison of Line-of-Sight Magnetograms Taken by the Solar Dynamics Observatory/Helioseismic and Magnetic Im-

ager and Solar and Heliospheric Observatory/Michelson Doppler Imager. *Solar Phys.*, 279:295–316, July 2012. doi: 10.1007/s11207-012-9976-x.

Y. Liu, J. T. Hoeksema, and X. Sun. Test of the Hemispheric Rule of Magnetic Helicity in the Sun Using the Helioseismic and Magnetic Imager (HMI) Data. *Astrophys. J.*, 783:L1, Mar 2014. doi: 10.1088/2041-8205/783/1/L1.

Y. Liu, J. T. Hoeksema, X. Sun, and K. Hayashi. Vector Magnetic Field Synoptic Charts from the Helioseismic and Magnetic Imager (HMI). *Solar Phys.*, 292:29, Feb. 2017. doi: 10.1007/s11207-017-1056-9.

D. W. Longcope, B. Ravindra, and G. Barnes. Determining the Source of Coronal Helicity through Measurements of Braiding and Spin Helicity Fluxes in Active Regions. *Astrophys. J.*, 668:571–585, Oct. 2007. doi: 10.1086/521095.

M. C. López Fuentes, P. Demoulin, C. H. Mandrini, and L. van Driel-Gesztelyi. The Counterkink Rotation of a Non-Hale Active Region. *Astrophys. J.*, 544:540–549, Nov. 2000. doi: 10.1086/317180.

M. L. Luoni, P. Démoulin, C. H. Mandrini, and L. van Driel-Gesztelyi. Twisted Flux Tube Emergence Evidenced in Longitudinal Magnetograms: Magnetic Tongues. *Solar Phys.*, 270:45–74, May 2011. doi: 10.1007/s11207-011-9731-8.

B. J. Lynch, S. K. Antiochos, C. R. DeVore, J. G. Luhmann, and T. H. Zurbuchen. Topological Evolution of a Fast Magnetic Breakout CME in Three Dimensions. *Astrophys. J.*, 683:1192-1206, Aug. 2008. doi: 10.1086/589738.

S. Ma, G. D. R. Attrill, L. Golub, and J. Lin. Statistical Study of Coronal Mass Ejections With and Without Distinct Low Coronal Signatures. *Astrophys. J.*, 722:289–301, Oct. 2010. doi: 10.1088/0004-637X/722/1/289.

D. H. Mackay, L. M. Green, and A. van Ballegooijen. Modeling the Dispersal of an Active Region: Quantifying Energy Input into the Corona. *Astrophys. J.*, 729: 97, Mar. 2011. doi: 10.1088/0004-637X/729/2/97.

W. Manchester, E. K. J. Kilpua, Y. D. Liu, N. Lugaz, P. Riley, T. Török, and B. Vršnak. The Physical Processes of CME/ICME Evolution. *Space Sci. Rev.*, 212:1159–1219, Nov 2017. doi: 10.1007/s11214-017-0394-0.

G. Mann, F. Jansen, R. J. MacDowall, M. L. Kaiser, and R. G. Stone. A heliospheric density model and type III radio bursts. *Astron. Astrophys.*, 348:614–620, Aug. 1999.

B. Marder. A Method for Incorporating Gauss' Law into Electromagnetic PIC Codes. *Journal of Computational Physics*, 68:48–55, Jan. 1987. doi: 10.1016/0021-9991(87)90043-X.

B. H. McClintock and A. A. Norton. Recovering Joy's Law as a Function of Solar Cycle, Hemisphere, and Longitude. *Solar Phys.*, 287:215–227, Oct 2013. doi: 10.1007/s11207-013-0338-0.

B. H. McClintock, A. A. Norton, and J. Li. Re-examining Sunspot Tilt Angle to Include Anti-Hale Statistics. *Astrophys. J.*, 797:130, Dec 2014. doi: 10.1088/0004-637X/797/2/130.

D. J. McLean and N. R. Labrum. *Solar Radiophysics: Studies of Emission from the Sun at Metre Wavelengths*. Cambridge University Press, 1985.

T. R. Metcalf. Resolving the 180-degree ambiguity in vector magnetic field measurements: The minimumenergy solution. *Solar Physics*, 155(2):235–242, 1994.

T. R. Metcalf, K. D. Leka, G. Barnes, B. W. Lites, M. K. Georgoulis, A. A. Pevtsov, K. S. Balasubramaniam, G. A. Gary, J. Jing, J. Li, Y. Liu, H. N. Wang, V. Abramenko, V. Yurchyshyn, and Y. J. Moon. An Overview of Existing Algorithms for Resolving the 180° Ambiguity in Vector Magnetic Fields: Quantitative Tests with Synthetic Data. *Solar Phys.*, 237:267–296, Sep 2006. doi: 10.1007/s11207-006-0170-x.

Z. Mikic and J. A. Linker. Disruption of coronal magnetic field arcades. *Astrophys. J.*, 430:898–912, Aug. 1994. doi: 10.1086/174460.

S. Min and J. Chae. The Rotating Sunspot in AR 10930. *Solar Phys.*, 258(2): 203–217, Sep 2009. doi: 10.1007/s11207-009-9425-7.

R. L. Moore and B. J. Labonte. The filament eruption in the 3B flare of July 29, 1973 - Onset and magnetic field configuration. In M. Dryer and E. Tandberg-Hanssen, editors, *Solar and Interplanetary Dynamics*, volume 91 of *IAU Symposium*, pages 207–210, 1980.

R. L. Moore, A. C. Sterling, H. S. Hudson, and J. R. Lemen. Onset of the Magnetic Explosion in Solar Flares and Coronal Mass Ejections. *Astrophys. J.*, 552:833–848, May 2001. doi: 10.1086/320559.

A. Nindos, S. Patsourakos, A. Vourlidas, and C. Tagikas. How Common Are Hot Magnetic Flux Ropes in the Low Solar Corona? A Statistical Study of EUV Observations. *Astrophys. J.*, 808:117, Aug. 2015. doi: 10.1088/0004-637X/808/2/117.

M. J. Owens. Solar Wind and Heavy Ion Properties of Interplanetary Coronal Mass Ejections. *Solar Phys.*, 293:122, Aug 2018. doi: 10.1007/s11207-018-1343-0.

E. Palmerio, E. K. J. Kilpua, A. W. James, L. M. Green, J. Pomoell, A. Isavnin, and G. Valori. Determining the Intrinsic CME Flux Rope Type Using Remote-sensing Solar Disk Observations. *Solar Phys.*, 292:39, Feb. 2017. doi: 10.1007/s11207-017-1063-x.

E. Palmerio, E. K. J. Kilpua, C. Möstl, V. Bothmer, A. W. James, L. M. Green, A. Isavnin, J. A. Davies, and R. A. Harrison. Coronal Magnetic Structure of Earthbound CMEs and In Situ Comparison. *Space Weather*, 16(5):442–460, May 2018. doi: 10.1002/2017SW001767.

E. Pariat, G. Aulanier, B. Schmieder, M. K. Georgoulis, D. M. Rust, and P. N. Bernasconi. Resistive Emergence of Undulatory Flux Tubes. *Astrophys. J.*, 614: 1099–1112, Oct 2004. doi: 10.1086/423891.

E. Pariat, J. E. Leake, G. Valori, M. G. Linton, F. P. Zuccarello, and K. Dalmasse. Relative magnetic helicity as a diagnostic of solar eruptivity. *Astron. Astrophys.*, 601:A125, May 2017. doi: 10.1051/0004-6361/201630043.

E. N. Parker. The Formation of Sunspots from the Solar Toroidal Field. *Astrophys. J.*, 121:491, Mar 1955. doi: 10.1086/146010.

E. N. Parker. Sweet's Mechanism for Merging Magnetic Fields in Conducting Fluids. *Journal of Geophysical Research*, 62:509–520, Dec 1957. doi: 10.1029/JZ062i004p00509.

S. Patsourakos, A. Vourlidas, and G. Stenborg. Direct Evidence for a Fast Coronal Mass Ejection Driven by the Prior Formation and Subsequent Destabilization of a Magnetic Flux Rope. *Astrophys. J.*, 764:125, Feb. 2013. doi: 10.1088/0004-637X/764/2/125.

W. D. Pesnell, B. J. Thompson, and P. C. Chamberlin. The Solar Dynamics Observatory (SDO). *Solar Phys.*, 275:3–15, Jan. 2012. doi: 10.1007/s11207-011-9841-3.

A. A. Pevtsov, R. C. Canfield, and T. R. Metcalf. Latitudinal Variation of Helicity of Photospheric Magnetic Fields. *Astrophys. J.*, 440:L109, Feb. 1995. doi: 10.1086/187773.

A. A. Pevtsov, R. C. Canfield, and A. N. McClymont. On the Subphotospheric Origin of Coronal Electric Currents. *Astrophys. J.*, 481:973–977, May 1997.

A. A. Pevtsov, R. C. Canfield, and S. M. Latushko. Hemispheric Helicity Trend for Solar Cycle 23. *Astrophys. J.*, 549:L261–L263, Mar 2001. doi: 10.1086/319179.

K. J. H. Phillips. *Guide to the Sun*. Cambridge University Press, Mar. 1995. ISBN 052139788X.

M. Pick and N. Vilmer. Sixty-five years of solar radioastronomy: flares, coronal mass ejections and Sun Earth connection. *Astron. Astrophys. Rev.*, 16:1–153, Oct. 2008. doi: 10.1007/s00159-008-0013-x.

V. Polito, G. Del Zanna, G. Valori, E. Pariat, H. E. Mason, J. Dudík, and M. Janvier. Analysis and modelling of recurrent solar flares observed with Hinode/EIS on March 9, 2012. *Astron. Astrophys.*, 601:A39, May 2017. doi: 10.1051/0004-6361/201629703.

E. R. Priest and P. Démoulin. Three-dimensional magnetic reconnection without null points. 1. Basic theory of magnetic flipping. *Journal of Geophysical Research*, 100:23443–23464, Dec 1995. doi: 10.1029/95JA02740.

F. Pucci and M. Velli. Reconnection of Quasi-singular Current Sheets: The "Ideal" Tearing Mode. *Astrophys. J.*, 780:L19, Jan 2014. doi: 10.1088/2041-8205/780/2/L19.

K. K. Reeves and L. Golub. Atmospheric Imaging Assembly Observations of Hot Flare Plasma. *Astrophys. J. Lett.*, 727:L52, Feb. 2011. doi: 10.1088/2041-8205/727/2/L52.

H. A. S. Reid and H. Ratcliffe. A review of solar type III radio bursts. *Res. Astron. Astrophys.*, 14:773–804, July 2014. doi: 10.1088/1674-4527/14/7/003.

I. G. Richardson and H. V. Cane. Near-Earth Interplanetary Coronal Mass Ejections During Solar Cycle 23 (1996 - 2009): Catalog and Summary of Properties. *Solar Phys.*, 264:189–237, June 2010. doi: 10.1007/s11207-010-9568-6.

M. Rieutord and F. Rincon. The Sun's Supergranulation. *Living Reviews in Solar Physics*, 7(1):2, Jun 2010. doi: 10.12942/lrsp-2010-2.

E. Robbrecht, S. Patsourakos, and A. Vourlidas. No Trace Left Behind: STEREO Observation of a Coronal Mass Ejection Without Low Coronal Signatures. *Astrophys. J.*, 701:283–291, Aug. 2009. doi: 10.1088/0004-637X/701/1/283.

G. Roumeliotis, P. A. Sturrock, and S. K. Antiochos. A Numerical Study of the Sudden Eruption of Sheared Magnetic Fields. *Astrophys. J.*, 423:847, Mar. 1994. doi: 10.1086/173862.

D. M. Rust. Spawning and shedding helical magnetic fields in the solar atmosphere. *Geophys. Res. Lett.*, 21:241–244, Feb. 1994. doi: 10.1029/94GL00003.

I.-J. Sackmann, A. I. Boothroyd, and K. E. Kraemer. Our Sun. III. Present and Future. *Astrophys. J.*, 418:457, Nov. 1993. doi: 10.1086/173407.

A. S. Savcheva, L. M. Green, A. A. van Ballegooijen, and E. E. DeLuca. Photospheric Flux Cancellation and the Build-up of Sigmoidal Flux Ropes on the Sun. *Astrophys. J.*, 759:105, Nov. 2012. doi: 10.1088/0004-637X/759/2/105.

M. W. Scheeler, W. M. van Rees, H. Kedia, D. Kleckner, and W. T. M. Irvine. Complete measurement of helicity and its dynamics in vortex tubes. *Science*, 357:487–491, Aug. 2017. doi: 10.1126/science.aam6897.

P. H. Scherrer, J. Schou, R. I. Bush, A. G. Kosovichev, R. S. Bogart, J. T. Hoeksema, Y. Liu, T. L. Duvall, J. Zhao, A. M. Title, C. J. Schrijver, T. D. Tarbell, and S. Tomczyk. The Helioseismic and Magnetic Imager (HMI) Investigation for the Solar Dynamics Observatory (SDO). *Solar Phys.*, 275:207–227, Jan. 2012. doi: 10.1007/s11207-011-9834-2.

W. Schmidt, O. von der Lühe, R. Volkmer, C. Denker, S. K. Solanki, H. Balthasar, N. Bello González, T. Berkefeld, M. Collados Vera, A. Hofmann, F. Kneer, A. Lagg, K. G. Puschmann, D. Schmidt, M. Sobotka, D. Soltau, and K. G. Strassmeier. The GREGOR Solar Telescope on Tenerife. In T. R. Rimmele, A. Tritschler, F. Wöger, M. Collados Vera, H. Socas-Navarro, R. Schlichenmaier, M. Carlsson, T. Berger, A. Cadavid, P. R. Gilbert, P. R. Goode, and M. Knölker, editors, *Second ATST-EAST Meeting: Magnetic Fields from the Photosphere to the Corona.*, volume 463 of *Astronomical Society of the Pacific Conference Series*, page 365, Dec 2012.

C. J. Schrijver, M. L. De Rosa, A. M. Title, and T. R. Metcalf. The Nonpotentiality of Active-Region Coronae and the Dynamics of the Photospheric Magnetic Field. *Astrophys. J.*, 628:501–513, July 2005. doi: 10.1086/430733.

N. Seehafer. Determination of constant α force-free solar magnetic fields from magnetograph data. *Solar Phys.*, 58:215–223, July 1978. doi: 10.1007/BF00157267.

N. Seehafer. Electric Current Helicity in the Solar Atmosphere. *Solar Phys.*, 125: 219–232, Sep 1990. doi: 10.1007/BF00158402.

K. Shibata, S. Masuda, M. Shimojo, H. Hara, T. Yokoyama, S. Tsuneta, T. Kosugi, and Y. Ogawara. Hot-Plasma Ejections Associated with Compact-Loop Solar Flares. *Astrophys. J. Lett.*, 451:L83, Oct. 1995. doi: 10.1086/309688.

P. A. Sturrock. Model of the High-Energy Phase of Solar Flares. *Nature*, 211: 695–697, Aug 1966. doi: 10.1038/211695a0.

Z. Sturrock, A. W. Hood, V. Archontis, and C. M. McNeill. Sunspot rotation. I. A consequence of flux emergence. *Astron. Astrophys.*, 582:A76, Oct 2015. doi: 10.1051/0004-6361/201526521.

SunPy Community, S. J. Mumford, S. Christe, D. Pérez-Suárez, J. Ireland, A. Y. Shih, A. R. Inglis, S. Liedtke, R. J. Hewett, F. Mayer, K. Hughitt, N. Freij, T. Meszaros, S. M. Bennett, M. Malocha, J. Evans, A. Agrawal, A. J. Leonard, T. P. Robitaille, B. Mampaey, J. I. Campos-Rozo, and M. S. Kirk. SunPy—Python for solar physics. *Computational Science and Discovery*, 8(1):014009, Jan. 2015. doi: 10.1088/1749-4699/8/1/014009.

P. A. Sweet. In proceedings of the international astronomical union symposium on electromagnetic phenomena in cosmical physics. Stockholm, 1956.

J. B. Taylor. Relaxation of Toroidal Plasma and Generation of Reverse Magnetic Fields. *Phys. Rev. Let.*, 33:1139–1141, Nov 1974. doi: 10.1103/PhysRevLett.33.1139.

M. Temmer, A. M. Veronig, E. P. Kontar, S. Krucker, and B. Vršnak. Combined STEREO/RHESSI Study of Coronal Mass Ejection Acceleration and Particle Acceleration in Solar Flares. *Astrophys. J.*, 712:1410–1420, Apr. 2010. doi: 10.1088/0004-637X/712/2/1410.

V. S. Titov and P. Démoulin. Basic topology of twisted magnetic configurations in solar flares. *Astron. Astrophys.*, 351:707–720, Nov. 1999.

T. Török and B. Kliem. The evolution of twisting coronal magnetic flux tubes. *Astron. Astrophys.*, 406:1043–1059, Aug. 2003. doi: 10.1051/0004-6361:20030692.

T. Török and B. Kliem. Confined and Ejective Eruptions of Kink-unstable Flux Ropes. *Astrophys. J. Lett.*, 630:L97–L100, Sept. 2005. doi: 10.1086/462412.

T. Török and B. Kliem. Numerical simulations of fast and slow coronal mass ejections. *Astronomische Nachrichten*, 328:743, Oct. 2007. doi: 10.1002/asna.200710795.

T. Török, M. A. Berger, and B. Kliem. The writhe of helical structures in the solar corona. *Astron. Astrophys.*, 516:A49, June 2010a. doi: 10.1051/0004-6361/200913578.

T. Török, M. A. Berger, and B. Kliem. The writhe of helical structures in the solar corona. *Astron. Astrophys.*, 516:A49, June 2010b. doi: 10.1051/0004-6361/200913578.

T. Török, M. Temmer, G. Valori, A. M. Veronig, L. van Driel-Gesztelyi, and B. Vršnak. Initiation of Coronal Mass Ejections by Sunspot Rotation. *Solar Phys.*, 286:453–477, Sept. 2013. doi: 10.1007/s11207-013-0269-9.

G. Valori, B. Kliem, and R. Keppens. Extrapolation of a nonlinear force-free field containing a highly twisted magnetic loop. *Astron. Astrophys.*, 433:335–347, Apr. 2005. doi: 10.1051/0004-6361:20042008.

G. Valori, B. Kliem, and M. Fuhrmann. Magnetofrictional Extrapolations of Low and Lou's Force-Free Equilibria. *Solar Phys.*, 245:263–285, Oct. 2007. doi: 10.1007/s11207-007-9046-y.

G. Valori, B. Kliem, T. Török, and V. S. Titov. Testing magnetofrictional extrapolation with the Titov-Démoulin model of solar active regions. *Astron. Astrophys.*, 519:A44, Sept. 2010. doi: 10.1051/0004-6361/201014416.

G. Valori, L. M. Green, P. Démoulin, S. Vargas Domínguez, L. van Driel-Gesztelyi, A. Wallace, D. Baker, and M. Fuhrmann. Nonlinear Force-Free Extrapolation of Emerging Flux with a Global Twist and Serpentine Fine Structures. *Solar Phys.*, 278:73–97, May 2012. doi: 10.1007/s11207-011-9865-8.

G. Valori, P. Démoulin, E. Pariat, and S. Masson. Accuracy of magnetic energy computations. *Astron. Astrophys.*, 553:A38, May 2013. doi: 10.1051/0004-6361/201220982.

A. A. van Ballegooijen and P. C. H. Martens. Formation and eruption of solar prominences. *Astrophys. J.*, 343:971–984, Aug. 1989. doi: 10.1086/167766.

L. van Driel-Gesztelyi and L. M. Green. Evolution of Active Regions. *Living Reviews in Solar Physics*, 12, Sept. 2015. doi: 10.1007/lrsp-2015-1.

W. van Tend and M. Kuperus. The development of coronal electric current systems in active regions and their relation to filaments and flares. *Solar Phys.*, 59:115–127, Sept. 1978. doi: 10.1007/BF00154935.

P. Vemareddy, X. Cheng, and B. Ravindra. Sunspot Rotation as a Driver of Major Solar Eruptions in the NOAA Active Region 12158. *Astrophys. J.*, 829:24, Sept. 2016. doi: 10.3847/0004-637X/829/1/24.

P. Vemareddy, N. Gopalswamy, and B. Ravindra. Prominence Eruption Initiated by Helical Kink Instability of an Embedded Flux Rope. *Astrophys. J.*, 850:38, Nov. 2017. doi: 10.3847/1538-4357/aa9020.

A. Vourlidas, B. J. Lynch, R. A. Howard, and Y. Li. How Many CMEs Have Flux Ropes? Deciphering the Signatures of Shocks, Flux Ropes, and Prominences in Coronagraph Observations of CMEs. *Solar Phys.*, 284:179–201, May 2013. doi: 10.1007/s11207-012-0084-8.

H. P. Warren, I. Ugarte-Urra, and E. Landi. The Absolute Calibration of the EUV Imaging Spectrometer on Hinode. *Astrophys. J. Suppl.*, 213:11, July 2014. doi: 10.1088/0067-0049/213/1/11.

M. S. Wheatland, P. A. Sturrock, and G. Roumeliotis. An Optimization Approach to Reconstructing Force-free Fields. *Astrophys. J.*, 540:1150–1155, Sept. 2000. doi: 10.1086/309355.

T. Wiegelmann and T. Sakurai. Solar Force-free Magnetic Fields. *Living Reviews in Solar Physics*, 9:5, Sept. 2012. doi: 10.12942/lrsp-2012-5.

T. Wiegelmann and S. K. Solanki. Why are Coronal Holes Indistinguishable from the Quiet Sun in Transition Region Radiation? In R. W. Walsh, J. Ireland, D. Danesy, and B. Fleck, editors, *SOHO 15 Coronal Heating*, volume 575 of *ESA Special Publication*, page 35, Dec 2004.

L. Woltjer. A Theorem on Force-Free Magnetic Fields. *Proceedings of the National Academy of Science*, 44:489–491, Jun 1958. doi: 10.1073/pnas.44.6.489.

X. L. Yan, Z. Q. Qu, D. F. Kong, and C. L. Xu. Sunspot Rotation, Sigmoidal Filament, Flare, and Coronal Mass Ejection: The Event on 2000 February 10. *Astrophys. J.*, 754:16, July 2012. doi: 10.1088/0004-637X/754/1/16.

W. H. Yang, P. A. Sturrock, and S. K. Antiochos. Force-free magnetic fields - The magneto-frictional method. *Astrophys. J.*, 309:383–391, Oct. 1986. doi: 10.1086/164610.

S. L. Yardley. *The role of flux cancellation in the formation of filaments and eruptive structures*. PhD thesis, University College London (United Kingdom), Feb. 2017. URL `http://discovery.ucl.ac.uk/id/eprint/1539954`.

S. L. Yardley, L. M. Green, L. van Driel-Gesztelyi, D. R. Williams, and D. H. Mackay. The Role of Flux Cancellation in Eruptions from Bipolar ARs. *Astrophys. J.*, 866:8, Oct 2018. doi: 10.3847/1538-4357/aade4a.

H. Zhang, S. Yang, Y. Gao, J. Su, D. D. Sokoloff, and K. Kuzanyan. Large-scale Soft X-ray Loops and Their Magnetic Chirality in Both Hemispheres. *Astrophys. J.*, 719:1955–1963, Aug 2010. doi: 10.1088/0004-637X/719/2/1955.

J. Zhang and K. P. Dere. A Statistical Study of Main and Residual Accelerations of Coronal Mass Ejections. *Astrophys. J.*, 649:1100–1109, Oct. 2006. doi: 10.1086/506903.

J. Zhang, X. Cheng, and M.-D. Ding. Observation of an evolving magnetic flux rope before and during a solar eruption. *Nat. Commun.*, 3:747, Mar. 2012. doi: 10.1038/ncomms1753.

F. P. Zuccarello, G. Aulanier, and S. A. Gilchrist. Critical Decay Index at the Onset of Solar Eruptions. *Astrophys. J.*, 814:126, Dec. 2015. doi: 10.1088/0004-637X/814/2/126.

F. P. Zuccarello, G. Aulanier, and S. A. Gilchrist. The Apparent Critical Decay Index at the Onset of Solar Prominence Eruptions. *Astrophys. J. Lett.*, 821:L23, Apr. 2016. doi: 10.3847/2041-8205/821/2/L23.